Fall 2014

Crossflow instability and transition on a circular cone at angle of attack in a Mach-6 quiet tunnel

Christopher A. C Ward
Purdue University

Graduate School Form 30
(Revised 08/14)

PURDUE UNIVERSITY
GRADUATE SCHOOL
Thesis/Dissertation Acceptance

This is to certify that the thesis/dissertation prepared

By Christopher A. C. Ward

Entitled
Crossflow Instability and Transition on a Circular Cone at Angle of Attack in a Mach-6 Quiet Tunnel

For the degree of Doctor of Philosophy

Is approved by the final examining committee:

Steven P. Schneider

Rudolph A. King

John P. Sullivan

Gregory A. Blaisdell

Meelan M. Choudhari

To the best of my knowledge and as understood by the student in the Thesis/Dissertation Agreement, Publication Delay, and Certification/Disclaimer (Graduate School Form 32), this thesis/dissertation adheres to the provisions of Purdue University's "Policy on Integrity in Research" and the use of copyrighted material.

Approved by Major Professor(s): Steven P. Schneider

Approved by: Tom Shih 10/02/2014

Head of the Department Graduate Program Date

CROSSFLOW INSTABILITY AND TRANSITION ON A CIRCULAR CONE AT ANGLE OF ATTACK IN A MACH-6 QUIET TUNNEL

A Dissertation

Submitted to the Faculty

of

Purdue University

by

Christopher A. C. Ward

In Partial Fulfillment of the

Requirements for the Degree

of

Doctor of Philosophy

December 2014

Purdue University

West Lafayette, Indiana

ACKNOWLEDGMENTS

First of all, I would like to thank Professor Steven Schneider for his help, advice and guidance. I would also like to thank Professor John Sullivan, Dr. Meelan Choudhari, Dr. Rudolph King and Professor Greg Blaisdell for their suggestions and insight as members on my committee.

I would also like to thank Jerry Hahn, Robin Snodgrass, and Jim Younts of the ASL machine shop for building my models used in the experiments, and for general advice when designing these models. Many thanks also go to John Phillips, who provided help in fixing my various sensor and wiring problems.

And of course I would like to thank all the members of Team Schneider: Brad Wheaton, Laura Steen, George Moraru, Greg McKiernan, Ryan Luersen, Laura Letterman, Tom Juliano, Ryan Henderson, Peter Gilbert, Brandon Chynoweth, Amanda Chou, Katya Casper, Matt Borg, Dennis Berridge and Andrew Abney. The long hours spent in the lab would have been an order of magnitude less amusing without you all. Last but not least, I would like to thank my family for all their love and support over the years.

Funding for this work was provided by the Air Force Office of Scientific Research (AFOSR).

TABLE OF CONTENTS

LIST OF TABLES

LIST OF FIGURES

Figure Page

Figure Page

Figure Page

Figure Page

Figure Page

SYMBOLS

A	amplitude of instability wave
c_r	wave phase velocity, m/s
D	dimple diameter, μm
f	frequency, kHz
k	thermal conductivity, W/K-m
L	paint thickness, mm
M	Mach number
N	Integrated amplification factor
n	Local azimuthal wavenumber per radian
p	pressure, psia
p'	pressure fluctuations, psia
p_c	edge pressure for cone at 0° angle of attack, psia
q	heat flux, kW/m^2
q_{th}	theoretical heat transfer for cone at 0° angle of attack, kW/m^2
Ra	average roughness, μm
Rq	root-mean square roughness, μm
Re	Reynolds number
St	Stanton number
T	temperature, K or °C
t	time, s
u	velocity, m/s
x	cone axial coordinate
y	cone spanwise coordinate

Greek

α	growth rate of instability wave, 1/m
γ^2	magnitude-squared coherence
Θ	phase difference, degrees
λ	wavelength of stationary crossflow instability
μ	kinematic viscosity, Pa-s
ρ	density, kg/m^3
τ	time delay, s
ϕ	azimuthal angle from windward ray, degrees

Subscripts

0	stagnation condition
∞	freestream condition
i	initial condition
th	theoretical laminar value
w	model wall condition

Abbreviations

AoA	Angle of Attack
BAM6QT	Boeing/AFOSR Mach-6 Quiet Tunnel
CFD	Computational Fluid Dynamics
PSE	Parabolized Stability Equations
LST	Linear Stability Theory
PSD	Power Spectral Density
RMS	Root Mean Square
TSP	Temperature-Sensitive Paint
SB	Schmidt-Boelter Heat Transfer Gauge

ABSTRACT

Ward, Christopher A. C. Ph.D., Purdue University, December 2014. Crossflow Instability and Transition on a Circular Cone at Angle of Attack in a Mach-6 Quiet Tunnel. Major Professor: Steven P. Schneider.

To investigate the effect of roughness on the stationary crossflow vortices, roughness elements 2 inches from the nosetip were created in a Torlon insert section of a 7-deg half-angle cone at 6-deg angle of attack in the Boeing/AFOSR Mach-6 Quiet Tunnel. Crossflow-induced transition was measured under fully quiet flow. Roughness elements with depths and diameters on the order of 500 microns were found to have a significant effect on the generation of the stationary vortices and the location of crossflow-induced transition under quiet flow. The controlled roughness elements also appeared to dominate the generation of the vortices, overwhelming the effect that the random roughness of the cone had on the stationary vortices. It was surprising that the stationary vortices did not break down until close to the lee ray, disagreeing with linear stability computations. The roughness elements had the biggest effect on the stationary vortices at approximately 150-deg to 180-deg from the windward ray, depending on conditions. The roughness elements had a minimal impact on boundary-layer transition under noisy flow.

The travelling crossflow waves were measured with Kulite pressure transducers under both noisy and quiet flow. The wave properties agreed well with computations by Texas A&M and experiments by TU Braunschweig under similar conditions. The amplitude of the waves was reduced by approximately 20 times when the noise levels in the BAM6QT were reduced from noisy to quiet.

An interaction between the stationary and travelling crossflow waves was observed. When large stationary waves were induced with either controlled or uncontrolled roughness and the stationary waves passed near or over a fast pressure transducer,

this fast pressure transducer measured a damped or distorted travelling crossflow wave. The nature of this stationary-travelling wave interaction is poorly understood but it may be a significant factor in crossflow-induced transition.

A high-frequency instability was measured near the breakdown of the stationary waves. The instability disappeared when the sensors were rotated by small angles. This instability may be caused by the secondary instability of the stationary crossflow, but computational comparisons are needed.

1. INTRODUCTION AND MOTIVATION

1.1 Boundary-Layer Transition and Tunnel Noise

Accurate prediction of hypersonic laminar-to-turbulent transition is crucial for accurate predictions of heat transfer, skin friction, separation, and other boundary-layer properties [1]. A turbulent boundary layer can have roughly 3–8 times higher heating than its laminar counterpart. Boundary-layer transition prediction is not exact, and the uncertainty affects the design of hypersonic vehicles. A conservative approach for a vehicle would involve designing a thermal protection system that would be able to withstand high turbulent boundary-layer heating, even though the boundary layer may be laminar [2]. The additional weight and complexity is costly and may be prohibitive.

Boundary-layer transition is a complicated and poorly understood process. Disturbances can be created in the freestream (acoustic radiation, vorticity) or by the vehicle surface (surface roughness, waviness) [3]. The disturbances enter the boundary layer through the process of receptivity. Receptivity determines the initial amplitude of the disturbances, along with the frequency and phase [4]. Receptivity can be affected by roughness, bluntness, Mach number and other factors [5]. These disturbances grow and may lead to transition, depending on the instabilities present in the boundary layer.

The initial growth of the disturbances is often linear [6], and the growth can be predicted reasonably well with linear stability theory (LST). LST works well if the disturbance amplitudes are relatively low. LST can be combined with semi-empirical methods such as the e^N method to predict transition [6], but these semi-empirical (or empirical) methods are not reliable for a wide range of cases and often neglect nonlinear and secondary-instability effects. Empirical methods are based solely on

observation or experimentation, while semi-empirical methods attempt to incorporate physical attributes or scientific law along with experimental results. A more basic understanding of the flow physics that causes transition is needed, thereby reducing empiricism.

There are many factors that can influence transition, including Reynolds number, Mach number, surface roughness, freestream vorticity and freestream noise levels. Freestream vorticity can have a significant effect on transition by crossflow instability modes, as will be discussed later. For hypersonic tunnels, acoustic noise is generally the dominant freestream fluctuation [7], and the magnitude of these noise levels is proportional to Mach number to the fourth power [8]. Typically a conventional wind tunnel will have a turbulent nozzle-wall boundary layer, which radiates much larger pressure fluctuations (noise) compared to a laminar boundary layer. This can readily be seen in Figure 1.1. The lower boundary-layer of the cone is fully turbulent, and acoustic waves can be seen radiating from the boundary-layer as striations in the shadowgraph. These acoustic waves radiate downstream at the Mach angle. On the upper surface, there exists an intermittently turbulent boundary layer. Above the turbulent spots, once again the acoustic noise can be seen radiating downstream at the Mach angle. There are also strong waves appearing where the spots originate and terminate. Above the laminar portion of the boundary-layer, these same acoustic waves cannot be seen.

Conventional hypersonic tunnels typically have noise levels much higher than atmospheric noise levels. The noise level of a flow is usually expressed as the ratio of the root-mean-square (RMS) pitot stagnation pressure to the mean pitot stagnation pressure. A conventional hypersonic tunnel has noise levels between 1 and 3%, while atmospheric noise levels are typically less than 0.05% [8]. The high conventional tunnel noise levels have been shown to change the parametric trends of transition and to lead to early transition [7]. A quiet wind tunnel maintains laminar nozzle-wall boundary layers and has noise levels on the order of 0.05%, much more similar to atmospheric noise levels. Although a quiet tunnel contains low freestream noise

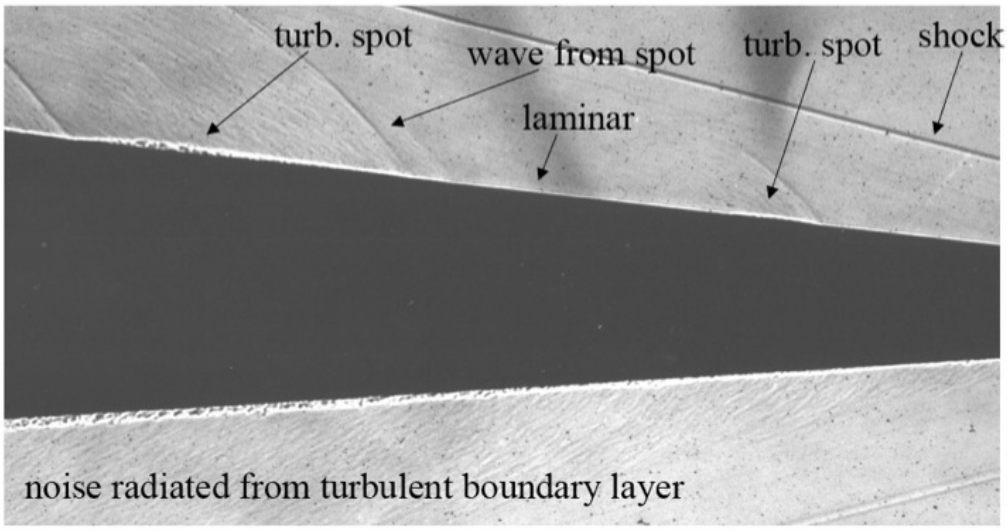

Figure 1.1.: Shadowgraph of sharp cone at M = 4.31. Image taken by Dan Reda and available in Reference [9]

levels similar to flight, no single tunnel can simulate all aspects of hypersonic flight. Quiet tunnels are limited to relatively low Reynolds numbers, Mach numbers and enthalpies. A conventional tunnel can provide a range of these parameters, but with an increase in tunnel noise. If the effect of noise can be understood, then methods can be developed to extrapolate data from both noisy and quiet ground test environments to flight to create a greater understanding of hypersonic transition.

1.2 Transition Mechanisms

There are several instabilities that can cause transition in a three-dimensional boundary layer. These include the attachment-line, streamwise, centrifugal and crossflow instabilities. Disturbances originating near the attachment line create the attachment-line instability. These disturbances can then feed downstream, causing boundary-layer transition [10]. The centrifugal instability is important in areas of concave curvature, and manifests as Görtler vortices [11]. The streamwise instability at low speeds creates Tollmien-Schlichting waves [12], and at high speeds manifests

itself as 1st and 2nd mode waves [13]. The crossflow instability occurs in regions where three-dimensional pressure gradients exist (e.g. swept surfaces, rotating disks and cones at angle of attack).

For a cone at angle of attack in supersonic flow, the shock is stronger near the windward ray than the leeward ray. A circumferential pressure gradient is created, causing the inviscid streamlines to be curved towards the lee ray. In the boundary layer approaching the wall, the streamwise velocity is reduced but the pressure gradient remains constant. Thus, an imbalance between the pressure gradient and the centripetal acceleration exists in the boundary layer, and a secondary flow perpendicular to the inviscid streamlines, known as crossflow, is created. Crossflow drives fluid from the windward to the leeward symmetry ray, causing a thinning of the windward and a thickening of the leeward boundary layers.

Figure 1.2 depicts a sample three-dimensional boundary-layer profile with the addition of the crossflow velocity component. The crossflow velocity profile is inflectional because crossflow must vanish at the walls and at the edge of the boundary layer (because of the no-slip condition at the wall and the balance of the centripetal acceleration and pressure gradient at the edge of the boundary layer) [10]. An inflection point is a source of an inviscid instability. The instability can manifest itself as co-rotating vortices forming around the inflection point, approximately aligned with the inviscid streamlines and stationary with respect to the surface [10]. A thorough description of the stationary crossflow vortices was provided by Gregory et al. [14]. The instability can also appear as vortices that travel with respect to the surface. The travelling vortices or waves may be inclined with respect to the inviscid streamlines [15]. Although both the travelling and stationary waves may be present, low-speed transition is typically caused by only one of these waves and depends on freestream turbulence levels [16]. It is not clear if one crossflow mode dominates transition at hypersonic speeds.

Whether the stationary or travelling waves dominate the transition process is related to the receptivity process. The stationary waves have been shown to be

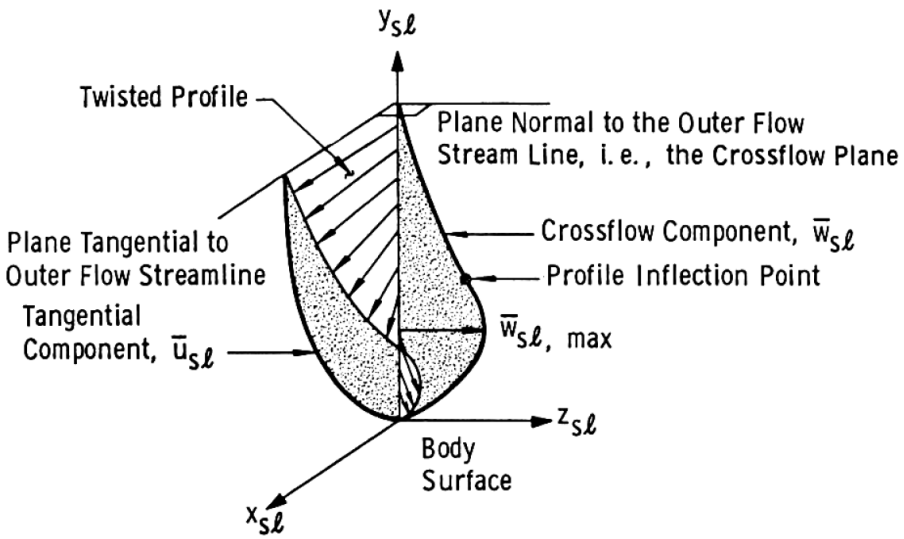

Figure 1.2.: Schematic of a three-dimensional boundary layer. The crossflow velocity profile is perpendicular to the inviscid streamlines and is inflectional. Image from Adams [17].

sensitive to surface roughness, and tend to dominate in low-disturbance environments such as quiet tunnels or in flight [16]. Travelling waves tend to be more sensitive to freestream turbulence, and are more likely to be the dominant mechanism for transition in high-disturbance environments [16, 18, 19]. Both of these ideas have been verified at low speeds, but not at high speeds.

When the stationary instability becomes saturated, a high-frequency secondary instability appears [20]. The secondary instability travels along the stationary vortex, and appears as a ring-like vortex [21]. The travelling secondary instability is created by an inflectional velocity profile in the high shear layer between the stationary vortex and the edge of the boundary layer. The frequency of the secondary instability at low speeds is significantly higher than the primary travelling instability by roughly an order of magnitude [22].

Once again, it is important to note that the majority of our knowledge of the crossflow instability comes from low-speed theoretical and experimental work. The

low-speed work may be used to help estimate the physics of high-speed crossflow, but these low-speed hypotheses need to be evaluated at high speeds.

1.3 Research Objectives

The purpose of the present research is to study and measure the stationary and travelling crossflow waves in a controlled manner. A real hypersonic lifting vehicle will have some finite roughness and the crossflow instability will be generated in the boundary layer due to the three-dimensionality of the flow. It is known that for low-speed flight the stationary crossflow instability dominates crossflow-induced boundary-layer transition, but it is not known if this is the case for hypersonic flight. It is possible that the travelling crossflow has a more pertinent role in crossflow-induced transition in high-speed low disturbance environments.

The research objectives are as follows:

- Create controlled stationary crossflow vortices with roughness elements on a cone at angle of attack.
- Alter the geometrical parameters of the roughness elements and study the effect these parameters have on the stationary crossflow vortices.
- Measure travelling crossflow wave properties with fast pressure transducers and determine if there is any interaction between the stationary and travelling crossflow modes.
- Study the breakdown of the stationary crossflow waves with both temperature-sensitive paint and fast pressure transducers.

2. REVIEW OF LITERATURE

2.1 Low-Speed Experiments and Simulations

There has been a wealth of experiments studying low-speed crossflow-induced transition on a swept plate, wing or cylinder, dating back to the 1940s. A crossflow component of flow exists in the boundary layer of a swept wing because the pressure gradient and streamlines are not parallel. The inviscid streamlines are curved because they must follow the swept attachment line, but are subsequently pushed back towards the root of the wing due to the favourable pressure gradient. Jones [23] and Sears [24] published theoretical papers discussing boundary-layer transition on a yawed cylinder. It was expected that transition would be caused by the two-dimensional Tolmien-Schlichting waves, and the transition location would be based on the chordwise Reynolds number. Therefore, for a given freestream velocity, it was thought that transition would occur further downstream on a yawed cylinder compared to a straight cylinder due to the sweep angle. Experiments by Gray showed that three dimensionality has a significant effect on boundary-layer transition [25]. Transition was found to occur much further upstream than what was expected based on the theoretical works of Jones and Sears. Gray noticed that if the wing sweep was great enough, a pattern of closely spaced streaks would appear, approximately aligned with the inviscid flow and stationary with respect to the wing's surface. The streaks were a manifestation of a three-dimensional instability not present on a two-dimensional wing.

The theoretical work was re-examined by Owen and Randall [26] and Squire [27]. They were able to calculate the crossflow component of the flow in the boundary layer. It was shown that the crossflow velocity profile was inflectional, and thus unstable at low crossflow Reynolds numbers (on the order of 100). It was also shown

that the streamwise streaks seen by Gray were a product of the unstable crossflow velocity profile. Additional experimental work by Allens and Burrows [28, 29] also showed that transition occurred earlier for the three-dimensional case compared to the two-dimensional case, and the streamwise streaks were again visible.

Approximately 20 years later, Poll [22] looked at flow over a yawed cylinder at Reynolds numbers between 0.5×10^6/m and 3.7×10^6/m, in a tunnel with a freestream turbulence level less than 0.16%. Using several different surface visualization techniques, Poll was able to observe the stationary streaks (stationary crossflow vortices). The transition front was found to be irregular, creating what Poll described as a "sawtooth" transition front. Transition due to crossflow is a localized event, explaining the irregular transition front [30]. Poll measured velocity fluctuations at 1.1 kHz and 17.5 kHz using a hot wire. The 1.1 kHz fluctuation was attributed to the primary travelling instability. The 17.5 kHz was detected just upstream of the onset of transition, and was incorrectly attributed to intermittently turbulent flow. Kohama suggested that the high-frequency fluctuation was not intermittently turbulent flow, but the footprint of a travelling secondary instability of the primary stationary instability [21]. Kohama's insight is now the widely accepted explanation for the high-frequency fluctuations [19].

Nitschke-Kowsky and Bippes [31, 32] measured both the travelling and stationary waves on a swept flat plate at low speeds. The stationary waves were measured with oil-flow visualization and hot-wire traverses. The travelling waves were measured with two hot wires since a single hot wire can only determine the frequency and amplitude of the wave, but not the wave's propagation direction. The stationary waves were approximately aligned with the inviscid streamlines, while the travelling waves were found to be inclined to the inviscid streamlines (although they did not provide a propagation angle).

Bippes et al. [33, 34] looked at varying the tunnel disturbance levels using speakers and screens far upstream of a swept flat plate. This was done in an attempt to determine at which conditions the stationary or the travelling modes dominate. It

was found that when the tunnel noise levels were varied with the speaker, no change in transition location was found. It was stated that the boundary layer receptivity to noise can probably be neglected, provided that the noise frequencies are less than the frequencies of the most unstable travelling waves. Turbulence levels were then varied with screens upstream of the test section. When the turbulence levels were low (less than 0.2%), the growth of the stationary modes was larger, and transition was assumed to be dominated by the stationary modes based on the larger stationary-mode amplitude. When turbulence levels were high (greater than 0.2%), the growth of the travelling modes was larger, and transition was assumed to be dominated by the travelling modes based on the larger travelling-mode amplitude. Further increases in turbulence levels caused transition to move upstream.

Computations by Malik and Poll [35] showed that on a yawed cylinder the most amplified crossflow instabilities are the travelling waves, and not the stationary waves. Others have also used local linear stability theory to compute that the travelling waves have greater amplitudes than the stationary waves, and this appears to be the general case for a boundary layer with crossflow [16, 33, 36]. Although linear theory predicts that the travelling waves have higher amplitudes, the stationary waves tend to dominate in low-disturbance environments. The incongruity between experiments and the linear calculations is likely due to nonlinear growth of the waves. The crossflow waves appear to saturate quickly, and nonlinear effects began to dominate. To accurately predict the growth of the waves, nonlinear effects need to be computed and accurate initial conditions are required.

Saric and Yeates [37] performed experiments with a swept wing in a tunnel with much lower turbulence levels (0.02%) compared to the Nitschke-Kowsky and Bippes experiments. They found that the stationary waves had larger amplitudes and appeared to be the dominant cause of transition. Radeztsky et al. [30] found that the stationary waves are relatively insensitive to freestream sound. Sound was introduced at a broad range of frequencies and the crossflow-induced transition did not seem to

be affected. Nitschke-Kowsky and Bippes [31] stated that the travelling waves may be more efficiently initiated by free-stream turbulence than the stationary waves.

Once it was determined that the stationary waves dominate in low-disturbance environments at low speeds, much work has gone into controlling the stationary waves, since they will likely be the dominant cause of crossflow-induced transition in low-speed flight. A swept wing with discrete roughness elements was studied by Radeztsky et al. in a low-disturbance wind tunnel [30]. A random distribution of roughness was shown to have a significant effect on the stationary waves and the location of transition. By polishing the surface, transition was found to move back by more than 50% of the chord. An array of isolated roughness elements were then placed near the attachment line of the polished surface. Radeztsky was able to control the formation of the stationary vortices with the roughness elements and promote crossflow-induced transition, provided that the roughness was placed close to the location of the first neutral point of the stationary modes. The neutral point refers to the location at which the waves begin to amplify. If the roughness was placed too far upstream of the neutral point, the waves would tend to decay. If the roughness was placed too far downstream of the neutral point, the waves would tend to not grow as large. Reynolds numbers based on the roughness height (Re_k) is defined as

$$Re_k = \frac{kU_k}{\nu_k}, \tag{2.1}$$

where k is the roughness height, and U_k and ν_k are the streamwise velocity and kinematic viscosity at a height k in the absence of the roughness element, respectively. Re_k values of less than 0.01 were found to effectively generate stationary waves. This was surprising at the time, because roughness with an Re_k of less than 25 was not expected to have an effect on boundary-layer transition [38]. Radeztsky also found that the diameter of the roughness element was significant. If the diameter of the element was too small, it did not effectively induce stationary waves, even if the roughness height was increased significantly. It was suggested the diameter of the roughness must be at least 10% of the stationary wavelength to be effective, and 50%

appears to be most effective. This work was the first time controlled measurements of the stationary crossflow instability were made.

Saric et al. furthered the work by Radetzky by attempting to manipulate the stationary waves to delay transition [39]. Roughness elements were first placed 12 mm apart in the spanwise direction in order to force the most unstable stationary mode, according to linear theory. Saric states that only the primary disturbance wavenumber and superharmonics appear in the boundary layer, no subharmonics. For example, if a stationary mode with a wavelength of 12 mm is forced, stationary waves with wavelengths of 12, 6 and 4 mm will appear in the boundary layer. Larger wavelengths are then subsequently suppressed. Saric's experiments confirmed this idea by placing roughness elements 6 mm apart (with 6 mm being a more stable wavelength than 12 mm). The growth of the 12 mm wavelengths was suppressed and crossflow-induced transition was delayed.

A limited number of experiments have looked at the secondary instability of the stationary crossflow mode. As mentioned earlier, Poll successfully measured the secondary instability [22] and Kohama successfully described Poll's measurements [21]. As far as the author is aware, this is the first measurement and description of the secondary instability of the stationary mode. White and Saric [40] performed experiments on a swept wing, and were able to measure a high-frequency secondary instability when the primary stationary mode saturated. It was stated that the secondary instability is the key factor in triggering breakdown of the saturated stationary crossflow. Computations have been performed by Choudhari et al. [41–43] looking at the secondary instability of the stationary mode at transonic speeds on a swept wing. It was found that the onset of the secondary instability moved upstream when the initial amplitude of the stationary waves was increased.

Malik et al. [20] developed a method for correlating transition location with secondary-mode N-factors. Malik stated that using the growth rate of the secondary instability as a prediction of transition onset, as opposed to basing transition predictions solely on the growth of the primary stationary instability, may produce a more

robust prediction method. It is not clear how well this method works outside of the low-speed swept wing experiments from which it was developed.

2.2 High-Speed Experiments and Simulations

Saric et al. attempted to delay transition on a supersonic swept wing with the same roughness element technique utilized in the subsonic experiments [44]. Experiments were done at Mach 2.4 with a highly swept wing (sweep angle of 73°) in order to create a subsonic leading edge. The roughness elements were placed near the leading edge, and spaced such that a more stable stationary wavenumber was forced. It was found that transition could be delayed from approximately 30% of the chord in the smooth wall case to approximately 50% of the chord with roughness elements. This transition delay was similar as to what was found in the subsonic experiments.

Semionov et al. also studied discrete roughness on a wing at Mach 2 [45]. The motivation was the same as Saric's: to use roughness elements to delay transition by forcing more stable stationary wavenumbers. Dots and longitudinal strips were used as the roughness elements, placed near the leading edge. The roughness dots were found to move transition forward by about 30%, presumably because a more unstable stationary wavenumber was being forced. The longitudinal strips were found to be more effective at delaying transition (by roughly 40%). The geometry of the roughness elements clearly has a significant effect on the stationary vortices and transition.

Schuele conducted experiments with a 7° half-angle cone at Mach 3.5 [46, 47] using discrete patterned roughness elements. The tests were performed in the NASA Langley Mach 3.5 Supersonic Low Disturbance Tunnel. The roughness elements were placed around the azimuth near the neutral point of the most amplified stationary waves. A needle was pushed into a Torlon section of the cone to create the roughness elements (dimples). Schuele, based on the work by Saric, utilized the roughness elements to force a weakly amplified stationary wave and suppress the most naturally amplified wave. Figure 2.1 plots the streamlines and vortex paths for the cone at

angle of attack. The computed stationary vortex path is approximately aligned with the streamline path, and the measured vortex path approximately agrees with the DNS computations by Balakumar [48]. The white region of the plot represents the surface that the streamlines passing over the roughness elements wet. This is the region where forcing is expected to have an effect. Because of the circumferential pressure gradient, a streamline passing over the roughness element will be deflected towards the lee ray moving downstream. The purple shaded region is an estimate of where the roughness elements would not have an effect on the stationary vortices. The measured vortices in this region were likely caused by random roughness on the cone. This chart cannot be precisely used for the present author's experiments at Mach 6 due to the differing conditions, but is a useful guide. A similar chart at the present author's test conditions is shown in Section 5.4.

Schuele found that if the spacing of the dimples was less than the spacing of the most amplified stationary waves (subcritical forcing), then transition could be delayed by 25–50%. If the spacing of the dimples was the same as the most amplified stationary waves (critical forcing), then transition could be promoted. It was shown that the technique of Saric et al. [39] is also valid at Mach 3.5.

King also studied crossflow on a cone at angle of attack in the NASA Langley Mach 3.5 Supersonic Low Disturbance Tunnel [49]. Boundary-layer transition was found to be lee-side forward under both noisy and quiet flow. King's work, along with previous work including Owen and Randall [26] and Chapman [50], attempted to use a single value of the crossflow Reynolds number to predict the location of transition. The crossflow Reynolds number (as used by King, Owen and Chapman) is defined as

$$\chi = \frac{\rho_e w_{max} \delta}{\mu_e} \tag{2.2}$$

where ρ_e and μ_e are the density and viscosity at the edge of the boundary layer, w_{max} is the maximum crossflow velocity, and δ is the boundary-layer thickness. Note that there are other definitions of the crossflow Reynolds number, for example by

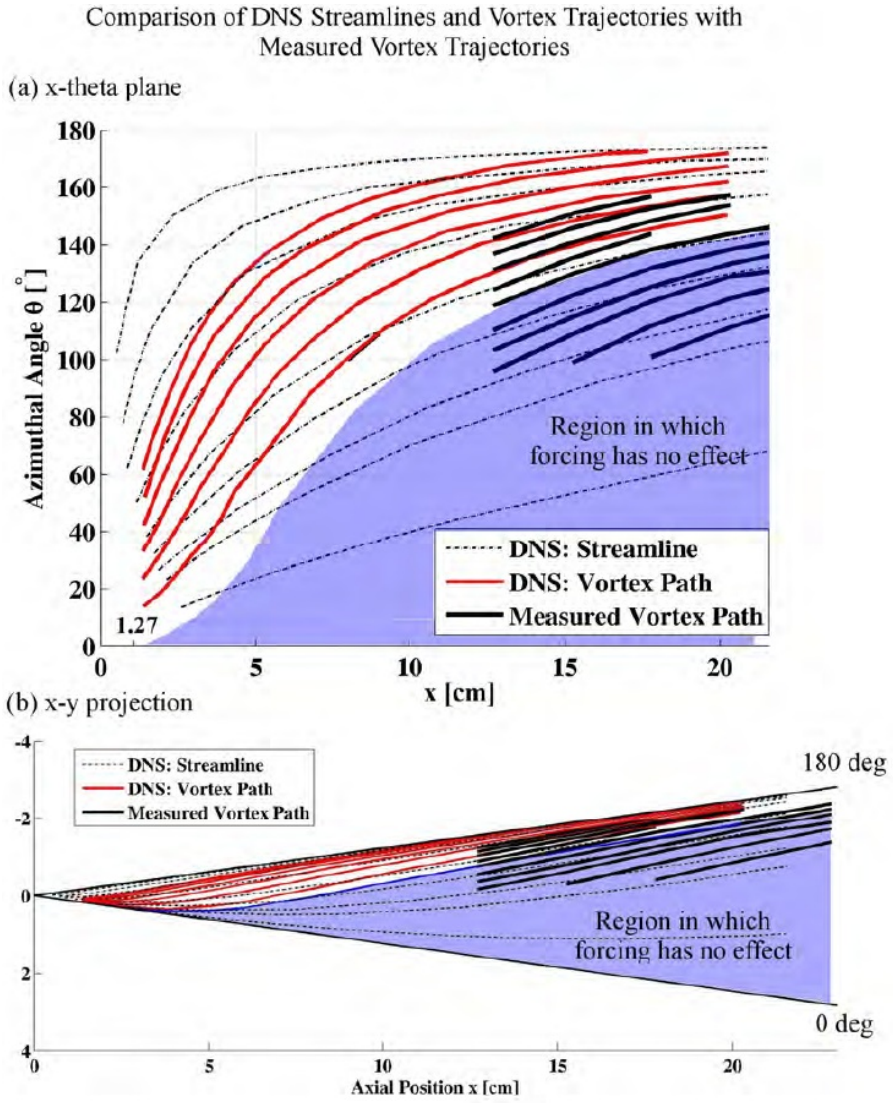

Figure 2.1.: Experimental crossflow vortex paths in comparison with DNS surface streamlines and crossflow vortex paths. Shaded purple region represents area where forcing has no effect. Image from Schuele et al. [47]. Printed with permission from Corke. DNS performed by Balakumar [48].

Dagenhart [51]. King found that a single value of χ was not sufficient in predicting crossflow-induced transition. A more complex correlation for crossflow-induced transition was developed by King, but it is not clear how well this or other complex crossflow-Reynolds-number-based correlations would work for general cases.

Measurements were made by Swanson on a nominally sharp 7° cone at 6° angle attack in the BAM6QT [52, 53]. It was found that transition was lee-side forward in noisy flow. Swanson was also able to move transition forward by placing roughness elements near the nosetip. The stationary vortices were visualized with temperature-sensitive paint (TSP) under both noisy and quiet flow, but transition was not observed under quiet flow. The roughness dots had no observable effect on the stationary vortices under quiet flow. Tunnel noise did not appear to have any effect on the stationary vortices for Swanson. Work by the author [54] and Juliano [55] in the BAM6QT showed that tunnel noise had an effect on the stationary vortices. The tunnel noise was either approximately 0.02% or 3%, depending if the nozzle-wall boundary layer was laminar or turbulent [56]. Low speed work showed that tunnel noise did not have a noticeable effect on the stationary vortices, but when acoustic disturbances pass through a shock the acoustic disturbances can be converted into vorticity or entropy disturbances [57]. It is not known how much the turbulence levels post-shock differ when the tunnel is run quiet or noisy. From the experiments by Ward and Juliano, it cannot be said if the acoustic or vortical disturbances had a more significant impact on crossflow-induced transition. The reason for the discrepancy between Juliano, Swanson and the author's work is not known.

Muñoz et al. [58] studied the crossflow instability on a 7° half-angle cone at 6° angle of attack in the Hypersonic Ludwieg Tube Braunschweig (HLB) at Mach 6. The HLB is a conventional tunnel, with noise levels between 1 and 1.6%. At a freestream unit Reynolds numbers near 10×10^6/m, Munõz was able to measure instabilities near 35 and 350 kHz with PCBs flush-mounted near the yaw (90°) ray of the cone (between 70 and 110° from the wind ray). The high-frequency instability was attributed to the second-mode waves. Muñoz suggests that the low-frequency instability is due to the first-mode waves, but computations by Perez et al. [59] and Muñoz et al. [60] have since shown that it is due to the travelling crossflow instability.

Additional tests in the HLB with a 7° cone at 6.6° angle of attack was performed by Kroonenberg et al. [61]. Infrared thermography was used to obtain global heat

transfer on the cone. Stationary crossflow vortices were seen at Reynolds numbers between 6.5 and 11.3×10^6/m. Crossflow-induced transition was visualized near the yaw ray. Discrete roughness elements were then placed near the nosetip. The elements did not appear to have a significant effect on the stationary waves.

Li et al. [62] simulated flow over a 7° cone at 6° angle of attack at Mach 6. The simulations were performed at conditions near the maximum quiet stagnation pressure of the BAM6QT. The Reynolds number was 10.8×10^6/m, the wall temperature was 300 K, the stagnation pressure was 965 kPa (140 psia) and the freestream static temperature was 52.4 K.

Li found the expected result that the windward shock is much stronger than the leeward shock. The windward ray has relatively low edge Mach numbers, raising the possibility of the first mode being the dominant instability near the windward ray. N-factors were calculated using linear stability theory (LST) and parabolized stability equations (PSE) [6, 63]. On the windward ray, the N-factors for the first and second-mode waves were approximately 4.0 and 4.8 respectively. The first and second-mode instabilities would not be expected to cause transition on the windward ray, since N-factors at transition under fully quiet flow in general are expected to be between 9 and 11 [64], but may be even larger [65]. On the leeward ray, the edge Mach number is greater (as compared to the windward ray), therefore the second-mode wave would be expected to be the dominant instability. Li calculated the second-mode waves to reach an N-factor of 16 at the downstream end of the cone on the leeward ray. Figure 2.2 shows the boundary layer near the leeward ray with a distinct mushroom shape. The significant shear layers near the edge of the mushroom-shaped boundary layer can substantially alter the stability characteristics of the lee ray [62].

Finally, Li calculated N-factors due to the stationary crossflow modes. The greatest N-factors were found to be in excess of 20 at the downstream end of the cone at an azimuthal angle of 130-140° from the windward ray. One would expect crossflow-induced transition to occur near this azimuthal angle. The neutral point of the most amplified stationary waves is approximately 1–3 inches from the nosetip. The most

unstable stationary mode also has wavenumbers per cone circumference between 45 and 55.

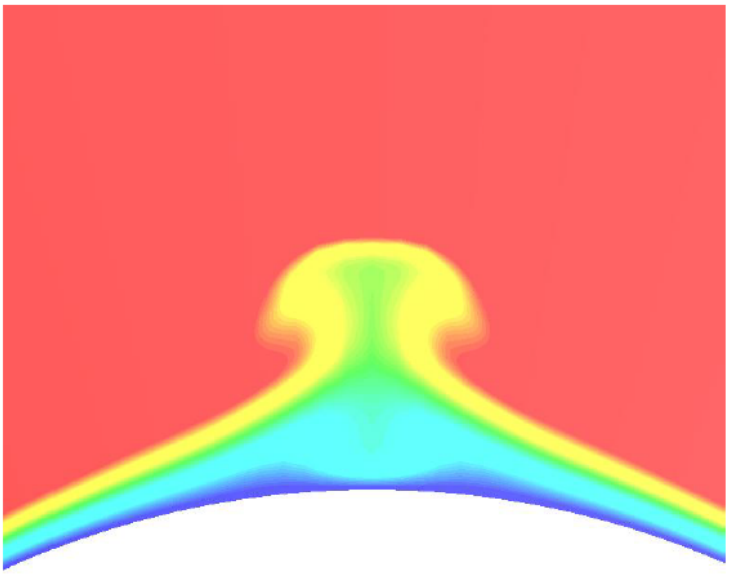

Figure 2.2.: Mach number contours near the leeward ray on a 7° half-angle cone at 6° angle of attack at Mach 6. Image from Li et al. [62].

Gronvall et al. [66] did DNS computations for the 7° cone at 6° angle of attack at Mach 6 with no freestream noise. The Reynolds number of Gronvall's computations was 9.5×10^6/m, the stagnation temperature was 433 K and the wall temperature was 300 K. A distributed roughness array was added from 5.1 cm (2 inches) to 20 cm (7.9 inches) from the nosetip, between the 12.5 and 27.5° rays. The roughness strip had an RMS roughness height of 10 or 20 μm, similar to the temperature-sensitive paint finish [54].

Figure 2.3 shows the density contours, and the edge and shear velocity streamlines. In the density contours, it is clear that the windward shock is stronger, producing more dense gas near the windward ray. The edge velocity streamlines are essentially the inviscid streamlines, which are curved due to the circumferential pressure gradient. The stationary crossflow vortices are expected to follow the edge velocity

streamlines [10]. The shear velocity streamlines represent the fluid very close to the wall. The circumferential pressure gradient has a more significant effect on the lower-momentum fluid near the wall compared to the higher-momentum fluid near the edge of the boundary layer.

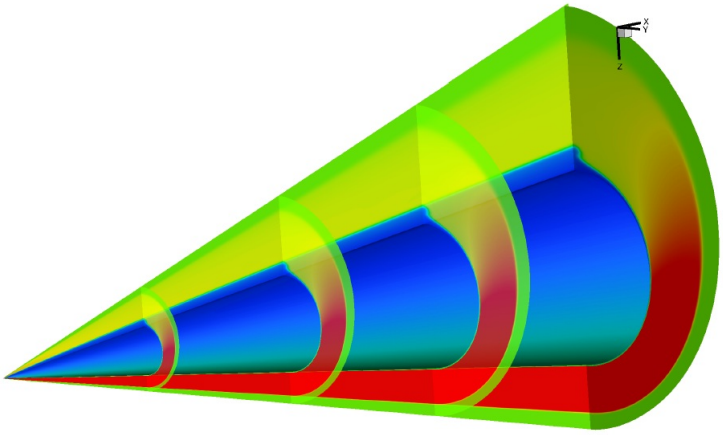

(a) Density contours

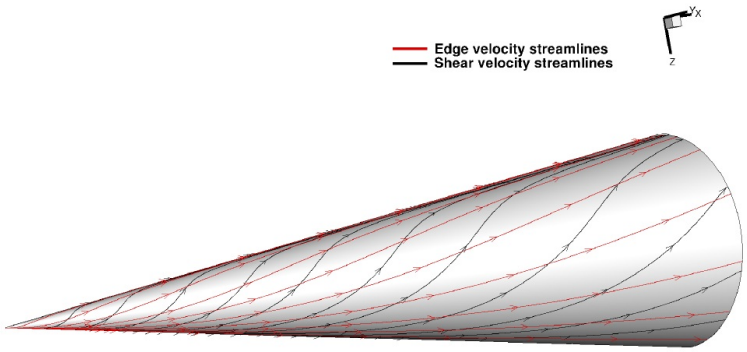

(b) Edge and shear velocity streamlines

Figure 2.3.: Laminar steady mean flow solution of cone at 6.0° angle of attack at Mach 6. Image from Figure 4 of Gronvall et al. [66]. Printed with permission from Gronvall.

Gronvall et al. also compared the simulations to experiments by Swanson [52]. The inclination of the crossflow vortices in the simulation were found to be similar to

the inclination of the experimentally measured crossflow vortices. The wavenumber of the stationary waves also matched well between the experiments and the simulations. It also appears in the simulations that the stationary waves are beginning to develop a secondary instability near the lee ray at the downstream end of the cone. Comparisons to current experiments will be made later in the report.

Elliptical cones have also been used to study the crossflow instability at hypersonic speeds. A crossflow component of the flowfield is created due to the non-axisymmetry of the geometry. Kimmel and Poggie looked at an elliptical cone at Mach 8 [67, 68]. They were able to measure a low-frequency wave off the centerline with a hot-film probe, attributed to the travelling crossflow instability. A higher-frequency instability was also measured on the centerline, matching the predicted frequency of the second-mode instability. Oil flow and schlieren were used for flow visualization. Transition was visualized near the centerline, and the stationary crossflow vortices were observed off-centerline. Crossflow-induced transition was not seen.

Huntley and Smits also tested an elliptical cone at Mach 8 [69]. Boundary-layer instabilities were visualized using the Filtered Rayleigh Scattering technique. Travelling crossflow waves were imaged, with wavelengths on the order of 4–5 times the boundary layer thickness. At higher unit Reynolds numbers, waves were observed with wavelengths twice the boundary-layer thickness, likely corresponding to the second-mode instability. The stationary vortices were also visualized.

Several recent experiments have looked at the HIFiRE-5 model (2:1 aspect-ratio elliptic cone) in Purdue's Mach-6 quiet tunnel. Juliano performed the initial tests, utilizing temperature-sensitive paint for flow visualization and PCB fast-pressure transducers to measure instabilities [70]. Transition under both noisy and quiet flow was found near the centerline (likely due to the second-mode instability) and off the centerline (likely due to the crossflow instability). Transition was seen under quiet flow, but occurred more than 100% further downstream (depending on the Reynolds number) than in the noisy case, based on the axial distance. PCB sensors were placed along the centerline, and were able to measure waves with frequencies near 110 kHz,

corresponding to the second-mode waves. Travelling crossflow waves could not be measured due to no sensors being present off-centerline.

Borg continued the work of Juliano [71, 72]. Stationary vortices were observed under both noisy and quiet flow, utilizing temperature-sensitive paint and oil flow. Boundary-layer transition was observed under noisy flow both along and off the centerline. It was assumed the off-centerline transition was caused by the crossflow instability, and the centerline transition was caused by the second-mode instability.

Roughness elements or strips were also placed near the leading edge of the elliptical cone. Depending on the geometry of the roughness, transition was induced under quiet flow. Under noisy flow, transition always occurred further upstream than under quiet flow, regardless of the roughness geometry.

The most recent experiments by Borg et al. [73] on the HIFiRE-5 model in the BAM6QT yielded some surprising results. Using Kulite sensors in the region of high travelling crossflow N-factors (based on computations by Choudhari et al. [74]), the travelling waves were measured under quiet flow but not under noisy flow. Under noisy flow, the Reynolds number was varied such that the boundary layer near the sensors ranged from fully laminar to fully turbulent yet no travelling waves were found. This result is the opposite of what would be expected, based on the low-speed work mentioned earlier. It is possible that secondary instabilities or nonlinear effects dominate over the primary travelling instability under noisy flow, although the power spectral density of the pressure sensors did not show any evidence. The complex three-dimensional geometry may also affect what is seen on the few available sensors.

3. EXPERIMENTAL METHODS

3.1 Boeing/AFOSR Mach 6 Quiet Tunnel

The Boeing/AFOSR Mach-6 Quiet Tunnel (BAM6QT), shown in Figure 3.1, is the largest hypersonic quiet tunnel in the world. The BAM6QT is a Ludwieg tube, consisting of a long driver tube with a converging-diverging nozzle at the downstream end. A Ludwieg tube design helps minimize costs and provides relatively high Reynolds numbers.

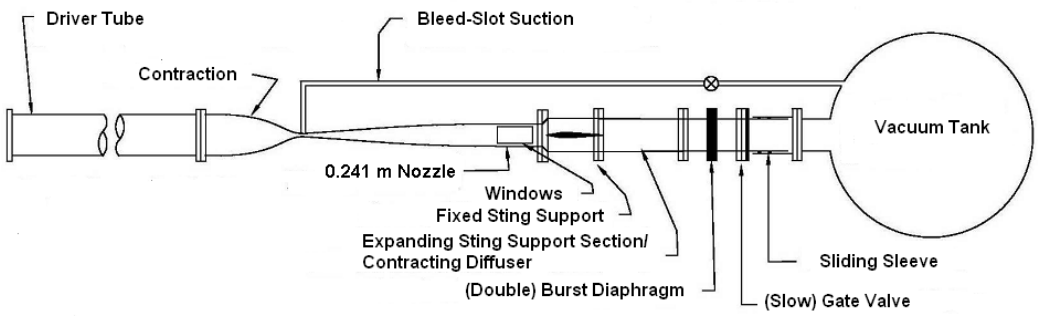

Figure 3.1.: Schematic of the Boeing/AFOSR Mach-6 Quiet Tunnel

To operate the tunnel, the upstream end of the tunnel is brought to the desired stagnation pressure and the downstream end is brought to vacuum, separated by a pair of burst diaphragms. To start the tunnel, the air is evacuated from between the two diaphragms, causing them to burst. An expansion fan then travels upstream and a shock wave travels downstream. Mach-6 flow is initiated after the expansion fan passes through the throat. The expansion fan reflects between the upstream end of the driver tube and the contraction, taking on the order of 200 ms. The stagnation pressure drops with each reflection. For each 200 ms time segment, the flow conditions

are quasi-static. A typical run lasts between 5 and 10 seconds, and therefore for any given run a range of Reynolds numbers can be tested.

The BAM6QT is capable of producing low noise levels on the order of 0.02% [56] and employs several features to maintain a laminar nozzle-wall boundary layer. A suction slot is present upstream of the throat and removes the boundary layer on the contraction wall, allowing a new undisturbed laminar boundary layer to grow on the nozzle wall. This suction slot is connected to the vacuum tank through a fast valve. The fast valve can be closed to allow a turbulent nozzle-wall boundary layer to develop on the nozzle. The noise levels with the fast valve closed are on the order of 3%, similar to conventional hypersonic tunnels. The tunnel also features a long nozzle designed to reduce the growth of Görtler vortices, a highly polished throat and nozzle, and high-quality air filters to reduce air-borne particulate in the tunnel.

3.1.1 BAM6QT Flow Conditions

Under quiet flow, the Mach number is approximately 6.0. Under noisy flow the effective area ratio between the nozzle exit and the throat is reduced because the nozzle-wall boundary layer is turbulent. This reduced area ratio produces a freestream Mach number of approximately 5.8.

To compute the instantaneous stagnation temperature and Reynolds number a MATLAB function was used, provided in Appendix D. The initial stagnation temperature is recorded from a thermocouple present at the upstream end of the driver tube. There is some uncertainty in the precise stagnation temperature as there are temperature variations in the axial and radial directions [56]. The stagnation pressure is determined from a Kulite pressure transducer just upstream of the contraction section. The pressure is monitored throughout a run, providing instantaneous stagnation pressures. The instantaneous temperature was calculated using the isentropic relation

$$T_0 = T_{0,i}\left(\frac{p_0}{p_{0,i}}\right)^{\frac{\gamma-1}{\gamma}} \tag{3.1}$$

where p_0 and T_0 are the instantaneous stagnation pressure and temperature, and $p_{0,i}$ and $T_{0,i}$ are the initial stagnation pressure and temperature. The dynamic viscosity (μ) was calculated using Sutherland's Law and the density was determined using the perfect gas law.

The dew point of the air in the tunnel was typically measured several times per tunnel entry. In the summer months, the average dew point was -15 °C. In the winter months, the average dew point was -20 °C.

3.2 Oscilloscopes

Data from most of the instrumentation were recorded with Tektronix TDS7104, DPO7054 and DPO7104 Digital Phosphor Oscilloscopes. The DPO oscilloscopes could record up to 50MB for each channel while the TDS oscilloscope could only record up to 4MB (each scope had four available channels). Both scopes were capable of recording AC or DC coupled signals. The oscilloscopes were operated in Hi-Res mode. In Hi-Res mode the scope samples 8-bit data at a higher frequency than the set sampling frequency, and averages this data in real time to obtain 12 bit data at the desired frequency. This provides a decrease in noise and a greater vertical resolution [75]. High-Res mode also acts as a low pass filter, reducing signal aliasing.

3.3 Pressure Measurements

3.3.1 Kulite Pressure Transducers

Kulite XCQ-062-15A fast-pressure transducers flush-mounted in the model were used to measure instabilities, specifically the travelling crossflow instability. Kulites use a silicon diaphragm as the sensing mechanism. The sensor has a range of 0–15 psia and a mechanical stop that protects the diaphragm when the pressure exceeds 15 psia

(which occurs during tunnel pressurization). The sensor has a resonance frequency typically between 200 and 300 kHz and a flat dynamic response up to approximately 60 to 120 kHz [76]. This makes the Kulite an ideal sensor for measuring low-frequency instabilities such as the travelling crossflow, but it will have difficulty providing accurate measurements of higher-frequency instabilities such as the hypersonic second mode.

The AC signal from the Kulite was processed by custom-built electronics and amplified with a gain of 10,000. According to the manufacturer's specifications, the Kulite has an infinitesimal pressure resolution. It is not known what the true pressure resolution is, but assuming the manufacturer's specifications are approximately true, then the limiting factor of the pressure data's resolution would be the oscilloscopes. When the scope is operated in Hi-Res mode, the data has a 12-bit vertical resolution. This gives a pressure resolution of 0.000016 psia.

The diameter of the Kulite sensor is 0.0625 inches (1.6 mm). The silicon diaphragm is protected by what is referred to as an A-screen. An A-screen has a large central hole, which creates an effective sensing area of 0.00125 inches^2 (0.81 mm^2). The Kulites are quoted as being temperature compensated between 70°F and 400°F (294 K to 478 K). The thermal sensitivity is ±1% of voltage amplitude per 100°F (56 K). Each Kulite was statically calibrated in the BAM6QT, once during a given tunnel entry. Dynamic calibrations were not available for the Kulites, but fortunately for diaphragm-type transducers, the static and dynamic calibrations only differ by a few percent [77].

3.3.2 PCB Piezoelectronic Pressure Transducers

PCB pressure transducers utilize piezoeletricity for measuring pressure fluctuations. When a piezoelectric material is stressed, a charge is released. The magnitude of the charge is proportional to the applied pressure. The magnitude of the elec-

tric charge tends towards zero over time, so therefore the sensors can only provide dynamic pressure measurements.

All the PCB sensors used in the experiments were PCB132A31 sensors. They provide a pressure resolution of 0.001 psi per the manufacturer's specifications, much coarser than the Kulite's pressure resolution. The sensors have a flat response between 20 and 300 kHz [76], are high-pass filtered at 11 kHz and have a resonant frequency above 1 MHz. Therefore, these sensors are well suited to measure high-frequency instabilities present in hypersonic boundary layers [78–81] that a Kulite sensor cannot.

The PCB132 sensor has a diameter of 0.125 inches (3.18 mm), and a sensing area of approximately 0.0025 inches^2 (1.66 mm^2). The sensors were designed as time-of-arrival sensors, and are not calibrated for measurements of small pressure fluctuations. The manufacturer's calibrations were used to convert voltage to pressure, and therefore the amplitude of measured pressure fluctuations has a level of uncertainty. A shock tube has been constructed and preliminary work has been completed on obtaining improved dynamic calibrations [82], but these calibrations were not available to the author at the time of the experiments.

3.3.3 Pressure Data Reduction

The Kulite and PCB AC signals were recorded at 2 MHz on the Tektronix oscilloscopes with Hi-Res mode activated. The voltage data were separated into 0.1-second samples for post-processing. The time segment was chosen because the flow conditions would be approximately constant for the duration, based on the time required for the expansion fan to reflect between the upstream end of the tunnel driver tube and the contraction. For the PCB sensors the manufacturer's calibration was used to convert voltage to pressure, and for the Kulite sensors a static calibration performed in the BAM6QT was used to convert voltage to pressure. The pressure fluctuations were non-dimensionalized by the theoretical edge pressure for a 7° cone at 0° angle of attack (p_c), determined by using the Taylor-Maccoll solution for conical flow [83].

The tangent-cone method may have been a more appropriate method to use for non-dimensionalization, but there were difficulties in obtaining a converged solution for small cone half angles (which would be required near the lee ray). The edge pressure for a 7° half-angle cone at 0° angle of attack is approximately half the edge pressure for a 13° half-angle cone at 0° angle of attack (which would be the effective cone angle on the windward ray). Therefore, simply utilizing the Taylor-Maccoll method for non-dimensionalization will produce a difference of up to 50% moving towards the windward ray as compared to the mean pressure. Future computational comparisons could readily account for this clearly defined difference in normalization.

Power spectral densities (PSD) were calculated for the 0.1 second time segments of pressure using Blackman windows with 70% overlap. The 0.1 second time segments were broken up into 100 windows of equal length, providing a frequency resolution of 1.0 kHz. The power spectral density yields units of non-dimensional pressure squared per Hertz $((p'/p_c)^2/Hz)$. The RMS of a frequency band was calculated by numerically integrating under the PSD over the desired frequency band. The square-root of the integration result was taken, yielding the RMS in units of non-dimensional pressure.

3.4 Heat Transfer and Temperature Measurements

3.4.1 Schmidt-Boelter Heat-Transfer Gauges

Schmidt-Boelter (SB) gauges were used to obtain heat transfer on the surface of the models and to calibrate the temperature-sensitive paint data to heat transfer. The gauge has an outside diameter of 3.175 mm (0.125 inches) and houses a thermopile in a 2.79 mm (0.11 inch) diameter cavity. The thermopile is coated with a black epoxy, allowing the gauge to more effectively absorb heat (although radiation is likely not significant in the present experiments). The epoxied region has a diameter of 3.175 mm, and the sensing region is assumed to have the same diameter. According to the Medtherm Corporation, the epoxy has a thickness of 30–80 μm (0.001–0.003 inches), but is typically closer to 30 μm (0.001 inches) [84].

Two different models of gauges from the Medtherm Corporation were used in testing, the 8-2-0.25-48-2083TBS and 8-1-0.25-48-2083TBS models. Both gauges contain two type T thermocouple readouts, one at the base and one at the surface of the thermopile. The former gauge has a calibration range of 0–22 kW/m^2 (0–2 Btu/ft^2/s), and the latter has a range of 0–11 kW/m^2 (0–1 Btu/ft^2/s).

The SB gauges were amplified by a Stanford Research Systems Low Noise Preamplifier (model SR560) before being digitized by the oscilloscopes. This was done to greatly increase the signal-to-noise ratio, as the SB gauge's unamplified output signal can be on the same order of magnitude as the noise. The SB gauge signal was then sampled by the oscilloscope at 500 Hz in Hi-Res mode. This sampling rate was chosen as it is low enough to remove random noise, but high enough to capture the initial peaks in the surface heat transfer at tunnel start up. A portion of these heat transfer peaks are necessary when attempting to calibrate the temperature-sensitive paint data to obtain heat transfer. Refer to Section 4 for an example of the heat-transfer reduction method. The heaters used to heat the air in the driver tube are also deactivated before the run to reduce electronic noise, and reactivated after the run [85].

3.4.2 Thermocouples

Thermocouples were used to determine the model temperature before and during a run. A thermocouple uses two dissimilar metals that form a junction at the sensing end. When a conductor is subjected to a temperature gradient a voltage is generated, which is known as the thermoelectric effect. The voltage at the sensing end is compared to the voltage from the reference end of the thermocouple. The voltage generated at the sensing end is proportional to temperature. The reference end of the thermocouple was maintained at a constant voltage electronically, through the use of an Omega MCJ miniature cold junction compensator.

The thermocouples were sampled at 200 kHz using the oscilloscope. The vertical resolution was typically set at 1 mV per division, where an increase of 1 mV corresponds to a temperature increase of roughly 26°C, depending on the type of thermocouple. Therefore, when available an Omega OMNI-AMP IIB thermocouple amplifier was used. With the scope running in Hi-Res mode, a resolution of approximately 0.11°C was obtained without amplification. The resolution was 0.0011°C with amplification.

The calibrations for the thermocouples (Type T, E and K) were taken from the National Institute of Standards and Technology (NIST) ITS-90 database. The type of thermocouple refers to the type of metal used. Type K thermocouples consists of chromel (90% nickel and 10 % chromium) and alumel (95% nickel, 2% manganese, 2% aluminium and 1% silicon). Type T thermocouples contain of copper and constantan (55% copper and 45% nickel). Finally, type E thermocouples consist of chromel and constantan.

3.4.3 Temperature-sensitive Paint

Temperature-sensitive paint is a luminescent paint that can be airbrushed onto a model to provide a global temperature distribution. The advantage of using TSP over discrete sensors, such as thermocouples, is the increased spatial resolution and the relatively low cost [86]. The temperature distribution can help map important flow features such as shocks or vortices. Temperature-sensitive paint can also help quantify the region of boundary-layer transition, since there is a sharp increase in temperature at the onset of transition.

The temperature-sensitive paint is created by doping a polymer coating with luminescent molecules. The luminescent molecules are typically dissolved in a solvent first. The luminescent molecule used is 99.95% Tris(2,22-bipyridine) dichlororuthenium(II) Hexahydrate (Ru(bpy)), and the solvent is ethanol.

The temperature-sensitive paint measures temperature through the process of thermal quenching. When the luminophore molecules absorb a photon of radiation, the molecule moves to an excited electronic state [86]. Upon returning to a lower energy state, a longer wavelength photon is emitted by the molecule [87]. There are two processes at work when the electron returns to its ground state, radiationless and radiative process [88]. At the experimental temperature range of the BAM6QT, radiationless processes dominate [86]. Thermal quenching occurs when the radiationless process dominates (intensity is inversely proportional to temperature). Since the intensity of the emitted photons is dependent on the temperature of the paint, surface temperature can be determined by measuring the emitted light intensity.

Typically an insulating layer of paint is placed between the model and the TSP to thermally insulate the TSP layer from the model. This is done to increase the signal-to-noise ratio. A higher signal-to-noise ratio is important when trying to visualize low amplitude phenomena such as stationary crossflow waves [54].

Figure 3.2 shows a schematic of how TSP works. A short wave incident light source is used to excite the luminescent molecules. The emitted photons are then captured by a camera with a high-pass filter. The intensity of the emitted photons can be converted to temperature.

Temperature-Sensitive Paint Apparatus

Two blue light-emitting-diode arrays are used to excite the temperature-sensitive paint, an Innovative Scientific Solutions (ISSI) Inc. LMA LM4 LED array and an ISSI LM2xLZ-460 LED array. The LMA LM4 array emits blue light with a 464 nm wavelength, and the LM2xLZ-460 array emits blue light with a 460 nm wavelength. Both LED arrays are used in order to illuminate the model as much as possible, increasing the signal from the TSP.

A Cooke Corporation PCO.1600 14-bit CCD camera is used. It is controlled by a PC via CamWare software. The CCD camera captures images with a resolution

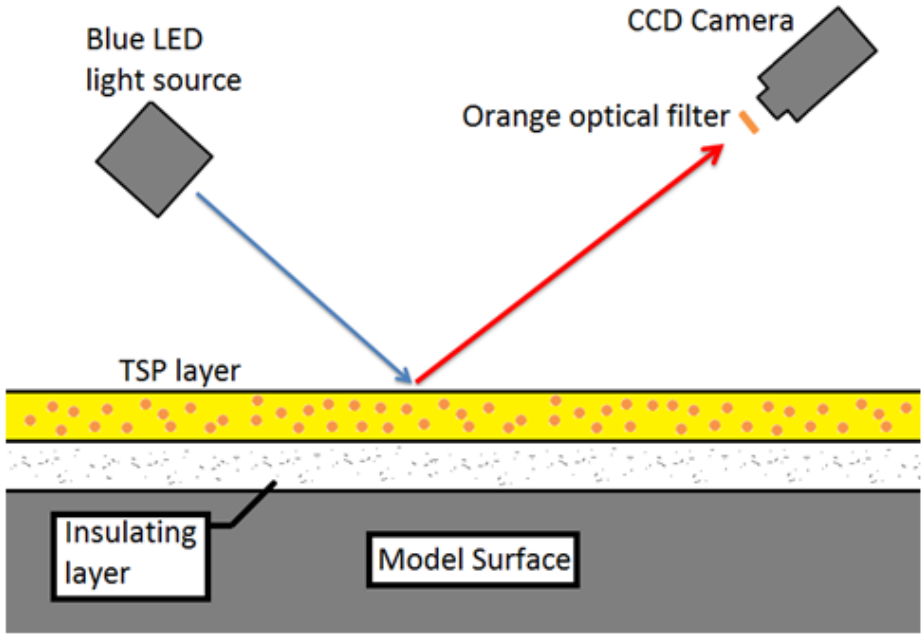

Figure 3.2.: Schematic of the temperature-sensitive paint layer. Re-drawn from Figure 1 of Reference [89].

of 1600 × 1200 pixels. The pixels are averaged to reduce noise; therefore the images presented here have a resolution of 800 × 600 pixels. Figure 3.3 shows the experimental setup with the CCD camera and the two LED arrays. The TSP fluoresces in the orange spectrum of light, so an orange 556 nm long-pass filter was used to block out the excitation source emission. The model can be seen through the porthole windows installed in the tunnel. There is a larger rectangular window also used in testing, but it is only rated for stagnation pressures up to 138 psig. Most testing entries in the tunnel required pressures greater than 138 psig, as the maximum quiet pressure was near 155 psig, therefore most TSP images shown were imaged through the smaller porthole window. In August 2013 a crack was found in the Plexiglas of the large rectangular window. This window has not been used in testing since this date. Figure 3.4 shows the difference in the field of view between the porthole and rectangular windows with a 7° cone at 0° angle of attack. TSP was not added to the nosetip region of the model.

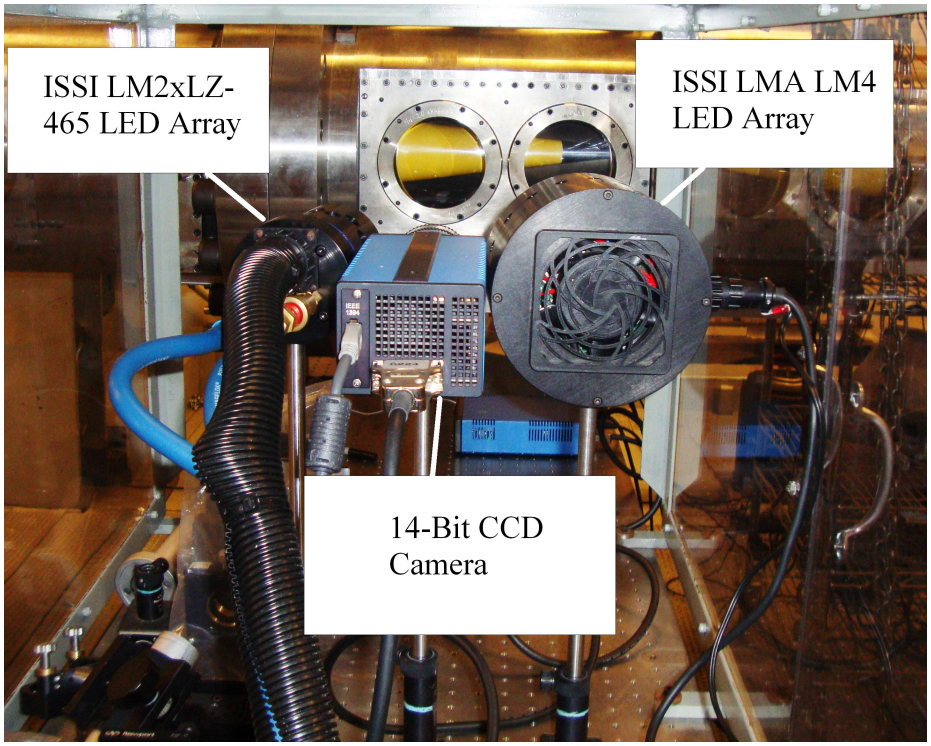

Figure 3.3.: TSP apparatus with CCD camera and 2 blue LED arrays.

.

Post-Processing the Temperature-Sensitive Paint Images

To convert the images from the CCD camera to temperature maps, several steps are required. Three images of the model are captured. First, a dark image is taken with all the lights off. An "off" image is taken just before the run starts, with the tunnel pressurized and the LED lights on. Finally, an "on" image is taken during the run. In practice, many "on" images are taken during a run, up to 50 images per second. The three intensity images can then be converted to temperature using the following equation [86]:

$$\Delta T = f\left(\frac{I_{on} - I_{dark}}{I_{off} - I_{dark}}\right) \tag{3.2}$$

The function f can be any function (for example an exponential or polynomial) that fits the TSP calibration data over the desired working temperature range [86]. ΔT

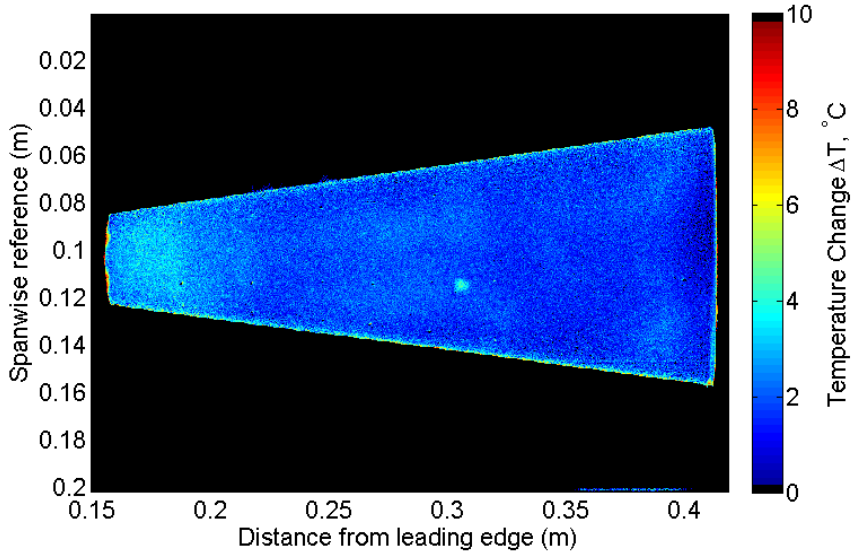

(a) TSP image with large rectangular window.

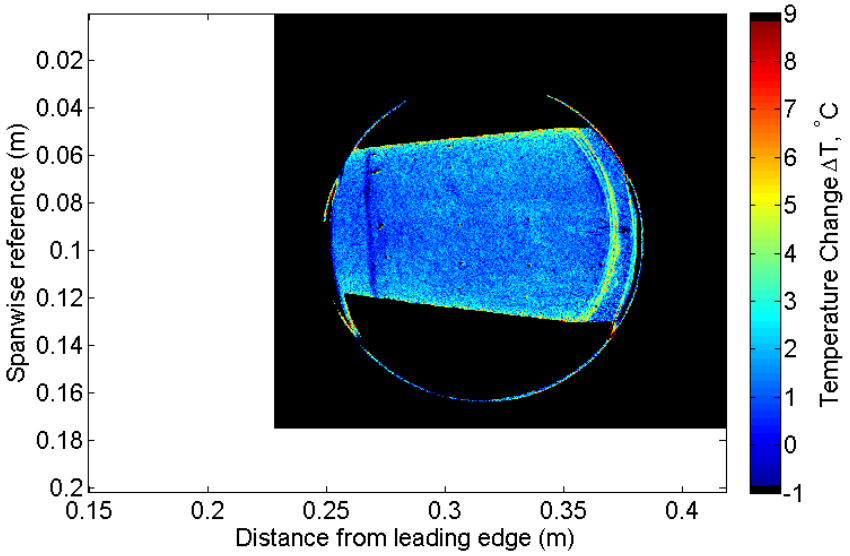

(b) TSP image with smaller porthole window

Figure 3.4.: Difference in field of view between windows.

is the number of degrees Celsius the temperature is above the "off" or initial model temperature. The "off" temperature is found by placing a thermocouple somewhere on the model, preferably at the base in order to be non-intrusive. The two thermocouples present in the Schmidt-Boelter gauges are also used to obtain the pre-run model temperature. This is assuming that the model temperature is approximately spatially uniform before the start of the run.

By taking the ratio of the "on" and "off" images any discrepancies in light uniformity should theoretically be removed since the same pixel is compared in the "on" and "off" images. In reality, when the BAM6QT starts, there is a slight shift in the model in the axial direction (on the order of 1–3 pixels). This means that a pixel will not necessarily have the same lighting conditions in the "off" image compared to the "on" image. To reduce errors caused by non-uniform lighting, the LED arrays are placed as far as possible from the tunnel window without sacrificing the TSP intensity.

The "off" and "on" images need to be aligned correctly due to the tunnel shift, and this was done through an image registration code written by Dr. John Sullivan and provided in Appendix D. This code uses the edges of the model to align the "on" and "off" images. Previous experiments in the BAM6QT used registration dots placed on the model to align the two images [55, 75, 90].

The TSP calibration was found using a linear fit to the data in Figure 3.13 of Reference [86]. The calibration curve is number 7 in the figure (Ru(bpy) in Dupont ChromaClear). The details behind the calibration can be found in Reference [89]. After performing a linear fit and changing the reference temperature from -150°C to the initial model temperature, the author found the following calibration:

$$\Delta T = (362 - T_{ref}) \left(1 - \frac{I_{on} - I_{dark}}{I_{off} - I_{dark}}\right) \tag{3.3}$$

The calibration is good for temperatures between 15°C and 60°C (288-340 K), which contains the range of model temperatures seen in the BAM6QT.

Extracting Heat Transfer from Temperature-Sensitive Paint Images

A method was devised by Dr. John P. Sullivan of Purdue University to calibrate the TSP using data from Schmidt-Boelter (SB) heat-transfer gauges [91]. A square patch of TSP is compared to the SB gauge, ideally in a location where the heat transfer rate seen by the patch and the gauge is nominally the same. Finding a TSP patch that meets this requirement is not always a trivial task, especially when dealing with a three-dimensional flowfield.

The local heat flux can be found using Fourier's law,

$$q = -k\nabla T \tag{3.4}$$

where q is the local heat flux and k is the thermal conductivity of the insulating paint layer. Several assumptions need to be made to simplify Equation 3.4. It is assumed that the heat transfer is one-dimensional (in the wall-normal direction). It is also assumed that the temperature profile in the wall-normal direction across the thin insulating layer is linear. Finally, the temperature at the base of the insulator (model temperature, T_{model}) is assumed to be constant during a run, both spatially and temporally. This spatially-uniform-model temperature assumption was found to be accurate to within roughly 4% [54], based on several tests near the maximum quiet stagnation pressure of the BAM6QT. The assumption that the temperature is temporally constant over the course of a run (roughly 10 seconds) was also shown to be valid in Figure 5.49 of Reference [54], once again based on several runs near the maximum quiet stagnation pressure of the BAM6QT. The first 10 seconds of a run showed negligible change in the model temperature. After 10 seconds, the model temperature would increase by approximately 10–20°C. The significant temperature increase occurs after Mach-6 flow ends and the flow density increases.

Fourier's law can then be simplified to the following linear equation, incorporating the finite thickness of the insulating paint layer,

$$q = \frac{k}{L}(T - T_{model}) \tag{3.5}$$

where L is the thickness of the insulating layer and T is the temperature of the surface during the run, obtained from the TSP. Finally, Equation 3.5 can be modified to include ΔT since all the TSP images can be calibrated to give ΔT,

$$q = \frac{k}{L}(\Delta T + T_{ref} - T_{model}) \tag{3.6}$$

$$\Delta T = T - T_{ref} \tag{3.7}$$

where T_{ref} is the temperature of the model surface just before the run starts. The calibration method works by iterating T_{model} and k/L until good agreement is found between the patch of TSP and a Schmidt-Boelter gauge on the model. A least-squares method was employed to find the values of the two constants. According to the definitions of T_{model} and T_{ref} and the assumption of a constant model temperature during a run, these two temperatures should be nominally the same. However, T_{model} was chosen to best fit the data, regardless of how much it varied from T_{ref}.

There are some inherent issues involved with obtaining quantitative heat transfer from the TSP in the BAM6QT. During tunnel startup, the model experiences significant heating. This large impulse of heating is thought to dissipate through the aluminium model before the run starts, but it is possible that the TSP might show some residual-heating effects. The residual heating, if present, would cause problems in obtaining accurate heat transfer from the TSP because the TSP might see a different heat transfer rate than the SB gauge. The low heat transfer in the BAM6QT also presents a problem. It may be difficult to obtain a good calibration if the heat transfer is low and the heat transfer range is small [80].

Theoretical Heat Transfer For a Cone at 0° Angle of Attack

The experimental heat transfer on a cone at 0° angle of attack can be compared to a theoretical solution developed by Dr. John Sullivan of Purdue University, along with Dr. Tianshu Liu of Western Michigan University. The theoretical solution is only good for laminar flow. Dr. Sullivan developed a theoretical solution using both a similarity solution and a reference temperature method. The similarity equations for a compressible boundary layer can be found in Reference [92]. The viscosity was modelled using the work of Lemmon and Jacobson [93]. The outer flow conditions were provided by solving the Taylor-Maccoll solution for conical flow [83]. For more information on the reference temperature method, refer to White [92]. One of the major uncertainties in determining the theoretical solution is deciding the initial wall (model) temperature. A constant and uniform wall temperature was assumed, and was taken as the measured model temperature before the run started. This is the same as T_{ref} in the TSP data reduction.

The heat transfer to the model wall is a function of, among other factors, stagnation pressure, stagnation temperature and wall temperature. For many of the heat transfer profiles shown for the cone at angle of attack, the heat transfer was non-dimensionalized by the mean theoretical heat transfer for a 7° half-angle cone at 0° AoA. This was chosen as the non-dimensionalization parameter because the author was able to obtain a solution from a fairly simple MATLAB code. The MATLAB code was written by Dr. Tianshu Liu and provided in Appendix D. It is not known how much the 0° AoA mean heat transfer solution varies from the 6° AoA mean heat transfer solution.

In several 0° angle of attack plots the non-dimensional heat transfer (Stanton Number) will be used. The Stanton number is defined as

$$St = \frac{q''}{\rho_\infty u_\infty (H_0 - h_w)} \tag{3.8}$$

$$H_0 - h_w = \left(c_p T_\infty + \frac{u_\infty^2}{2} \right) - c_p T_w \tag{3.9}$$

where ρ is the density, u is the velocity, H is the total enthalpy, h is the enthalpy, T is the temperature and c_p is the specific heat. The subscript 0 is the total value, w is the model wall value and ∞ is the freestream value.

Paint Feathering

For previous experiments in the BAM6QT [54, 94, 95], TSP was applied over the entire frustum, with the nosetip removed. When the nosetip was installed there was a forward facing step of about 200 μm created by the addition of the TSP at the nosetip-frustum junction. The slope of this forward facing step was roughly 900–1200 μm per mm, as measured with a Mitutoyo surface roughness tester.

A new method of painting was used for all the experiments presented here. Here the paint is now feathered at the leading edge. The paint is added sparingly near the upstream end and then sanded down, so there is a smooth, gradual increase of paint thickness going from the bare metal surface to the full paint thickness. The slope measured with the surface roughness tester near the upstream end of the paint was typically near 5–10 μm per mm. The paint feathering technique appears to have essentially eliminated, or vastly reduced, the forward-facing step created by the paint.

Paint Thickness Measurement Technique

It is important to obtain an accurate measurement of the paint thickness to verify the assumption that the paint thickness is approximately constant. A method to measure paint thickness on a curved surface was devised using an Elcometer 456 capacitance gauge. The raw numbers from the gauge are not necessarily accurate on a curved model surface since the capacitance-gauge sensing surface is flat. As the curvature of the model surface increases, the error of the gauge increases. To test the accuracy of the gauge, a roll of 3M 471 vinyl tape was used, with a known thickness

of 127 μm. Thickness measurements at 10 random locations on the bare flat metallic surface yielded an average reading of 0.6 μm. The vinyl tape was then placed on a flat metallic surface. Thickness measurements were then taken at 10 random locations on the vinyl tape, giving an average reading of 125 μm. The gauge appears to have a high accuracy when measurements are taken on a flat metallic surface.

The next test was done with the vinyl tape placed on a 7° half-angle cone. The tape was placed along the surface of the cone in the axial direction. Measurements of the tape thickness were taken at 4 inches to 15 inches from the nosetip, at 1 inch intervals. Measurements were then taken at the same axial positions on the bare surface of the cone. The results are shown in Figure 3.5. The red symbols are the thickness of the tape measured by the capacitance gauge. The green symbols are thickness measured by the gauge when it is placed on the bare aluminum surface of the cone. The gauge placed on the bare aluminum surface should theoretically give a thickness reading of zero, but error is introduced due to the curvature of the cone. Note that the error is greater the further upstream, since the curvature of the cone increases towards the nosetip. The non-zero thickness measured by the gauge when placed on a bare aluminum surface will be referred to as the "thickness offset". The blue symbols are the offset thickness subtracted from the measured thickness. The black line is the actual thickness of the tape. The maximum error in the blue symbols is about 6%.

This method was used to measure the combined thickness of the TSP and insulator. Figure 3.6 plots the variation in paint thickness in the axial and azimuthal direction. At each axial location three paint-thickness measurements are shown. These paint-thickness measurements were taken at points spaced 120° in the azimuthal direction. The feathered portion of the paint was not included. Note that the paint was feathered much further downstream for Case 2 than Case 1. Both cases have a similar paint thickness, approximately 200 μm, and the variation from the mean in the axial direction is near 6% for both cases. A similar paint thickness variation of approximately 6% was found in the azimuthal direction.

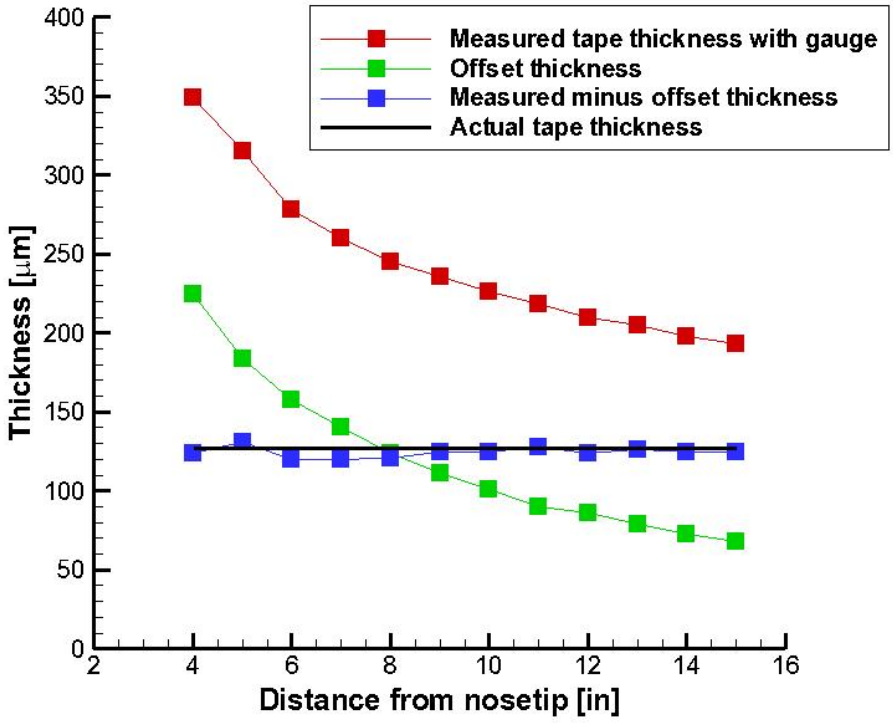

Figure 3.5.: Measurements of tape thickness on the surface of a 7° half-angle cone.

.

3.5 Surface Roughness Measurements

A Mitutoyo surface roughness tester (Model number SJ-301) was used for all measurements of the average and RMS roughness of the painted surface and the nosetips. The surface roughness tester was also used to measure the thickness profile of the feathered paint edge. The roughness tester measures roughness and steps by traversing a probe that rests on the surface. The probe follows the contour of the surface over a set distance and records the variations in the height. The traversing device for the probe was placed on the surface of the cone. Two profiles were generally used when taking measurements, the primary and roughness profiles. The primary profile (P-profile) is a profile of the real surface with no filtering. It is the type of profile used to obtain steps. The roughness profile (R-profile) is found by high-pass

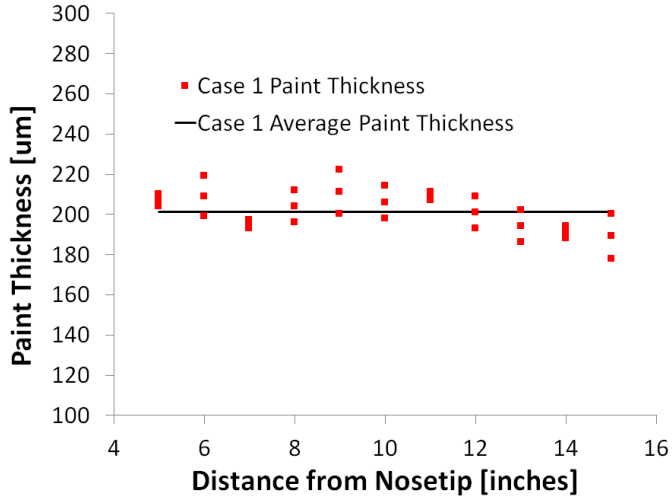

(a) Case 1 paint thickness.

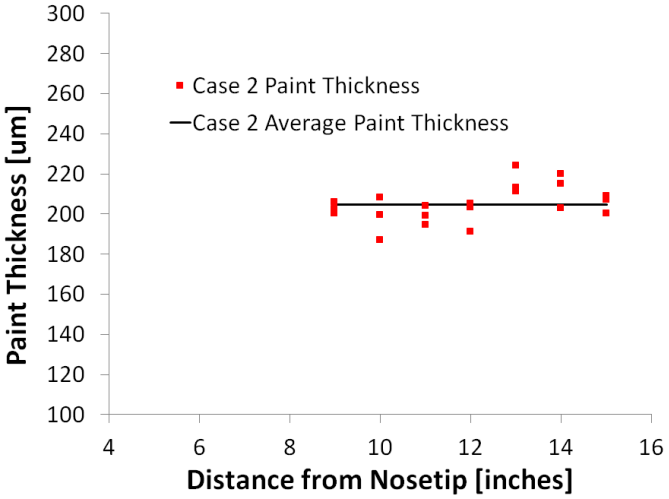

(b) Case 2 paint thickness.

Figure 3.6.: Variation of paint thickness in the axial direction.

filtering the P-profile to remove any long wavelength components. The R-profile from the roughness tester was not used since this profile could be found by manually filtering the P-profile.

Two parameters were used in determining the roughness of the surface, the arithmetic mean deviation of the profile (or average roughness, R_a) and the root-mean-square deviation of the profile (or RMS roughness, R_q). The average and RMS rough-

ness profiles are found by the following equations. Y_i is the difference in height of the surface from the mean height and N is the number of samples.

$$R_a = \frac{1}{N}\sum_{i=1}^{N}|Y_i| \tag{3.10}$$

$$R_q = \left(\frac{1}{N}\sum_{i=1}^{N}Y_i^2\right)^{\frac{1}{2}} \tag{3.11}$$

3.6 Hot Films

An uncalibrated hot-film array (Senflex multi-element hot film from Tao of Systems, Inc) was present on the nozzle wall to detect the wall-shear fluctuations in the boundary layer. From the level of these fluctuations it can be qualitatively determined if the nozzle-wall boundary layer was laminar or turbulent (quiet or noisy). The hot-film array can also provide an indication if the nozzle-wall boundary layer was separated [96]. The temperature through each hot-film was kept constant with a Bruhn-6 Constant Temperature Anemometer, where the operating resistance was set at 11 ohms (the operating resistance is the resistance that balances the Wheatstone bridge). Two hot-film elements were recorded during every run. They were typically located 74.4 and 81.5 inches from the throat. The output voltage from the hot film was typically offset to read zero before the run starts to ensure that the trace would not exceed the scale on the oscilloscope.

3.7 Models

3.7.1 Crossflow Cone

The Crossflow Cone is a 7° half-angle cone with a nominally sharp nosetip. A schematic of the cone is shown in Figures 3.7 and a picture of the cone with TSP applied is shown in Figure 3.8. The model is 0.406-m (16-inches) long and consists of five segments. The nosetip extends 0.0381 m (1.5 inches) axially. The second segment

(roughness insert) is manufactured from either Torlon or aluminum, and extends axially from 0.0381 to 0.0635 m (1.5 to 2.5 inches) from the nosetip. Roughness elements can be added to the second segment, where the neutral point of the most amplified stationary waves occurs [62]. The remaining portion of the frustum is divided into three sections. Segment 3 (front frustum) is 0.239-m (9.415-inches) long, and contains several sensor ports. Segment 4 is 0.003-m (0.125-inches) long, and can be used to add roughness elements far downstream of the neutral point. Roughness elements were not added to this section for the experiments presented in this document. Finally, segment 5 (aft frustum) is 0.101-m (3.960-inches) long and also contains several sensor ports. The sensors in segments 3 and 5 can be rotated with respect to each other. The model was coated with TSP from approximately half the front frustum downstream through the 5th segment(aft frustum).

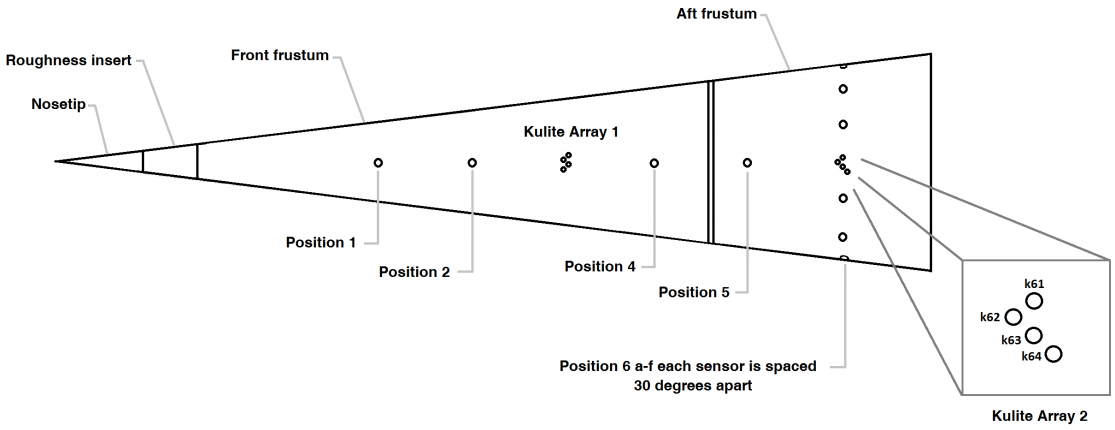

Figure 3.7.: Schematic of the 7° half-angle Crossflow cone.

An image of the nosetip under a microscope with a circle fitted to the nosetip is shown in Figure 3.9. The nosetip is magnified 20 times, and the image was captured with a Moticam 3 microscope camera. The scale was determined by taking an image of a circle on a calibration slide with a known diameter. The nose radius is approximately 221.5 μm. The junction between the nosetip and the upstream end of the Torlon

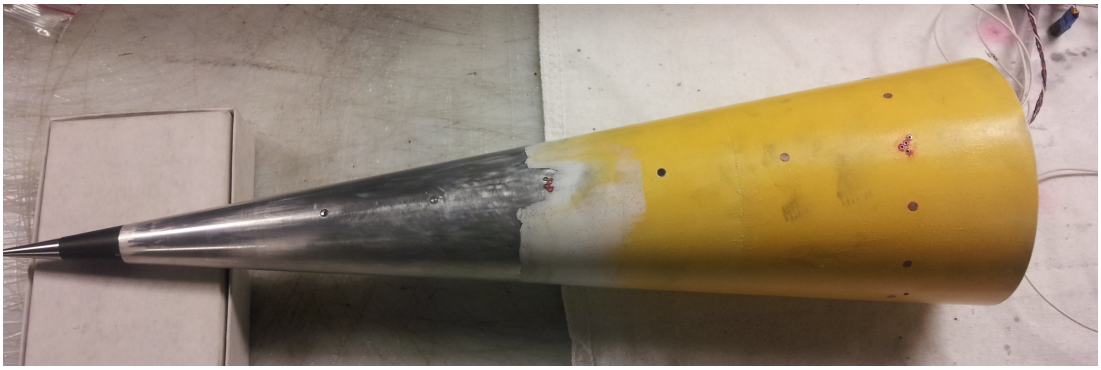

Figure 3.8.: Picture of the 7° half-angle Crossflow cone.

section had an average step of -3μm (backward facing step). The junction between the downstream end of the the Torlon section and the upstream frustum had an average step of 1.5μm.

Figure 3.9.: Nosetip of 7° half-angle Crossflow magnified 20 times.

The model is equipped with eighteen ports for PCB, SB and Kulite sensors. The locations of the PCB and SB sensors are shown in Table 3.1. The locations of the Kulite sensors are shown in Table 3.2. Six of the sensor ports are along a single axial ray (listed with an azimuthal angle of 0°). One or two of these sensor ports (Positions 1 and 4 or only Position 4) were used to measure the surface heat transfer with Schmidt-Boelter heat transfer gauges. The Schmidt-Boelter gauges were used to

calibrate the temperature-sensitive paint to heat transfer using the method discussed in Section 3.4.3. PCB gauges were used in two or three of the axial-ray sensor ports (Positions 1, 2 and 5 or only Positions 2 and 5). The PCB gauges are useful for measuring instabilities on the lee ray (for example the second-mode instability), but have had limited success measuring the travelling crossflow waves closer to the yaw ray, as discussed in Section 6.5. The final two locations in the axial ray contained an array of Kulite sensors (again locations listed in Table 3.2). The Kulites were used to measure aspects of the travelling crossflow waves. Kulites have been shown to be more useful for measuring the travelling waves since the frequency of the waves for the author's experiments were found to be near the lower end of the spectrum that a PCB can measure. The magnitude of the travelling wave pressure fluctuations were also found to be on the order of the PCB's pressure resolution, likely creating difficulties in measuring the waves. The spacing between the Kulites is 1.7 mm, which corresponds to less than half the wavelength of the most unstable travelling wave based on computations by Choudhari [97]. A spacing of larger than half the wavelength will lead to ambiguity in determining the wavelength. An additional six PCBs were added at the furthest downstream axial location (Positions 6a–6f in Figure 3.7 and Table 3.1), offset by $\pm 30^{\circ}$ increments in the azimuthal direction from the main sensor array.

Crossflow Cone Roughness Inserts

Segment 2 of the Crossflow cone was used to add discrete roughness elements to the cone. The discrete roughness elements, or dimples, were created by pressing a conical stainless steel rod into a Torlon section of the cone. This method is similar to the one used by Schuele [46]. Discrete roughness elements were placed around the azimuth, 50.8 mm (2 inches) axially from the nosetip. Several different Torlon sections were manufactured, varying the number of dimples around the azimuth, the depth of the dimples, and the diameter of the dimples. The specifications for each

Table 3.1.: Axial and azimuthal locations of PCB and SB sensor ports in the 7° half-angle Crossflow cone. All azimuthal angles measured with respect to main sensor ray.

Position	**Frustum**	**Axial Location [m]**	**Azimuthal Angle [degrees]**	**Gauge Type**
1	Front	0.147	0	SB or PCB
2	Front	0.191	0	PCB
4	Front	0.277	0	SB
5	Aft	0.320	0	PCB
6a	Aft	0.363	-90	PCB
6b	Aft	0.363	-60	PCB
6c	Aft	0.363	-30	PCB
6d	Aft	0.363	30	PCB
6e	Aft	0.363	60	PCB
6f	Aft	0.363	90	PCB

Torlon piece are listed in Table 3.3. The depths and diameters (D) listed are nominal. λ is the wavelength of the forced stationary crossflow wave.

There is one insert with no dimples (insert #1), four inserts with 50 dimples (spaced 7.2° apart), and one insert with 72 dimples (spaced 5° apart). A Torlon insert with 50 dimples (insert #2) is shown in Figure 3.10. The 50-dimple inserts should, theoretically, force the most unstable stationary crossflow wavenumber, according to calculations by Li [62]. The 72-dimple case should force a wavenumber greater than the most unstable wavenumber. Although, with the spanwise spreading of the stationary vortices due to the azimuthal pressure gradient, the forced wavenumber at 0.05 m will not be the same as the measured wavenumber downstream near 0.35 m from the nosetip. This will be discussed further in Section 5.4. As mentioned earlier, Saric [39] and Corke [98] found that forcing a wavenumber greater than the most

Table 3.2.: Axial and azimuthal locations of the Kulite sensor ports in the 7° half-angle Crossflow cone. All azimuthal angles measured with respect to main sensor ray.

	Segment	**Position**	**Axial Location [m]**	**Azimuthal Angle [degrees]**
Kulite Array 1	Front	k31	0.235	4.5
		k32	0.234	2.25
		k33	0.235	0
		k34	0.234	-2.25
Kulite Array 2	Aft	k61	0.363	4.5
		k62	0.361	2.25
		k63	0.363	0
		k64	0.365	-2.25

Table 3.3.: Nominal depth and diameter of roughness dots on the Torlon inserts. Roughness is 2 inches from the nosetip.

Insert Number	**# of Dots Around Azimuth**	**Depth [inches]**	**Diameter (D) [inches]**	**D/λ**
1	-	-	-	-
2	50	0.011	0.015	0.49
3	50	0.022	0.031	1.0
4	50	0.024	0.030	0.97
5	50	0.012	0.030	0.97
6	72	0.007	0.010	0.47

unstable wavenumber suppressed the most unstable modes, and crossflow-induced transition was delayed. It is not known if the same effect can be seen at Mach 6.

Figure 3.10.: Torlon section and 50-dimple case.

Radeztsky et al. [30] suggested that the diameter of the roughness elements divided by the wavelength of the desired forced stationary wave (D/λ) should be greater than 0.5 for effective forcing. It is not known if this ratio should be altered for hypersonic speeds. All the inserts are close to or exceed this ratio. Note that these diameters and depths are not the true values, since complete plastic deformation of the Torlon did not occur. Therefore the D/λ may not be accurate. Accurate measurements of the dimples will be made in the future when a white-light interferometer is made available.

A Mitutoyo Surftest SJ-301 surface roughness profilometer was used to measure the profile of the dimples. The 72-dimple case created dimples too small for the profilometer to measure. Figure 3.11 shows the profile of a dimple created for the 50-dimpled insert #2. A smooth case was added for reference. The depth was measured as approximately 40 μm, much smaller than the expected value of 280 μm. When the stainless-steel rod was pressed into the Torlon, some material was pushed out,

creating the peaks in the profile. This created a larger effective depth of the dimple, approximately 70 μm. The effective diameter of the dimple is 300 μm. It could also be said that the dimple has an effective diameter of approximately 600 μm, based on where the profile departs and returns to the smooth case. There is some uncertainty in the measurements since it is not known if the profilometer traversed the middle of the dot, and therefore the depth and diameter may be not be accurate. A drill press was used to push the conical rod into the Torlon by bringing the rod down to the surface of the Torlon, and lifting up the table with the vertical adjustment crank. This method created an uncertainty in the initial depth of approximately 20-μm. A Newmark RT-5DR Manual Rotary Stage was used to determine azimuthal placement of each dimple, and has a quoted accuracy of 0.002°. Larger dimples with diameters of approximately 1000 μm were created on a test piece of Torlon. The diameter and the depth of the dimples were uniform within 5%, although the measurements of the larger dimples will have the same uncertainties as the measurements of the smaller dimples. It is difficult to determine the uniformity of the dimples used in the experiments due to the errors associated with the current measuring technique. More advanced measuring techniques using white light interferometry are currently being explored. The most important aspects of the dimple for effective forcing are not known at hypersonic speeds. They may be the protruding surface height, the cavity depth or the dimple diameter.

3.7.2 Heat Transfer Cone

The second model, which will be referred to as the Heat Transfer Cone, is shown in Figure 3.12. The cone was mainly used in tests to validate the method for calibrating TSP to heat transfer, hence the name. The cone has a 7° half angle, a length of 0.406 m (16 inches), and a base diameter of 0.10 m (3.93 inches). The cone was manufactured in two pieces, nosetip and frustum, with the nominally sharp nosetip having a length of 0.076 m (3 inches). The material used for the nosetip and frustum

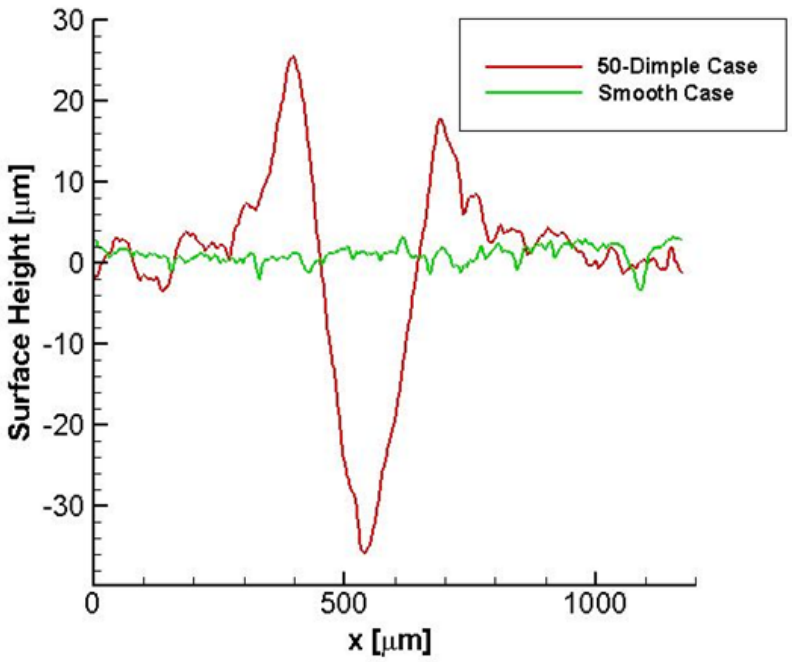

Figure 3.11.: Profile of discrete roughness element (dimple).

are stainless steel (17–4PH–Cond–H1100) and 6061-T6 aluminum, respectively. The TSP was typically feathered 0.10–0.15 m (4–6 inches) downstream of the nosetip. Detailed drawings of the Heat Transfer Cone can be found in Appendix C.

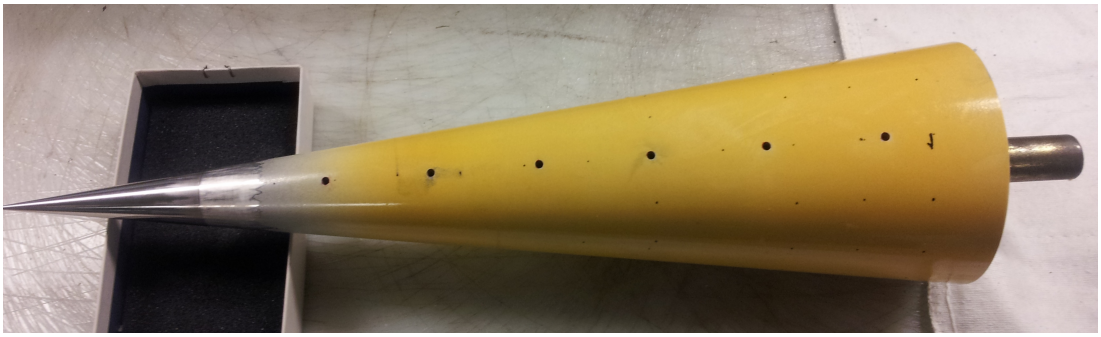

Figure 3.12.: 7° half-angle Heat Transfer Cone with temperature-sensitive paint applied to the frustum. The sensor ports are visible as the larger black dots along a single ray. The smaller black dots were used as reference points.

An image of the nosetip under a microscope with a circle fitted to the nosetip is shown in Figure 3.13. The nosetip is magnified 20 times, and the image was captured with a Moticam 3 microscope camera. The nose radius is approximately 67.8 μm. The step at the junction between the nosetip and frustum was 2 μm.

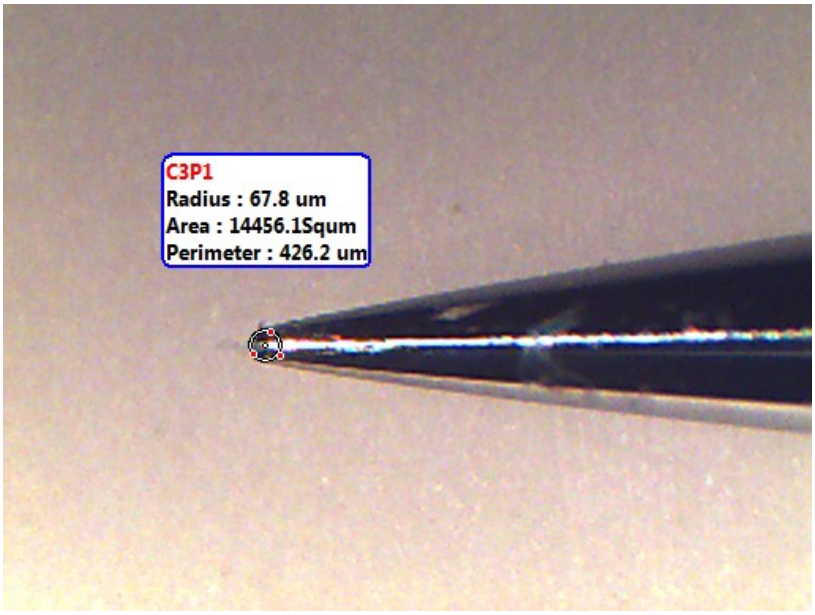

Figure 3.13.: Nosetip of 7° half-angle Heat Transfer Cone magnified 20 times.

The Heat Transfer cone was equipped with six sensor ports at varying axial distances along a single ray. The sensor axial locations are shown in Table 3.4. All sensor ports have the same diameter and can house either PCB or SB gauges.

Table 3.4.: Axial location of sensors for the Heat Transfer Cone. All sensors along a single axial ray.

Sensor Position	**Axial Location [m]**	**Sensor Type**
1	0.147	SB or PCB
2	0.190	SB or PCB
3	0.234	SB or PCB
4	0.277	SB or PCB
5	0.320	SB or PCB
6	0.363	SB or PCB

4. DETERMINING HEAT TRANSFER FROM TEMPERATURE-SENSITIVE PAINT MEASUREMENTS

NASA funded a joint project to develop a method for obtaining quantitative heat transfer from the paints [91]. There are several difficulties in obtaining heat transfer from the TSP in the BAM6QT, including non-uniform paint thickness, painting imperfections, the low levels of heating seen in the tunnel, and the large transient heat transfer that occurs during the tunnel startup.

The first set of results to test the validity of the heat-transfer data-reduction method was measured in January 2011 using the Heat Transfer Cone at 0° angle of attack. The Schmidt-Boelter heat transfer sensors used in this set of experiments are shown in Table 4.1 (no pressure transducers were used).

Table 4.1.: Position and serial number of the Schmidt-Boelter heat transfer gauges for the January 2011 experiments.

Position	**Gauge Name**	**Serial Number**	**Calibration Range**
1	SB–A	168636	0–22 kW/m^2
2	SB–B	168635	0–22 kW/m^2
3	SB–C	167032	0–22 kW/m^2
4	SB–D	167034	0–22 kW/m^2
5	SB–E	168136	0–22 kW/m^2
6	SB–F	168633	0–22 kW/m^2

Figure 4.1 shows the TSP image of an experiment performed under quiet flow at a stagnation pressure of 131 psia and a freestream Reynolds number of 9.9×10^6/m.

The SB gauges can be seen along the model centerline as black dots. The TSP image shows a roughly uniform temperature distribution in the spanwise direction, which is to be expected. It also appears that the boundary layer is fully laminar since the TSP shows low, even heating. The higher heating near the nosetip is due to the thinner boundary layer.

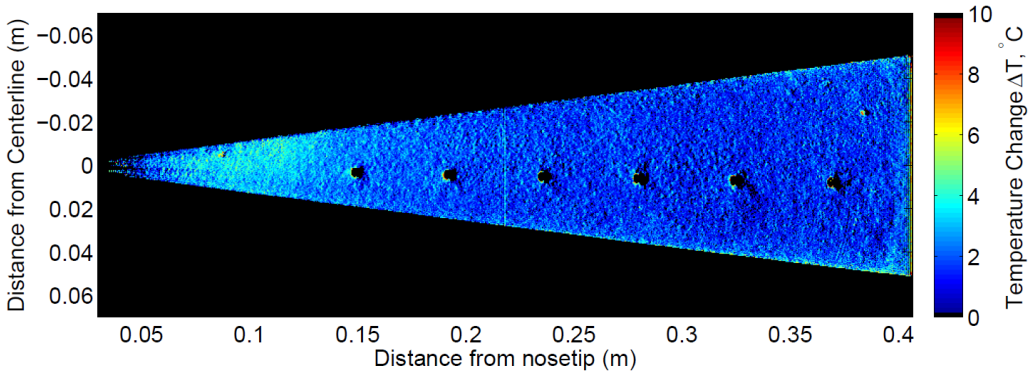

Figure 4.1.: TSP image of the 7° half-angle cone at 0° angle of attack. p_0 = 131 psia, Re = 9.9×10^6/m, T_0 = 425 K and T_w = 301 K. Quiet flow. January 2011 tests.

The data collected from sensors SB–A and SB–F are shown in Figure 4.2., along with the heat transfer calculated at the comparison patch of TSP. The TSP and SB data were compared at roughly t = 0.2 s to t = 2 s. The fits are fairly good. Table 4.2 shows the values for k/L and T_{model} (from Equation 3.6) for sensors SB–A and SB–F. Note that the constants for the two sensors are different. The heat transfer calibration process simply varies the model temperature, thermal conductivity and thickness of the paint, until good agreement is found between the TSP and the SB gauge. Therefore, it is possible that the two constants (k/L and T_{model}) can differ if different sensors are used in the heat transfer calibration method on the same model during the same run.

For each experiment the signals from three of the six SB gauges were amplified 100 times by three separate Stanford Research Systems SR560 low-noise voltage pream-

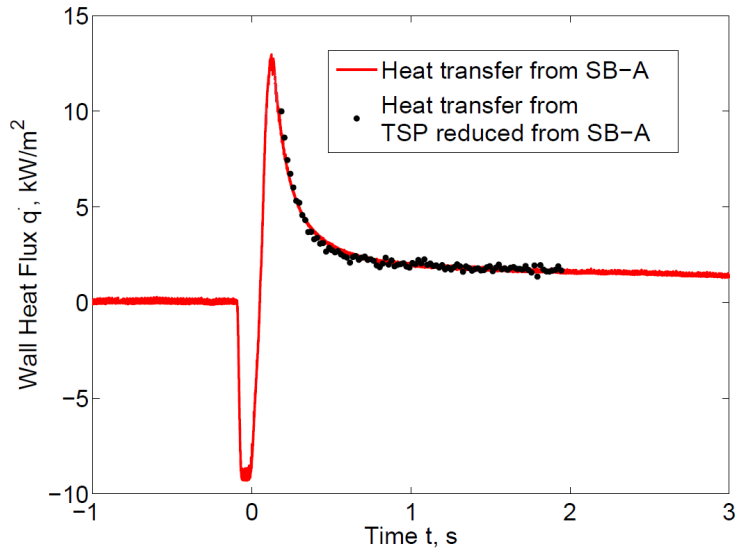

(a) SB–A

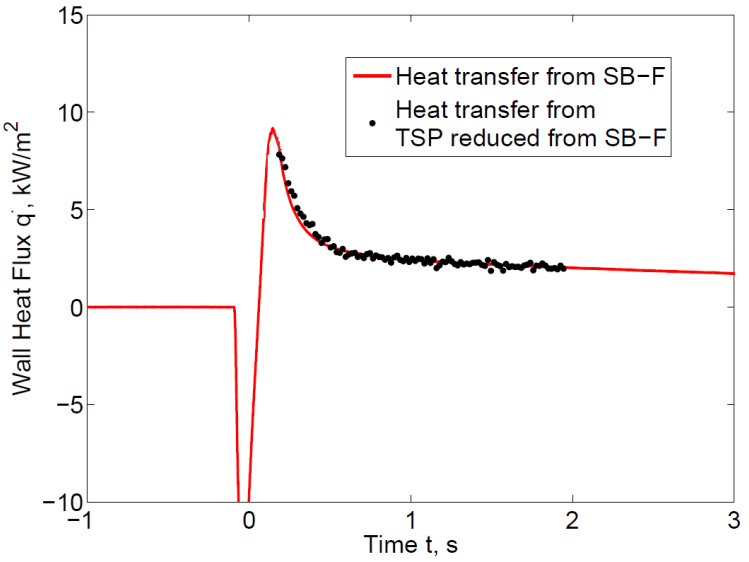

(b) SB–F

Figure 4.2.: Plot of heat transfer from the SB gauge along with the heat transfer calculated at the comparison patch of TSP. $p_0 = 131$ psia, Re $= 9.9\times10^6$/m. Quiet flow. January 2011 tests.

Table 4.2.: Constants used in the linear fit converting the TSP temperature to heat transfer.

	$\mathbf{k/L}$ $[\mathbf{W/K{\cdot}m^2}]$	$\mathbf{T}_{model}$ $[\mathbf{K}]$
SB–A	1.16	300.9
SB–F	0.86	297.8

plifiers before being digitized by the oscilloscopes. For the January 2011 experiments, the SB gauges were sampled at 50 kHz by the oscilloscopes.

Before each run, the tunnel is allowed to "settle" for 10-15 minutes after pressurizing the tunnel. Therefore the model should probably be in thermal equilibrium after this settling period, but the gauges typically gave a non-zero heat transfer likely due to ground loops or other sources of electrical noise. It was decided to shift the heat transfer data so that it would read 0.0 W/m^2 before the run began. The magnitude of this shift will be referred to as the "offset". The calibrated heat transfer is plotted along with the theoretical laminar heat transfer in Figure 4.3. In this figure, SB–D, SB–E and SB–F were amplified 100 times. The solid green and red lines represent the global heat transfer along the model centerline when calibrating the TSP using SB–A and SB–F respectively. To produce the line plots five pixels in the azimuthal direction were averaged and a moving average was used in the streamwise direction. The `smooth` function in MATLAB was used which is simply a moving average with a span of 10 pixels (in the streamwise direction). For this case 1 pixel was approximately 0.15 mm. The solid squares in the figure are the heat transfer obtained from the SB gauges. The blue squares show the heat transfer with no offset subtracted, while the pink squares show the heat transfer with the pre-run offset subtracted.

Four of the six SB gauges (SB–A, SB–C, SB–D, and SB–E) are within 25% of the theoretical heat transfer, once the offset is subtracted. SB–B is within 30% of the theory, and SB–F is within roughly 50% of the theory. Although this accuracy leaves much to be desired, it is difficult to make measurements of such low levels of heat

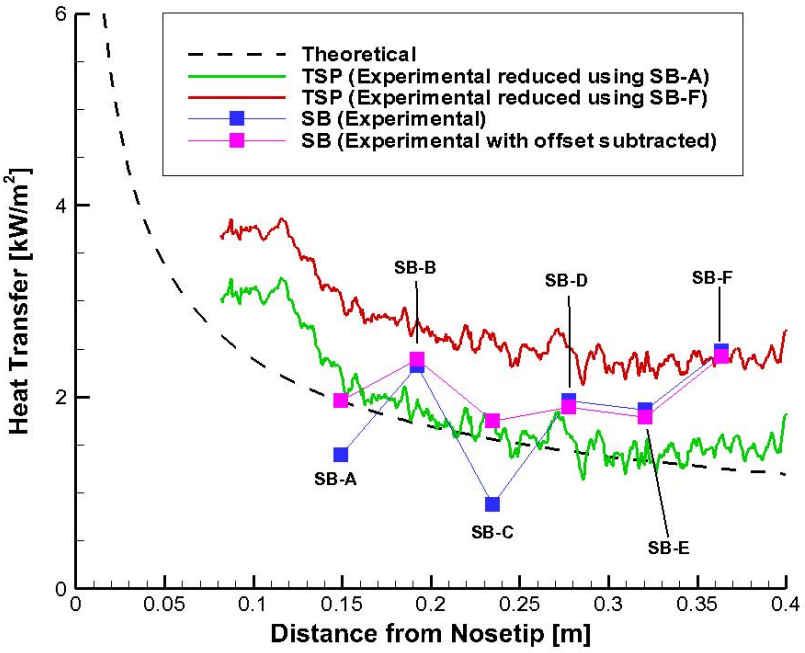

Figure 4.3.: Heat transfer rates calculated from TSP with the reduction method and compared to theory. $p_0 = 131$ psia, Re $= 9.9\times10^6$/m, Quiet flow, January 2011 tests.

.

transfer. The present measurements use only a small portion of the range of the most-sensitive SB gauges that are commercially available. For the three un-amplified SB gauges, the offset appears to have a significant impact on the calibrated heat transfer rates. If accurate data from the SB gauges are used to calibrate the TSP to heat transfer, the results are in good agreement with theory. However if the inaccurate data from the last SB gauge is used, the red curve shows poor agreement with theory.

The discrepancy between the reduced and theoretical data also tends to increase upstream of the first sensor. This may be due to the breakdown of the assumptions made to reduce Fourier's law to a linear relationship. For example, it was assumed that the model temperature is spatially uniform, but this may not be true approaching the nosetip. However the most likely reason for the discrepancy is the feathering of

the paint near the nosetip. The TSP is thinner because of the sanding in this region near the nosetip, so this data should be ignored.

A set of tests were done at a lower Reynolds number (7.9×10^6 /m) to see if the point-calibration method and the heat transfer from the gauges would produce similar results. These tests were also performed in January 2011. Figure 4.4 shows the TSP image at a freestream Reynolds number of 7.9×10^6 /m and a stagnation pressure of 103 psia. Once again the boundary layer appears to be fully laminar since the TSP shows low even heating.

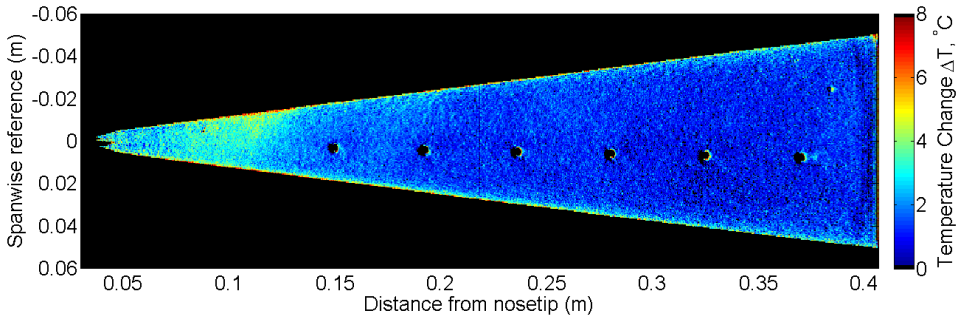

Figure 4.4.: TSP image of the 7° half-angle cone at 0° angle of attack. $p_0 = 103$ psia, Re = 7.9×10^6/m, $T_0 = 427$ K, $T_w = 303$ K. Quiet flow, January 2011 tests.

The data collected from sensor SB–A at this lower Reynolds number are shown in Figure 4.5, along with the heat transfer calculated at the comparison patch of TSP. The TSP and SB data were compared at roughly t = 0.2 s to t = 1.2 s. The entire heat transfer peak near t = 0.0 s is not used in the heat transfer reduction method, because the assumption of a spatially uniform model temperature is probably not valid right at tunnel start up. The data was also not used near t = 2.0 s, where an increase in heat transfer is seen. This is due to the nozzle-wall boundary layer separating. It is unclear how the flow conditions change when this occurs. The curve fit algorithm creates good agreement between the reduced heat transfer and the heat transfer from the SB gauge.

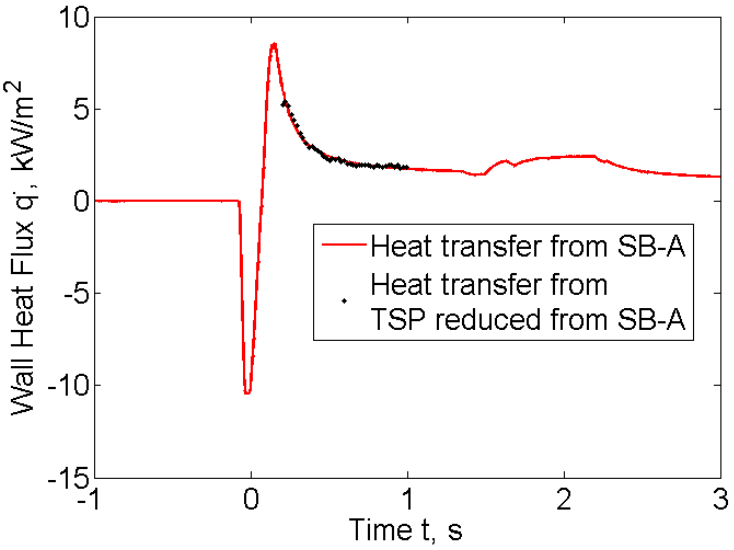

Figure 4.5.: Plot of heat transfer from the SB gauge along with the heat transfer calculated at the comparison patch of TSP. p_0 = 103 psia, Re = 7.9×10^6/m. Quiet flow. January 2011 tests.

The calibrated heat transfer is plotted along with the theoretical laminar heat transfer in Figure 4.6. In this figure, SB–A, SB–B and SB–C were amplified 100 times. Once again, the solid green and red lines represent the global heat transfer along the model centerline when calibrating the TSP using SB–A and SB–F respectively. The same `smooth` function in MATLAB was used to filter the line plots. The solid squares in the figure are the heat transfer obtained from the SB gauges. The blue squares show the heat transfer with no offset subtracted, while the pink squares show the heat transfer with the pre-run offset subtracted. The results are similar to the results presented in Figure 4.3. If an inaccurate gauge is used to calibrate the TSP, the calibration is inaccurate (red curve). If an accurate gauge is used to calibrate the TSP, the calibration agrees well with the theory (green curve).

Another set of experiments were performed during the same January 2011 entry at roughly the same Reynolds number as the first test (9.9×10^6/m) to examine the effect of amplifying different SB gauges. Figure 4.7 shows the heat transfer from

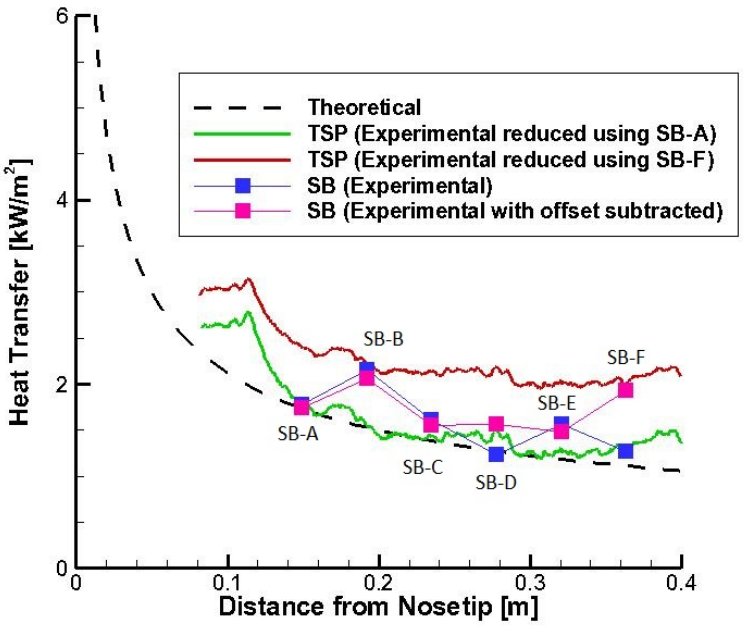

Figure 4.6.: Heat transfer rates calculated from TSP with the reduction method and compared to theory. $p_0 = 103$ psia, Re $= 7.9\times10^6$/m. Quiet flow. January 2011 tests.

the SB gauges (with the offset subtracted) for four different tests, along with the theoretical heat transfer. Table 4.3 shows the specifics of each test.

When the SB gauge is not amplified, subtracting the offset seems to give good agreement with the amplified gauge. Therefore, if no amplifiers are available, simply subtracting this pre-run offset seems to work well. Also note that SB–B and SB–F consistently read significantly higher heat transfer than the theory. This seems to suggest that there is some inherent error with the gauges, or that the calibration is not precise, since swapping the electronics still yields these inaccurate readings.

Table 4.3.: Specifics of each test looking at the effect of amplification on SB gauges. January 2011 tests.

Test	Notes
Case 1	SB–D, SB–E and SB–F amplified 100 times.
Case 2	SB–A, SB–B and SB–C amplified 100 times.
Case 3	no SB gauges amplified.
Case 4	only SB–B collecting data and not amplified.

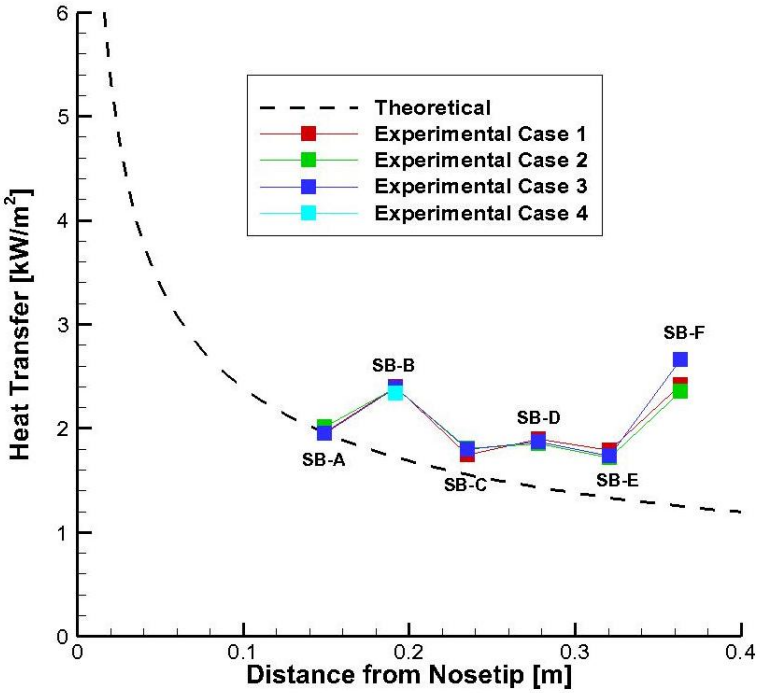

Figure 4.7.: Heat transfer rates with different SB gauges amplified. p_0 = 131 psia, Re = 9.9×10^6/m, T_0 = 424 K, T_w = 304 K. Quiet flow. All data shown with pre-run offset subtracted. January 2011 tests.

.

A second set of experiments were performed in April 2011 with some of the sensor positions swapped and some sensors replaced. This was done to see if SB–B in the

previous tests would still produce inaccurate readings, and if SB–A and SB–E would still yield accurate readings. The gauges used in this set of experiments are shown in Table 4.4. Note that the gauges in positions 1, 2 and 5 from the January 2011 tests (Table 4.1) have been moved to positions 2, 5 and 6 respectively.

The April 2011 experiments were performed under quiet flow at a stagnation pressure of 131 psia, and a freestream unit Reynolds number of 9.9×10^6/m. The heat transfer from the SB gauges along with the theoretical heat transfer is shown in Figure 4.8. Three of the six sensors appear to give accurate readings. SB–B once again shows heat transfer higher than the theory. SB–E shows fairly accurate heat transfer readings during both set of experiments. Finally, SB–A gave accurate readings in the January 2011 experiments, but was inaccurate in the April 2011 experiments. It is not clear why SB–A now provides inaccurate heat transfer data.

Table 4.4.: Position and serial number of the Schmidt-Boelter heat transfer gauges for the April 2011 experiments.

Position	**Gauge Name**	**Serial Number**	**Calibration Range**
1	SB–G	169256	0–11 kW/m^2
2	SB–A	168636	0–22 kW/m^2
3	SB–H	169251	0–11 kW/m^2
4	SB–I	169255	0–11 kW/m^2
5	SB–B	168635	0–22 kW/m^2
6	SB–E	168136	0–22 kW/m^2

These two sets of experiments show that the point-calibration of heat transfer from the TSP agrees well with the theory, if the SB gauge used in the calibration process is accurate. The experiments showed that roughly half the SB gauges were within 25% of the theoretical heat transfer. Since the point-calibration method is heavily dependent on the gauge used for the calibrations, it was decided that the factory

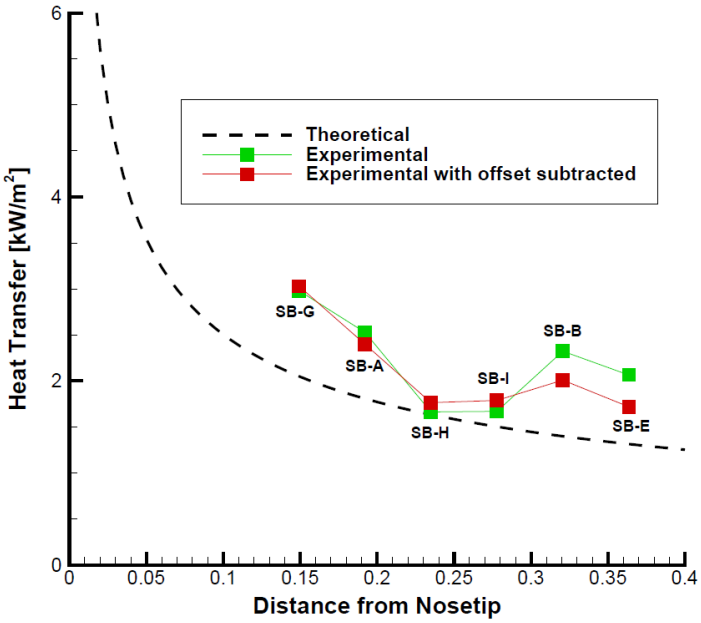

Figure 4.8.: Heat transfer rates with SB gauges swapped. p_0 = 131 psia, Re = 9.9×10^6/m, T_0 = 428 K, T_w = 302 K. Quiet flow. All data shown with pre-run offset subtracted.

calibrations should be verified. Several SB gauges were sent back to the Medtherm Corporation in August 2011 for recalibration, including SB–E and SB–F. The new calibrations only differed by 0.5%. Therefore, an error in the calibrations does not appear to be the reason for the higher than theoretical heat transfer readings from these gauges. Unfortunately, at the time of these tests, the step created by the sensor was not measured. Appendix B shows that this step can have a significant impact on the measured heat transfer. If the gauge is protruding into the boundary layer, the measured heat transfer was much higher than the theoretical heat transfer. When the gauge was close to flush with the surface, the measured heat transfer was in much better agreement with the theoretical heat transfer.

4.1 Determining Heat Transfer Using Known Paint Thickness and Model Temperature

Finally, tests were done to determine if the TSP data could be reduced to heat transfer using the measured paint thickness and the measured model temperature, removing the need for a Schmidt-Boelter gauge. For this case, T_{model} and T_{ref} are assumed to be equal; therefore the heat transfer equation reduces to

$$q = \frac{k}{L}\Delta T. \tag{4.1}$$

According to Dr. Tianshu Liu, the thermal conductivity (k) for the insulating paint is between 0.21 and 0.50 W/m-K, with a typical value being 0.25 W/m-K [99]. The paint thickness was measured using an Elcometer 456 capacitance gauge with the method discussed in Section 3.4.3. The average paint thickness in the June 2011 tests was 277 μm, with a $\pm$15% variation from the average. The August-September tests had an average thickness of 201 μm with a $\pm$5% variation from the mean.

Figure 4.9 shows data from the June 2011 tests, with the heat transfer calibrated from the TSP with the point-calibration method (green curve). This plot also shows the heat transfer calculated with the known paint thickness, thermal conductivity and model temperature (red and turquoise curve). The turquoise curve is the lower limit of the calculated heat transfer assuming the paint thickness is 15% below the mean, and the red curve is assuming the paint thickness is 15% above the mean. From this plot, it can be seen that the calibration method needs to be anchored with a SB gauge due to the larger error in the red and turquoise curves. It is not clear if the error is largest in the estimated thermal conductivity, the measured model temperature or the measured paint thickness.

Figure 4.10 shows the results from the August–September 2011 tests. This plot shows the same results. The heat transfer calculated from the known paint thickness, model temperature and thermal conductivity yielded heat transfer levels 2–3 times

higher than the theory. Therefore, the calibration method needs to have a Schmidt-Boelter gauge to anchor it.

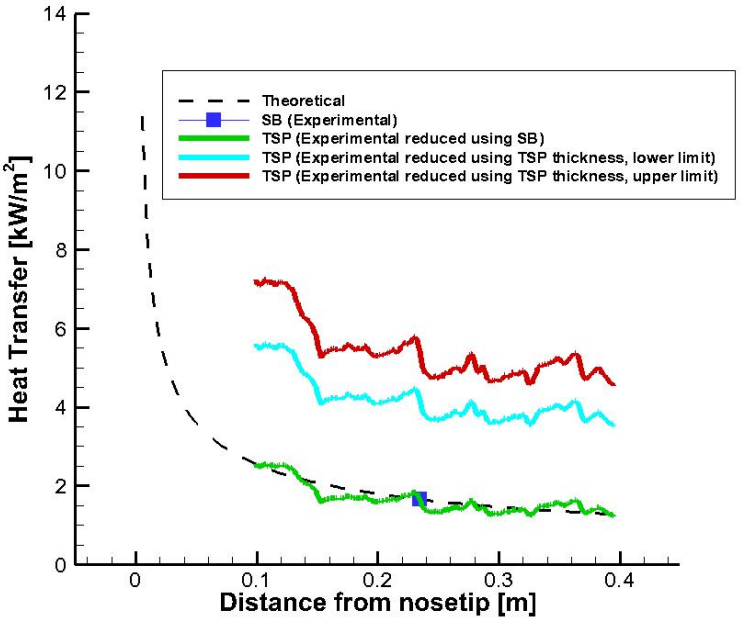

Figure 4.9.: Heat transfer rates calibrated from TSP with the point-calibration method and known paint thickness and model temperature. p_0 = 131 psia, Re = 9.9×10^6/m. Quiet flow. June 2011 tests.

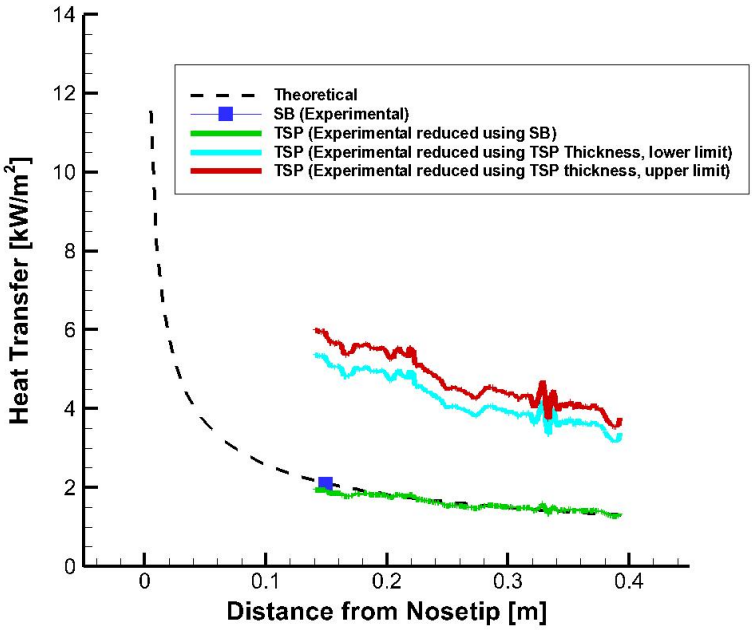

Figure 4.10.: Heat transfer rates calculated from TSP with the reduction method and known paint thickness and model temperature. $p_0 = 131$ psia, Re $= 9.9\times10^6$/m. Quiet flow. August-September 2011 tests.

4.2 Example of the Calibration Method at Angle of Attack

This section provides an example of the TSP calibration method for a cone at angle of attack. A temperature-sensitive paint image with no additional processing is shown in Figure 4.11 plotted in terms of degrees Celsius above the pre-run temperature. The yaw side of the cone is imaged. The pre-run temperature is determined by averaging the readings from the thermocouples in the SB gauges and a thermocouple pasted on the base of the model. The thermocouple readings differed by up to 1 K. The red square represents the patch of TSP to which the data from SB gauge is compared (refer to Section 3.4.3 for more details on the calibration method). The SB gauge is the black circle just downstream of the red square. The red lines show a typical region at where a spanwise heat transfer profile is taken. The heat transfer is averaged

between the two lines, along the streamwise direction. The vertical line at an axial pixel of 400 is an artifact of using two analog-to-digital converters in the PCO camera. This line will be present in many images, and changes in width depending on how much the tunnel shifts during a run compared to before the run.

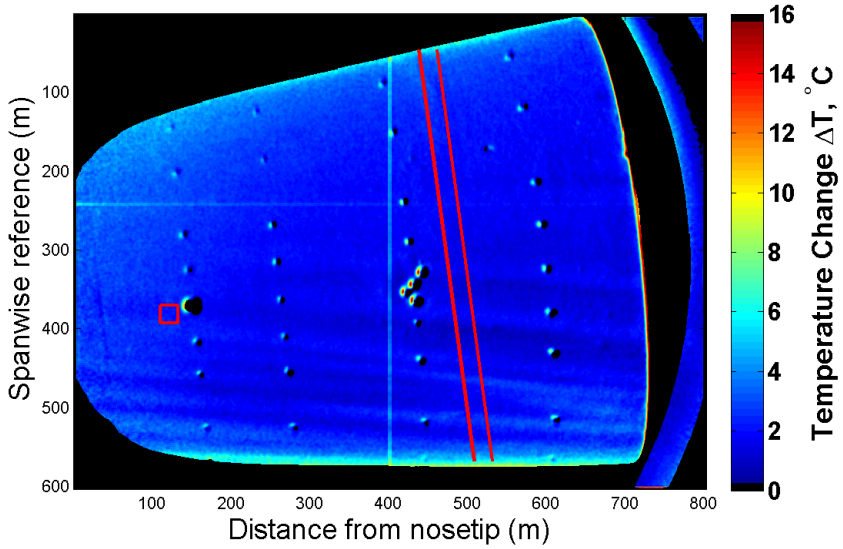

Figure 4.11.: Temperature-sensitive paint image. Yaw side of the cone imaged.

Figure 4.12 plots the heat transfer from the SB gauge over the course of a run (black line). The diaphragms burst at approximately 0.0 seconds. The pre-run data is used to determine if any offset should be applied to the SB gauge signal, since it is assumed that the model is in thermal equilibrium just before the run. The blue squares represent the heat transfer from the SB gauge averaged over the exposure time of the camera. The exposure time is typically on the order of 10 ms. In practice, the averaged heat transfer is compared to the temperature from the TSP patch. The red dots represent the data from the comparison patch of TSP calibrated to heat transfer using equation 3.6. The constants k/L and T_{model} were found by performing a least-squares fit between the calibrated TSP and the SB readings.

The large decrease in heating near the start of the run is caused when the expansion fan created by the diaphragm burst passes over the model. This is followed by a large heating impulse when the hot gas from upstream passes over the model, before Mach-6 flow begins. Only the data after the heating impulse is used in the calibration, because the assumption of a uniform model temperature may not be valid during the heating impulse. Data is also not included after two seconds due to an unexplained increase in tunnel noise [56]. The fit between the calibrated heat transfer from the comparison patch of TSP and the SB gauge is good, with a coefficient of determination (R^2) of 0.987. Luersen attempted to use the same calibration method on a flared cone in the BAM6QT [80] and did not obtain desirable results. It is not known why Luersen was not able to obtain good calibrations. It is possible that the difference in geometry was the reason, but Chynoweth in new experiments using the same flared cone was able to get a good fit between the two data sets [100]. Chynoweth obtained R^2 values between 0.96 and 0.99, similar to the author. The R^2 values for Luersen's data is not known. It is not known why Chynoweth obtained better TSP calibrations than Luersen.

One of the assumptions made when calibrating the TSP to heat transfer is that there is a linear relationship between the heat transfer measured by the SB gauge and the temperature measured by the TSP. Figure 4.13 plots the heat transfer from the SB gauge against the temperature change from the TSP. The plot confirms the linear relation between the two data sets.

Figure 4.14 is a TSP image calibrated to heat transfer using the constants determined from the least-squares fit. A new set of constants is found for each run. The image was obtained with the camera viewing from the yaw side of the cone, at 90° to the pitch plane ("yawside image"). Many such images will be presented in this fashion.

Many tests were performed imaging the lee side of the cone. A sample calibration with the lee side of the cone imaged is described here. A temperature-sensitive paint image with no additional processing is shown in Figure 4.15 plotted in terms of degrees

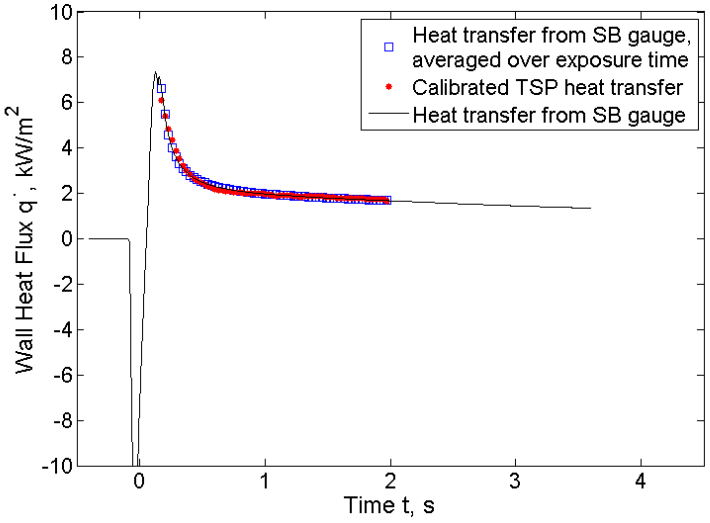

Figure 4.12.: Plot of heat transfer from the SB gauge for the duration of the run, along with the heat transfer calculated at the comparison patch of TSP using the equation 3.5. SB gauge on the yaw side of the cone.

Celsius above the pre-run temperature. The red square represents the patch of TSP to which the SB data is compared. The SB gauge is just above the red square, at a spanwise reference of approximately 140 pixels. The red lines show a typical region where a spanwise heat transfer profile is taken. The streaks in the TSP image are due to stationary crossflow vortices, and will be discussed in detail in Chapter 5.

Figure 4.16 plots the heat transfer from the SB gauge over the course of a run (black line). The blue squares represent the heat transfer from the SB gauge averaged over the exposure time of the camera. The exposure time is typically on the order of 10 ms. The red dots represent the data from the comparison patch of TSP calibrated to heat transfer using equation 3.6. The fit between the calibrated heat transfer from the comparison patch of TSP and the SB gauge is good, with a coefficient of determination (R^2) of 0.996.

Figure 4.17 plots the heat transfer from the SB gauge against the temperature change from the TSP. Again, there is a linear relation between the two data sets.

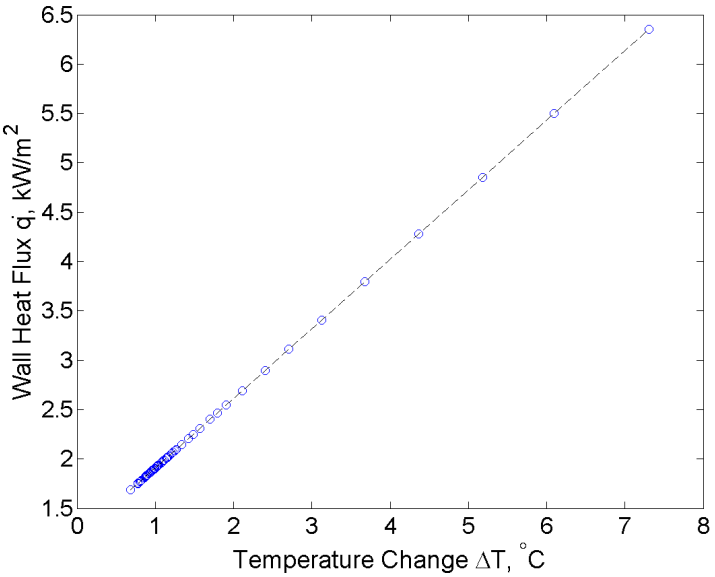

Figure 4.13.: Heat flux measured by the SB gauge plotted against the temperature change measured by the TSP at the comparison patch. SB gauge on the yaw side of the cone.

Figure 4.18 is the TSP image in Figure 4.15 calibrated to heat transfer using the constants determined from the least-squares fit. The lee side of the cone is imaged.

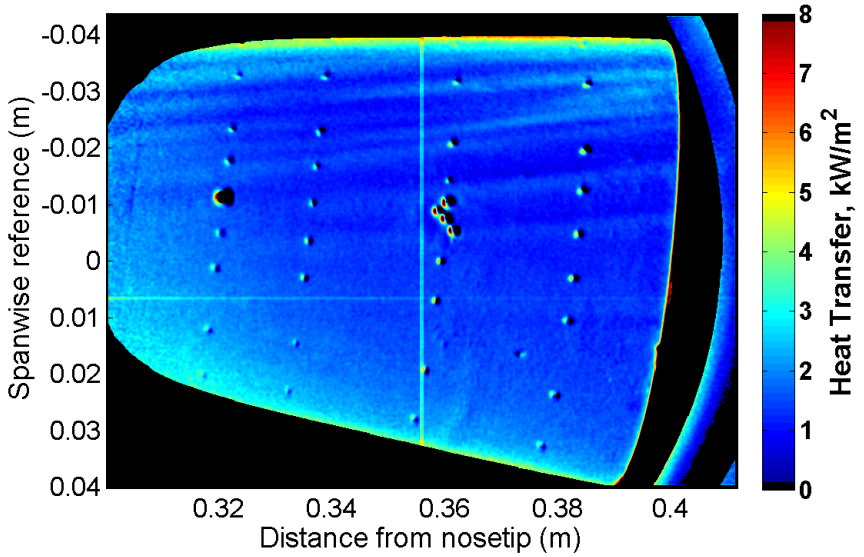

Figure 4.14.: Temperature-sensitive paint image calibrated to heat transfer. Yaw side of the cone imaged.

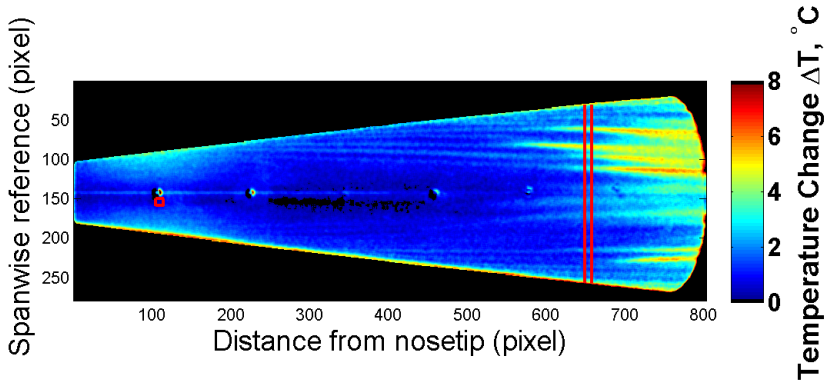

Figure 4.15.: Temperature-sensitive paint image. Lee side of the cone imaged.

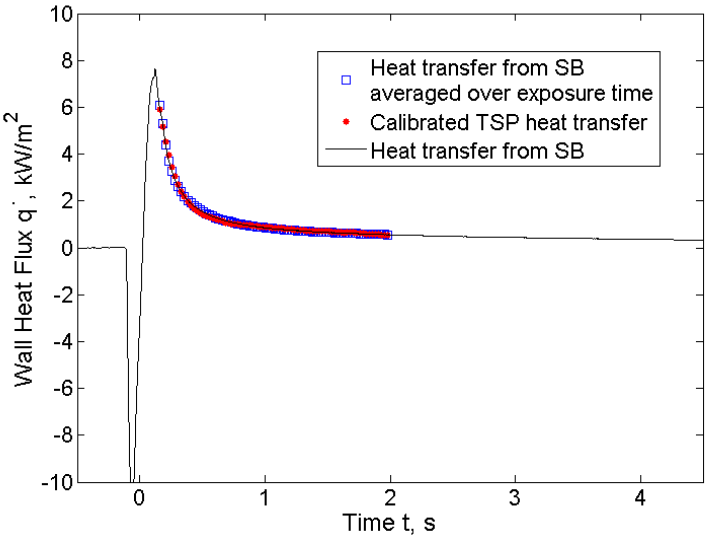

Figure 4.16.: Plot of heat transfer from the SB gauge for the duration of the run, along with the heat transfer calculated at the comparison patch of TSP using the equation 3.5. SB gauge on the lee side of the cone.

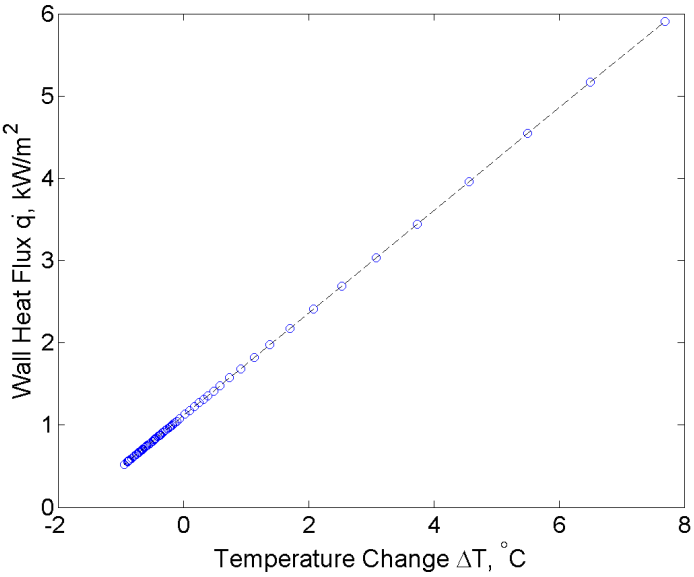

Figure 4.17.: Heat flux measured by the SB gauge plotted against the temperature change measured by the TSP at the comparison patch. SB gauge on the lee side of the cone.

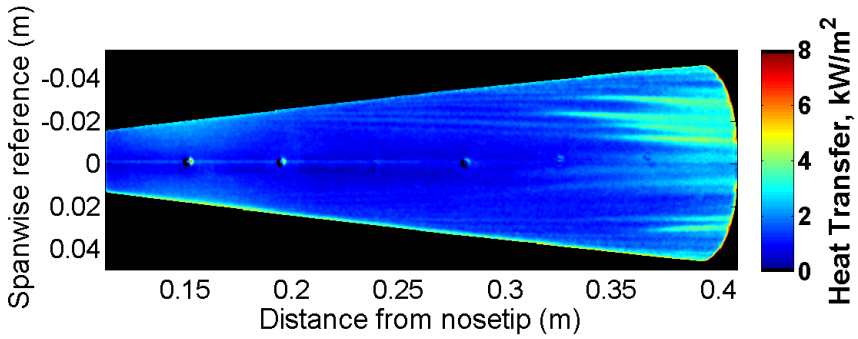

Figure 4.18.: Temperature-sensitive paint image calibrated to heat transfer. Lee side of the cone imaged.

5. EFFECT OF ROUGHNESS ON STATIONARY CROSSFLOW WAVES

5.1 Processing of Heat Transfer from TSP Images

This section will show several possible methods of scaling heat transfer profiles for determining where the boundary layer transitions to turbulence, along with the method to determine the growth of the stationary waves. Five sample TSP images under noisy flow at increasing Reynolds are shown in Figure 5.1. The yaw side of the cone is imaged and flow is from left to right. At the two highest Reynolds number, boundary-layer transition appears to be occurring upstream or near the upstream edge of the imaged area. At a Reynolds number of 8.0×10^6/m, transition may be occurring near 0.36 m. At the two lowest Reynolds numbers, the boundary layer appears to be fully laminar.

Axial heat transfer profiles along the 80° ray (denoted in red in Figure 5.1(a)) for the five TSP images are shown in Figure 5.2. From this plot, it is difficult to make inferences regarding the state of the boundary layer. For example, at the highest Reynolds number, based on this plot alone it would difficult to conclude if the boundary layer is laminar or turbulent because there is no sharp increase in heat transfer. There are several ways the data can be scaled. The laminar data should scale with the square-root of the Reynolds number [101]. The Reynolds number will be based on axial distance from the nosetip. The laminar data should also approximately scale with the laminar theoretical solution for a cone at 0° angle of attack. The theoretical solution was found with the method discussed in Section 3.4.3. The theoretical heat transfer solution is proportional to the square-root of the distance from the nosetip, therefore scaling with either the square-root of the Reynolds number or the laminar

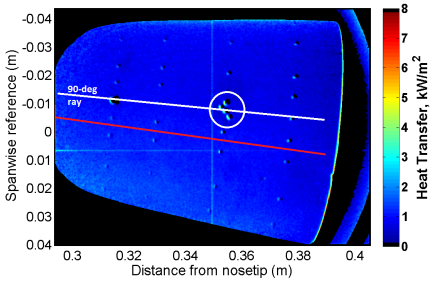

(a) Re = 3.1×10^6/m, p_0 = 37.1 psia, T_0 = 421 K, T_w = 305 K.

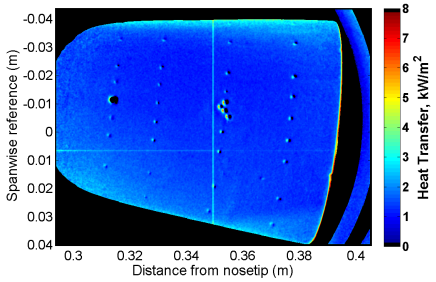

(b) Re = 6.3×10^6/m, p_0 = 76.8 psia, T_0 = 423 K, T_w = 304 K.

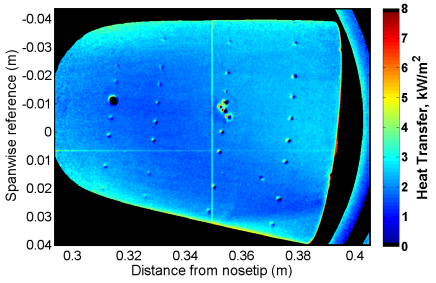

(c) Re = 8.0×10^6/m, p_0 = 98.5 psia, T_0 = 425 K, T_w = 302 K.

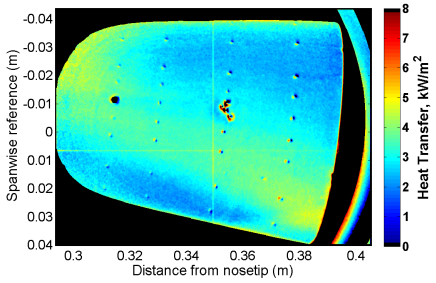

(d) Re = 10.6×10^6/m, p_0 = 130.2 psia, T_0 = 425 K, T_w = 304 K.

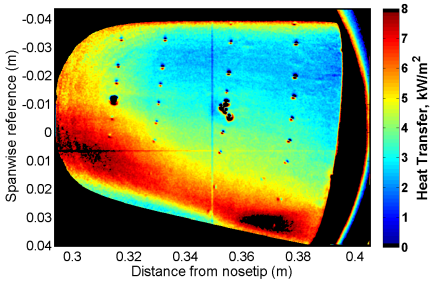

(e) Re = 13.3×10^6/m, p_0 = 162.8 psia, T_0 = 424 K, T_w = 306 K.

Figure 5.1.: TSP images for varying Reynolds number with smooth Torlon insert under noisy flow. Yaw side of the cone.

theoretical solution should produce similar results. Finally, the turbulent data should scale with the fifth root of the Reynolds number [101].

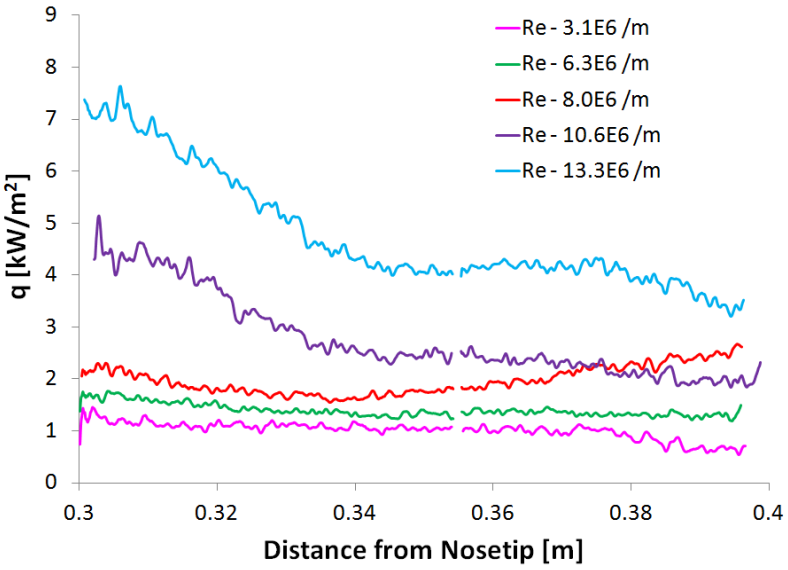

Figure 5.2.: Axial heat transfer of the TSP images in Figure 5.1 along the 80° ray.

Figure 5.3 plots the heat transfer profiles scaled by the square-root of the Reynolds number, the laminar theoretical heat transfer for a cone at 0° AoA, and by the fifth root of the Reynolds number. When the data is scaled by the square-root of the Reynolds number, the heat transfer for the three lowest Reynolds number cases collapses upstream of approximately 0.36 m. At 0.36 m, the heat transfer at a Reynolds number of 8.0×10^6/m begins to depart from the other two profiles, suggesting that the boundary layer is beginning to transition. Far downstream, near 0.39 m, the 6.3 and 8.0×10^6/m profiles begin to depart, suggesting that at a Reynolds number of 6.3×10^6/m the boundary layer is beginning to transition. The heat transfer profiles at a Reynolds number of 10.6 and 13.3×10^6/m do not collapse on top of the other profiles, suggesting that the boundary layer is either transitional or turbulent. Scaling by the theoretical heat transfer (q_{th}) produces the same trends as scaling with the square-root of the Reynolds number. One advantage of scaling with the theoretical heat transfer is the non-dimensional heat transfer values are more intuitive

than the values produced when scaled by the square-root of the Reynolds number. For example, when the boundary layer is laminar, it would be expected that the non-dimensional heat transfer is approximately 1, and when the boundary layer is transitional or turbulent it would be expected that the non-dimensional heat transfer would be up to 3–8 times higher [1].

When scaling by the fifth root of the Reynolds number, it is expected that the turbulent heat transfer profiles will collapse on top of each other. That does not appear to be the case. The profiles at a Reynolds number of 10.6 and 13.3×10^6/m do not collapse. It is possible that the boundary layer is not fully turbulent but still transitional. This document will use the laminar theoretical heat transfer on a sharp cone at zero AoA as the scaling factor because of the intuitive numbers yielded and the ease at identifying the onset of transition. Figure 5.4 plots the theoretical laminar heat transfer on a cone at zero AoA for the conditions of the TSP images in Figure 5.3. As expected, the heat transfer increases at a given axial location when the Reynolds number is increased.

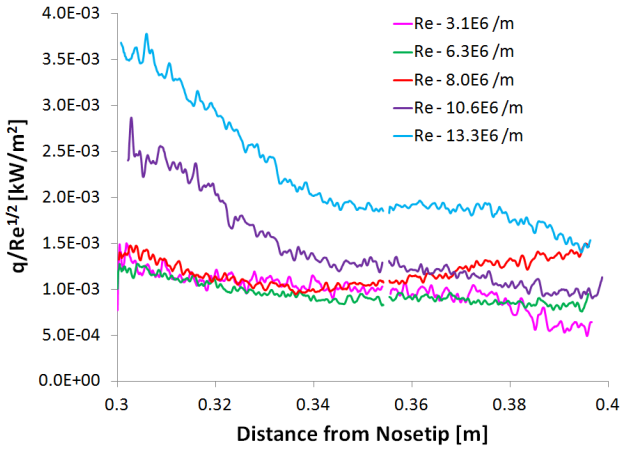

(a) Scaled by $\mathrm{Re}^{1/2}$.

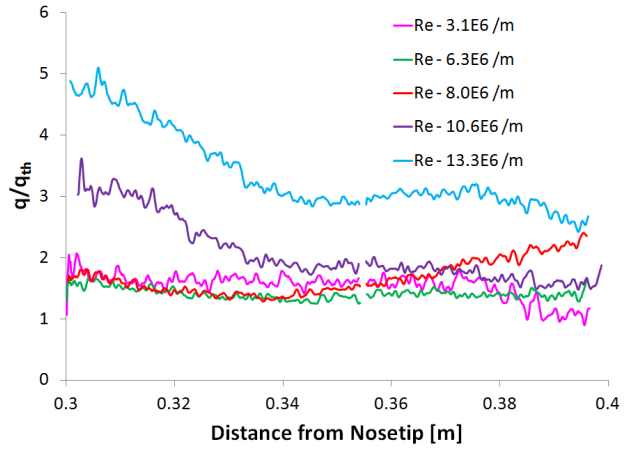

(b) Scaled by q_{th}.

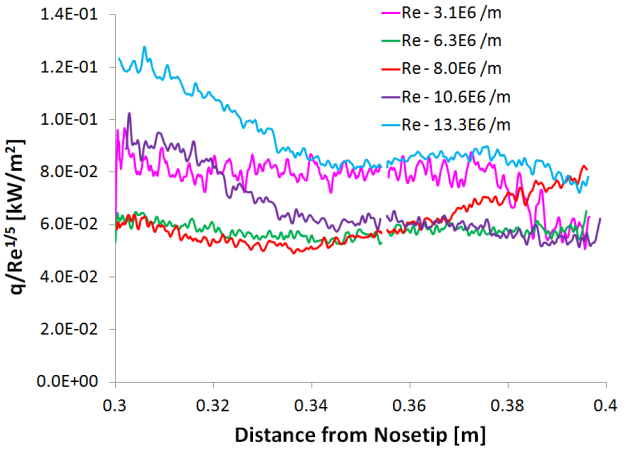

(c) Scaled by $\mathrm{Re}^{1/5}$.

Figure 5.3.: Different scaling methods of the axial heat transfer profiles.

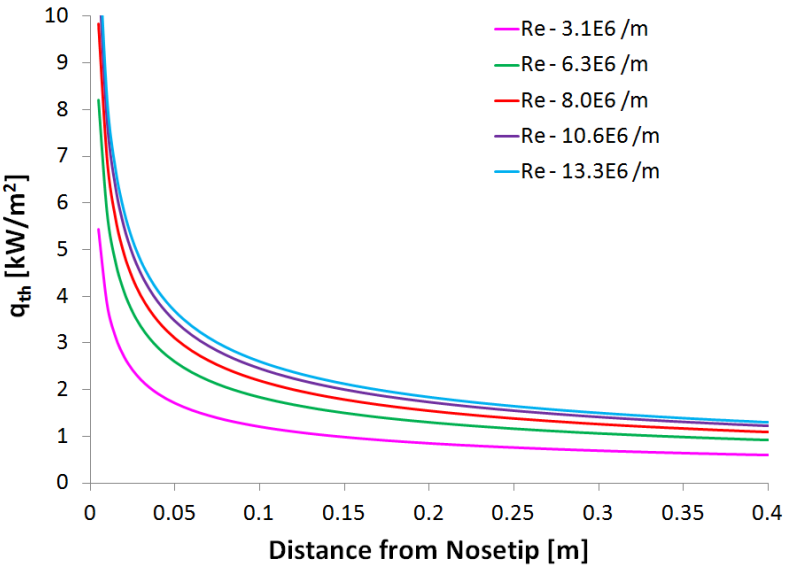

Figure 5.4.: Theoretical heat transfer on the sharp cone at zero AoA at the same conditions as the TSP images in Figure 5.1.

Another sample TSP image is shown in Figure 5.5 under quiet flow. The lee side of the cone is imaged. In the image, a stationary vortex is easily distinguishable and is possibly breaking down to turbulence. The upstream tip of the stationary vortex of interest is labelled in the figure.

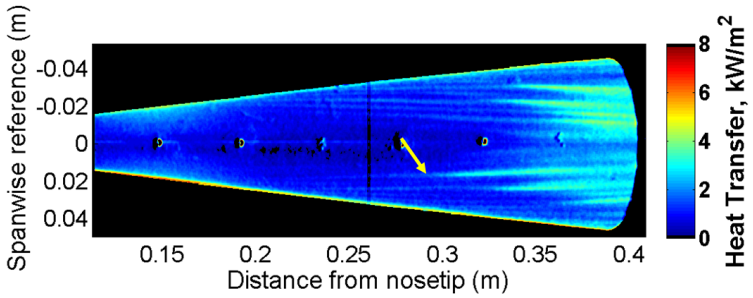

Figure 5.5.: TSP image with a single distinguishable stationary vortex growing large and possibly breaking down to turbulence under quiet flow. 72 dimples (insert #6). Lee side of the cone. T_w = 297 K, Re = 10.4×10^6/m, p_0 = 138 psia, T_0 = 426 K.

Several methods have been tested for measuring the growth and decay of the stationary wave. Figure 5.6 shows both the maximum heat transfer and the maximum amplitude of the stationary vortex. The maximum heat transfer was found by taking spanwise heat-transfer profiles at each axial pixel location, and determining the maximum value. The maximum amplitude was found by determining the maximum heat transfer at each axial location, then subtracting the laminar theoretical heat transfer on a sharp cone at zero AoA at this axial location, and then dividing the result by the same theoretical heat transfer.

$$A = \frac{q_{max} - q_{th}}{q_{th}} \tag{5.1}$$

The stationary vortex maximum heat transfer and amplitude agree qualitatively with the trends seen in low speed experiments [33] and high-speed nonlinear PSE computations [62] where there appears to be linear growth followed by a saturation and decay of the stationary vortex. Saturation appears to be occurring near 0.35 m,

and decay appears to occur just downstream, perhaps after the onset of turbulence. The heat transfer is approximately equal to the laminar theoretical value on a cone at zero AoA just upstream of where the stationary vortex is visible in the TSP.

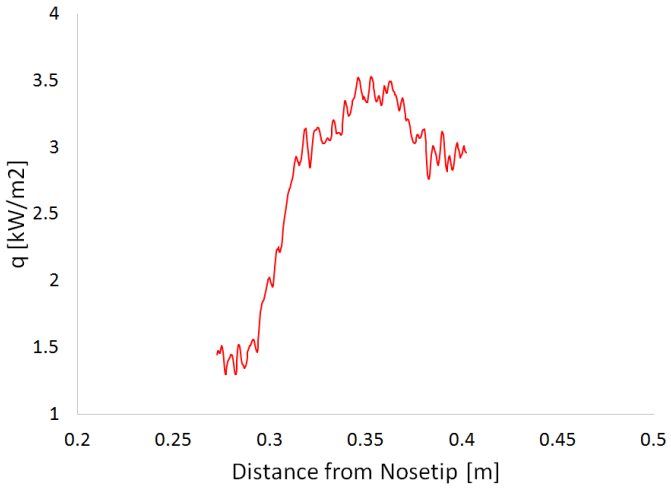

(a) Maximum heat transfer of stationary vortex.

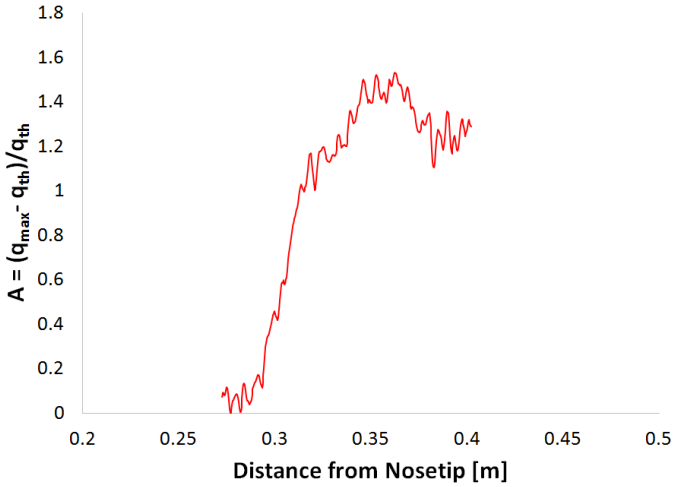

(b) Amplitude of stationary vortex.

Figure 5.6.: Maximum heat transfer and amplitude of the stationary vortex labelled in Figure 5.5 under quiet flow.

The growth rate of the stationary vortex is found with the following equation:

$$\alpha = \frac{\ln\left(\frac{A_2}{A_1}\right)}{x_2 - x_1} \tag{5.2}$$

where A and x are the amplitude of the wave and the axial distance at the specified location. The amplitude was found using equation 5.1. The local growth rate of the stationary wave is shown in Figure 5.7. There is significant scatter in the growth rate plot because of the fluctuations in the amplitude profile. The general trend is that the growth rate is a maximum when the stationary vortex becomes visible in the TSP images. The growth rate approaches zero when the stationary vortex saturates, and becomes negative when the stationary vortex decays.

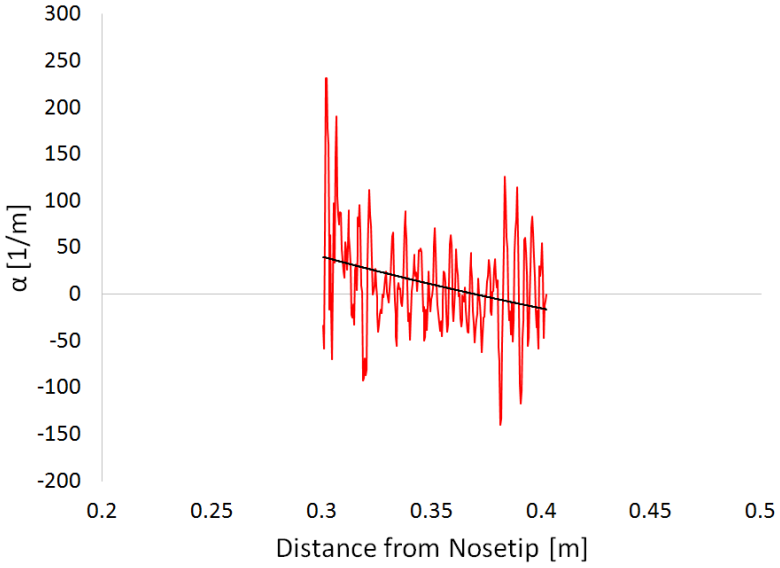

Figure 5.7.: Growth rate of the stationary vortex labelled in Figure 5.5 along the 80° ray.

Figure 5.8 shows a sample spanwise heat transfer profile obtained from a temperature sensitive paint image. The heat transfer is non-dimensionalized by the theoretical laminar heat transfer on a sharp cone at zero AoA. Often the average heat transfer varies with azimuthal angle due to a varying boundary layer thickness and the varying intensity of the TSP signal due to the cone rolling away from the camera. This can be

seen in the spanwise profile plot. The black line represents a second-order polynomial fit to the data, along with the equation of the polynomial shown.

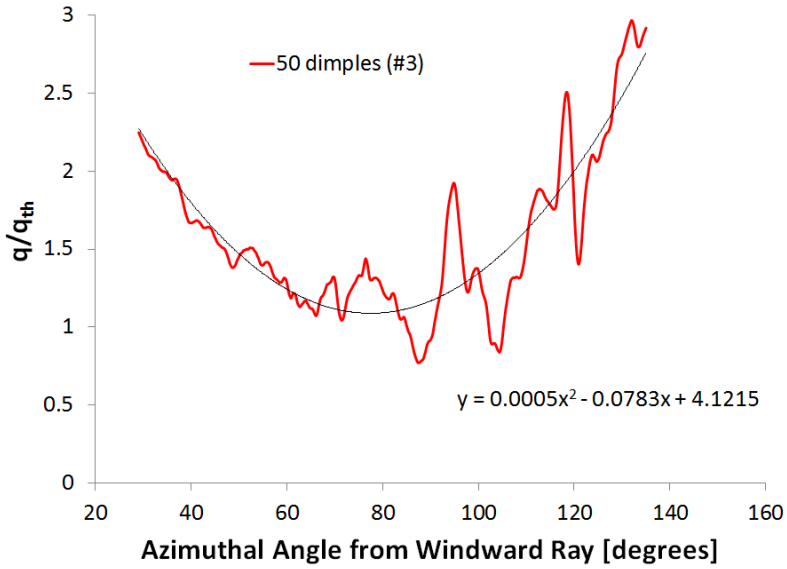

Figure 5.8.: Sample spanwise heat-transfer profile obtained from a TSP image.

Figure 5.9 plots the spanwise heat transfer with the polynomial subtracted. The value of the polynomial represents the mean local non-dimensional heat transfer. The values yielded from the mean local non-dimensional heat transfer subtracted from the non-dimensional heat transfer will be used to determine the RMS of the non-dimensional heat transfer.

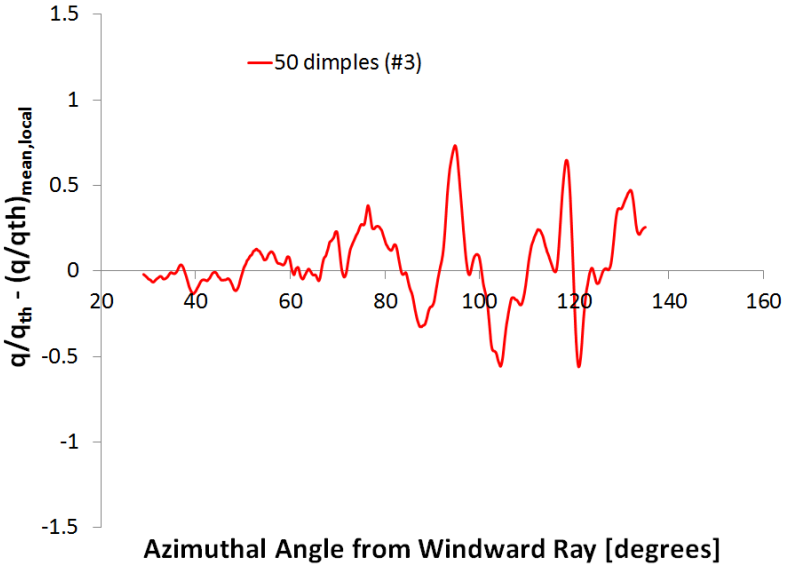

Figure 5.9.: Sample spanwise heat-transfer profile obtained from a TSP image with the mean local heat transfer subtracted.

5.2 Smooth Wall Experiments

Experiments were performed in April 2012 to obtain global heat transfer from the temperature-sensitive paint on a 7° half-angle cone at 6° angle of attack with no discrete roughness elements. The TSP had an RMS roughness of 0.55 μm and the step at the leading edge of the paint had a slope of 10 μm per mm. Previous experiments by the author had a paint step of 150–200 μm and a slope at the leading edge of the paint of 900–1200 μm per mm [54, 95]. The paint edge appeared to dominate the generation of the stationary vortices. The significantly reduced step in the paint should allow for a better smooth-wall case, and a clearer determination of the effect of discrete roughness near the nosetip.

Figure 5.10 shows two experimental TSP images taken at increasing Reynolds numbers under quiet flow, along with a DNS computation provided by Gronvall [102]. At the lowest unit Reynolds number of 8.03×10^6/m (Figure 5.10(a)), the flow appears to be fully laminar. Crossflow vortices are faintly visible near the downstream end

of the cone, but do not appear to be breaking down to turbulence. Increasing the Reynolds number to 9.82×10^6/m (Figure 5.10(b)), the crossflow vortices appear to grow in magnitude near the downstream end of the cone. It is possible that transition is occurring near the lee ray at this Reynolds number, but the TSP image is inconclusive (PCB sensor data will be shown later).

As mentioned in Section 2.2, direct numerical simulations (DNS) were performed at the University of Minnesota by Joel Gronvall for a 7° half-angle cone at 6° angle of attack. The simulations were performed at a Reynolds number of 9.5×10^6/m with no freestream disturbances. A randomly distributed roughness patch was placed near the nose along the windward ray [66]. The DNS results in Figure 5.10(c) show that the stationary vortices appear to be breaking down to turbulence near the lee ray, qualitatively matching what is seen in the experiments. The DNS image in Figure 5.10(c) is at approximately the same conditions as the TSP image in Figure 5.10(b).

Returning to experimental results, increasing the Reynolds number to 10.6 and 12.0×10^6/m (Figure 5.11(a) and 5.11(b)) creates even larger stationary vortices. Note that for the highest Reynolds number the large rectangular window could not be used because the stagnation pressure exceeded the pressure rating of the window. It also appears that transition is occurring close to the lee ray for both Reynolds numbers. It is surprising that the stationary vortices amplify all the way to the lee side before breaking down to turbulence. Recall that Li et al. [62] found that the maximum N-factors due to the stationary crossflow modes were in excess of 20 at the downstream end of the cone, at an azimuthal angle of approximately 130–140° from the windward ray, with linear parabolized stability equations (PSE). From the PSE computations, it would thus be expected that the stationary vortices would break down to turbulence near 130–140°, but the experiments do not agree. The difference may be due to the nonlinear growth and breakdown of the stationary waves necessary to cause transition. Also, the PSE computations did not account for nonlinearity or the effect of secondary instabilities.

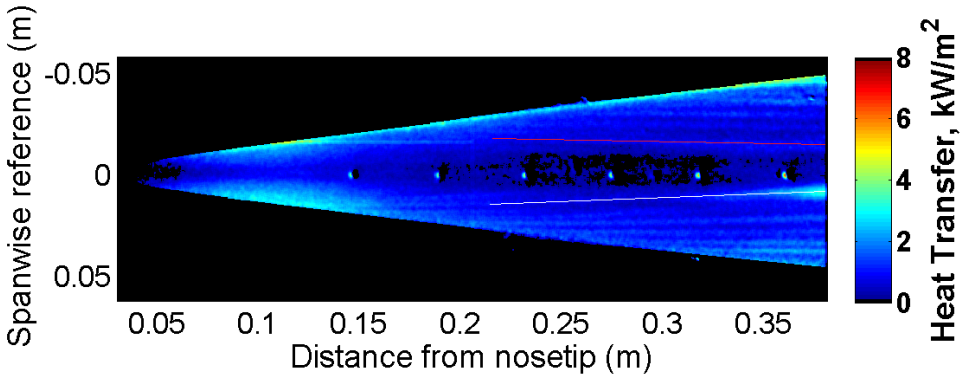

(a) p_0 = 105.8 psia, Re = 8.03×10^6/m, T_0 = 425.2 K, T_w = 297 K

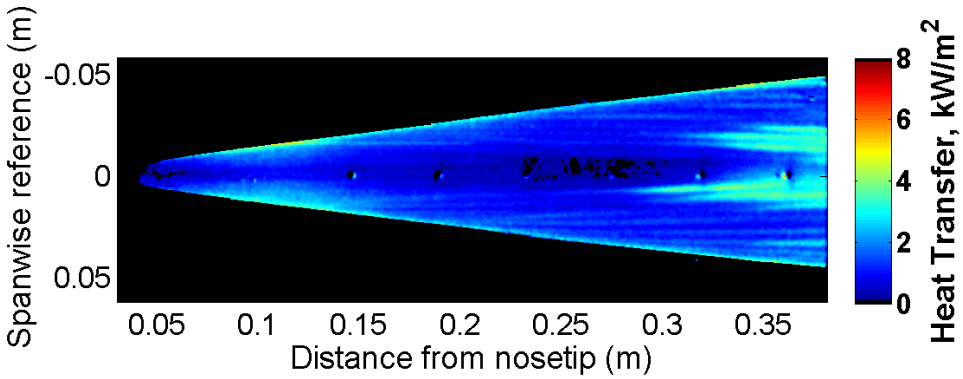

(b) p_0 = 129.5 psia, Re = 9.82×10^6/m, T_0 = 425.2 K, T_w = 301 K

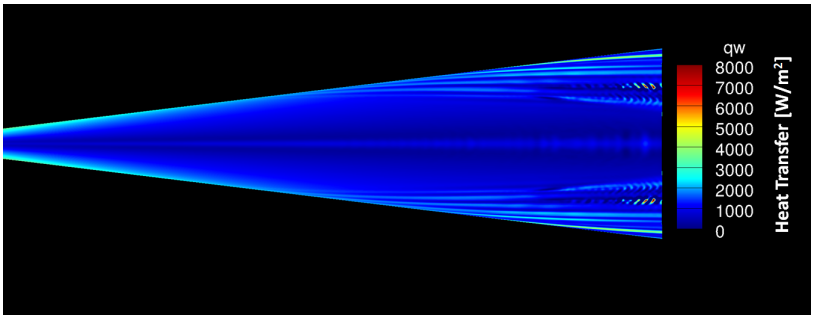

(c) DNS image provided by Gronvall [102]. p_0 = 134.4 psia, Re = 9.5×10^6/m, T_0 = 433 K, T_w = 300 K

Figure 5.10.: TSP and DNS images of the 7° half-angle cone at 6° angle of attack at lower Reynolds numbers. Lee side of the cone. Quiet flow.

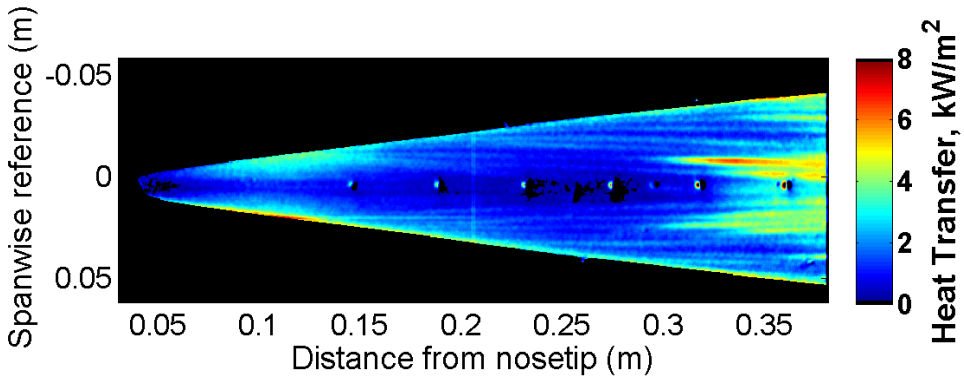

(a) $p_0 = 139.5$ psia, Re $= 10.6\times10^6$/m, $T_0 = 424.5$ K, $T_w = 297$ K

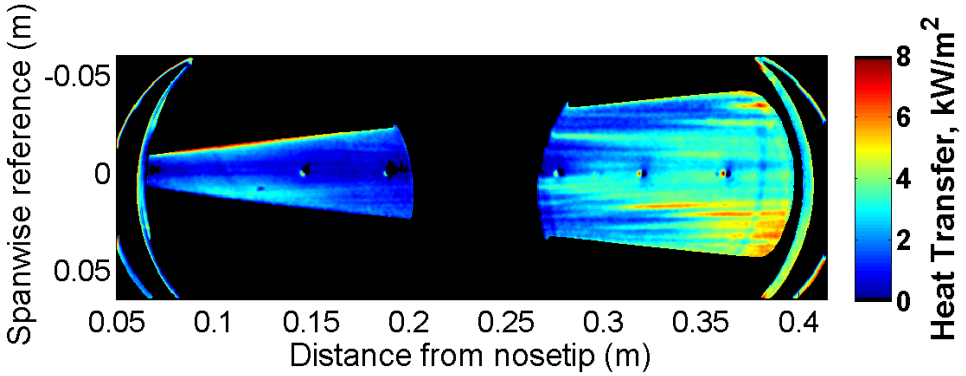

(b) $p_0 = 158.0$ psia, Re $= 12.0\times10^6$/m, $T_0 = 424.4$ K, $T_w = 300$ K

Figure 5.11.: TSP images of the 7° half-angle cone at 6° angle of attack at higher Reynolds numbers. Lee side of the cone. Quiet flow.

Figure 5.12 plots amplitudes of two stationary vortices for the four TSP images in Figures 5.10 and 5.11. The amplitudes were found by taking heat transfer profiles along the same two streamlines for the four TSP images (denoted as red and white lines in Figure 5.10(a)). The red line is approximately along the 195° ray, and the white line is approximately along the 165° ray. At the lowest Reynolds number along the 165° streamline, the wave begins to grow near an axial distance of 0.30 m. Increasing the Reynolds number to 9.82×10^6/m, the wave begins to grow near 0.27 m from the nosetip. The growth appears to saturate near 0.35 m from the nosetip.

Increasing the Reynolds number to 10.6×10^6/m, the wave begins to grow slightly further upstream, and growth saturation occurs near 0.35 m. Finally, at the highest Reynolds number, the growth begins at 0.26 m from the nosetip, and saturation occurs near 0.30 m. The wave appears to decay downstream of 0.32 m. As Reynolds number increases, the location of initial wave growth and wave saturation moves upstream. The wave amplitude also increases with increasing Reynolds number at a given axial location. Note that the initial wave growth may be further upstream than what is seen in the TSP images because the wave amplitude may be too small to measure with the TSP.

Along the 195° streamline (denoted in red), a similar trend is seen for the three lowest Reynolds numbers. The initial growth of the wave and the saturation point moves upstream with increasing Reynolds number, and the amplitude of the waves increase with increasing Reynolds number. At the highest Reynolds number, the amplitude remains constant. Looking at the TSP images, it appears that the stationary vortex has begun to break down to turbulence based on the spreading of the streak, so therefore the amplitude shown in the plot may not be significant. Nonetheless, value of the amplitude is near 2, which means the heat transfer is 3 times larger than the laminar theoretical heat transfer, suggesting that the boundary layer is turbulent.

Surface-pressure power spectra for the four experimental Reynolds numbers were taken with the two PCB gauges installed flush with the model and shown in Figure 5.13. The PCBs are located at an axial distance of 0.279 and 0.363 m from the nosetip. The gauges were installed along the lee ray of the cone. At the lowest Reynolds number, there appears to be an instability at approximately 62 kHz that begins growing downstream of PCB–4. Increasing the Reynolds number to 9.82×10^6/m, the instability appears further upstream, shown by the peak in the spectra at 82 kHz at PCB–4. The peak appears to be broadening, suggesting that transitional flow may be occurring near PCB–4. PCB–6 yields data indicative of transitional flow, as the spectra show a broadband increase in power, and the peak at 82 kHz is no longer present. Once again increasing the Reynolds number, the peak in the spectra at PCB–

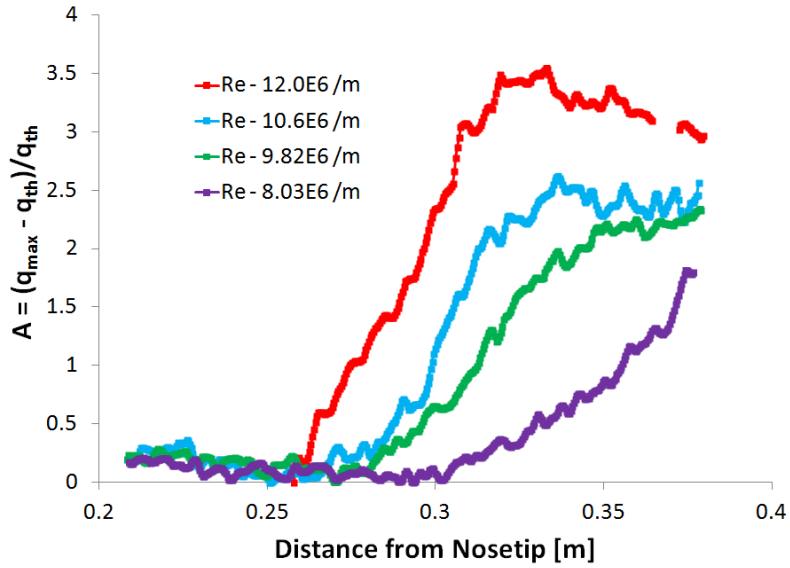

(a) Profiles along the 165°streamline (denoted in white in Figure 5.10(a)).

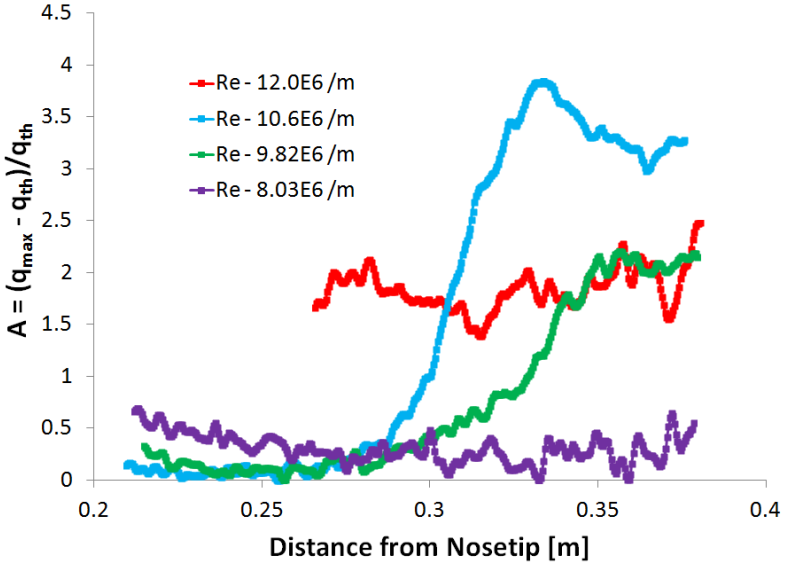

(b) Profiles along the 195°streamline (denoted in red in Figure 5.10(a)).

Figure 5.12.: Amplitude of the stationary crossflow vortices for the TSP images in Figures 5.10 and 5.11 along the streamlines denoted in Figure 5.10(a).

4 has moved to 94 kHz, and the peak appears to have broadened with the increase in Reynolds number. The increase of the peak frequency with Reynolds number seems to suggest that an instability is causing the peak, because often the frequency of an instability is inversely related to the boundary-layer thickness. As the boundary-layer thickness decreases with increasing Reynolds number, the frequency of the instability should increase. Moving to the highest Reynolds number, the spectrum at PCB–4 shows a very broad peak near 126 kHz, suggesting that transition may be occurring closer to PCB–4. The TSP image (5.11(b)) also shows what appears to be transitional flow at the axial location of PCB–4.

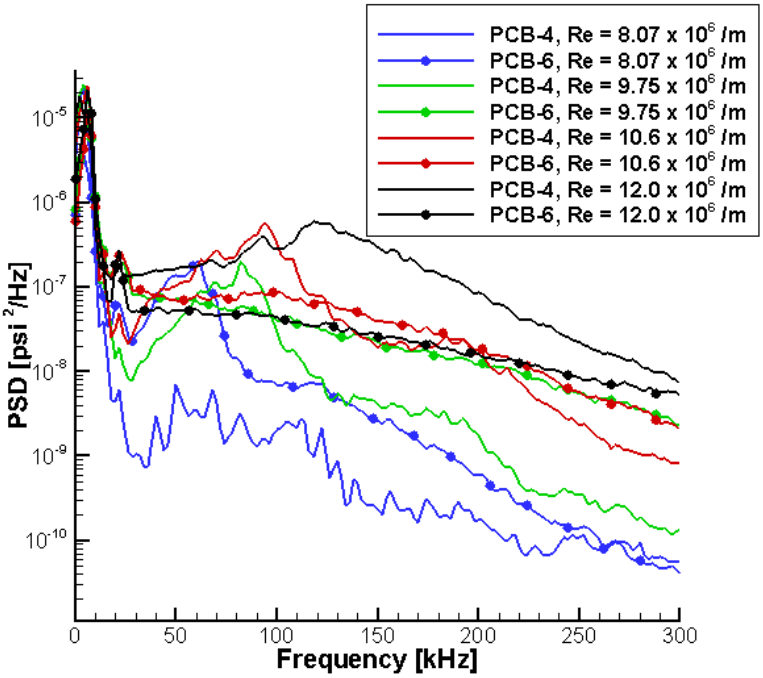

Figure 5.13.: Power spectra of surface pressure at 0.279 m (PCB–4) and 0.363 m (PCB–6) from the nosetip, at four different Reynolds numbers. Sensors along the lee ray. Quiet flow.

Tests were also performed with the yaw side of the cone in view under quiet flow and the sensor array at 90° from the windward ray. The TSP images calibrated to heat transfer at lower Reynolds numbers are shown in Figure 5.14, along with Gronvall's

DNS computation. At the lowest Reynolds number, the crossflow vortices are only faintly visible. Increasing the Reynolds number creates slightly higher-amplitude stationary vortices, but they do not appear to be breaking down to turbulence on the yaw side of the cone. In the DNS image (Figure 5.14(c)), the crossflow vortices are visible but do not begin to break down to turbulence, once again qualitatively agreeing with the experimental results. It is difficult to make quantitative comparisons between the DNS and the experimental results because the roughness and the initial stationary wave amplitude were not matched between the experiments and the computations. The DNS image in Figure 5.14(c) is at approximately the same conditions as the TSP image in Figure 5.14(b). At the higher experimental unit Reynolds number (Figures 5.15(a) and 5.15(b)), the stationary vortices appear larger in magnitude, but transition still does not appear to be occurring on the yaw side.

Figure 5.16 plots the amplitude of a stationary vortex for the four TSP images in Figures 5.14 and 5.15. The amplitudes were found by taking heat transfer profiles along the same streamline for the four TSP images (denoted in red in Figure 5.14(a)). At the lowest Reynolds number, the wave does not begin to grow until near an axial distance of 0.37 m. Increasing the Reynolds number to 9.82×10^6/m, the wave begins to grow near 0.33 m from the nosetip and reaches a larger amplitude than in the lower Reynolds number case. There does not appear to be any wave-growth saturation. Increasing the Reynolds number to 10.6×10^6/m, the wave growth looks similar to the 9.82×10^6/m Reynolds number case. It is not known why the increase in Reynolds number does not produce an increase in amplitude and an upstream movement of the initial growth location. Finally, at the highest Reynolds number, the initial growth location appears to occur upstream of the imaged area. There is an increase in amplitude as compared to the lower Reynolds number cases. Again, there is no saturation or decay of the stationary vortex. The stationary vortices are breaking down to turbulence near the lee ray but not near the 90° ray. The missing data points in the plot corresponds to sensor locations or irregularities in the TSP.

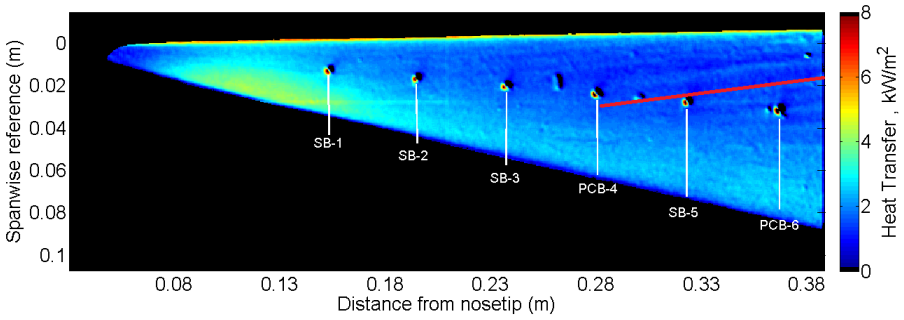

(a) $p_0 = 106.5$ psia, Re $= 8.07\times10^6$/m, $T_0 = 425.3$ K, $T_w = 296$ K

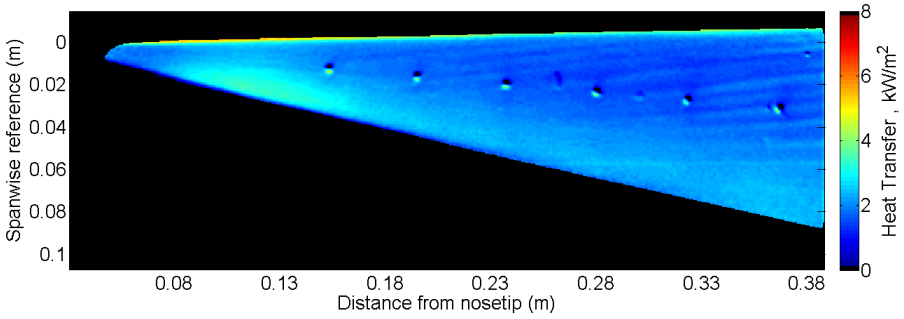

(b) $p_0 = 128.5$ psia, Re $= 9.75\times10^6$/m, $T_0 = 425.0$ K, $T_w = 303$ K

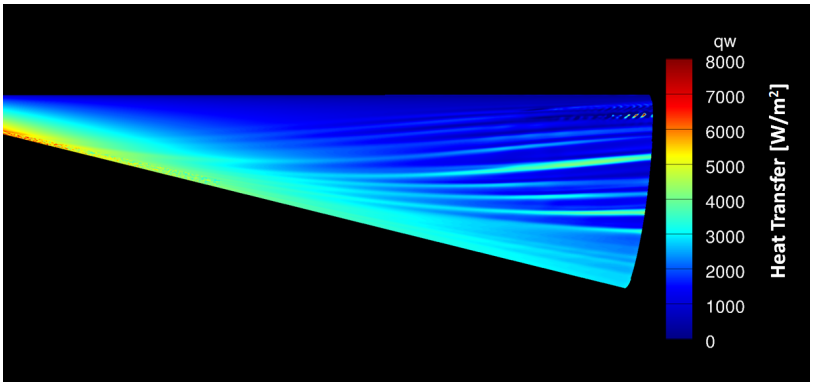

(c) DNS image provided by Gronvall [102]. $p_0 = 134.4$ psia, Re $= 9.5\times10^6$/m, $T_0 = 433$ K, $T_w = 300$ K

Figure 5.14.: TSP and DNS images of the 7° half-angle cone at 6° angle of attack at lower Reynolds numbers. Yaw side of the cone. Quiet flow.

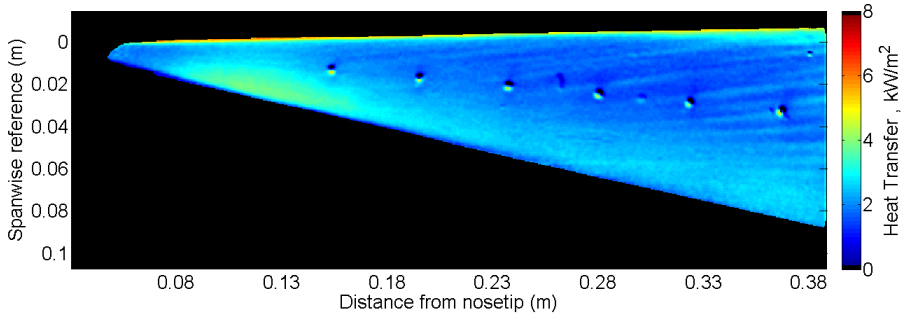

(a) $p_0 = 139.5$ psia, Re $= 10.6\times10^6$/m, $T_0 = 424.6$ K, $T_w = 302$ K

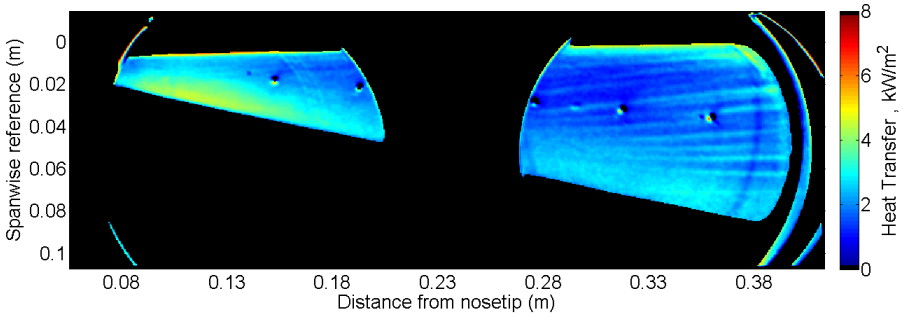

(b) $p_0 = 158.1$ psia, Re $= 12.0\times10^6$/m, $T_0 = 424.5$ K, $T_w = 298$ K

Figure 5.15.: TSP images of the 7° half-angle cone at 6° angle of attack at higher Reynolds numbers. Yaw side of the cone. Quiet flow.

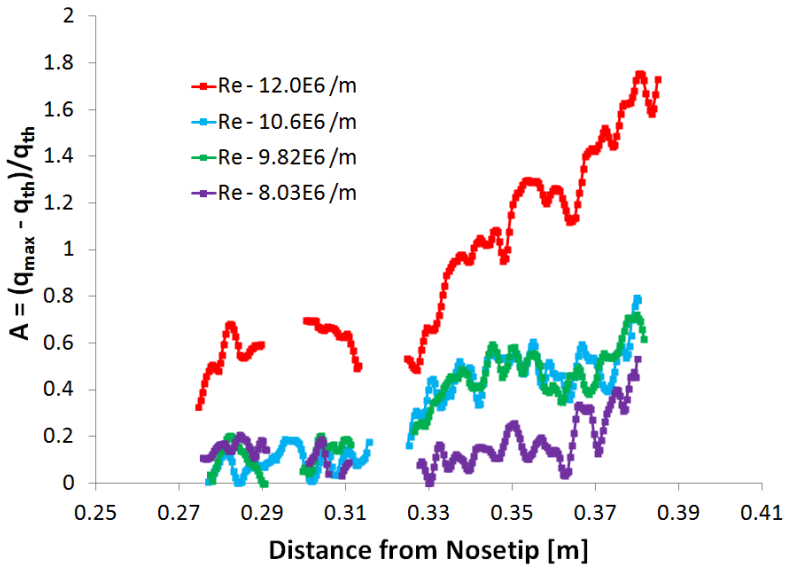

Figure 5.16.: Amplitude of a stationary crossflow vortex for the TSP images in Figures 5.14 and 5.15 along the streamline denoted in Figure 5.14(a).

5.2.1 Effect of Tunnel Noise on Crossflow-Induced Transition With No Roughness

Shown in Figure 5.17 are two TSP images at approximately the same Reynolds number under both quiet and noisy flow. The images are taken from the author's Masters thesis [54] and are repeated here because they provide a good qualitative example of the effect that tunnel noise has on the stationary vortices and crossflow-induced transition. Under quiet flow, the stationary crossflow vortices are seen. It is not clear if the vortices are breaking down to turbulence near the downstream end of the cone but they do not appear to. When the tunnel noise is increased, the stationary vortices are not clearly visible. There may be stationary vortices visible near 0.3 m from the nosetip, but it is not clear. Unfortunately, these tests were done before SB gauges were added to the model to obtain quantitative heat transfer, so this image can only be discussed qualitatively. This was also the only run in which the author has seen any evidence of the stationary vortices under noisy flow. It is not known why this is the only case that possibly shows the stationary waves under noisy flow. Under noisy flow, boundary-layer transition occurs near the 90° ray and propagates towards the windward and leeward rays. Clearly when the tunnel noise is increased from approximately 0.02% to 3% there is a significant effect on crossflow-induced transition.

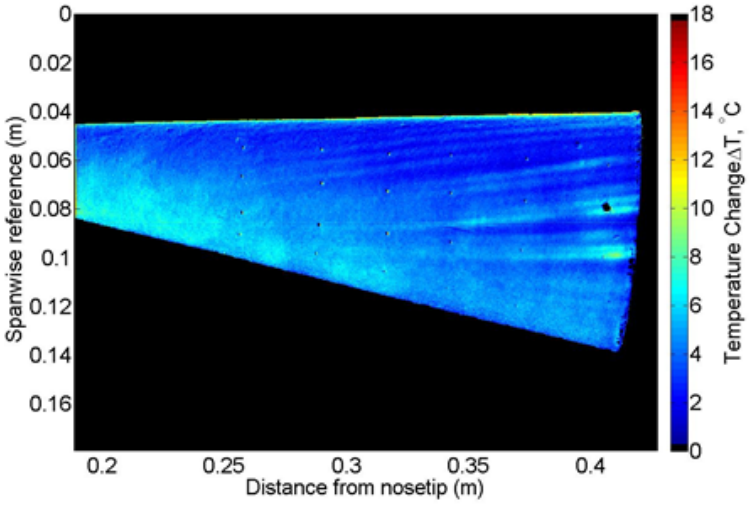

(a) Quiet flow. Re = 9.58×10^6/m, p_0 = 125 psia, T_0 = 423 K.

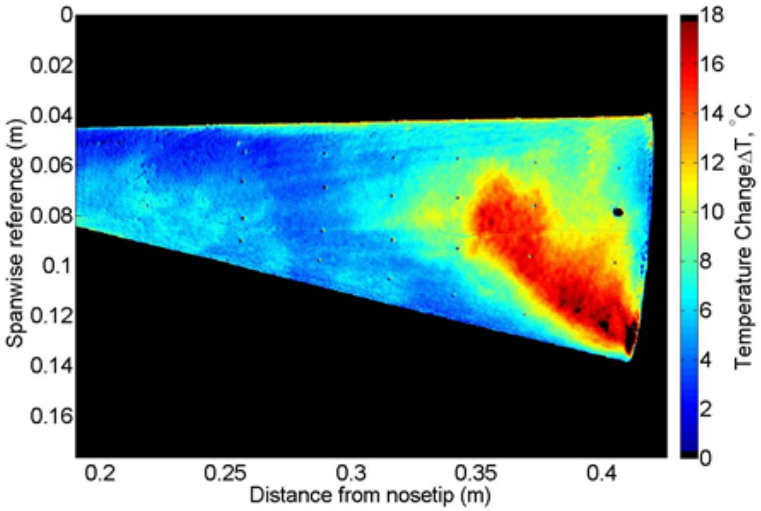

(b) Noisy flow. Re = 9.33×10^6/m, p_0 = 105 psia, T_0 = 405 K.

Figure 5.17.: TSP images under both noisy and quiet flow at approximately the same Reynolds number. Yaw side of the cone imaged.

5.3 Characteristics of Roughness and Steps

All of the TSP paint finishes had similar average and RMS roughnesses, due to spending approximately the same amount of time sanding each paint finish with the

same grit sandpaper in the same way. The average roughness for the TSP varied between 0.1 and 0.4 μm (3.9 and 16 μin), and the RMS roughness varied between 0.5 and 1 μm (20 and 79 μin). The average and RMS roughness of the stainless steel nosetip for the Crossflow cone was 0.34 and 0.35 μm (13 and 14 μin), respectively. The average and RMS roughness of the bare aluminum frustum was 0.28 and 1.5 μm (14 and 98 μin), respectively. The TSP roughness is similar to the bare aluminum and nosetip roughness.

The step between the Torlon insert and the upstream nosetip or the downstream aluminum frustum is approximately 20 μm (590 μin). The slope of the paint edge was approximately 10 μm per mm. For convenience, the properties of each Torlon roughness insert are reprinted in Table 5.1. The average roughness of each cone segment and the steps at junctions were all at least an order of magnitude smaller than the dimpled roughness (based on diameter or depth).

Table 5.1.: Nominal depth and diameter of roughness dots on the Torlon inserts. Roughness is 2 inches from the nosetip.

Insert Number	**# of Dots Around Azimuth**	**Depth [inches]**	**Diameter (D) [inches]**	**D/λ**
1	-	-	-	-
2	50	0.011	0.015	0.49
3	50	0.022	0.031	1.0
4	50	0.024	0.030	0.97
5	50	0.012	0.030	0.97
6	72	0.007	0.010	0.47

5.4 Spanwise Spreading of Streamlines

As discussed in Section 1.2, the streamlines are swept from the windward to the leeward ray due to the azimuthal pressure gradient, and stationary crossflow waves are approximately aligned with the inviscid streamlines. Therefore, any stationary vortices generated by the dimple roughness elements will approximately follow the inviscid streamlines [103]. Figure 5.18 plots the streamlines at the edge of the boundary layer (approximated as the inviscid surface streamlines) that pass over the middle of each dimpled roughness on the Torlon section. The dimples are 2.0 inches (50.8 mm) from the nosetip. The plot shows 50 streamlines about the azimuth. Note that half of the streamlines were not included in the plot in order to reduce clutter. The streamlines were calculated and provided to the author by Joel Gronvall [104]. The computations were performed at a Reynolds number of 9.5×10^6/m, a stagnation pressure of 134.4 psia, a stagnation temperature of 433 K and a wall temperature of 300 K. Gronvall used the University of Minnesota in-house CFD code US3D to compute the flow, which is a three-dimensional, unstructured, cell-centered finite volume flow solver.

As can be seen in the plot, all the streamlines except for the one exactly on the windward ray are swept towards the lee ray. For many of the TSP tests the cone is imaged at an axial location of 0.30 to 0.40 m from the nosetip. Tests with the larger rectangular window often show that the stationary vortices do not become large enough to visualize in the TSP until these axial locations. At this range of axial locations it would be expected that the roughness would show the most significant effect between approximately 150° and 210° from the windward ray (this plot only shows streamlines from 0–180° azimuthally but the streamlines are symmetric about the lee ray). Although the roughness is expected to input a wavenumber per radian of approximately 8 (for the case shown), the downstream location at which the vortices are visualized will not yield a wavenumber per radian of 8. For example, at an axial location of 0.35 m between 150° and 180°, there are 18 streamlines that have passed

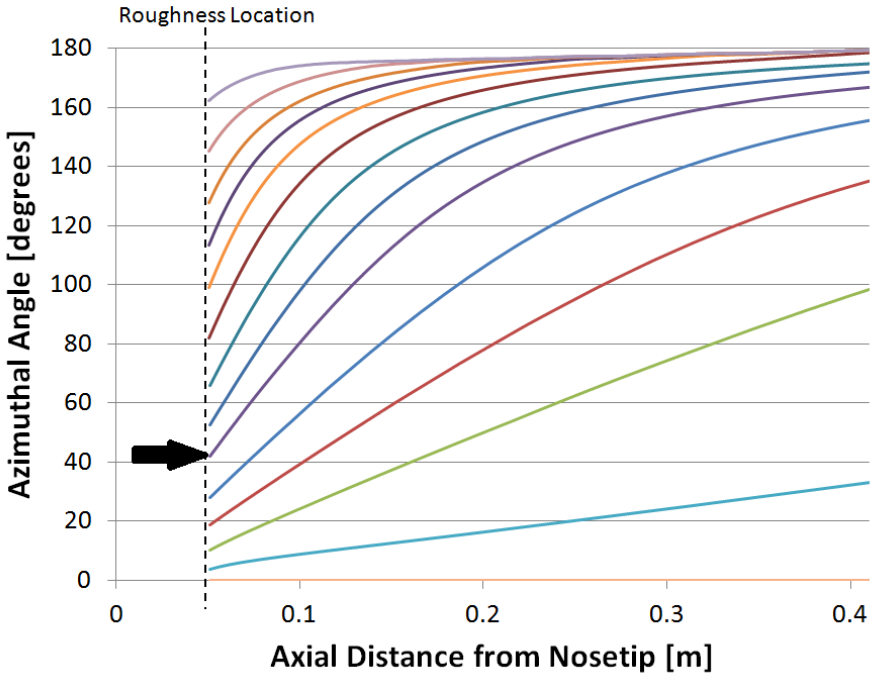

Figure 5.18.: Plot of streamlines at the edge of the boundary layer for a 7° half-angle at 6° angle of attack. 50-dimple case. Re = 9.5×10^6/m, p_0 = 134.4 psia, T_0 = 433 K, T_w = 300 K. Data courtesy of Gronvall [104]. Azimuthal angle measured with respect to the windward ray.

over the roughness elements producing a wavenumber per radian of approximately 50 (assuming each roughness element generates a stationary vortex that follows the inviscid streamlines). Between the 90° and 150° rays at an axial location of 0.35 m, there are only 4 streamlines in this region that have passed over the roughness elements, resulting in a wavenumber per radian of 12. Note that the streamlines are almost on top of each other downstream near the lee ray. So it is possible that some of the stationary vortices could coalesce, yielding a lower wavenumber (assuming that each streamline would also have a corresponding stationary vortex).

Figure 5.19 plots the local wavenumber (per radian) between the 150° and 180° rays. This is assuming that each roughness element generates a corresponding stationary vortex, and this stationary vortex follows the inviscid streamline. At the location of

the roughness elements, the local wavenumber per radian is the expected number of 8. Moving downstream, it is clear that the local wavenumber increases as the streamlines become more condensed, reaching a maximum local wavenumber per radian of 50.

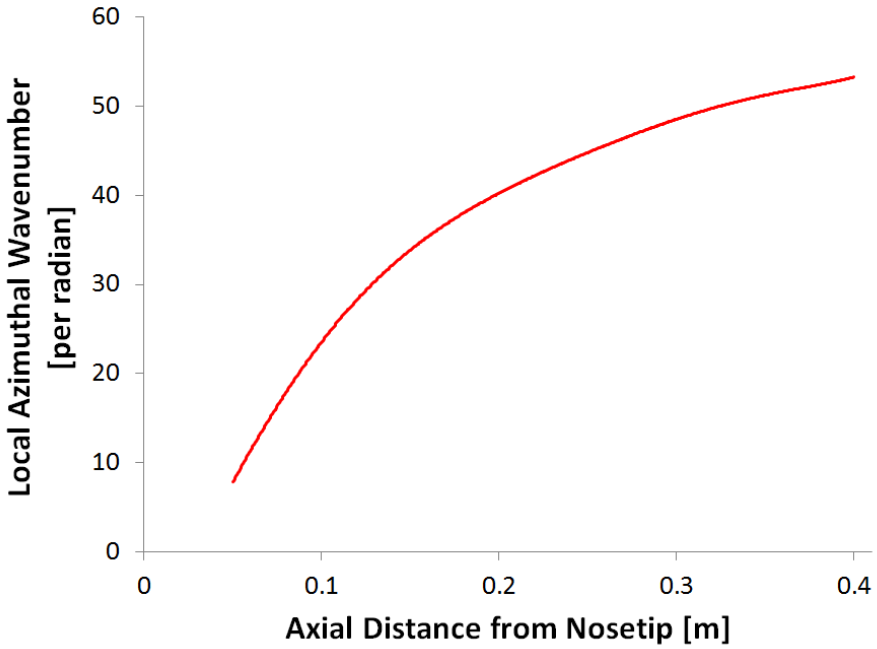

Figure 5.19.: Local wavenumber per radian between the 150° and 180° rays (as measured from the windward ray). 50-dimple case. Re = 9.5×10^6/m, p_0 = 134.4 psia, T_0 = 433 K, T_w = 300 K. Data courtesy of Gronvall [104]. Azimuthal angle measured with respect to the windward ray.

Figure 5.20 plots the average local wavenumber per radian between the streamline originating at 43.2° (denoted by an arrow in Figure 5.18) and the leeward ray on the primary y-axis. Once again, this is assuming each roughness element generates a corresponding stationary vortex, and this stationary vortex follows the inviscid streamline. The purple region represents the physical area between the streamline originating at 43.2° and the leeward ray (with the azimuthal degrees on the secondary y-axis). Again, it can be seen that the local wavenumber per radian increases moving

downstream, while the region between the streamline and the leeward ray decreases (i.e. the region for which this wavenumber per radian is valid).

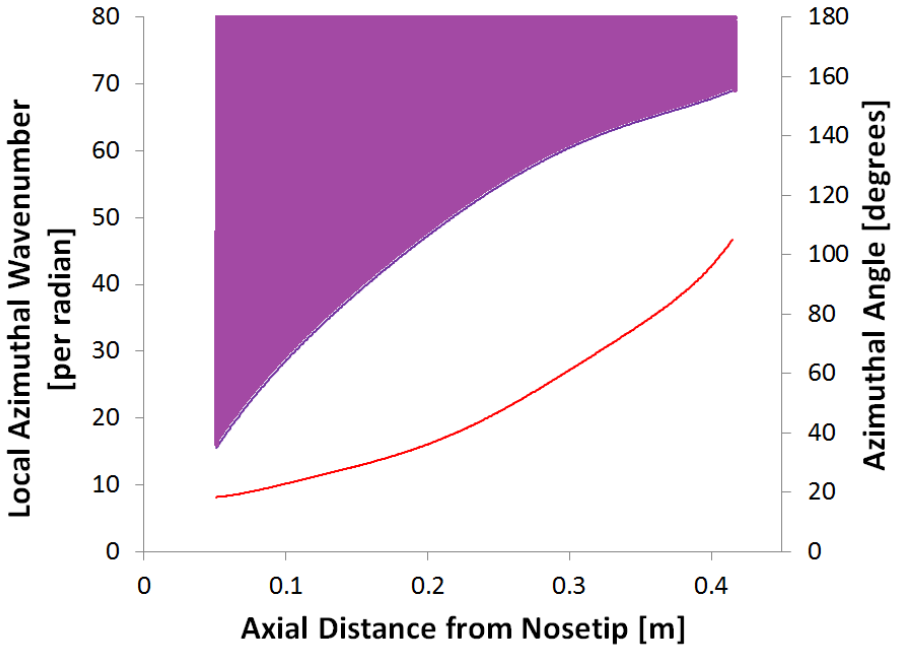

Figure 5.20.: Local wavenumber between the streamline originating at 43.2° and the leeward ray (180°). 50-dimple case. Re = 9.5×10^6/m, p_0 = 134.4 psia, T_0 = 433 K, T_w = 300 K. Data courtesy of Gronvall [104]. Azimuthal angle measured with respect to the windward ray.

5.5 Torlon Roughness Experiments

5.5.1 50-Dimpled Case

Effect Near Lee Ray

Three different Reynolds numbers were tested under quiet flow with the smooth and 50-dimpled Torlon (#3) inserts with the lee side of the cone imaged. Data at a Reynolds number of approximately 8.1×10^6/m are shown in Figure 5.21. The image on the upper side is smooth, and the image on the lower side is with the 50 dimples.

At this Reynolds number, the roughness elements appear to produce larger amplitude stationary vortices.

Spanwise heat transfer profiles of the TSP images in Figure 5.21 are shown in Figure 5.22. The heat transfer is non-dimensionalized by the theoretical heat transfer for a cone at 0° AoA at the same conditions. The theoretical heat transfer solution is discussed in Section 3.4.3. The spanwise profile was taken at an axial location of 0.37 m. The stationary vortices differ near 190–220°. The RMS of the non-dimensional heat transfer between 150° and 220° is 0.14 for the smooth case and 0.18 for the 50-dimpled case.

Figure 5.23 is a reprint of the TSP images in Figure 5.21 and show the location of the sensors and the streamlines over which axial wave-amplitude profiles were taken. The wave amplitudes along the 160° ray (white line) in Figure 5.23 is shown in Figure 5.24. The amplitude of the stationary wave is much larger when the roughness is added, agreeing with the spanwise profile results. The stationary vortex does not appear to be breaking down to turbulence as the amplitude is still increasing with distance from the nosetip.

PSD of a Kulite and PCB sensor (circled in white and black in Figure 5.23, respectively) were calculated for the three Reynolds numbers. The PCB is at an axial location of 0.32 m, and the Kulite at an axial location of 0.36 m. Both sensors are at 165° from windward. Figure 5.25 shows the PSD for the low Reynolds number case. The PCB spectra for the smooth case shows a peak near 200 kHz, and when the roughness is added the peak disappears. It is possible that this peak is due to the 2nd-mode wave, because this frequency is near the 2nd-mode peak frequency measured by Casper at similar conditions on the BAM6QT on a 7° half-angle cone at 0° angle of attack [105]. It is not known how the stationary crossflow vortices interact with the second-mode waves, although there are no visible stationary vortices near the PCB sensor. It is possible that the roughness or the stationary crossflow waves are disrupting the growth of this potential second-mode wave.

The PSD of the Kulite pressure data shows a peak near 190 kHz, and when the roughness is added the peak disappears. The peak frequency measured by the PCB (0.32 m from the nosetip) and Kulite (0.36 m from the nosetip) for the smooth case decrease from 200 to 190 kHz with an increasing boundary-layer thickness, which is consistent with the characteristic of a second-mode wave. Again, the mechanism that is causing the peak near 200 kHz appears to be sensitive to roughness as the peak disappears when roughness is added. It is unlikely that this peak is being caused by the secondary instability of the stationary crossflow wave because the amplitude of the stationary wave for the smooth case is small at the sensor location (0.36 m), as seen in Figure 5.24.

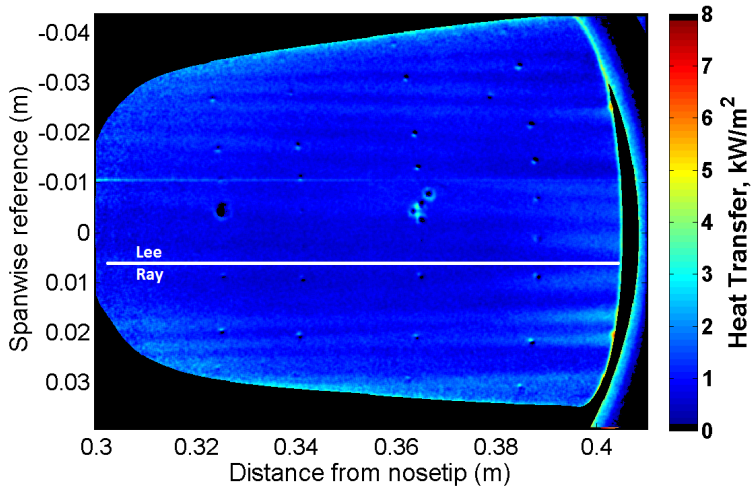

(a) Smooth. $p_0 = 109$ psia, Re $= 8.2\times10^6$/m, $T_0 = 426$ K, $T_w = 301$ K.

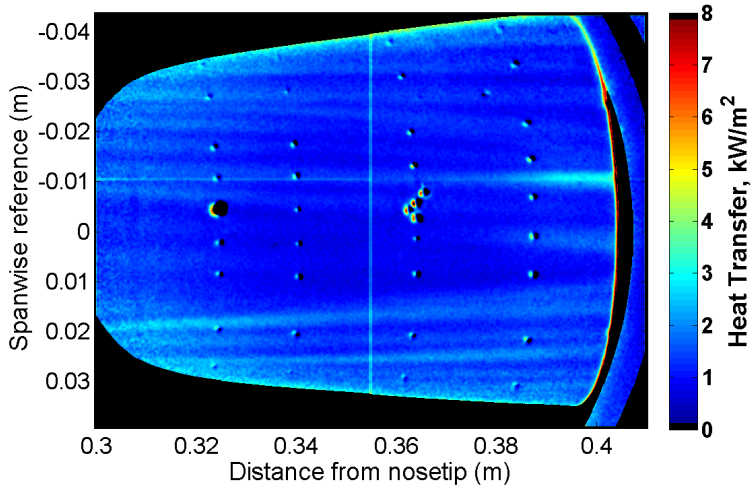

(b) 50-dimples (#3). $p_0 = 109$ psia, Re $= 8.1\times10^6$/m, $T_0 = 429$ K, $T_w = 297$ K.

Figure 5.21.: TSP images under quiet flow at a Reynolds number of approximately 8.1×10^6/m with smooth and rough Torlon inserts (50 dimples, #3). Lee side of the cone imaged.

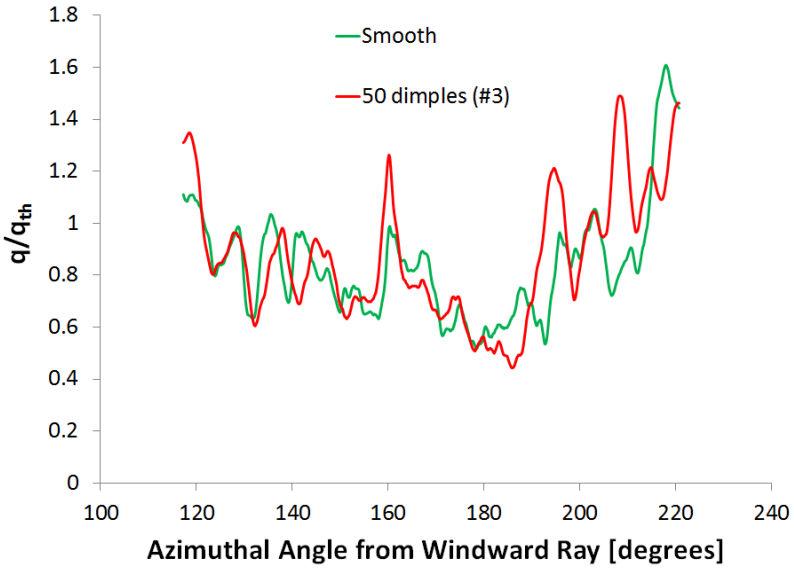

Figure 5.22.: Spanwise heat transfer profile at an axial distance of 0.37 m of the TSP images in Figure 5.21. Quiet flow, Re = 8.2×10^6/m.

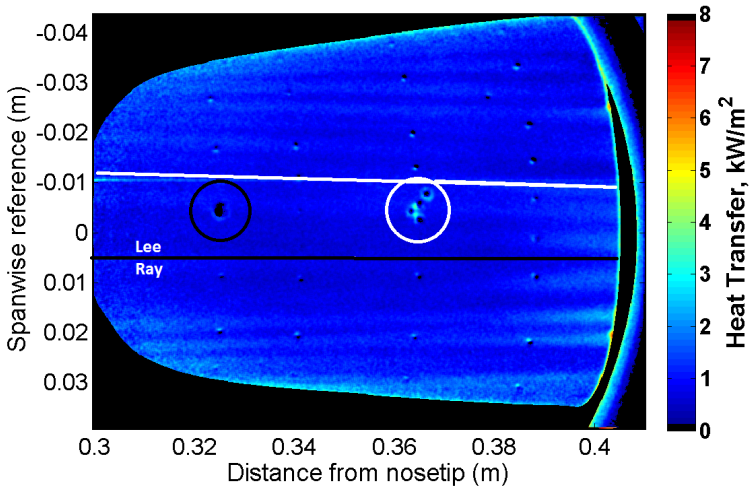

(a) Smooth. $p_0 = 109$ psia, Re $= 8.2\times10^6$/m, $T_0 = 426$ K, $T_w = 301$ K.

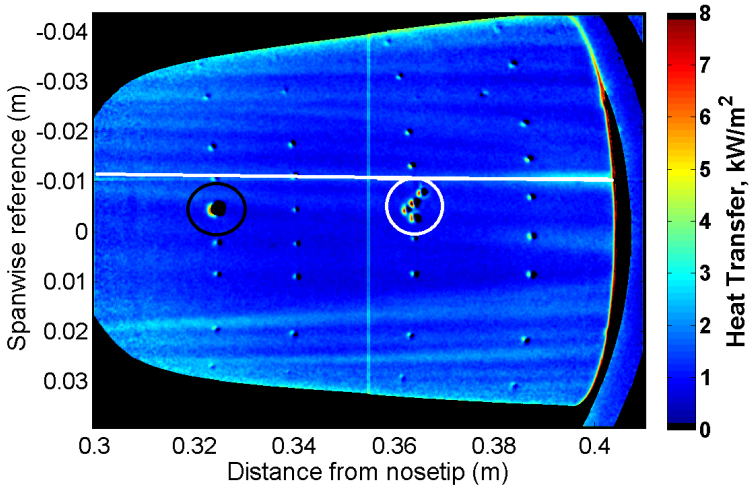

(b) 50-dimples (#3). $p_0 = 109$ psia, Re $= 8.1\times10^6$/m, $T_0 = 429$ K, $T_w = 297$ K.

Figure 5.23.: TSP images under quiet flow at a Reynolds number of approximately 8.1×10^6/m with smooth and rough Torlon inserts (50 dimples). Lee side of the cone imaged. Reprint of Figure 5.21, with sensor and axial profile locations shown.

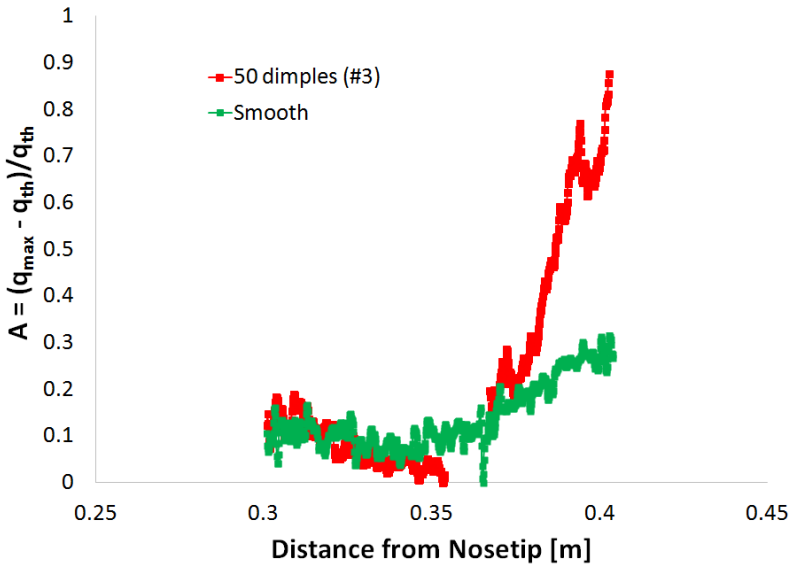

Figure 5.24.: Stationary vortex amplitude along the 160° ray (white line) on the TSP images in Figure 5.23. Quiet flow, Re = 8.2×10^6/m.

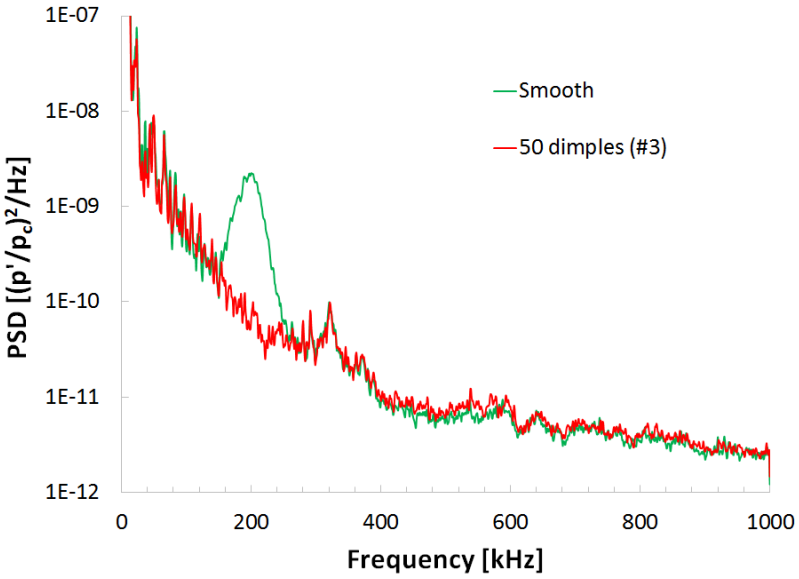

(a) PCB (circled in black). x = 0.32 m.

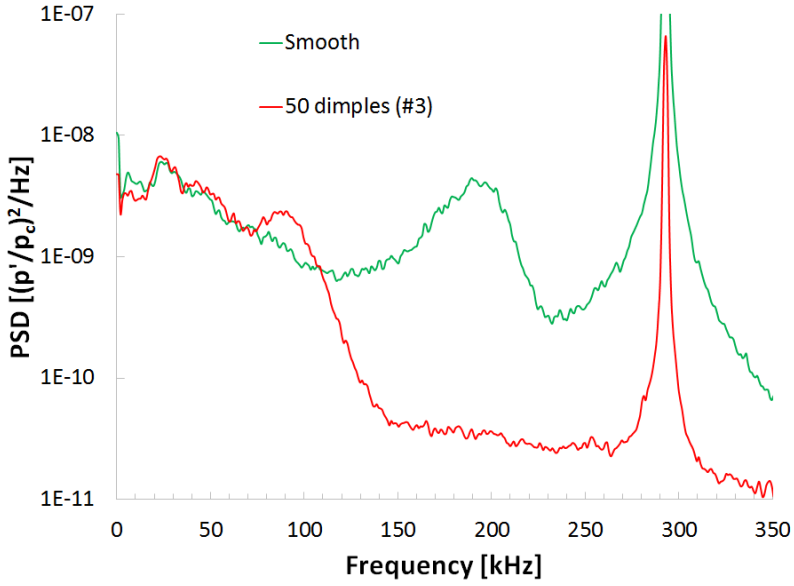

(b) Kulite (circled in white). x = 0.36 m.

Figure 5.25.: PSD of sensors (circled in Figure 5.21) on the 165° ray at a Reynolds number of 8.2×10^6/m

The effect of the roughness elements becomes more pronounced at a Reynolds number of 10.5×10^6/m. The TSP images are shown in Figure 5.26. When the roughness is added, a different pattern of stationary vortices is created and transition appears to be delayed compared to the smooth case. It is not known why the roughness elements produce larger-amplitude stationary vortices at a Reynolds number of 8.2×10^6/m but smaller-amplitude stationary vortices at a Reynolds number of 10.5×10^6/m (as compared to the smooth cases). At this Reynolds number, the roughness elements appear to be creating a more regular pattern of stationary vortices compared to the smooth case, and therefore appear to be dominating the generation of the stationary vortices. For the nominally smooth case, the stationary vortices are thought to arise from the random roughness on the cone.

Spanwise heat transfer profiles at an axial distance of 0.37 m at a Reynolds number of 10.4×10^6/m are shown in Figure 5.27. At this Reynolds number, the 50 dimples create a more regular pattern of stationary vortices, which is also seen in the TSP images. The wavenumber between 150° and 210° for the smooth case is 7 per radian and for the 50 dimple case is 10 per radian. The 50 dimpled case is producing a wavenumber per radian much smaller than the expected value of approximately 50 waves per radian. The lower measured wavenumber may be due to the inability to resolve all the stationary vortices in this region on the cone, or it may be possible that some vortices are coalescing thus yielding a smaller wavenumber. There is no visual evidence of the stationary vortices coalescing. If coalescing is occurring it may be occurring upstream of the visualized region but this is pure speculation. It is also possible that the roughness elements away from the wind ray are not as effective in generating stationary vortices as the roughness elements near the wind ray due to the thicker boundary layer moving towards the lee ray. If that is the case, the measured wavenumber would be smaller than the expected wavenumber. Computations are needed to help understand the differences in measured and expected wavenumber. The RMS of the non-dimensional heat transfer between 150° and 210° is 0.12 for the smooth case and 0.38 for the rough case. The rough case RMS is much higher because

the stationary vortices may be already breaking down to turbulence for the smooth case at this location.

Figure 5.28 is a reprint of the TSP images in Figure 5.26 and shows the location of the sensors and the streamlines over which axial profiles were taken. The amplitude of the stationary vortices along the white and black lines are plotted in Figure 5.29. The white line is approximately along the 165° ray, and the black line is approximately along the 215° ray. Along the 165° ray (white line), the stationary wave amplitude for the smooth case reaches a larger amplitude and saturates earlier than the 50 dimple case. Saturation occurs near 0.34 m for the smooth case and 0.36 m for the rough case. Along the 215° ray (black line), once again the smooth case shows a larger stationary vortex amplitude at the upstream end of the TSP image. Interestingly, the stationary vortex in the rough case begins to grow further downstream than the smooth case (near 0.33 m) and has a much more rapid growth rate than the smooth case. Both cases reach saturation near 0.37 m and begin to decay just downstream of the saturation point.

The PSD of the sensors for the middle Reynolds number case is shown in Figure 5.30. The two sensors are circled in Figure 5.28 and both approximately lie along the 165° ray. Both sensors for the smooth case show an increase in broadband noise as compared to the rough case, suggesting that the boundary layer is transitional or turbulent at these locations. This agrees with the stationary wave amplitude plotted in Figure 5.29(a) where stationary-vortex saturation was seen to occur near the upstream sensor (0.32 m) and amplitude decays near the downstream sensor (0.36 m). This time, the 50-dimple case shows a peak near 200 kHz. Again, it is not clear what causes this peak in the spectra. It may be the second-mode wave but this is not known. The RMS of the non-dimensional pressure between 0 and 500 kHz is equal to 0.40 for the smooth case and 0.31 for the rough case. At the downstream location, the Kulite shows a small peak near 40 kHz for the rough case, which is likely caused by the primary travelling crossflow instability. The smooth case does not show the peak near 40 kHz likely because the waves have already begun to break down to

turbulence. Stationary-vortex saturation for the rough case occurs just downstream of the downstream sensor. The RMS of the non-dimensional pressure between 0 and 100 kHz is equal to 0.035 for the smooth case and 0.025 for the rough case. The travelling crossflow instability will be discussed in further detail in the next chapter. The large peak near 300 kHz is due to the Kulite sensor resonance.

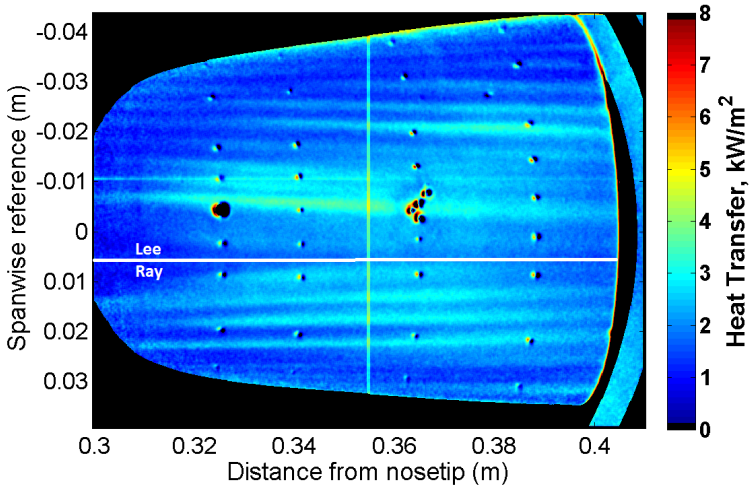

(a) Smooth. Re = 10.5×10^6/m, p_0 = 139 psia, T_0 = 425 K, T_w = 299 K.

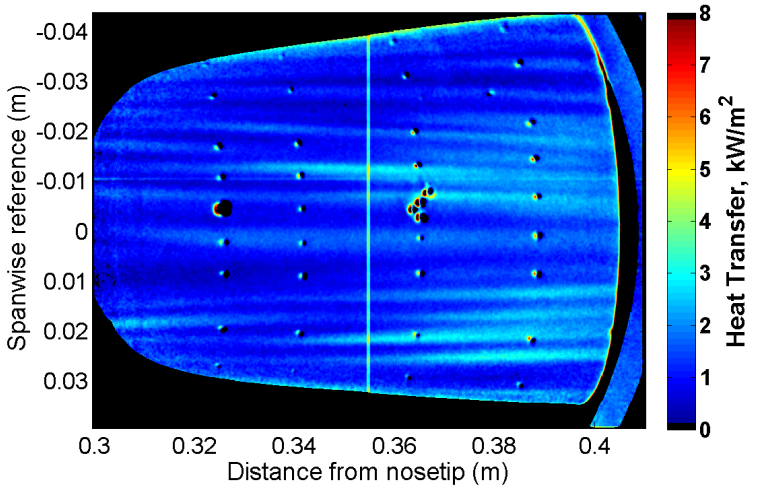

(b) 50-dimples (#3). p_0 = 139 psia, Re = 10.4×10^6/m, T_0 = 428 K, T_w = 303 K.

Figure 5.26.: TSP images under quiet flow and varying Reynolds number with smooth and rough Torlon inserts (50 dimples). Lee side of the cone imaged.

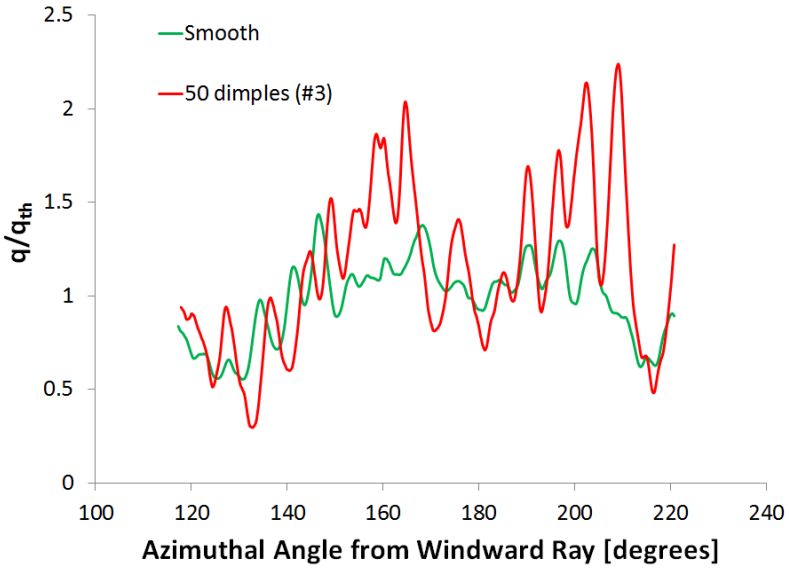

Figure 5.27.: Spanwise heat transfer profile at an axial distance of 0.37 m of the TSP images in Figure 5.26. Quiet flow, Re = 10.5×10^6/m.

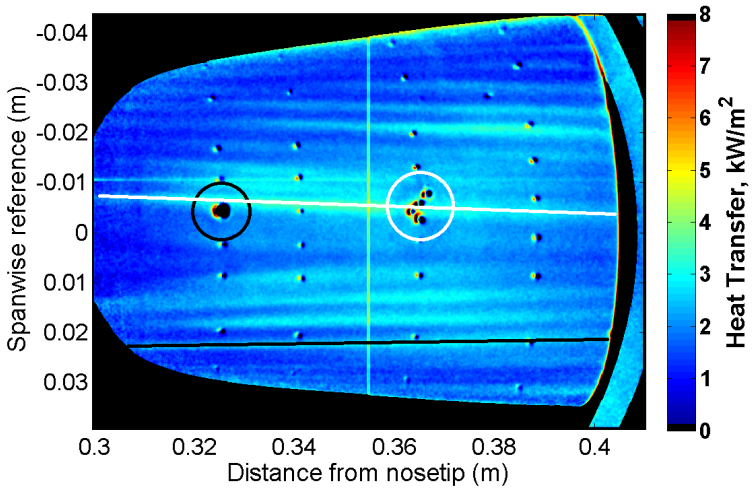

(a) Smooth. Re = 10.5×10^6/m, p_0 = 139 psia, T_0 = 425 K, T_w = 299 K.

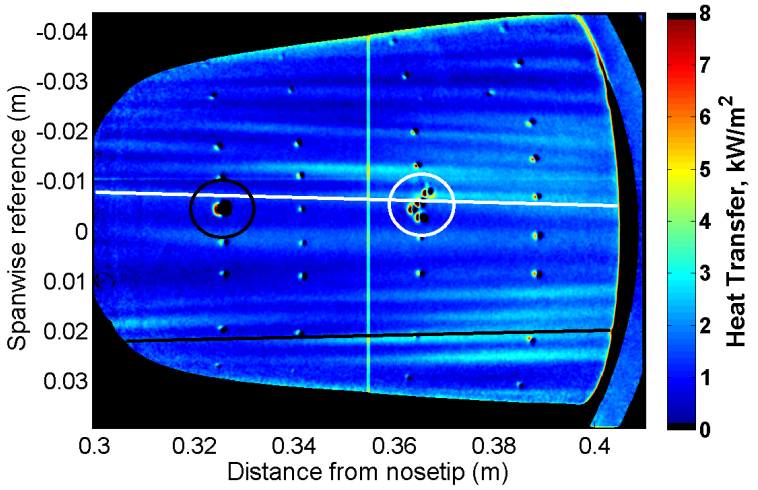

(b) 50-dimples (#3). p_0 = 139 psia, Re = 10.4×10^6/m, T_0 = 428 K, T_w = 303 K.

Figure 5.28.: TSP images under quiet flow and varying Reynolds number with smooth and rough Torlon inserts (50 dimples). Lee side of the cone imaged. Reprint of Figure 5.26, with sensor and axial profile locations shown.

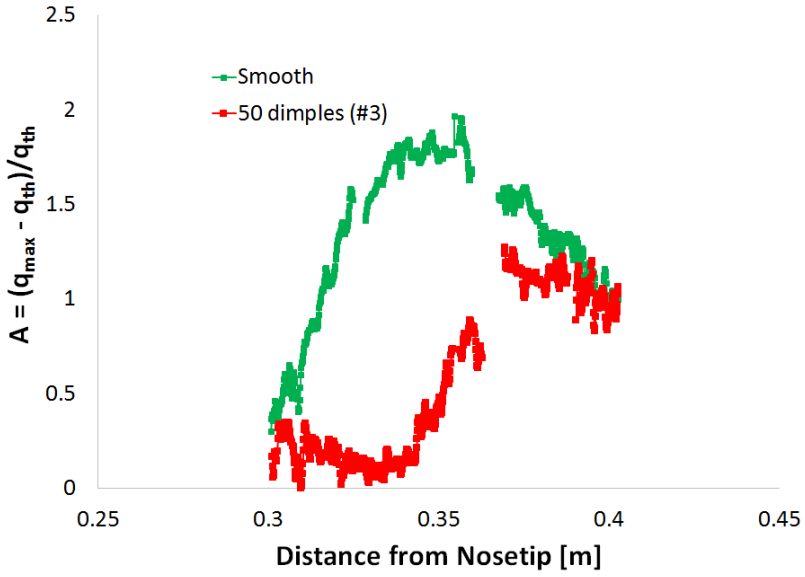

(a) Amplitude along the 165° ray (white line in Figure 5.28).

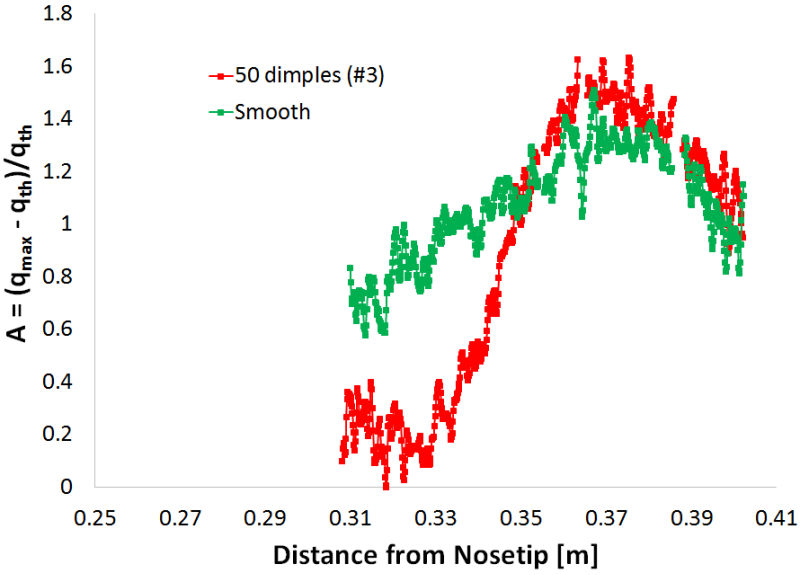

(b) Amplitude along the 215° ray (black line in Figure 5.28).

Figure 5.29.: Stationary vortex amplitude along the streamlines denoted in Figure 5.28. Quiet flow, Re = 10.4×10^6/m.

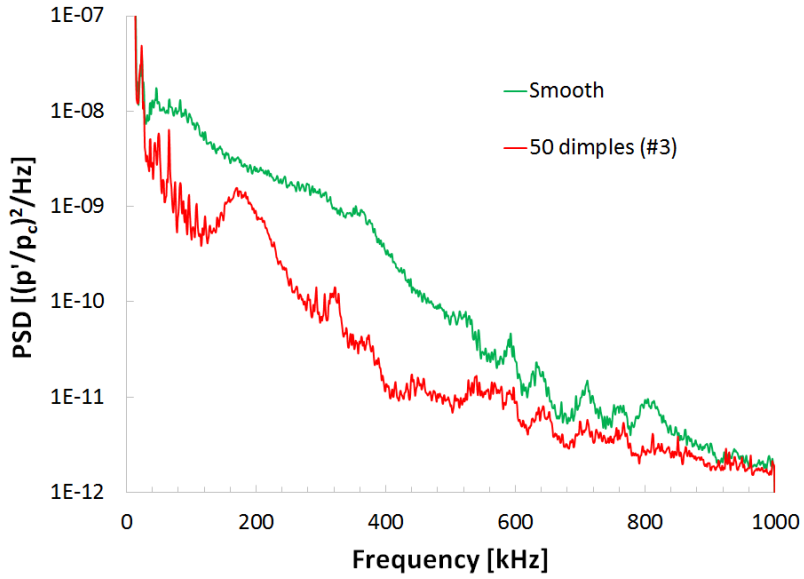

(a) PCB (circled in black). x = 0.32 m.

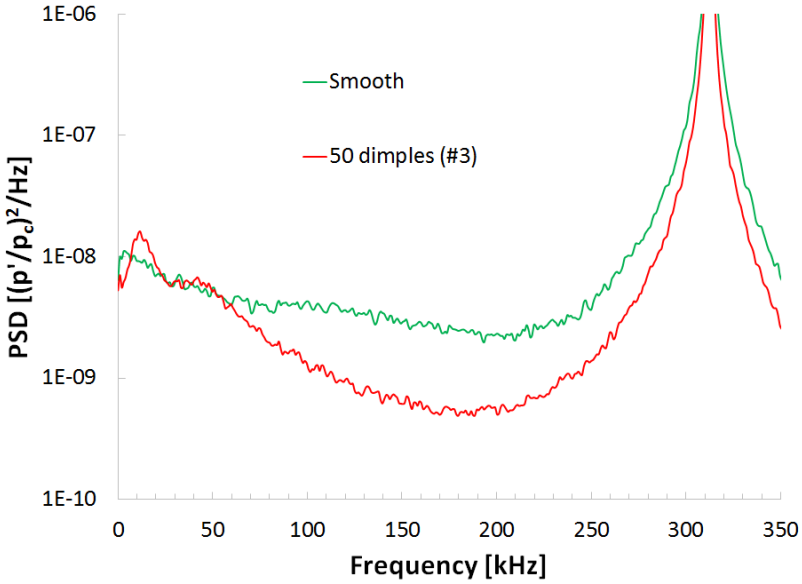

(b) Kulite (circled in white). x = 0.36 m.

Figure 5.30.: PSD of sensors (circled in Figure 5.28) on the 165° ray at a Reynolds number of 10.4×10^6/m.

The effect of the roughness elements is not as clear at the largest Reynolds number of 12.0×10^6/m. The TSP images are shown in Figure 5.31. The difference between the two cases is not entirely clear in the TSP images.

The spanwise heat transfer profiles at an axial distance of 0.34 m for the two TSP images in Figure 5.31 are shown in Figure 5.32. Both smooth and rough cases produce stationary vortices with similar magnitudes but at different azimuthal locations. The wavenumber (per radian) for the smooth case is 8.5 per radian and the 50-dimple case is 10.3 per radian (between 150° and 210°). Again, the 50 dimple case is producing a larger wavenumber than the smooth case, but a much smaller wavenumber than expected. The expected wavenumber per radian is approximately 50. The RMS of the non-dimensional heat transfer between 150° and 210° is 0.25 and 0.28 for the smooth and rough cases, respectively.

Figure 5.33 is a reprint of the TSP images in Figure 5.31 and shows the location of the sensors and the streamlines over which axial profiles were taken. The amplitude of the stationary vortices along the white and black lines are plotted in Figure 5.34. The white line is approximately along the 165° ray, and the black line is approximately along the 185° ray. Wave amplitudes along the two streamlines are similar for the rough and smooth cases. Both profiles show a high level of heat transfer at the upstream end of the image suggesting that the stationary vortex may be transitioning to turbulence. The heat transfer trends down as the stationary vortex decays and breaks down to turbulence.

At this highest Reynolds number, the TSP images and the axial wave amplitude plots showed what appeared to be a transitional boundary layer near both sensor locations. The PSD of the two sensors is shown in Figure 5.35. Both the PCB and Kulite sensors show what appears to be a turbulent boundary layer (comparing power levels to Figure 5.25). There is no appreciable difference between the PSD's for the smooth and 50-dimple cases. It appears that crossflow-induced boundary-layer transition is occurring under fully quiet flow. This is important, because this allows

for a better study of how roughness alters the growth and breakdown of the crossflow waves.

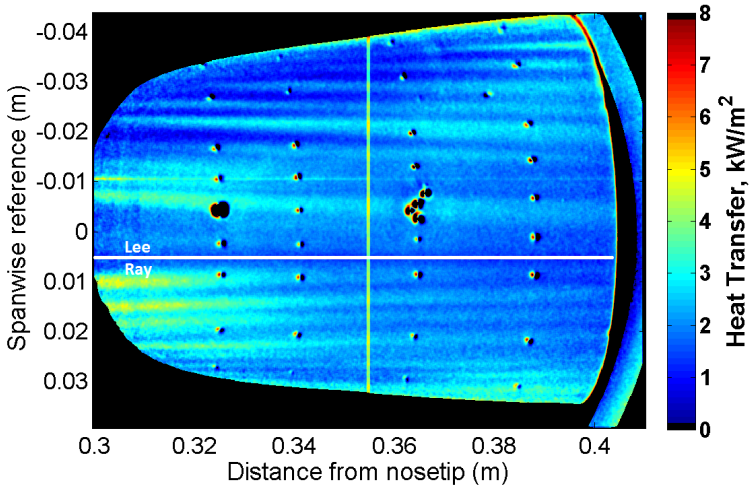

(a) Smooth. $p_0 = 157$ psia, Re $= 12.0\times10^6$/m, $T_0 = 423$ K, $T_w = 304$ K.

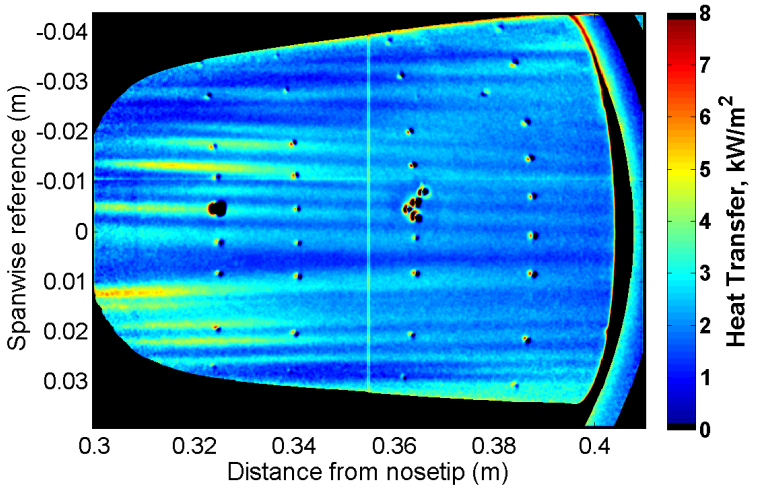

(b) 50-dimples (#3). $p_0 = 158$ psia, Re $= 12.1\times10^6$/m, $T_0 = 426$ K, $T_w = 302$ K.

Figure 5.31.: TSP images under quiet flow and varying Reynolds number with smooth and rough Torlon inserts (50 dimples). Lee side of the cone imaged.

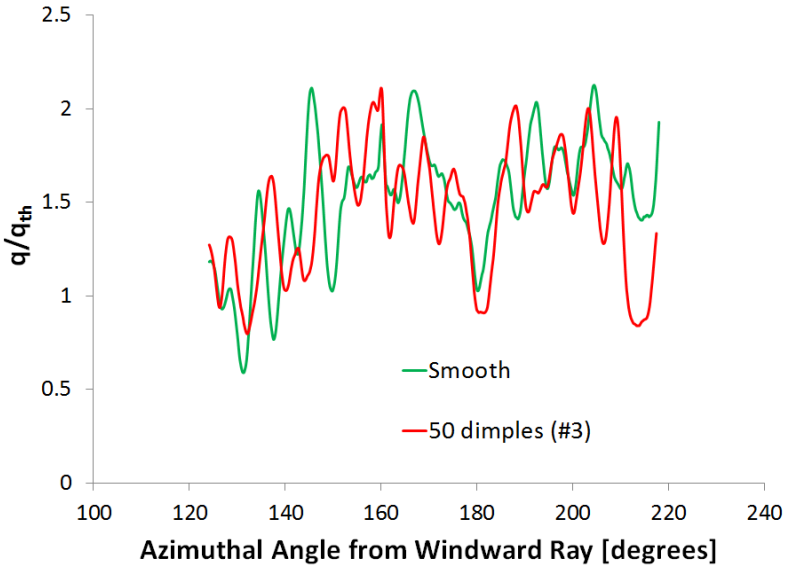

Figure 5.32.: Spanwise heat transfer profile at an axial distance of 0.34 m of the TSP images in Figure 5.31. Quiet flow, Re = 12.0×10^6/m.

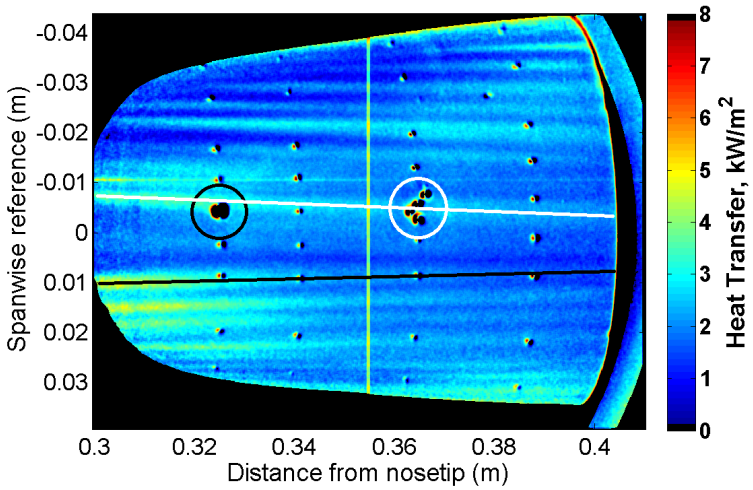

(a) Smooth. $p_0 = 157$ psia, Re $= 12.0\times10^6$/m, $T_0 = 423$ K, $T_w = 304$ K.

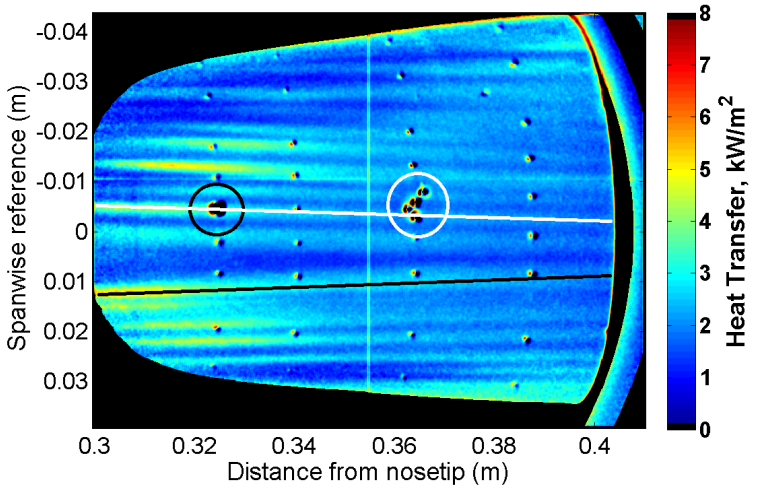

(b) 50-dimples (#3). $p_0 = 158$ psia, Re $= 12.1\times10^6$/m, $T_0 = 426$ K, $T_w = 302$ K.

Figure 5.33.: TSP images under quiet flow and varying Reynolds number with smooth and rough Torlon inserts (50 dimples). Lee side of the cone imaged. Reprint of Figure 5.31, with sensor and axial profile locations shown.

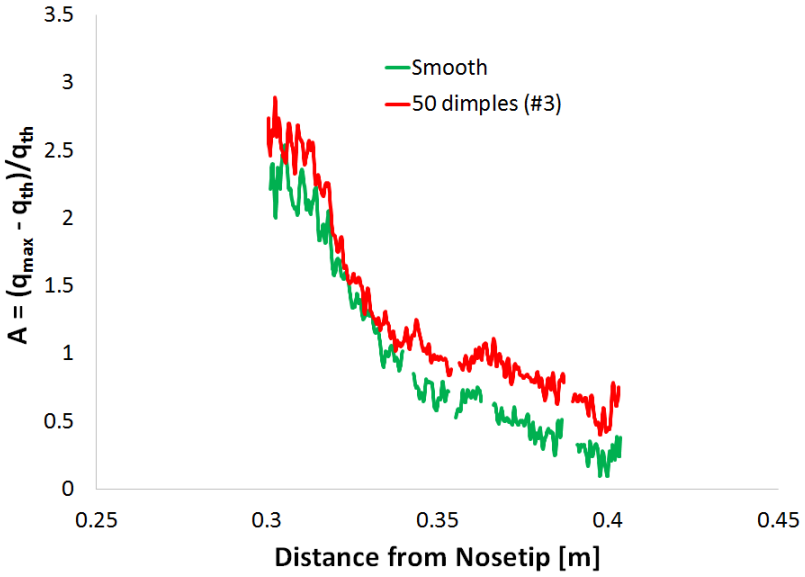

(a) Amplitude along the 165° ray (white line in Figure 5.28).

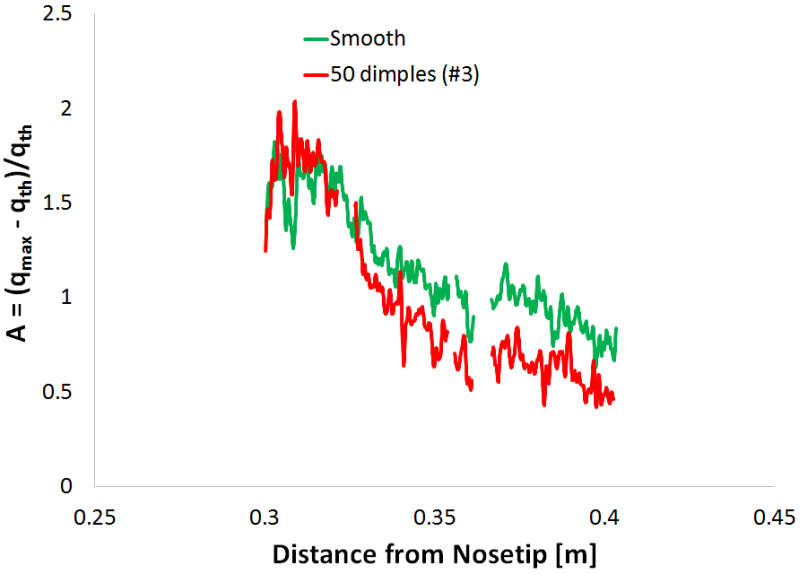

(b) Amplitude along the 185° ray (black line in Figure 5.28).

Figure 5.34.: Stationary vortex amplitude along the streamlines denoted in Figure 5.28. Quiet flow, Re = 12.0×10^6/m.

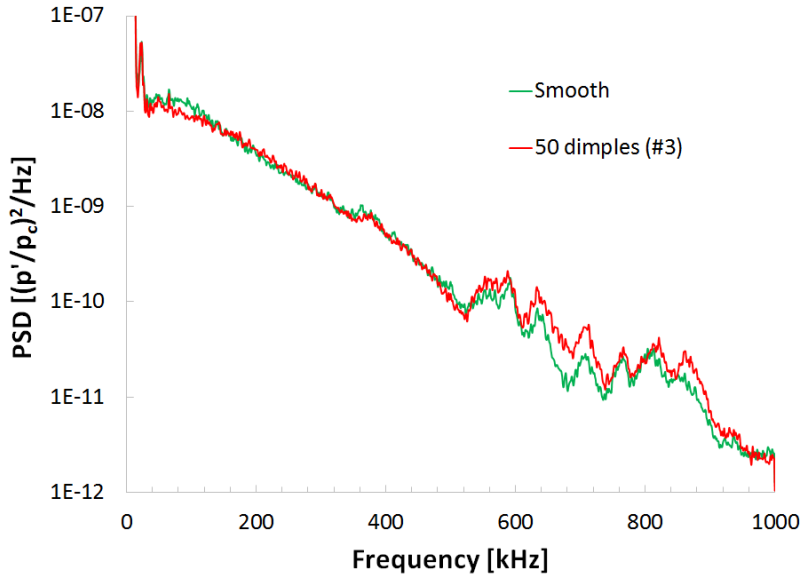

(a) PCB (circled in black). x = 0.32 m.

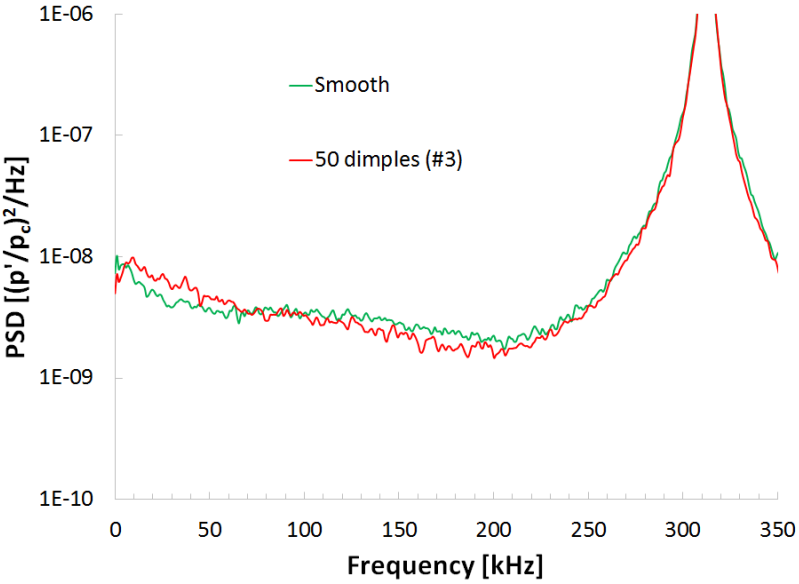

(b) Kulite (circled in white). x = 0.36 m.

Figure 5.35.: PSD of sensors (circled in Figure 5.28) at 165° from windward. Quiet flow, Re = 12.0×10^6/m.

Figure 5.36 plots the wave amplitude along the 165° ray with both the smooth insert and the rough Torlon insert for all Reynolds numbers. With increasing Reynolds number, the initial growth of the stationary waves moves upstream. The location of the saturation point also moves upstream with increasing Reynolds number. At the highest Reynolds number, the saturation point appears to occur upstream of the imaged area.

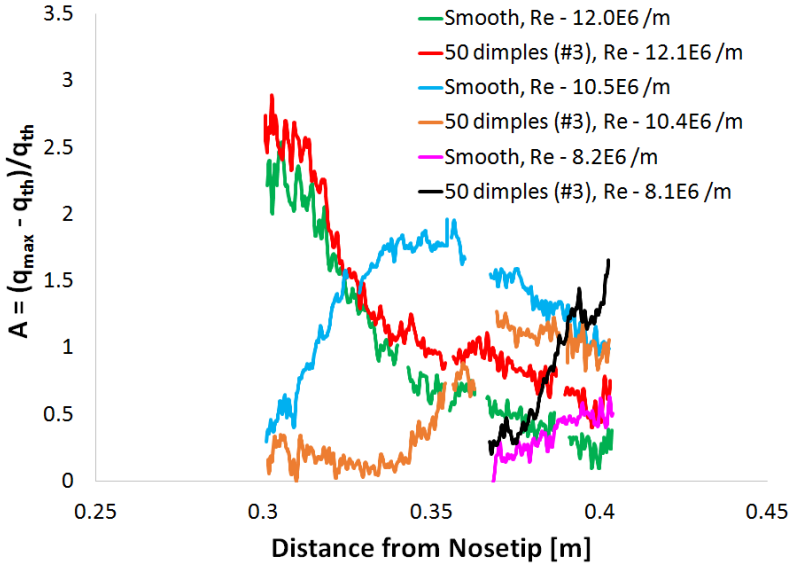

Figure 5.36.: Stationary vortex amplitude along 165° ray (denoted in white in Figures 5.23, 5.28 and 5.33). Quiet flow.

The PSD of the PCB sensor for all three Reynolds numbers is shown in Figure 5.37. The PCB sensor is circled in black and along the 165° ray in the TSP images in Figures 5.23, 5.28 and 5.33. For the smooth case, at the lowest Reynolds number a peak at 200 kHz is visible, which may be caused by the second-mode. It does not appear to be the secondary instability of the stationary wave because the TSP image in Figure 5.21(a) does not show any large stationary vortices near the sensor. Increasing the Reynolds number, the flow appears to be turbulent based on the increase in broadband noise. For the rough case at the lowest Reynolds number, the PSD shows low level of broadband noise and no peaks in the spectra. Increasing

the Reynolds number to 10.4×10^6/m, a peak appears near 200 kHz. Again this peak may be caused by the second-mode wave. Increasing the Reynolds number, a broad-band increase in noise is seen, likely due to a turbulent or transitional boundary layer over the sensor.

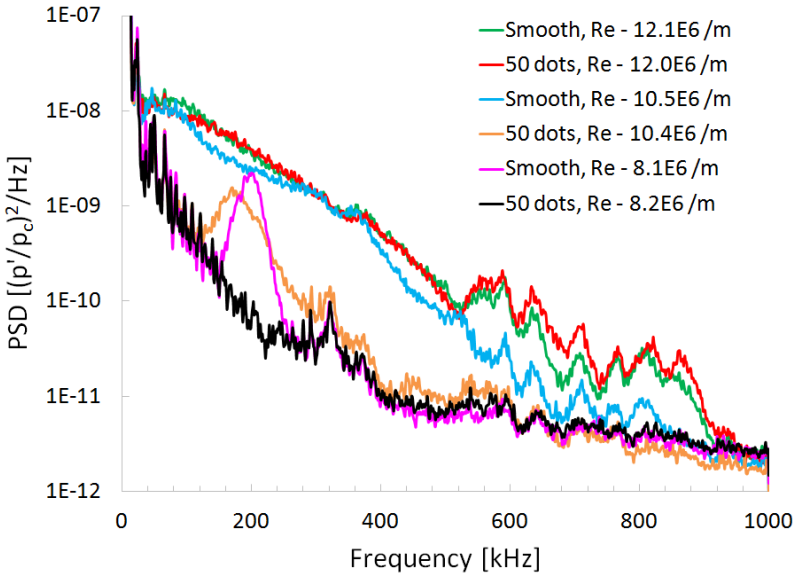

Figure 5.37.: PSD of PCB sensor on the 165° ray at a Reynolds number of 8.2×10^6/m for the TSP images in Figures 5.23, 5.28 and 5.33. Quiet flow. Sensor circled in black.

Figure 5.38 plots the RMS of the non-dimensional heat transfer between 150° and 210° at an axial distance of 0.37 m and the RMS of the non-dimensional pressure fluctuations between 0 and 500 kHz at an axial distance of 0.36 m for the three Reynolds numbers. The plot of the heat transfer RMS shows that the dimples on average produce larger stationary waves than the smooth case. A peak is seen at the middle Reynolds number, where the waves grew the largest. At the higher Reynolds number, the waves were beginning to break down and the RMS heat transfer reduced. The plot of RMS pressure shows that the smooth case on average produced larger pressure fluctuations than the rough case. The RMS pressure increases with increasing Reynolds number as the boundary layer transitioned to turbulence.

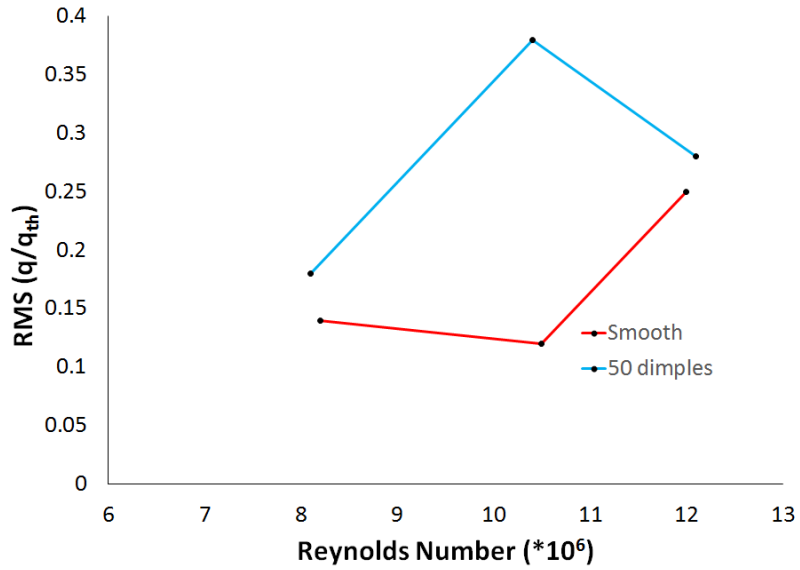

(a) RMS of q/q_{th} between 150° and 210°.

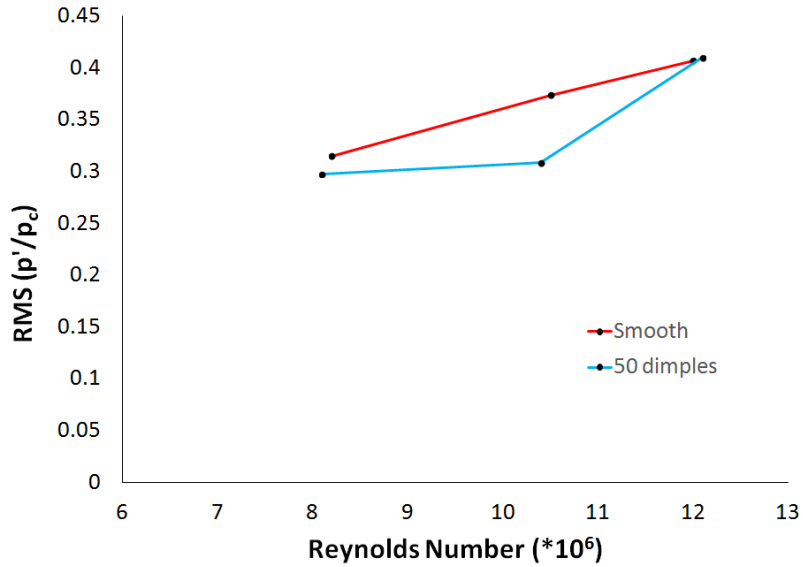

(b) RMS of p'/p_c between 0 and 500 kHz.

Figure 5.38.: RMS of the non-dimensional heat transfer and pressure for the TSP images in Figures 5.23, 5.28 and 5.33. Quiet flow.

Effect Near Yaw Ray

Tests were done with the yaw side of the cone imaged. Based on the computations and analysis in Section 5.4, it would be expected that the roughness elements would

show a much diminished effect near the yaw side of the cone. TSP images are shown in Figure 5.39 with both the smooth and 50-dimpled (#3) Torlon inserts at a Reynolds number of approximately 8.5×10^6/m under quiet flow. The yaw side of the cone is imaged, and the upper portion of the image is moving towards the wind ray. There appears to be slightly larger stationary vortices moving towards the lee ray when the roughness is added, but for the most part the two cases appear similar.

Spanwise heat transfer profiles at an axial distance of 0.38 m of the TSP images in Figure 5.39 are shown in Figure 5.40. For this Reynolds number, the two cases are similar from 30° to approximately 100°. The rough case appears to have larger stationary vortices near 100 and 120°. Between 30° and 100°, the RMS of the non-dimensional heat transfer is approximately 0.06 for both the smooth and rough cases. Between 100° and 120°, the RMS of the non-dimensional heat transfer is 0.09 and 0.21 for the smooth and rough cases, respectively.

Figure 5.41 is a reprint of the TSP images in Figure 5.39 with the sensor and axial profile locations shown. Figure 5.42 plots the amplitude of the stationary waves along the black line in Figure 5.41. As was seen in the TSP images, there is not a significant difference in the wave amplitude whether the rough or the smooth Torlon insert is used.

Figure 5.43 plots the PSD of the pressure data from the two sensors circled in Figure 5.41. The sensors are along the 90° ray. The spectra for both the rough and smooth cases are similar at both sensor locations. The PCB sensors show a small peak near 300 kHz. This may be caused by the second-mode wave, and the peak frequency approximately agrees with an LST computation done by Balakumar et al. [106]. The computations were done at a slightly higher Reynolds number of 10.4×10^6/m. This peak is not likely caused by the secondary instability of the stationary crossflow wave because the TSP images (Figure 5.39) do not show large stationary waves near the sensor. The Kulite sensor shows a peak near 40 kHz, which corresponds to the travelling crossflow instability. The roughness appears to slightly damp this instability.

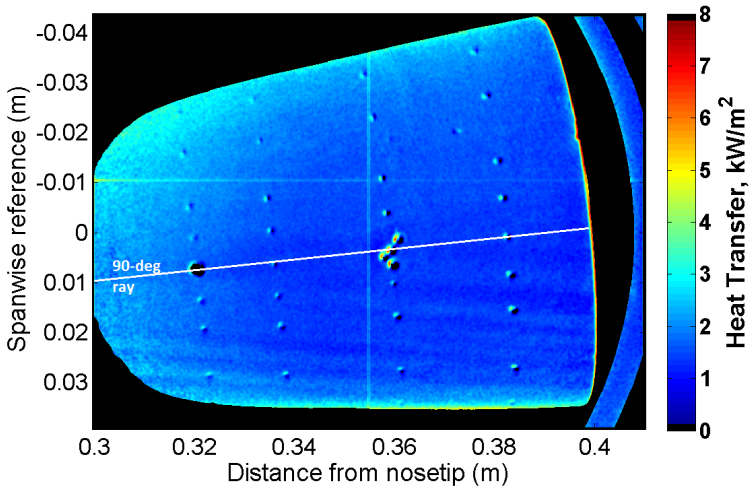

(a) Smooth. $p_0 = 110$ psia, Re $= 8.5\times10^6$/m, $T_0 = 420$ K, $T_w = 306$ K

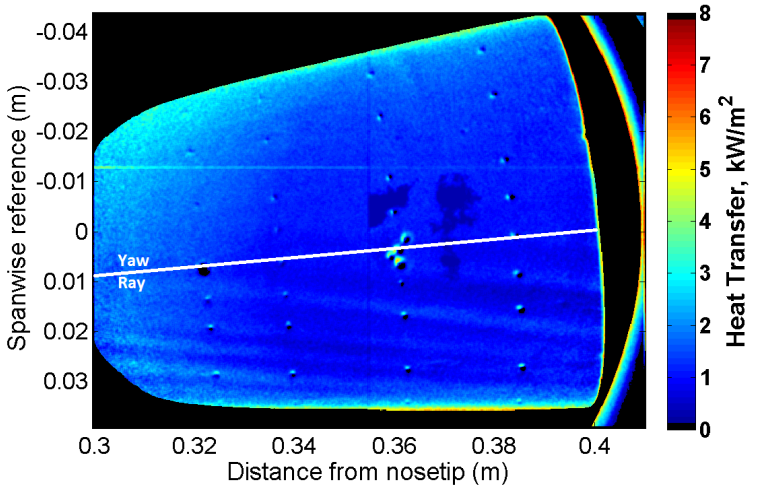

(b) 50 dimples (#3). $p_0 = 110$ psia, Re $= 8.4\times10^6$/m, $T_0 = 425$ K, $T_w = 298$ K

Figure 5.39.: TSP images under quiet flow with smooth and 50-dimpled insert. Yaw side of the cone. Reynolds number of approximately 8.5×10^6/m.

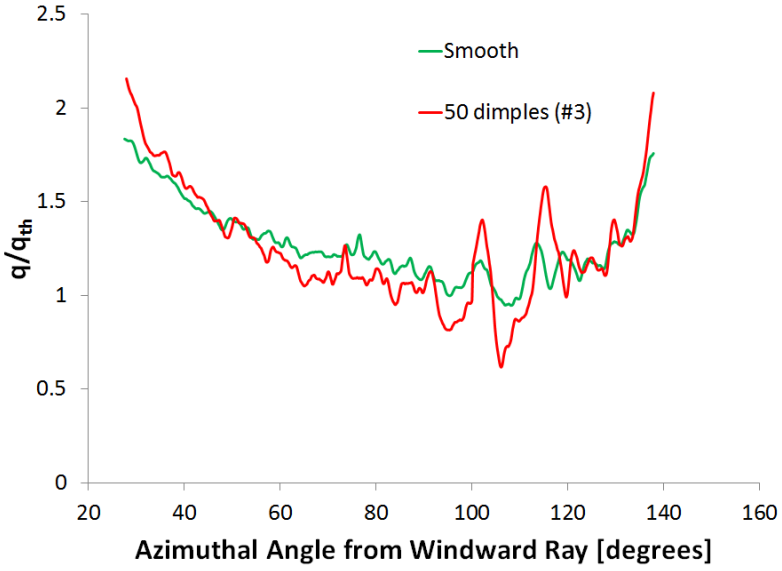

Figure 5.40.: Spanwise heat transfer profile at an axial distance of 0.38 m of the TSP images in Figure 5.39. Quiet flow, Re = 8.5×10^6/m.

The travelling crossflow instability and the interaction between the stationary and travelling crossflow instabilities will be discussed in Chapters 6 and 7.

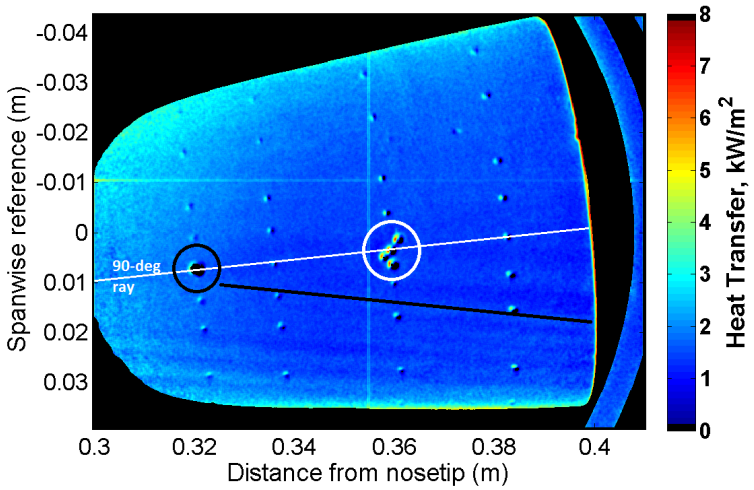

(a) Smooth. $p_0 = 110$ psia, Re $= 8.5\times10^6$/m, $T_0 = 420$ K, $T_w = 306$ K

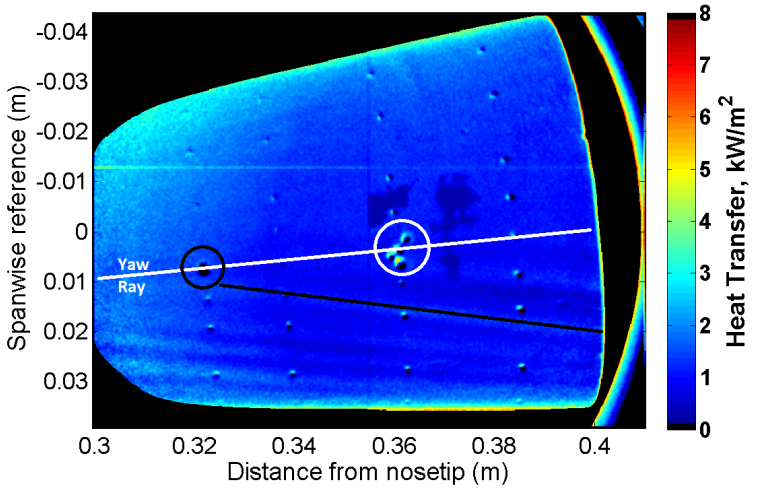

(b) 50 dimples (#3). $p_0 = 110$ psia, Re $= 8.4\times10^6$/m, $T_0 = 425$ K, $T_w = 298$ K

Figure 5.41.: TSP images under quiet flow with smooth and 50-dimpled insert. Yaw side of the cone. Reynolds number of approximately 8.5×10^6/m. Reprint of Figure 5.39, with sensor and axial profile locations shown.

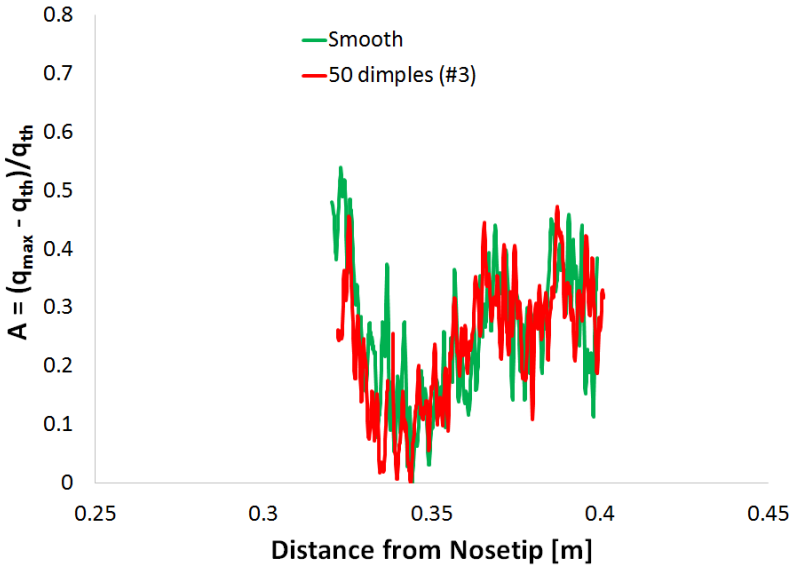

Figure 5.42.: Stationary vortex amplitude along black line on the TSP images in Figure 5.39. Quiet flow, Re = 8.5×10^6/m.

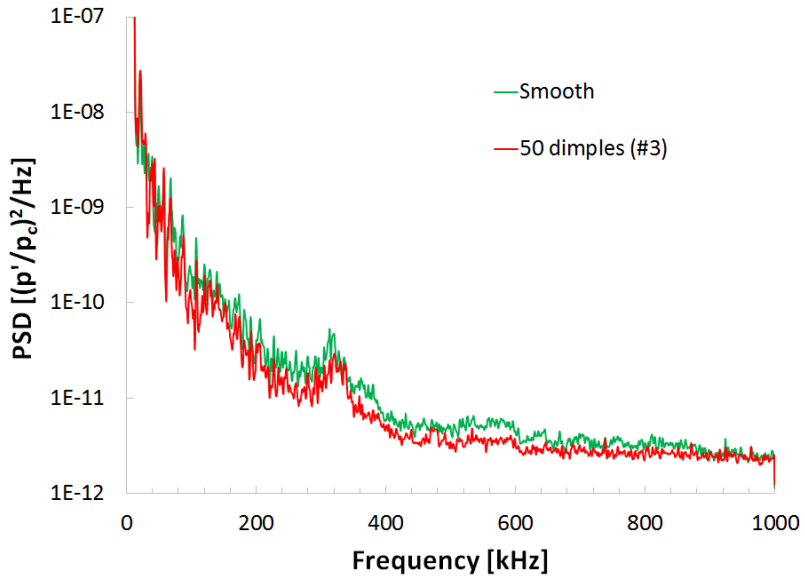

(a) PCB (circled in black). x = 0.32 m.

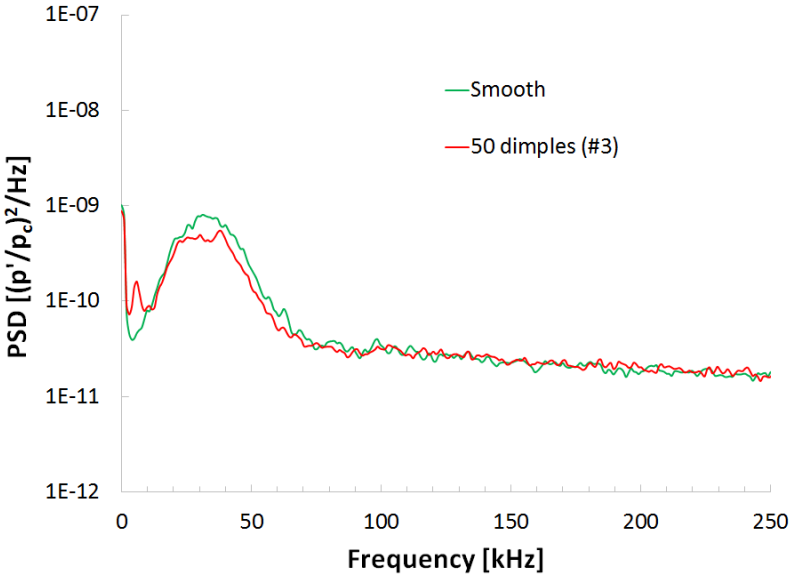

(b) Kulite (circled in white). x = 0.36 m.

Figure 5.43.: PSD of sensors (circled in Figure 5.41) at 90° from windward. Re = 8.5×10^6/m.

Tests were then performed at a Reynolds number of approximately 10.8×10^6/m. The TSP images with both the smooth and 50-dimpled insert are shown in Figure 5.44. The yaw side of the cone is imaged, and the wind ray is close to the upper portion of the image. The rough case appears to generate slightly larger stationary vortices, especially nearer to the lee ray. Closer to the wind ray, the two images look similar. This is likely because any disturbances generated by the roughness elements will be swept close to the lee ray at the axial locations imaged.

Figure 5.45 plots the spanwise heat transfer profiles at an axial distance of 0.38 m of the TSP images in Figure 5.44. The two profiles are quite similar from 30° to 90°, where at 90° the rough case generates a larger stationary vortex. There are some differences in spacing and vortex amplitude when moving towards the lee ray. The RMS of the non-dimensional heat transfer between 30 and 90° is 0.05 and 0.07 for the smooth and rough cases, respectively. The RMS of the non-dimensional heat transfer between 90 and 120° is 0.09 and 0.14 for the smooth and rough cases, respectively.

Figure 5.46 is a reprint of the TSP images in Figure 5.44 with the sensor and axial profile locations shown. Figure 5.47 plots the amplitude of the stationary waves along the black line in Figure 5.46. There does not appear to be significant growth of the stationary vortices for either cases. Although the profile shapes are different, it does not appear that the vortices are breaking down to turbulence for either case.

Looking at the PSD of the sensors circled in Figure 5.46 can help determine if the vortices along the black line are breaking down to turbulence. The sensors are along the 90° ray. The spectra for the PCB sensor at 0.32 m are similar for both the smooth and rough cases. The power of the broadband noise is low compared to turbulent spectra seen earlier, therefore it appears that the boundary layer is laminar. The spectra for the Kulite at the downstream location shows a dampening of the travelling crossflow instability when the roughness insert is used. It appears that the stationary vortices are not breaking down to turbulence at these axial locations. Again, the interaction between the travelling and stationary crossflow waves will be discussed in Chapter 7.

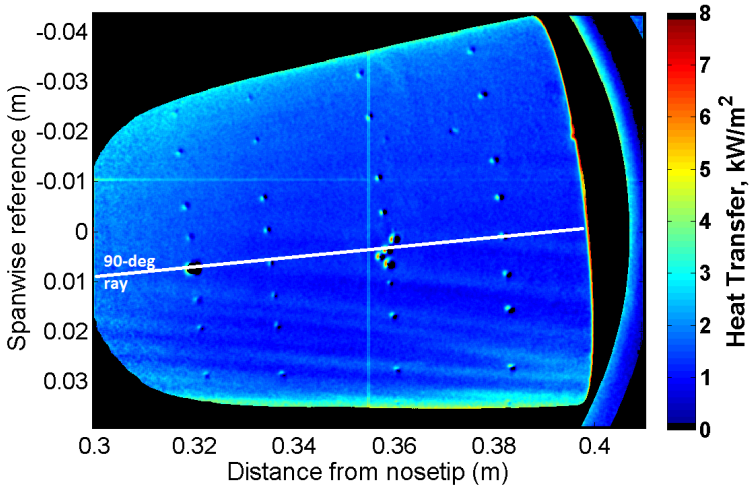

(a) Smooth. $p_0 = 140$ psia, Re $= 10.8\times10^6$/m, $T_0 = 420$ K, $T_w = 307$ K

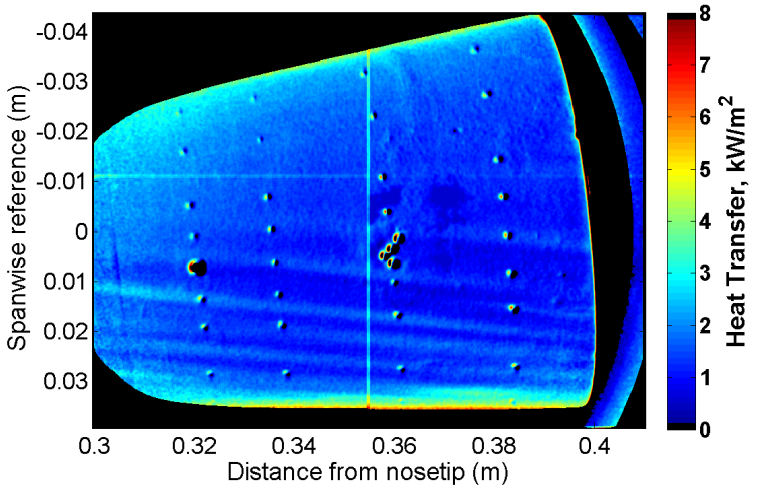

(b) 50 dimples (#3). $p_0 = 141$ psia, Re $= 10.7\times10^6$/m, $T_0 = 424$ K, $T_w = 301$ K

Figure 5.44.: TSP images under quiet flow with smooth and 50-dimpled insert. Yaw side of the cone. Reynolds number of approximately 10.8×10^6/m.

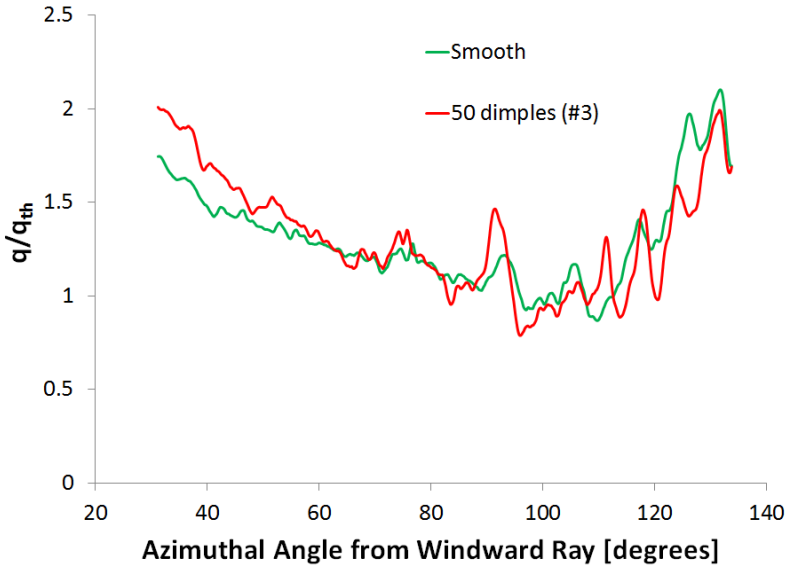

Figure 5.45.: Spanwise heat transfer profile at an axial distance of 0.38 m of the TSP images in Figure 5.44. Quiet flow, Re = 10.8×10^6/m.

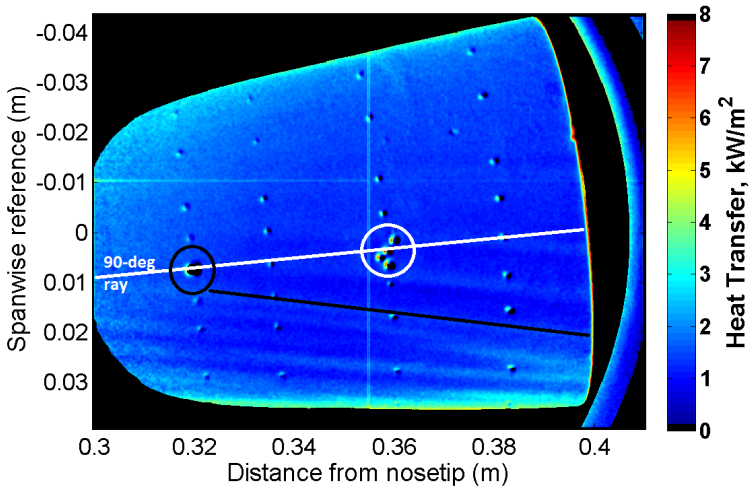

(a) Smooth. $p_0 = 140$ psia, Re $= 10.8\times10^6$/m, $T_0 = 420$ K, $T_w = 307$ K

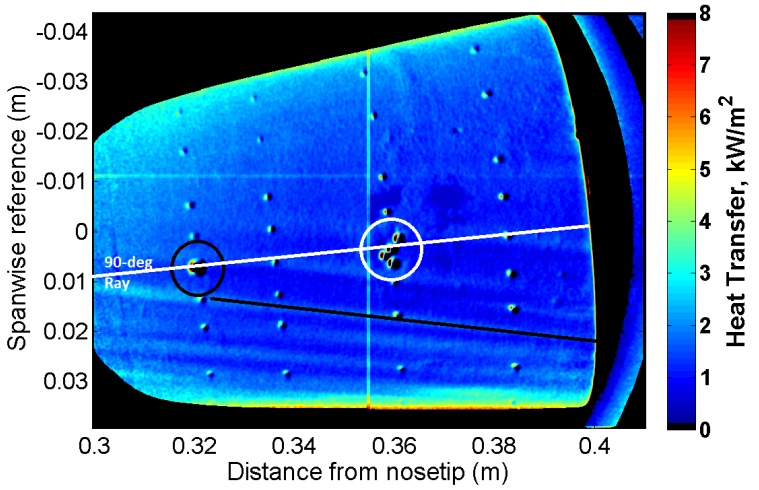

(b) 50 dimples (#3). $p_0 = 141$ psia, Re $= 10.7\times10^6$/m, $T_0 = 424$ K, $T_w = 301$ K

Figure 5.46.: TSP images under quiet flow with smooth and 50-dimpled insert. Yaw side of the cone. Reynolds number of approximately 10.8×10^6/m. Reprint of Figure 5.44, with sensor and axial profile locations shown.

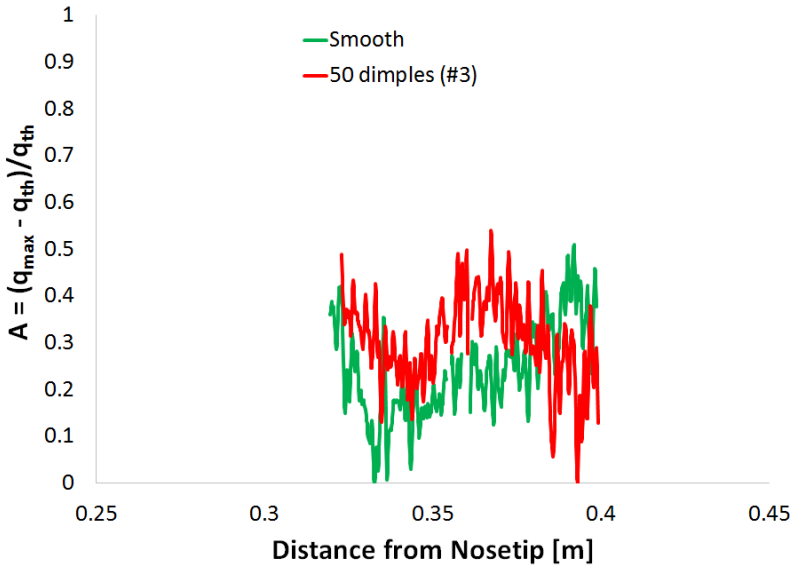

Figure 5.47.: Stationary vortex amplitude along black line on the TSP images in Figure 5.44. Quiet flow, Re = 10.8×10^6/m.

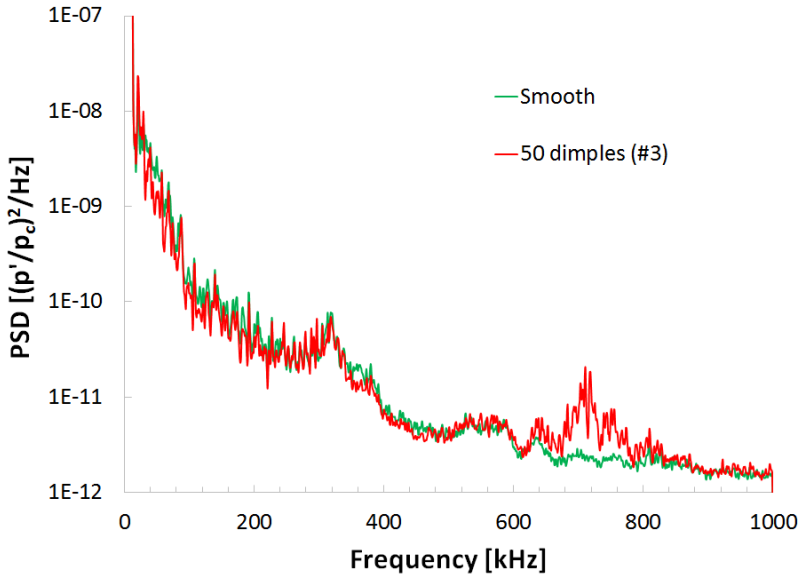

(a) PCB (circled in black). x = 0.32 m.

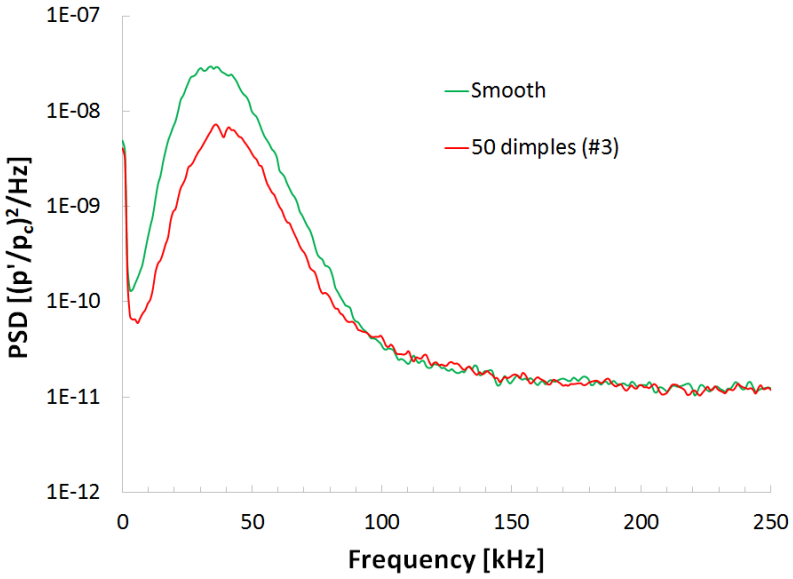

(b) Kulite (circled in white). x = 0.36 m.

Figure 5.48.: PSD of sensors (circled in Figure 5.46) at 90° from windward. Re = 10.8×10^6/m.

Finally, tests were performed at a higher Reynolds number of approximately 12.4×10^6/m. The TSP images at this Reynolds number under quiet flow with both the smooth and 50-dimpled Torlon insert are shown in Figure 5.49. The rough insert appears to be producing larger amplitude stationary vortices, although this may be an artifact of slightly differing tunnel conditions.

Spanwise heat transfer profiles shown in Figure 5.50 were taken at an axial distance of 0.38 m for the TSP images in Figure 5.49. The heat transfer is non-dimensionalized by the theoretical heat transfer, which should help remove the effect of slightly differing tunnel conditions. The rough profile shows a large stationary vortex occurring near 95°. The smooth and rough inserts appear to produce a similar stationary vortex at 120°. The RMS of the non-dimensional heat transfer between 30 and 90° is 0.11 and 0.15 for the smooth and rough cases, respectively. The RMS of the non-dimensional heat transfer between 90 and 120° is 0.41 and 0.32 for the smooth and rough cases, respectively. Although the rough case appears to be creating larger stationary vortices between 90 and 120°, the smooth case produces the larger RMS non-dimensional heat transfer values.

Figure 5.51 is a reprint of the TSP images in Figure 5.49 with the sensor and axial profile locations shown. Figure 5.52 plots the amplitude of the stationary waves along the black line in Figure 5.51. The growth of the stationary vortices appears to be similar regardless of which insert is used. It is not clear if the waves are reaching a peak or saturating for both the smooth and rough cases, and therefore it is not clear if the waves are breaking down to turbulence.

Power spectra of the pressure data from the two sensors circled in Figure 5.51 is shown in Figure 5.53. The sensors are along the 90° ray. At the upstream location, the two spectra are similar. Once again it appears that the roughness is having a minimal impact on the stationary vortices near the 90° ray. At the downstream location, a dampening of the travelling crossflow waves is seen when the roughness is added. Additional analyses have been done in Chapter 7 looking at the small effects the roughness may have near the 90° ray. From this section, it appears that the

roughness insert shows a greater effect nearer to the lee side than the yaw side, as was expected.

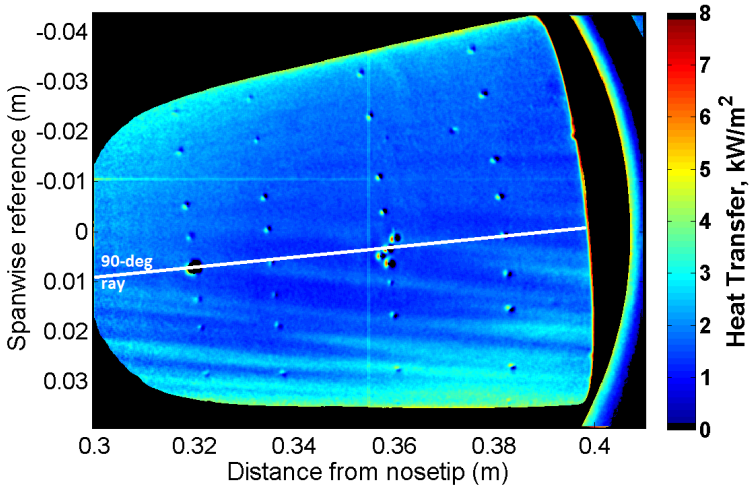

(a) Smooth. $p_0 = 160$ psia, Re $= 12.4\times10^6$/m, $T_0 = 419$ K, $T_w = 306$ K

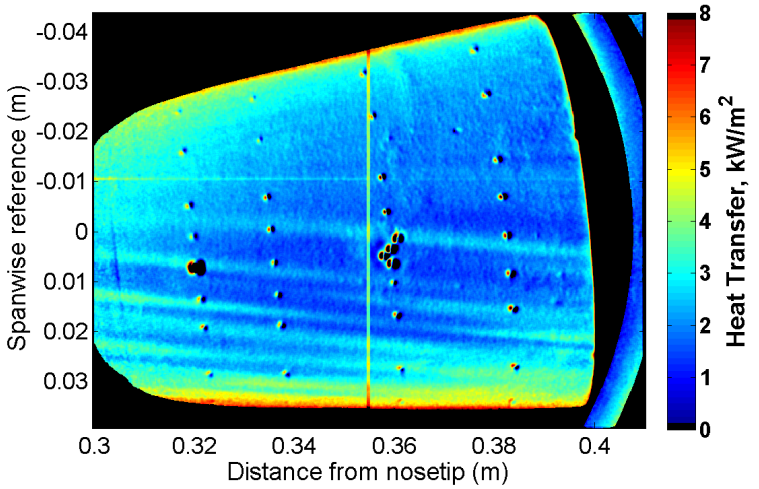

(b) 50 dimples (#3). $p_0 = 161$ psia, Re $= 12.3\times10^6$/m, $T_0 = 422$ K, $T_w = 304$ K

Figure 5.49.: TSP images under quiet flow with smooth and 50-dimpled insert. Yaw side of the cone. Reynolds number of approximately 12.4×10^6/m.

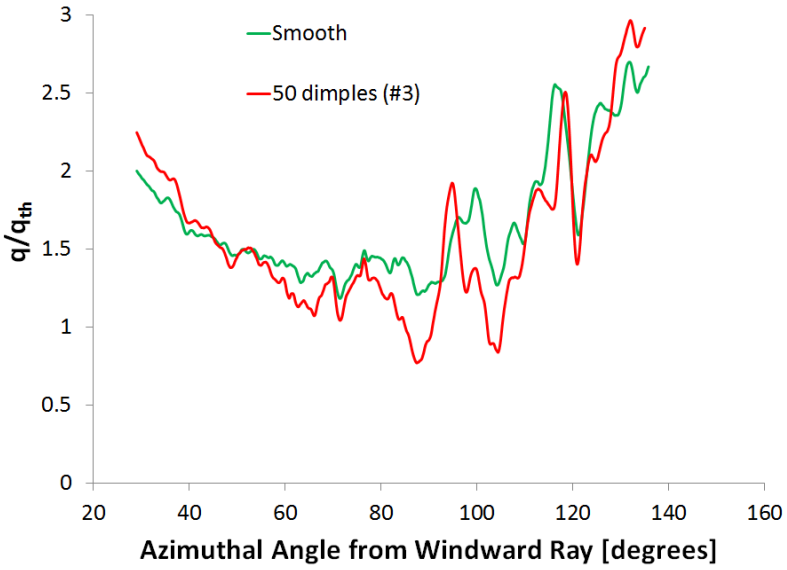

Figure 5.50.: Spanwise heat transfer profile at an axial distance of 0.38 m of the TSP images in Figure 5.49. Quiet flow, Re = 12.3×10^6/m.

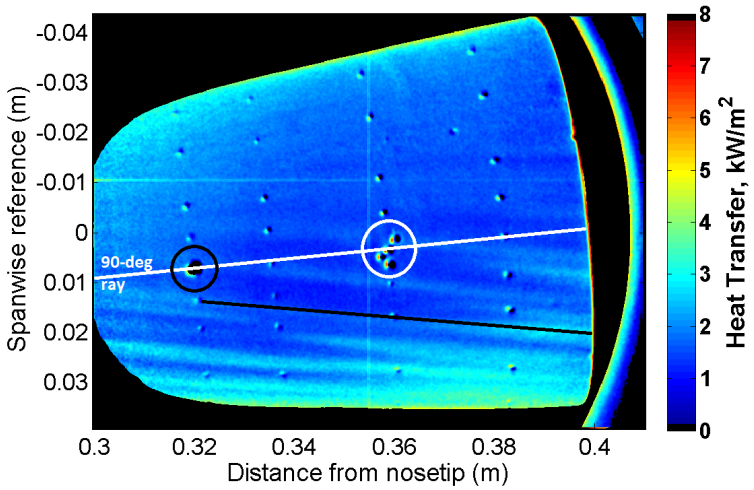

(a) Smooth. $p_0 = 160$ psia, Re $= 12.4\times10^6$/m, $T_0 = 419$ K, $T_w = 306$ K

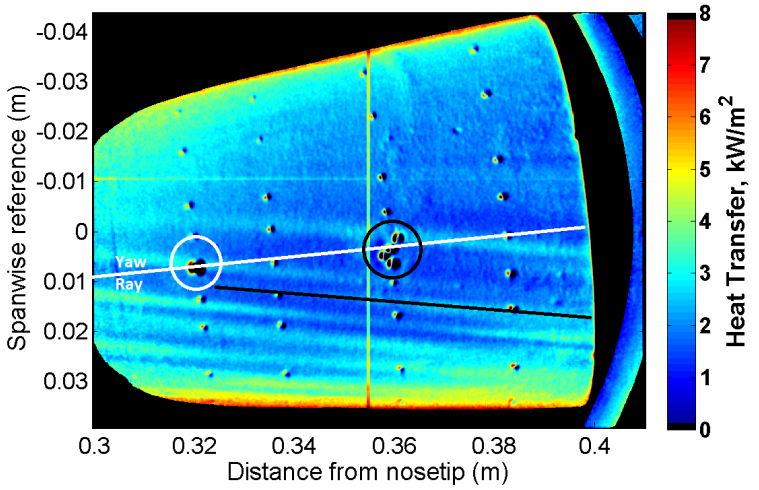

(b) 50 dimples (#3). $p_0 = 161$ psia, Re $= 12.3\times10^6$/m, $T_0 = 422$ K, $T_w = 304$ K

Figure 5.51.: TSP images under quiet flow with smooth and 50-dimpled insert. Yaw side of the cone. Reynolds number of approximately 12.4×10^6/m. Reprint of Figure 5.49, with sensor and axial profile locations shown.

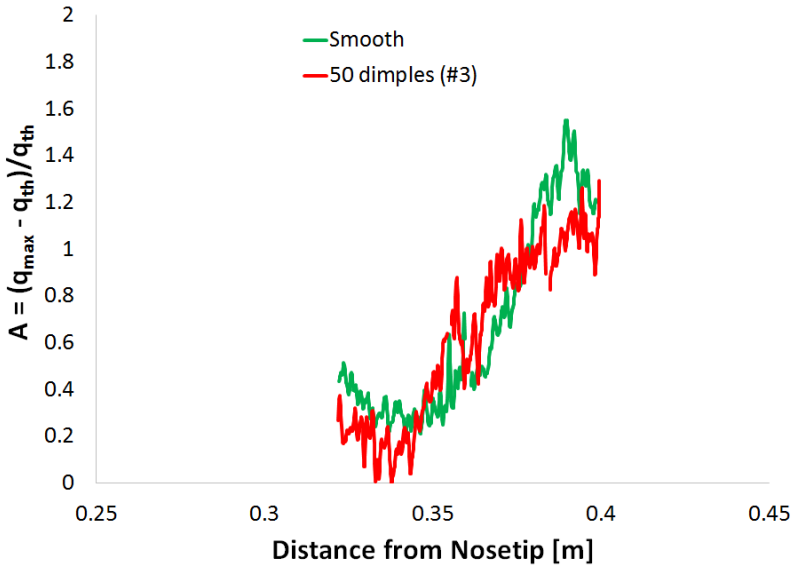

Figure 5.52.: Stationary vortex amplitude along black line on the TSP images in Figure 5.49. Quiet flow, Re = 12.4×10^6/m.

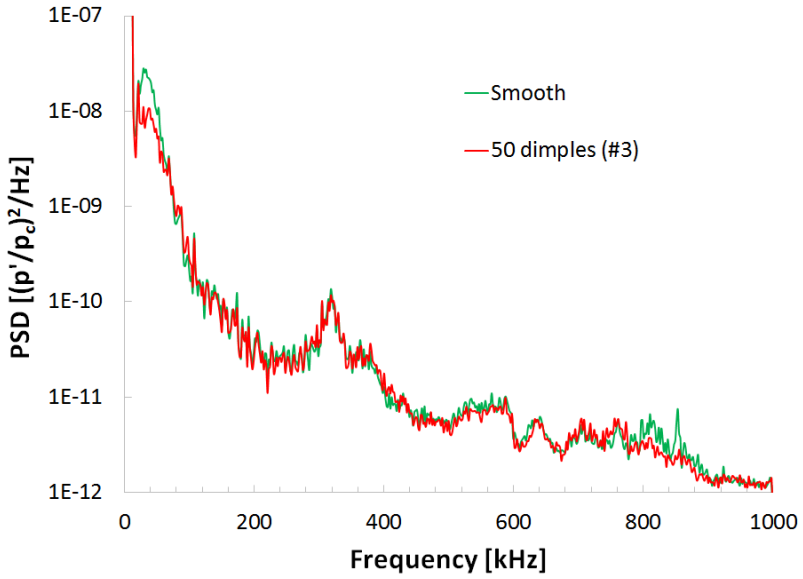

(a) PCB (circled in black). x = 0.32 m.

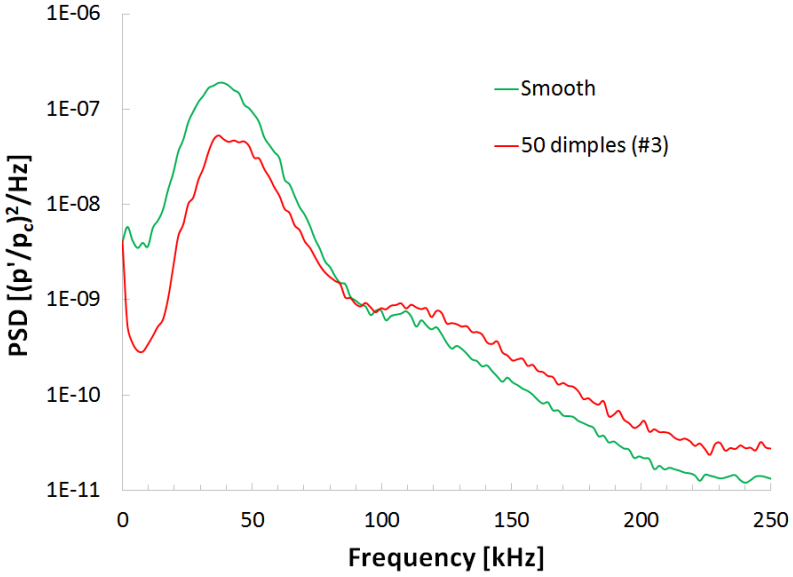

(b) Kulite (circled in white). x = 0.36 m.

Figure 5.53.: PSD of sensors (circled in Figure 5.51) at 90° from windward. Re = 12.4×10^6/m.

5.5.2 Varying Number of Dimples Around Azimuth

The effect of roughness spacing was looked at by varying the number of evenly spaced roughness elements around the azimuth of the Torlon section. Tests were performed with smooth, 50 dimpled (insert #2, dimples spaced 7.2° apart) and 72 dimpled (insert #6, dimples spaced 5° apart) Torlon inserts. When creating the two roughness inserts, the D/λ (diameter divided by the forced stationary crossflow wavelength) was kept approximately constant, therefore the 72 dimple case has smaller diameters and consequently less protruding material. These tests were performed with the same paint finish and same nosetip, only differing in the Torlon insert used. TSP images with the three different Torlon inserts are shown in Figure 5.54 at a Reynolds number of 10.4×10^6/m under quiet flow. The lee side of the cone is imaged. Comparing the smooth and 50 dimples case, once again the roughness elements are having a significant effect on the generation of stationary vortices. As expected, the biggest effect is seen near the lee ray especially on the lower half of the image. When the 72-dimpled insert is used, again the pattern of stationary vortices differs. Solely from the TSP images, it is not clear what effect the spacing has.

Spanwise heat transfer profiles of the TSP images from Figure 5.54 at an axial location of 0.35 m are shown in Figure 5.55. The 50 dimple case appears to generate a much different pattern and spacing than the other two cases. For angles between 120° and 190°, the 72 dimple and smooth profiles do not show a significant difference. For angles between 190° and 240°, the 72-dimple case produces much larger stationary vortices than the smooth case. It is possible that the depth, diameter or protruding material is not large enough for the 72-dimple insert compared to the random roughness in order to dominate the generation of the stationary vortices from 120–190°. The depth of the 50-dimple insert roughness was almost 50% larger than the depth of the 72-dimple insert roughness.

Figure 5.56 is a reprint of the TSP images in Figure 5.54 with the sensor and axial profile locations shown. Figure 5.57 plots the amplitude of the stationary waves

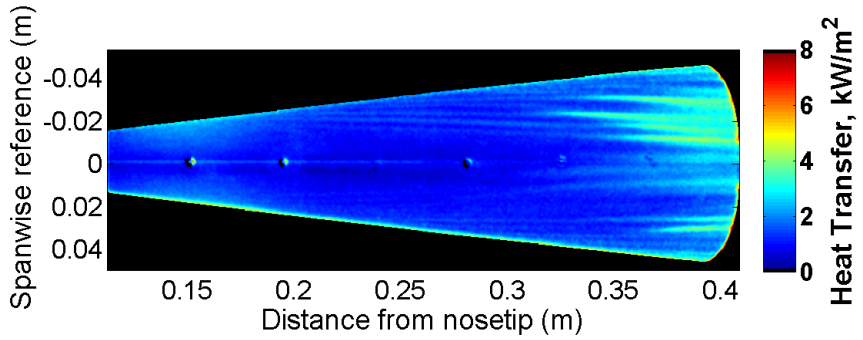

(a) Smooth (insert #1). $T_w = 300$ K.

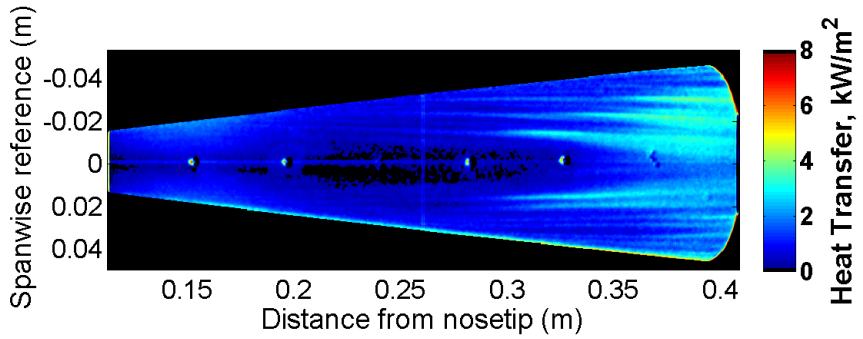

(b) 50 dimples (insert #2). $T_w = 300$ K.

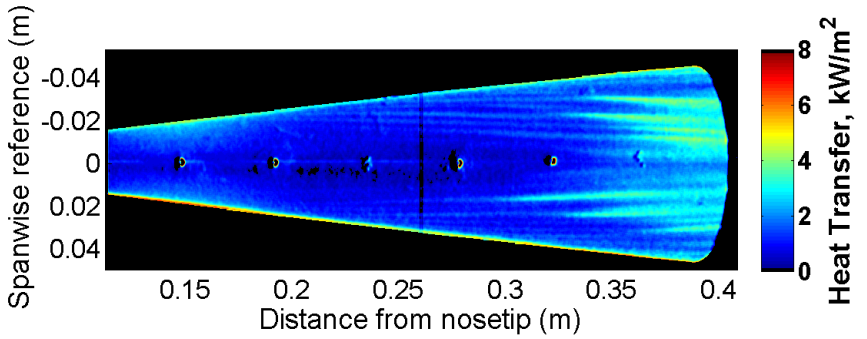

(c) 72 dimples (insert #6). $T_w = 297$ K.

Figure 5.54.: TSP images under quiet flow with smooth, 50-dimpled and 72-dimpled Torlon inserts. Lee side of the cone. Sensors along the lee ray. Re = 10.4×10^6/m, $p_0 = 138$ psia, $T_0 = 426$ K.

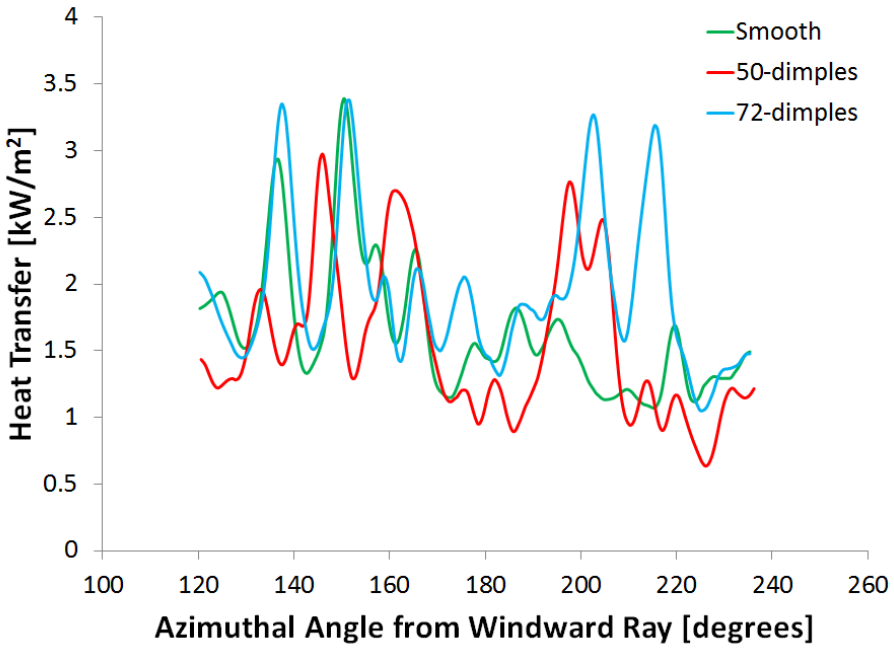

Figure 5.55.: Spanwise heat transfer profiles at an axial distance of 0.35 m from the nosetip of the TSP images in Figure 5.54. Quiet flow.

along the red, black and white lines in Figure 5.56. Along the red line, the TSP image showed what appeared to be a similar stationary vortex for all three cases. The amplitude plot shows a similar growth of this particular stationary wave, and saturation occurring at roughly the same location. There is a slight delay in the saturation of the 50 dimple case compared to the other two. This may be due to the addition of the roughness elements. Along the black line, there is a clear difference in the stationary vortices for the three cases. The 50-dimpled case shows a much earlier growth of the stationary wave, along with the amplitude saturation location. The 72-dimpled case shows the wave beginning to grow furthest downstream, and reaching the smallest amplitude. Along the white line, the two rough cases produce similar stationary vortices that reach similar amplitudes and begin to decay at similar axial locations.

PSD of the PCB sensors 0.19 and 0.32 m from the nosetip on the lee ray are shown in Figure 5.58 for the three insert cases. The sensors are circled in Figure 5.56. For both axial locations, the spectra are similar regardless of the roughness inserts used. The TSP images also show similar heat transfer at these two axial locations for all three roughness insert cases. All three spectra are similar, which agrees with the TSP data. At the upstream PCB location, all three sensors show a peak in the spectra near 60 kHz. At the downstream PCB location, all three sensors show an increase in amplitude and frequency of this peak in the spectra as compared to the upstream spectra. The peak is near approximately 70 kHz at the downstream location. Not enough data is available to determine if this is an instability present on the lee ray. The boundary layer does not appear to be turbulent at the downstream PCB location, because there is not an increase in broadband noise compared to the upstream location, and the TSP does not give any indication of a turbulent or transitional boundary layer. Unfortunately there were no Kulites installed in the sensor array 0.36 m from the nosetip. The downstream sensors would be more likely to show a difference between the three cases based on the TSP. Also, sensors slightly off of the lee ray would also be more likely to show differences between the three cases.

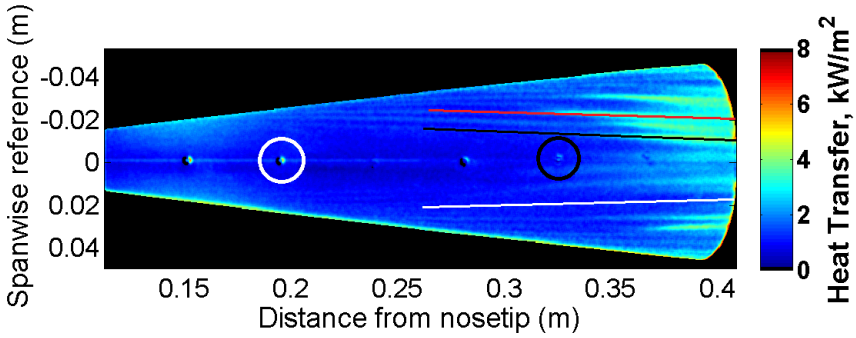

(a) Smooth (insert #1). $T_w = 300$ K.

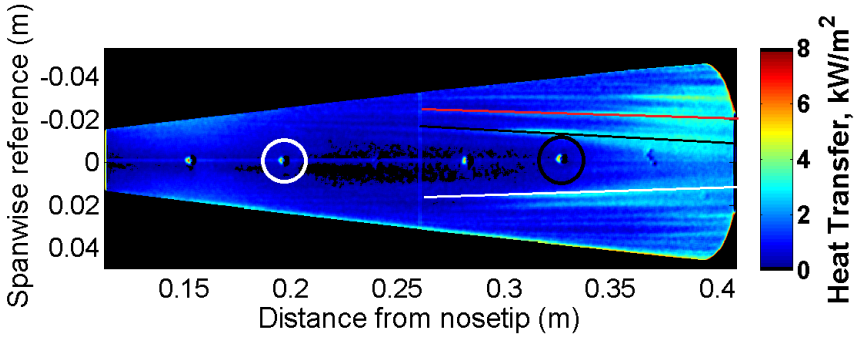

(b) 50 dimples (insert #2). $T_w = 300$ K.

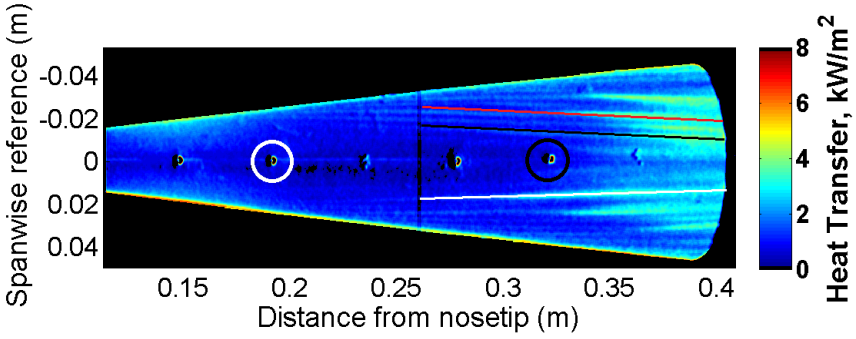

(c) 72 dimples (insert #6). $T_w = 297$ K.

Figure 5.56.: TSP images under quiet flow with smooth, 50-dimpled and 72-dimpled Torlon inserts. Lee side of the cone. Sensors along the lee ray. Re = 10.4×10^6/m, $p_0 = 138$ psia, $T_0 = 426$ K. Reprint of Figure 5.54, with sensor and axial profile locations shown.

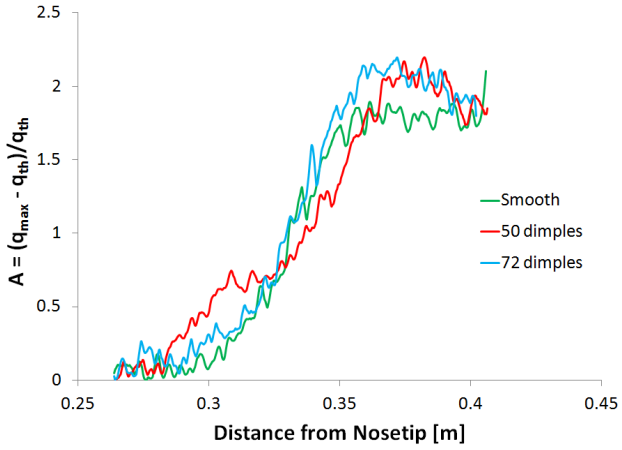

(a) Amplitude along the red line in Figure 5.56.

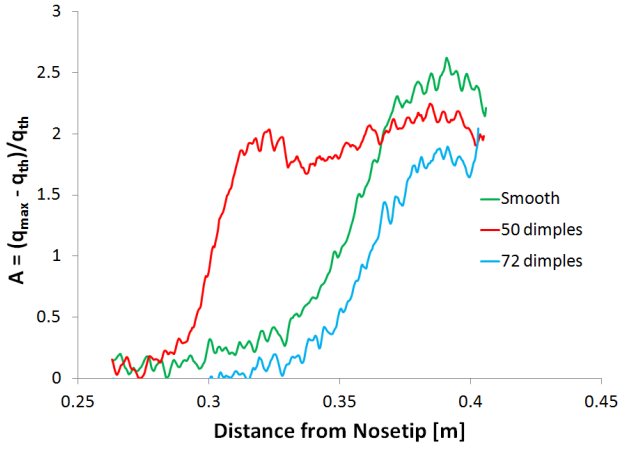

(b) Amplitude along the black line in Figure 5.56.

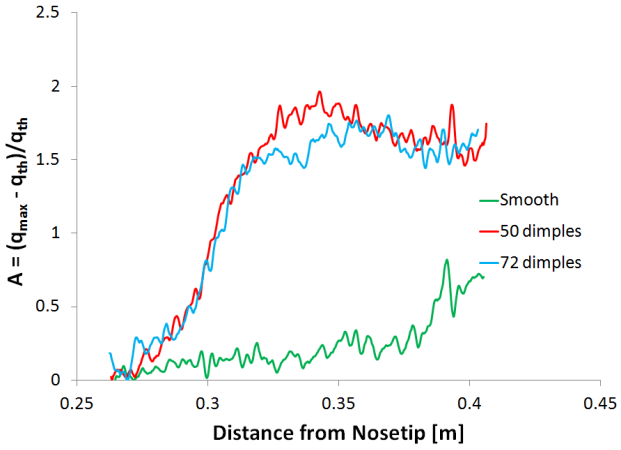

(c) Amplitude along the white line in Figure 5.56.

Figure 5.57.: Stationary vortex amplitude along white and black lines on the TSP images in Figure 5.28. Quiet flow, Re = 10.4×10^6/m.

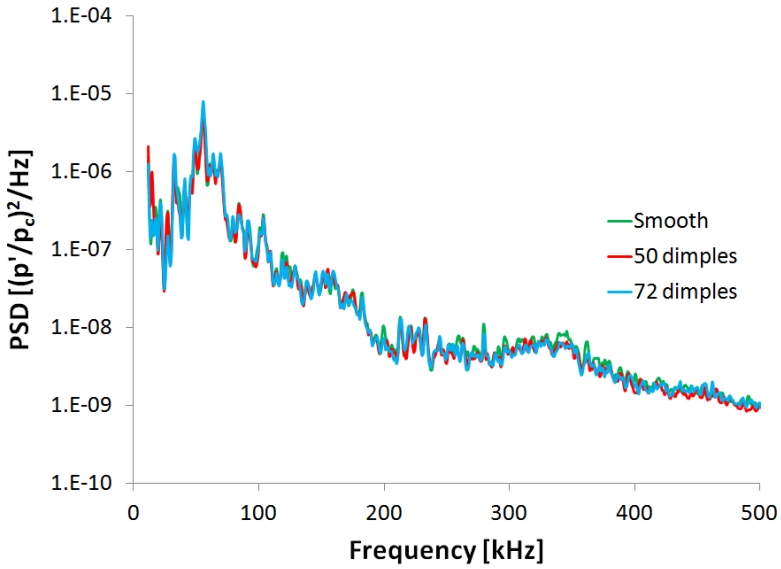

(a) x = 0.19 m. Circled in white in Figure 5.56.

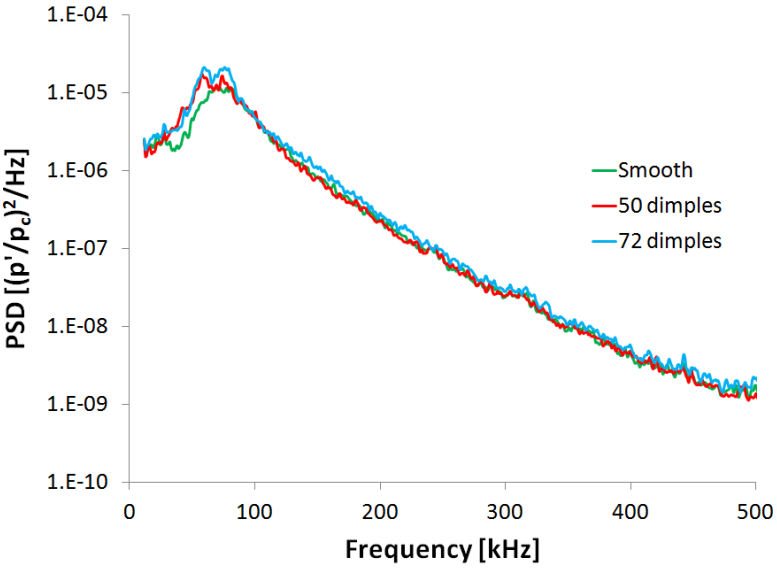

(b) x = 0.32 m. Circled in black in Figure 5.56.

Figure 5.58.: PSD of PCB 0.19 and 0.32 m from the nosetip on the lee ray of the cone. Quiet flow. Re = 10.4×10^6/m.

The same set of tests were then performed at a lower Reynolds number of 8.4×10^6/m. The TSP images are shown in Figure 5.59 with the lee side of the cone imaged under quiet flow. Qualitatively, the smooth and 72 dimple cases appear the same, with a single large amplitude stationary vortex, and several similar faintly visible vortices. The 50 dimple case shows the same large stationary vortex as the other two cases, but also generates two large vortices symmetric about the lee ray. It is possible that a patch of the paint contained a larger than typical roughness, producing the same large stationary vortex seen in the three cases. It is not known if this is the case.

Spanwise heat transfer profiles from the TSP images from Figure 5.59 at an axial location of 0.38 m are shown in Figure 5.60. All three cases show the large stationary vortex at 210°. For the most part, the smooth and 72-dimple profiles show very similar trends. It is possible that with the thicker boundary layer at lower Reynolds numbers the relatively small roughness of the 72-dimple case does not have a significant impact on the generation of the stationary vortices. Between 130° and 230°, the 50 dimple profile shows significant differences in stationary vortex location and amplitude. It is clear that the 50 dimple Torlon insert has a significant effect on the stationary vortices, while the 72 dimple insert may have roughness geometrical parameters that are too small to effectively generate stationary vortices.

Figure 5.61 is a reprint of the TSP images in Figure 5.59 with the sensor and axial profile locations shown. Figure 5.62 plots the amplitude of the stationary waves along the black and white lines in Figure 5.61. Along the black line, the TSP image showed what appeared to be a similar stationary vortex for all three cases. The amplitude plot shows a similar growth of this particular stationary wave. The wave does not grow large enough such that amplitude saturation is seen. Therefore it does not appear that this wave is breaking down to turbulence. Along the white line, only the 50-dimpled case is producing a large stationary vortex as seen in the TSP images. The plot of the wave amplitude also shows this. The 50-dimpled case is producing a large stationary vortex that saturates and begins to decay near 0.37 m from the

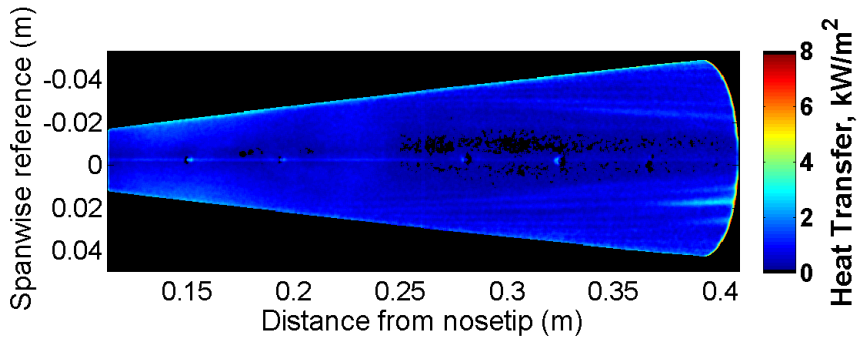

(a) Smooth (insert #1). $T_w = 301$ K.

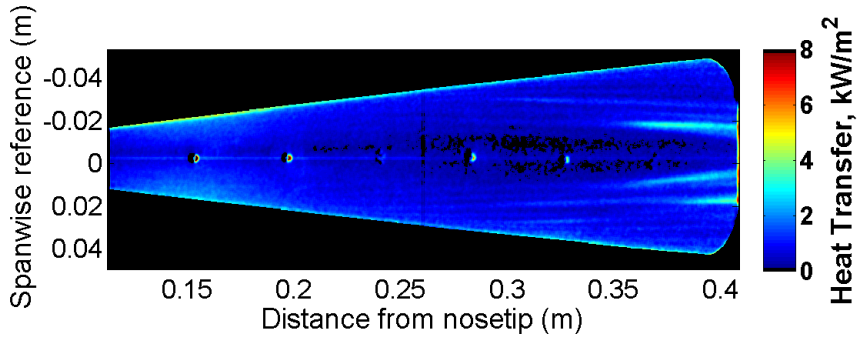

(b) 50 dimples (insert #2). $T_w = 300$ K.

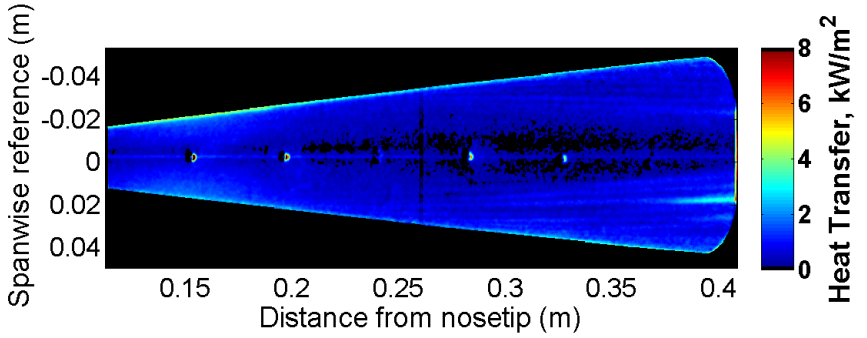

(c) 72 dimples (insert #6). $T_w = 302$ K.

Figure 5.59.: TSP images under quiet flow with smooth, 50-dimpled and 72-dimpled Torlon inserts. Lee side of the cone. Re $= 8.4\times10^6$/m, $p_0 = 109$ psia, $T_0 = 422$ K.

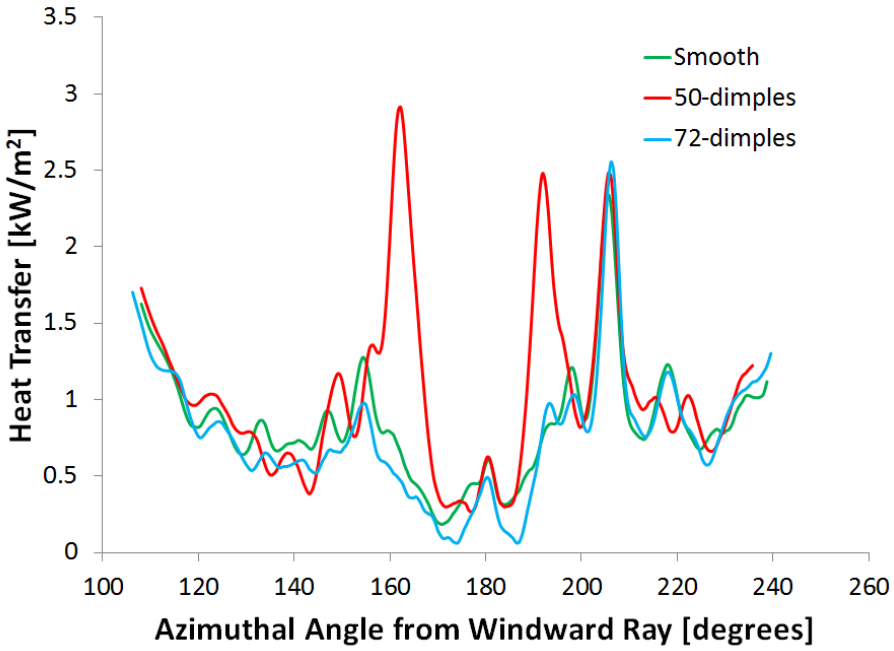

Figure 5.60.: Spanwise heat transfer profiles at an axial distance of 0.38 m from the nosetip of the TSP images in Figure 5.59. Quiet flow.

nosetip. The other two cases do not appear to be producing a stationary vortex at this location.

The PSD's of the PCB sensors 0.19 and 0.32 m from the nosetip on the lee ray are shown in Figure 5.63 for the three insert cases. The sensors are circled in Figure 5.61. At the two axial locations, the PCB spectra for all three inserts appear similar, agreeing with the TSP data. There is a peak in the spectra near 60 kHz that decreases in amplitude and frequency moving downstream. It is not known if the peak is caused by a lee-ray instability. There is no evidence in the TSP that a transitional or turbulent boundary layer is present near the downstream sensor.

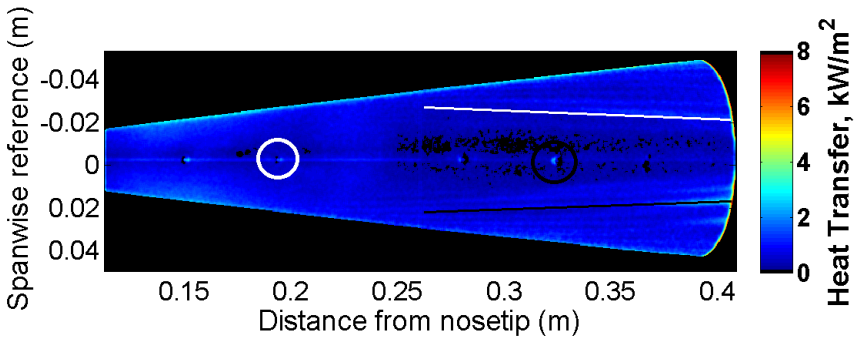

(a) Smooth (insert #1). $T_w = 301$ K.

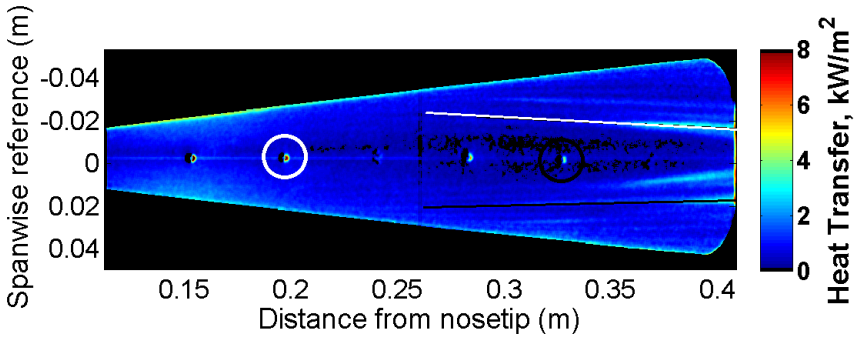

(b) 50 dimples (insert #2). $T_w = 300$ K.

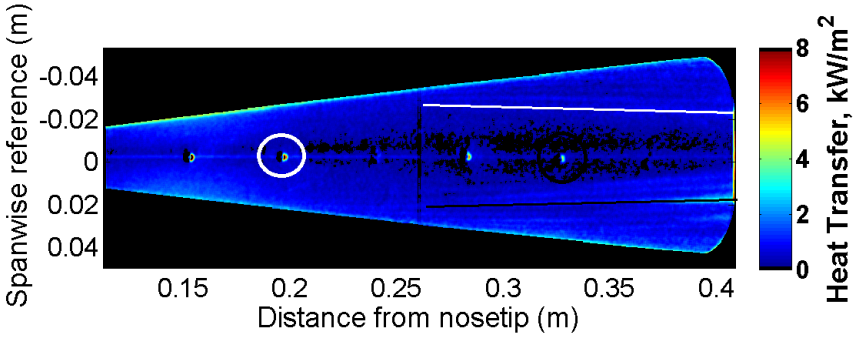

(c) 72 dimples (insert #6). $T_w = 302$ K.

Figure 5.61.: TSP images under quiet flow with smooth, 50-dimpled and 72-dimpled Torlon inserts. Lee side of the cone. Re $= 8.4\times10^6$/m, $p_0 = 109$ psia, $T_0 = 422$ K. Reprint of Figure 5.59, with sensor and axial profile locations shown.

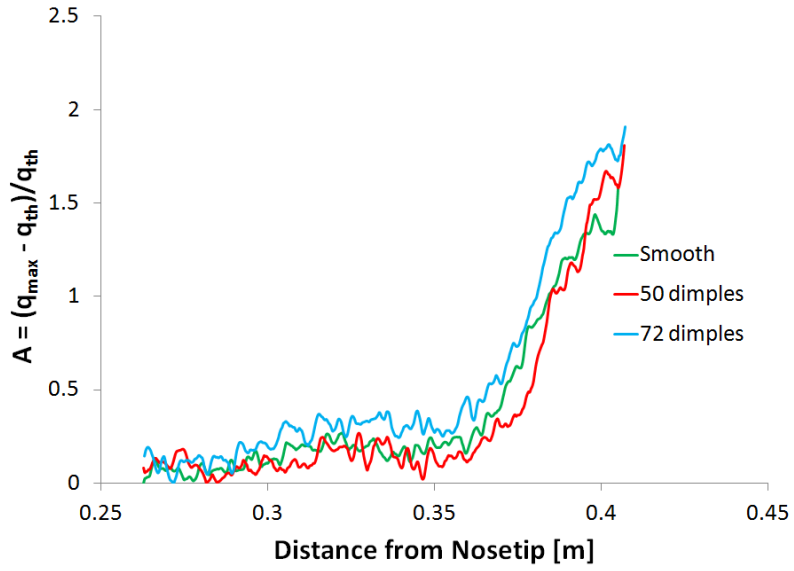

(a) Amplitude along the black line in Figure 5.61.

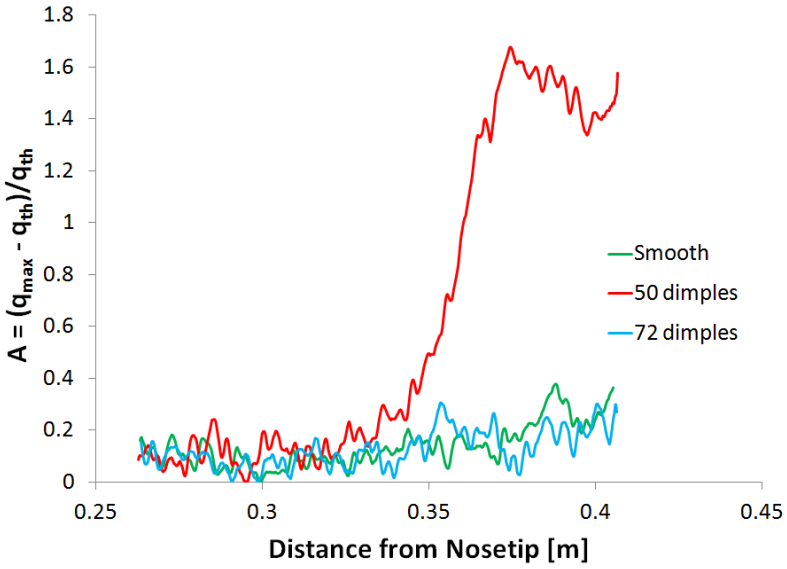

(b) Amplitude along the white line in Figure 5.61.

Figure 5.62.: Stationary vortex amplitude along white and black lines on the TSP images in Figure 5.28. Quiet flow, Re = 12.0×10^6/m.

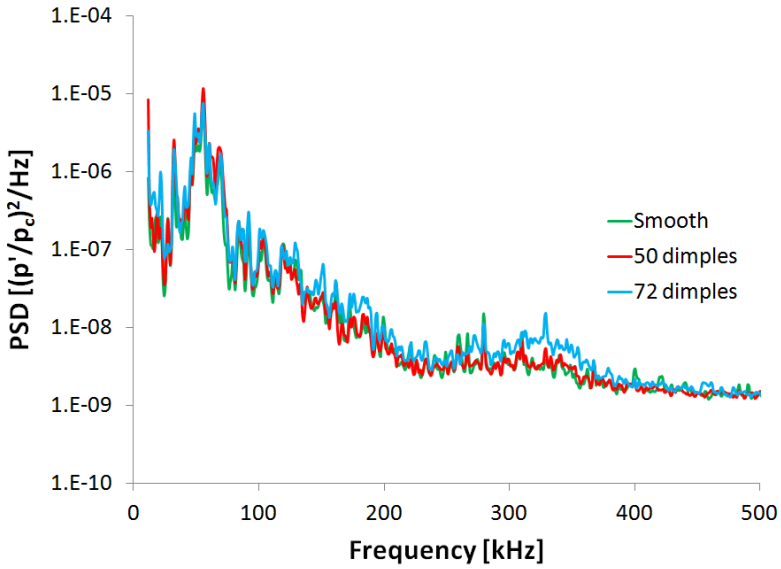

(a) x = 0.19 m. Circled in white in Figure 5.61.

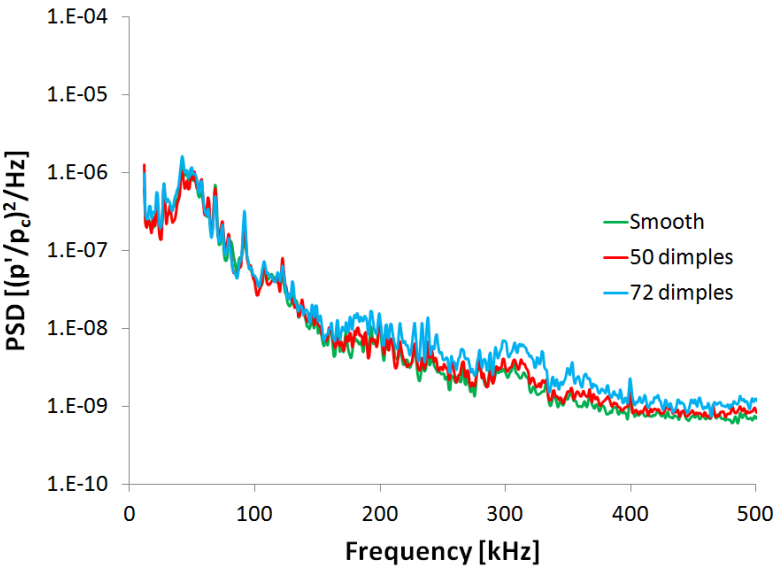

(b) x = 0.19 m. Circled in black in Figure 5.61.

Figure 5.63.: PSD of PCB 0.19 and 0.32 m from the nosetip on the lee ray of the cone. Quiet flow. Re = 8.4×10^6/m.

5.5.3 Effect of Random Roughness of TSP on Stationary Vortices

Sometimes between entries the TSP had to be repainted, typically because of photo-degradation. Each repainted surface had a similar RMS roughness, but the location of the random roughness varied from paint finish to paint finish. In order to determine if the roughness insert was still the dominating the generation of the stationary vortices when the random roughness was altered, tests were done under similar conditions with the same Torlon roughness insert (#4) but with two different paint finishes. Two runs with the smooth inserts were also performed. The TSP images for these four cases are shown in Figure 5.64. The two smooth cases show a very different pattern of stationary vortices. The second paint finish is inducing large stationary vortices that are breaking down to turbulence much further upstream than the first paint finish. It is quite clear that the random roughness on the cone is important in the generation of the stationary vortices. The two cases with the 50-dimpled Torlon insert appear to be similar. This is crucial, because it appears that the controlled roughness is dominating the generation of the stationary vortices.

Spanwise heat transfer profiles of the four cases are shown in Figure 5.65. Again, the two smooth cases shows a significantly different spanwise profile. The two 50-dimpled profiles are similar, but there are some differences, for example near 190° and 220°. Even though the controlled roughness elements appear to dominate the generation of the stationary vortices, there may be some interaction with the random roughness of the cone producing differences in the stationary vortex pattern and crossflow-induced transition.

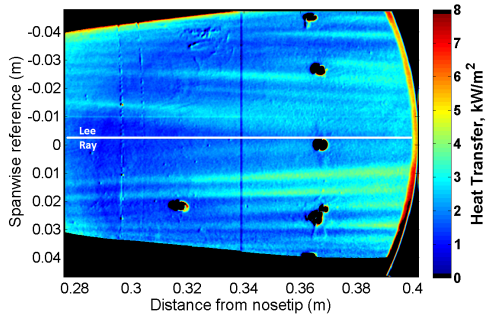

(a) Smooth. Paint Finish #1. $p_0 = 141$ psia, Re $= 10.8\times10^6$/m, $T_0 = 420$ K, $T_w = 303$ K

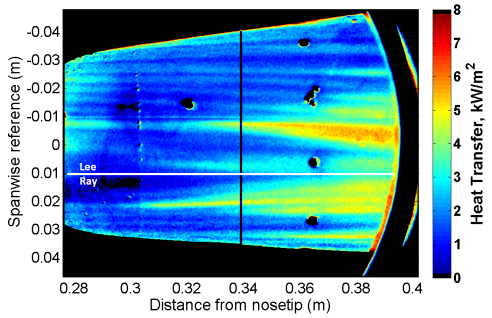

(b) Smooth. Paint Finish #2. $p_0 = 140$ psia, Re $= 10.7\times10^6$/m, $T_0 = 422$ K, $T_w = 301$ K

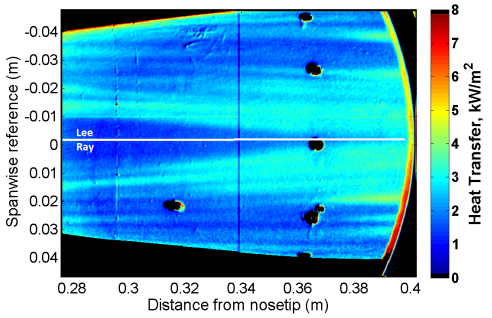

(c) 50 dimples (insert #4). Paint Finish #1. $p_0 = 139$ psia, Re $= 10.7\times10^6$/m, $T_0 = 422$ K, $T_w = 304$ K

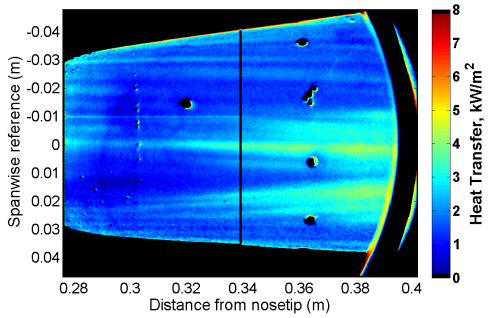

(d) 50 dimples (insert #4). Paint Finish #2. $p_0 = 140$ psia, Re $= 10.8\times10^6$/m, $T_0 = 419$ K, $T_w = 299$ K

Figure 5.64.: TSP images under quiet flow with smooth and 50-dimpled and two different paint finishes.

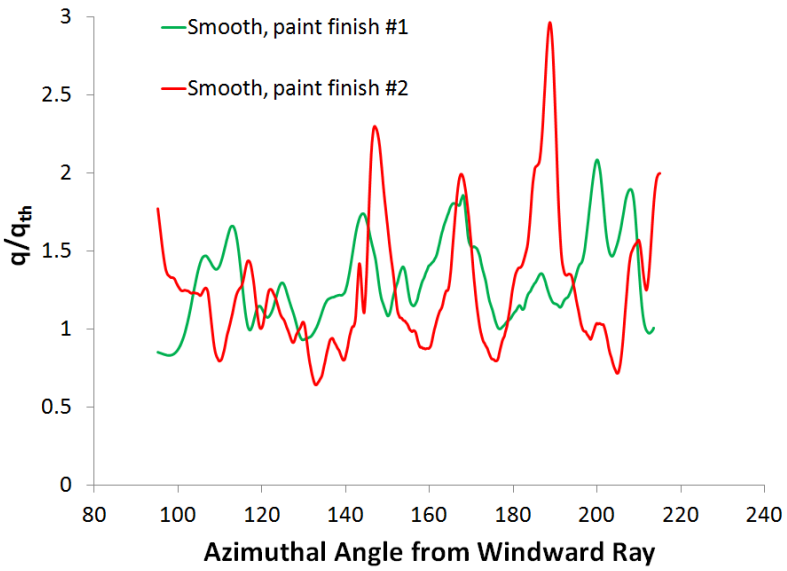

(a) Smooth, x = 0.31 m.

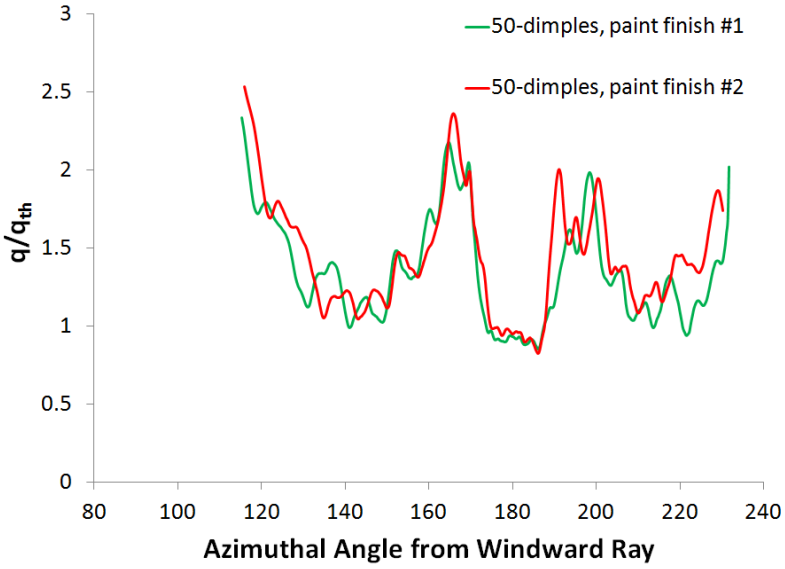

(b) 50-dimples, x = 0.33 m.

Figure 5.65.: Spanwise heat transfer profiles of the TSP images in Figure 5.64.

Body-Fixed Stationary Vortices

To further the argument that the stationary vortices are in fact being created by the roughness elements, the windward ray was rotated by 10°. If the stationary vortices roll with the cone, then they are body fixed and not fixed to the velocity vectors. A case with a 50-dimple insert (#2) is shown in Figure 5.66. The spanwise heat transfer profiles are plotted at an axial distance of 0.35 m. The sensor array was either on the leeward ray or rotated to the 170° ray. For the 50-dot case, the peaks and valleys of the stationary waves show good agreement. The discrepancies in heat transfer between the two tests is likely caused by slightly different tunnel conditions, model wall temperatures, or the different flowfield seen by the streaks when at an azimuth shifted by 10°.

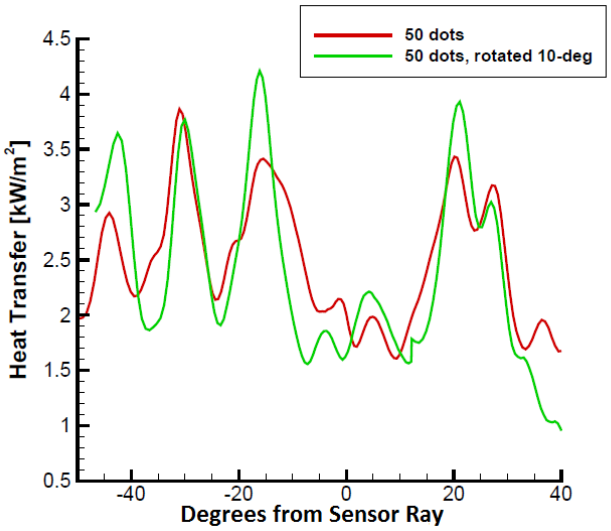

Figure 5.66.: Spanwise heat transfer profiles at an axial distance of 0.35 m. Quiet flow. 50 dimple Torlon insert (#2). Re = 10.7×10^6/m, p_0 = 149 psia, T_0 = 423 K.

The 72-dimpled insert (#6) was also tested to determine if the stationary vortices for this case are also body fixed. Spanwise heat transfer is plotted in Figure 5.67. As with the 50-dot case, the peaks and valleys of the stationary vortices agree well. Once again the discrepancies in heat transfer between the two tests is likely caused

by slightly different tunnel conditions, model wall temperatures, or the cone rotation. There is an additional vortex created by the initial run near 20° that is not present in the rotated case. The cause of this discrepancy is not known. Based on this data, it appears that the stationary vortices are fixed to the body and not the velocity vectors.

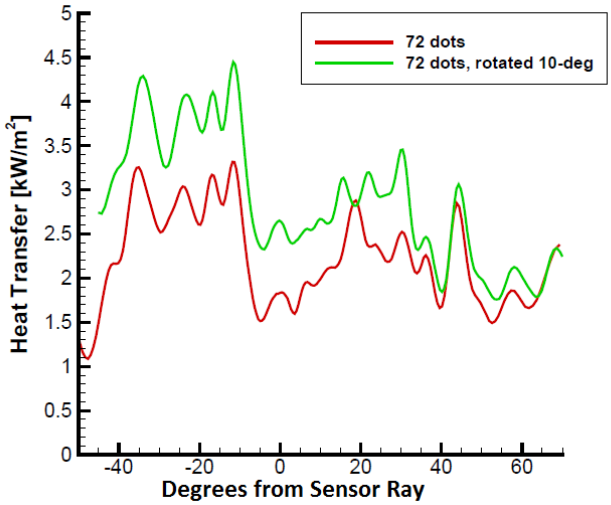

Figure 5.67.: Spanwise heat transfer profiles at an axial distance of 0.35 m. Quiet flow. 72 dimple Torlon insert (#6). Re = 10.5×10^6/m, p_0 = 149 psia, T_0 = 427 K.

Repeatability of Torlon Roughness Measurements

Three cases were tested (smooth, 50 and 72 dimples) twice at approximately the same Reynolds number to determine the repeatability of the measurements. For the smooth case, these two tests were performed back-to-back without opening the tunnel. For the 50 and 72 dimple cases, the tunnel was opened, the Torlon section was removed and reinstalled, and the repeat test was performed immediately after.

Figure 5.68 shows spanwise heat transfer or temperature profiles at an axial location of 0.35 m. For the smooth case, the two profiles are very similar. Note that for the 50-dimple case, the Schmidt-Boelter heat transfer gauge did not work for the re-

peat run, therefore the temperature is plotted instead of the heat transfer. The peaks and the valleys in the 50-dimple case profile appear to line up quite well. The repeat run shows higher overall temperatures, but this is likely due to the lower wall temperature of the model or slightly different tunnel conditions. Finally, the 72-dimple case shows decent repeatability. At 210°, there is an additional peak in the repeat case. It is not known why this peak does not appear in the original run. Overall, the three cases appear to create repeatable results.

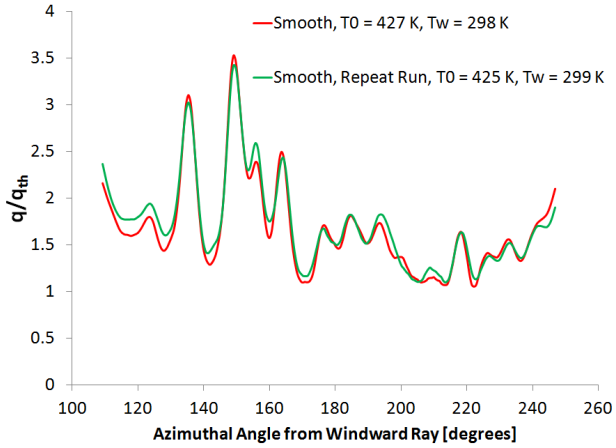

(a) Smooth.

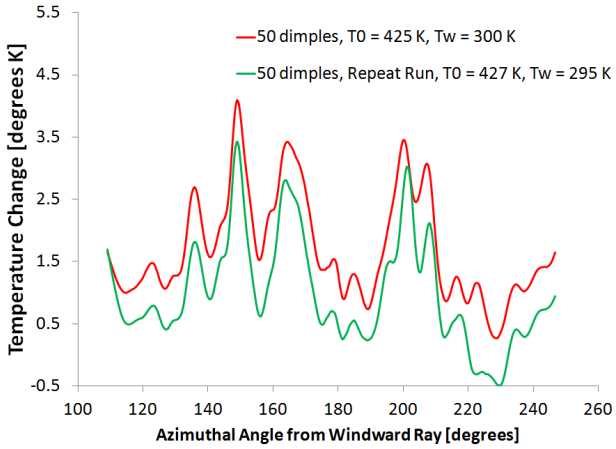

(b) 50 dimples insert (#2).

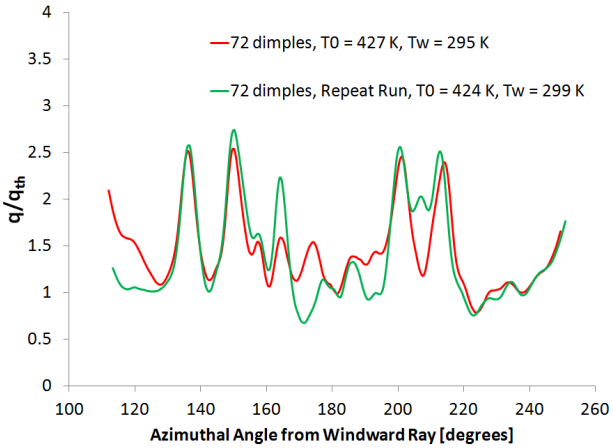

(c) 72 dimples insert (#6).

Figure 5.68.: Spanwise heat transfer and temperature profiles at an axial distance of 0.35 m. Re = 10.5×10^6/m. p_0 = 149 psia. T_0 = 426 K.

5.5.4 Effect of Altering Depth and Height of Dimple While Maintaining a Constant Diameter

Low Reynolds Number

Tests were done at varying Reynolds number with the smooth, 50-dimpled #4 and #5 Torlon inserts. Inserts #4 and #5 have the same nominal dimple diameter and D/λ (diameter of dimple divided by the wavelength of the forced stationary wave), but differ in dimple depth by approximately a factor of 2 (#4 has the deeper dimple). Therefore the portion of the material protruding from the surface is larger for the deeper dimpled insert. TSP images at the low Reynolds number (8.4×10^6/m) are shown in Figure 5.69. The lee side of the cone is imaged. For all three cases, the stationary vortices are readily visible. The deepest dimpled case (#4) produces the largest stationary vortices, especially near the -0.02 m reference location. The shallower dimpled case (#5) also produces larger stationary vortices compared to the smooth case, especially near the 0.0 m reference location, but not as large as the deeper dimpled case.

Spanwise heat transfer profiles of the TSP images in Figures 5.69 at an axial distance of 0.37 m are shown in Figure 5.70. At this low Reynolds number, the difference in the three profiles is clear, especially near 200° (spanwise reference -0.02 m) where the deeper dimpled case shows two large stationary vortices.

Figure 5.71 is a reprint of the TSP images in Figure 5.69 with the sensor and axial profile locations shown. Figure 5.72 plots the amplitude of the stationary waves along the black and white lines in Figure 5.71. Along the black line, all three cases show a similar initial growth of the stationary wave. The amplitude plot shows a similar growth of this particular stationary wave. Downstream of approximately 0.36 m, the two rough cases show an a more rapid growth of the stationary vortices, reaching a higher amplitude. It does not appear that the vortices are breaking down to turbulence. Along the white line, once again the three cases show a similar initial growth of the stationary vortices. Downstream of 0.36 m, the deeper roughness case

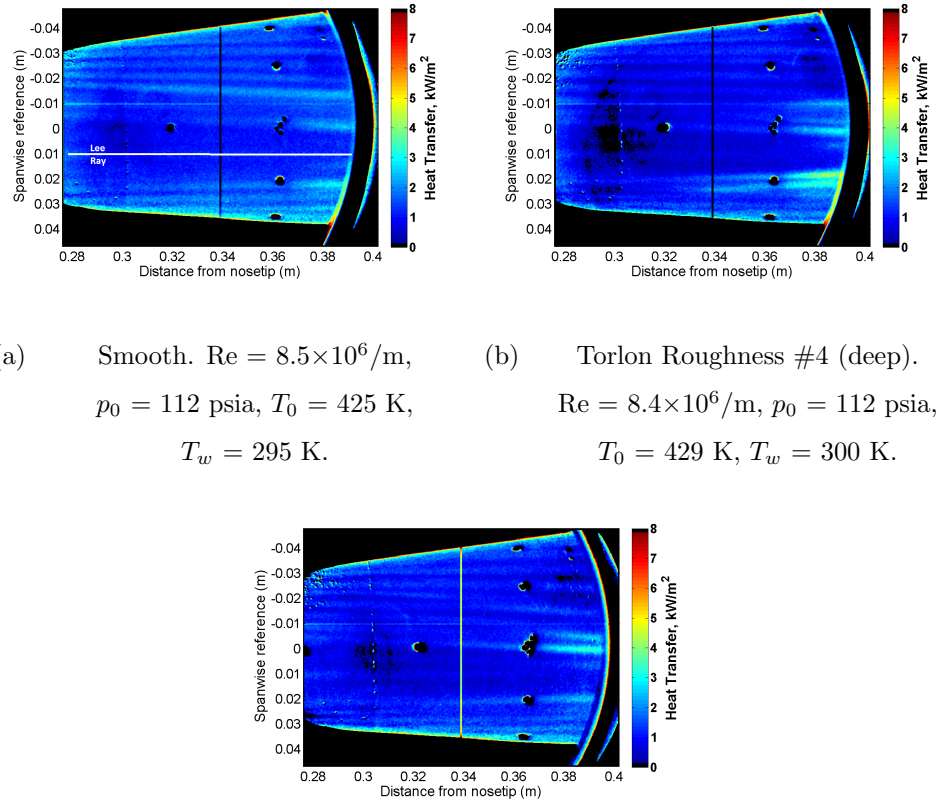

(a) Smooth. Re = 8.5×10^6/m, p_0 = 112 psia, T_0 = 425 K, T_w = 295 K.

(b) Torlon Roughness #4 (deep). Re = 8.4×10^6/m, p_0 = 112 psia, T_0 = 429 K, T_w = 300 K.

(c) Torlon Roughness #5 (shallow). Re = 8.3×10^6/m, p_0 = 113 psia, T_0 = 433 K, T_w = 297 K.

Figure 5.69.: TSP images under quiet flow with smooth and 50 dimple Torlon inserts with a constant dimple diameter. Reynolds number of approximately 8.4×10^6/m. Lee side of the cone imaged.

shows an increased growth rate and the stationary vortex reaches a larger amplitude. It appears that the depth of the dimple or the height of the protruding surface has a noticeable effect on the stationary vortices.

For the three cases the PSD's of pressure data from the PCB circled in white Figure 5.71, are shown in Figure 5.73(a). This sensor lies along the white line and is 0.36 m from the nosetip. For the smooth case, the PSD shows what appears to

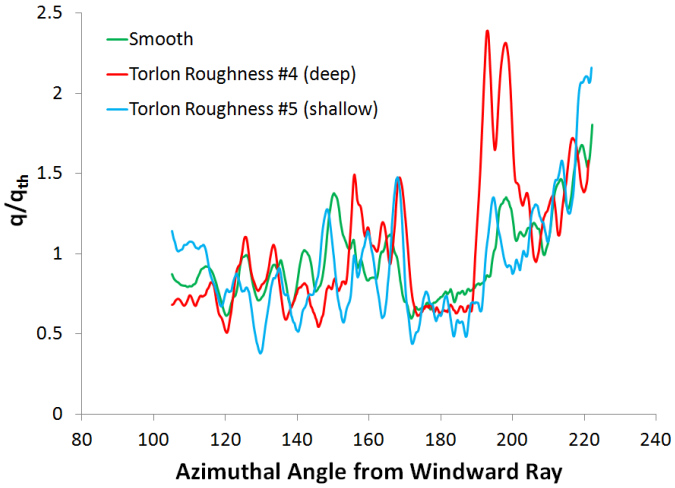

Figure 5.70.: Spanwise heat transfer profiles at an axial distance of x = 0.37 m for the TSP images in Figures 5.69. Quiet flow. Re = 8.4×10^6/m.

be a laminar boundary layer. When the shallow insert is used, there is a broadband increase in noise, suggesting that the boundary layer may be transitional. When the deep insert is used, the broadband noise increases further, and there is a peak near 200 kHz. This peak may be evidence of the secondary instability of the stationary waves, and will be discussed further in Chapter 8. The axial stationary-vortex amplitude profile in Figure 5.72(b) showed that when the deep insert was used, there was an increased growth rate near 0.36 m, and the PSD shows an increase in broadband noise. The RMS of the non-dimensional pressure fluctuations between 0 and 500 kHz for the smooth, deep and shallow cases are 0.0117, 0.0654 and 0.0119, respectively. It appears that for the deep case the boundary layer is transitional or turbulent near the sensor based on the significantly larger RMS value.

The PSD for the pressure data from the Kulite sensor 0.36 m from the nosetip along the 165° ray is shown in Figure 5.73(b). The Kulite sensor lies along the black ray. The axial stationary-vortex amplitude profile showed that all three cases produced a similar stationary vortex, and this agrees with the PSD data. All three cases show similar spectra. There is broad peak near 40 kHz. This may be caused

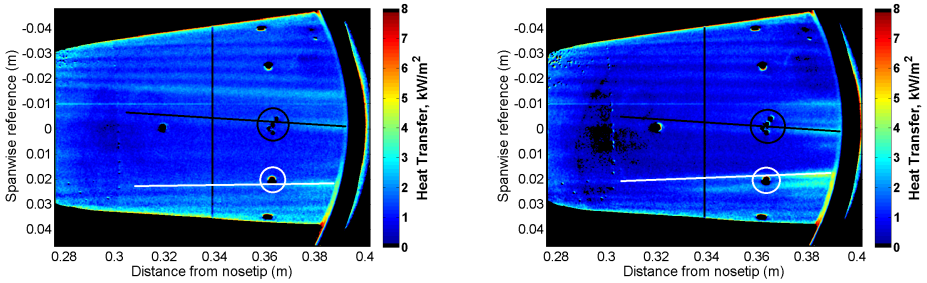

(a) Smooth. Re = 8.5×10^6/m, p_0 = 112 psia, T_0 = 425 K, T_w = 295 K.

(b) Torlon Roughness #4 (deep). Re = 8.4×10^6/m, p_0 = 112 psia, T_0 = 429 K, T_w = 300 K.

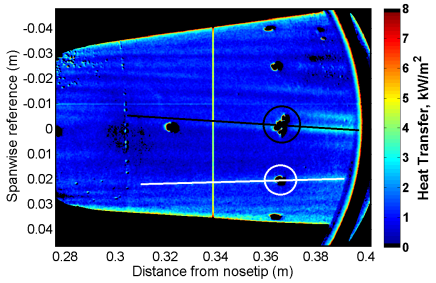

(c) Torlon Roughness #5 (shallow). Re = 8.3×10^6/m, p_0 = 113 psia, T_0 = 433 K, T_w = 297 K.

Figure 5.71.: TSP images under quiet flow with smooth and 50 dimple Torlon inserts with a constant dimple diameter. Reynolds number of approximately 8.4×10^6/m. Lee side of the cone imaged. Reprint of Figure 5.69, with sensor and axial profile locations shown.

by the primary travelling crossflow instability. The power levels in Figure 5.73(b) are similar to the PSD for the deep case in Figure 5.73(a), therefore it appears that the boundary layer is transitional for all three cases at the Kulite location.

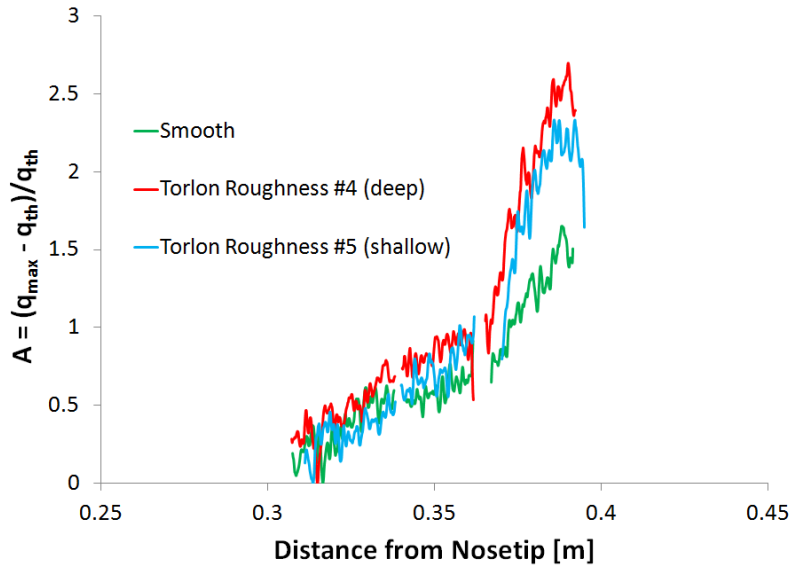

(a) Amplitude along the black line in Figure 5.71.

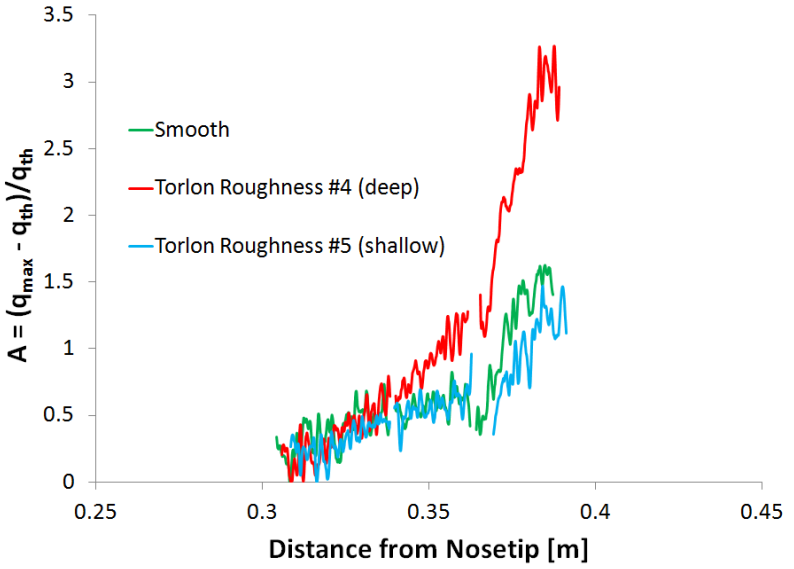

(b) Amplitude along the white line in Figure 5.71.

Figure 5.72.: Stationary vortex amplitude along white and black lines on the TSP images in Figure 5.71. Quiet flow, Re = 8.4×10^6/m.

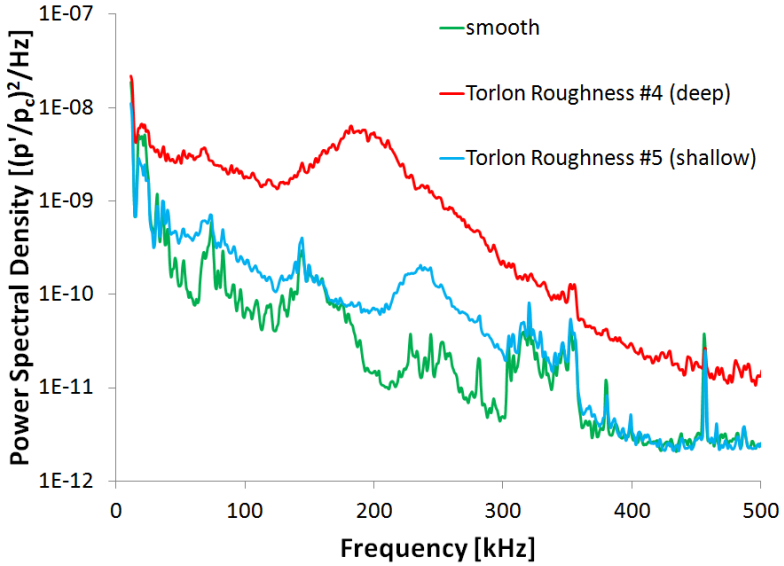

(a) PCB sensor. Azimuthal angle of 195°. Circled in white in Figure 5.71.

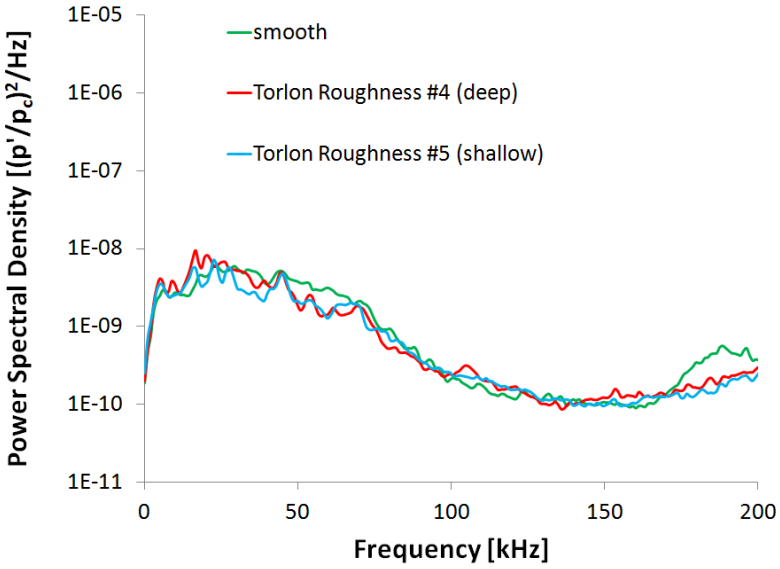

(b) Kulite sensor. Azimuthal angle of 165°. Circled in black in Figure 5.71.

Figure 5.73.: PSD of a PCB and Kulite sensor at an axial distance of x = 0.36 m with varying dimple depths. Quiet flow. Re = 8.4×10^6/m.

High Reynolds Number

The TSP images for the high Reynolds number case (10.4×10^6/m) are shown in Figure 5.74. Again there is a significant difference between the smooth and rough cases. The location of crossflow induced boundary-layer transition appears to have moved upstream for both rough cases as compared to the smooth case, based on the location where the vortices begin to spread and merge. The smooth case does have larger stationary vortices near the downstream end of the cone, but this is because the vortices have likely already begun to break down for the rough cases. There is also a difference between the two rough cases. Boundary layer transition appears to have moved upstream for the deeper dimpled case (#4). Looking at an axial distance of 0.33 m, the stationary vortices have begun to break down for the deeper dimpled case, but not for the shallow dimpled case. It is interesting that for these cases the roughness elements promote boundary-layer transition, while in Section 5.5.1 transition was delayed by the roughness elements. It is possible that the different dimple depth and height of protruding surface used in Section 5.5.1 worked to delay transition compared to the smooth case, or it is possible that the different random roughness of the TSP worked to promote transition compared to the rough insert case in Section 5.5.1.

Spanwise heat transfer profiles from the TSP images in Figures 5.74 at an axial distance of 0.33 m are shown in Figure 5.75. At this high Reynolds number, the effect of the roughness is a bit obscured. For example, at 140 and 165°, the smooth case produces fairly larger stationary vortices, compared to the rough cases. This might be due to the fact that the stationary vortices for the rough case are beginning to break down in this region.

Figure 5.76 is a reprint of the TSP images in Figure 5.74 but with the locations of sensors and axial heat transfer profiles shown. Figure 5.77 plots the amplitude of the stationary vortices along the white, red and pink lines in Figure 5.76. Along the white line, the TSP image showed the stationary waves growing larger with the smooth

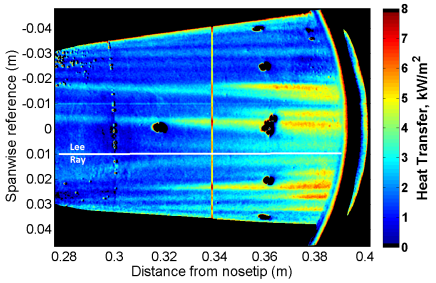

(a) Smooth. Re = 10.4×10^6/m, p_0 = 140 psia, T_0 = 428 K, T_w = 297 K.

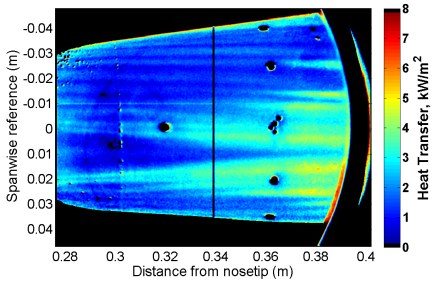

(b) Torlon Roughness #4 (deep). Re = 10.4×10^6/m, p_0 = 140 psia, T_0 = 428 K, T_w = 302 K.

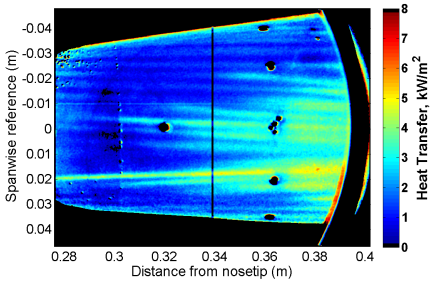

(c) Torlon Roughness #5 (shallow). Re = 10.4×10^6/m, p_0 = 140 psia, T_0 = 431 K, T_w = 300 K.

Figure 5.74.: TSP images under quiet flow with smooth and 50 dimple Torlon inserts with a constant dimple diameter. Reynolds number of 10.4×10^6/m. Lee side of the cone imaged.

insert, and possibly breaking down to turbulence when the rough inserts were used. The plot of the stationary wave amplitude appears to agree with this. The smooth case shows the stationary wave growing to a large amplitude, while the two rough cases show the stationary waves saturating near the downstream end of the cone. The deeper case reaches a slightly lower amplitude than the shallow case, possibly because

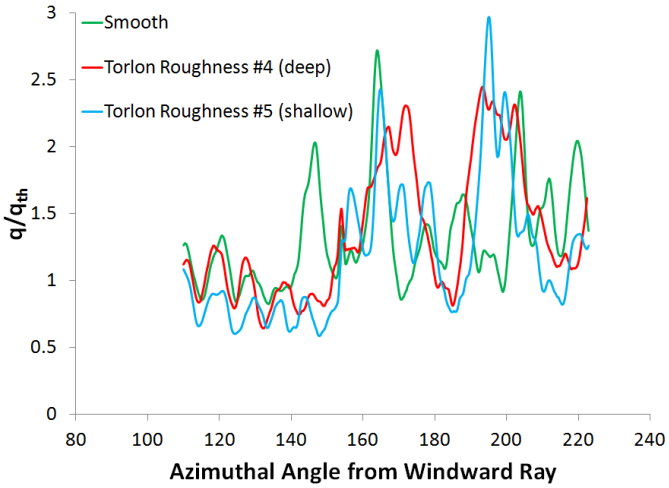

Figure 5.75.: Spanwise heat transfer profiles at an axial distance of x = 0.33 m for the TSP images in Figures 5.74. Quiet flow. Re = 10.4×10^6/m.

the stationary vortex for the deeper case is breaking down to turbulence earlier than the stationary vortex for the shallow case.

Along the red line, the two rough cases show the stationary waves to be at a much higher amplitude at the upstream end of the imaged area as compared to the smooth case. The smooth case shows a still growing stationary wave at the downstream end of the imaged area, while the two rough cases show a stationary wave that has saturated in growth and may be breaking down to turbulence. Along the pink line, the two rough cases show a similar stationary vortex growing to a similar amplitude. The smooth case produces a larger stationary vortex that grows to a larger amplitude. It appears that transition may depend on more than just the max local vortex amplitude.

A plot of the axial heat transfer divided by the laminar theoretical heat transfer can help discern the difference between the three cases. Axial non-dimensional heat transfer profiles along the red line in Figure 5.76 are shown in Figure 5.78 for the three cases. The red line is approximately 190° from the windward ray. For the smooth case, the measured heat transfer begins to depart from the theoretical laminar heat transfer at approximately 0.35 m from the nosetip, which likely corresponds to the

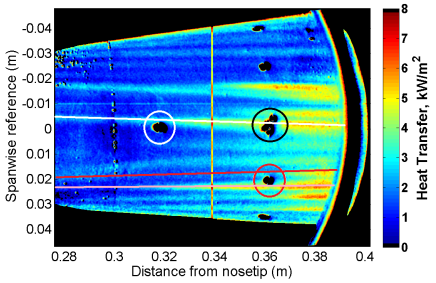

(a) Smooth. Re = 10.4×10^6/m, p_0 = 140 psia, T_0 = 428 K, T_w = 297 K.

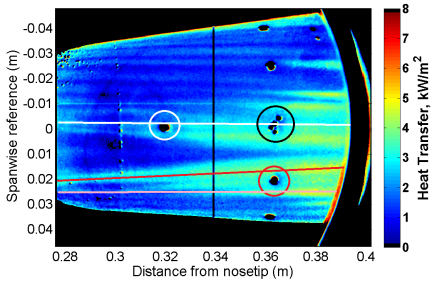

(b) Torlon Roughness #4 (deep). Re = 10.4×10^6/m, p_0 = 140 psia, T_0 = 428 K, T_w = 302 K.

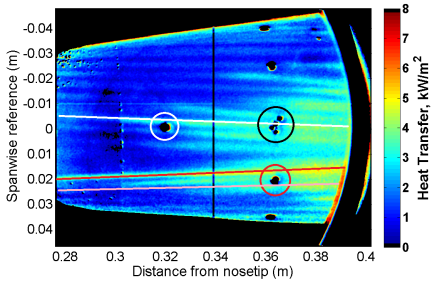

(c) Torlon Roughness #5 (shallow). Re = 10.4×10^6/m, p_0 = 140 psia, T_0 = 431 K, T_w = 300 K.

Figure 5.76.: Reprinting of TSP images in Figure 5.74 with sensor and axial cut locations denoted. Reynolds number of 10.4×10^6/m. Lee side of the cone imaged.

onset of transition. The onset of transition for the shallow-dimpled case (blue line) appears to occur near 0.3 m. The onset of transition for the deeper-dimpled case (red) appears to occur upstream of the imaged area.

The PSDs of the PCB sensor 0.32 m from the nosetip (circled in white Figure 5.76) for the three cases are shown in Figure 5.79. The sensor lies along the white line. As was seen in the TSP, the two rougher cases show a possibly turbulent or transitional boundary layer based on the increase in broadband noise compared to the smooth

case. Figure 5.77(a) showed the stationary vortex for the two rough profiles begin to saturate near the sensor's axial location of 0.32 m. The shallow case shows a broad peak near 275 kHz, which once again may correspond to the secondary instability of the stationary waves (discussed in Chapter 8). The peak near 275 kHz is no longer seen for the deeper roughness case, suggesting that the boundary layer may be further along in the transition process. The RMS of the non-dimensional pressure between 0 and 500 kHz for the smooth, deep and shallow cases are 0.188, 0.239 and 0.207, respectively.

The PSDs of the Kulite sensor 0.36 m from the nosetip (circled in black Figure 5.76) for the three cases are shown in Figure 5.80. This sensor also lies along the white line. At this downstream location, all three spectra are similar, suggesting that the boundary layer has begun to transition to turbulence for all three cases. The two cases with the roughness show an increase in power at low frequencies. It is not clear what is causing the increase in power at the low frequencies. The smooth case also shows a broad peak near 40 kHz. This may correspond to the travelling crossflow waves, suggesting that the boundary layer process for the smooth case is not as far along as it is for the two rough cases.

The PSD of the PCB sensor 195° from the windward ray, 0.36 m from the nosetip (circled in red in Figure 5.81). The sensor lies approximately on the red line. Figure 5.77(b) showed that the stationary vortex for the two rough cases had already begin to saturate at the sensor location of 0.36 m, while the stationary vortex for the smooth case was still growing. In the PSD, the two rough cases show an increase in broadband noise compared to the smooth case, suggesting that the boundary layer is turbulent, agreeing with the axial profile (Figure 5.78) and the stationary wave growth (Figure 5.77(b)) along the 190° ray. The axial profile for the smooth case at 0.36 m shows an increase in heat transfer from the laminar theoretical value, but still lower than the two rough cases. The PSD of the sensor at 0.36 m for the smooth case shows a peak near 40 kHz, likely caused by the travelling crossflow instability, and it appears that the boundary layer has not yet broken down to turbulence. The

RMS of the non-dimensional pressure between 0 and 500 kHz for the smooth, deep and shallow cases are 0.205, 0.284 and 0.276, respectively.

Based on this data showing the effect of a constant dimple diameter and a constant D/λ parameter with a varying dimple depth, it appears that D/λ cannot be solely used to determine the effectiveness of the roughness element for these cases. The raised up portion of the roughness element appears to be significant. Perhaps the effective dimple diameter should include the protruding portion. More research is needed with various roughness shapes.

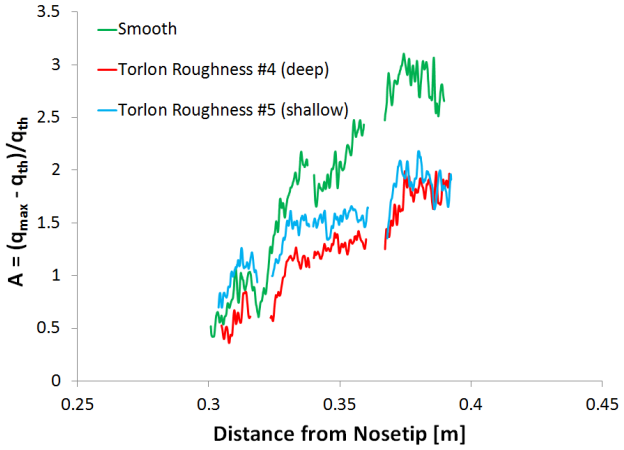

(a) Amplitude along the white line in Figure 5.76.

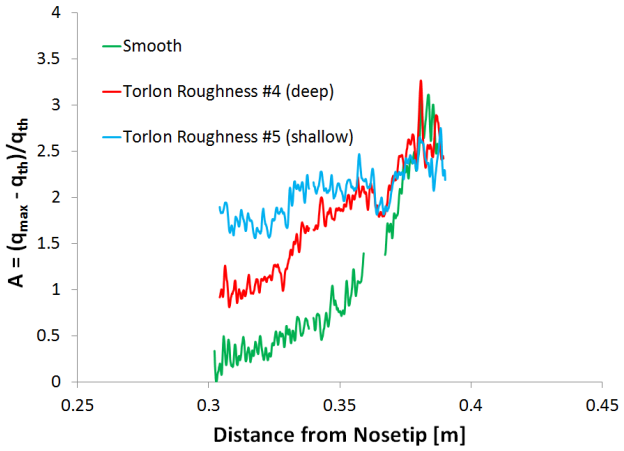

(b) Amplitude along the red line in Figure 5.76.

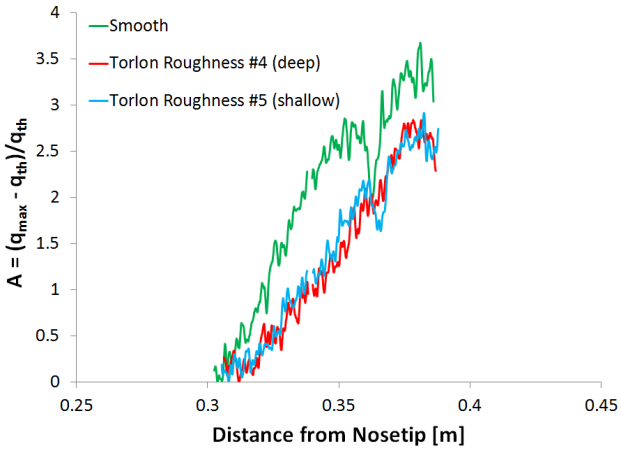

(c) Amplitude along the pink line in Figure 5.76.

Figure 5.77.: Stationary vortex amplitude along white, red and pink lines on the TSP images in Figure 5.76. Quiet flow, Re = 10.4×10^6/m.

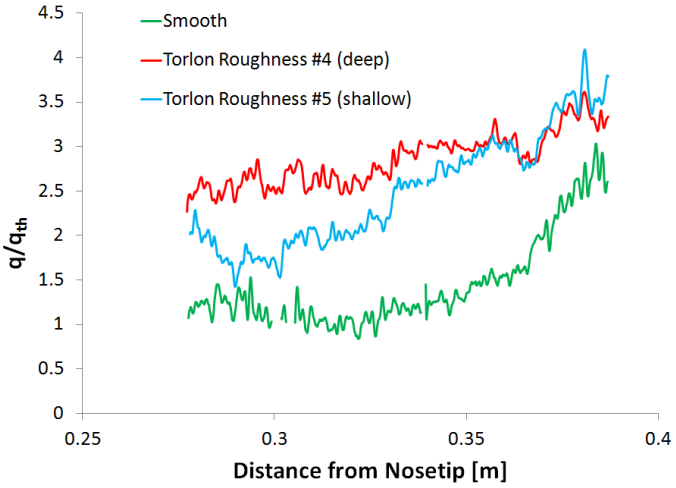

Figure 5.78.: Axial heat transfer profiles along the red line for the TSP images in Figure 5.74. 190° from the windward ray. Quiet flow. Re = 10.4×10^6/m.

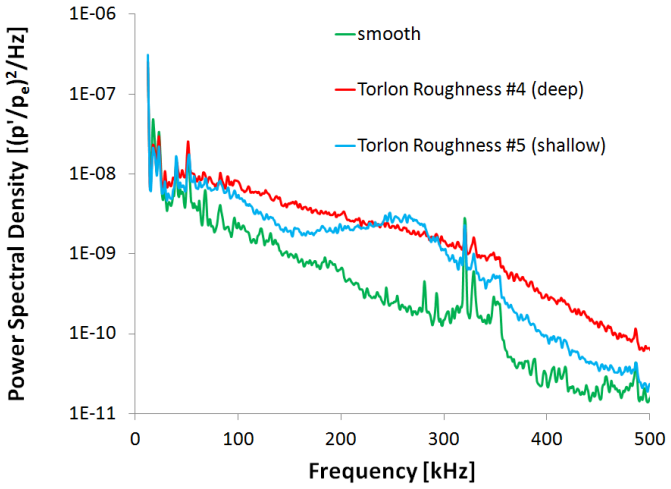

Figure 5.79.: PSD of PCB sensor at an axial distance of x = 0.32 m (circled in white in Figure 5.76) at an azimuthal angle of 165° with varying dimple depths. Quiet flow. Re = 10.4×10^6/m.

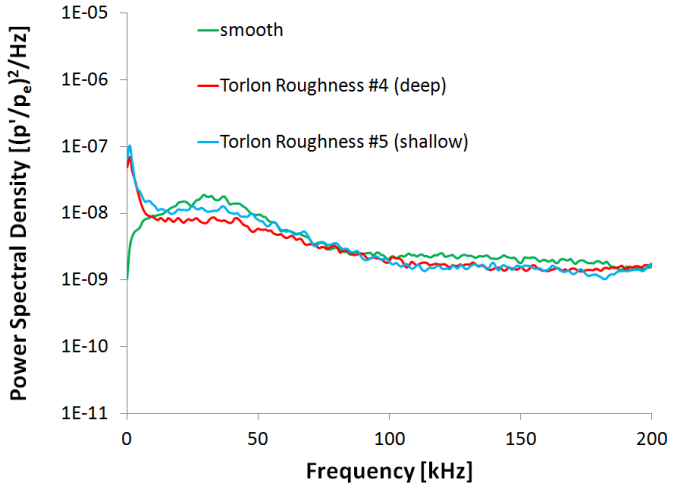

Figure 5.80.: PSD of Kulite sensor at an axial distance of x = 0.36 m (circled in black in Figure 5.76) at an azimuthal angle of 165° with varying dimple depths. Quiet flow. Re = 10.4×10^6/m.

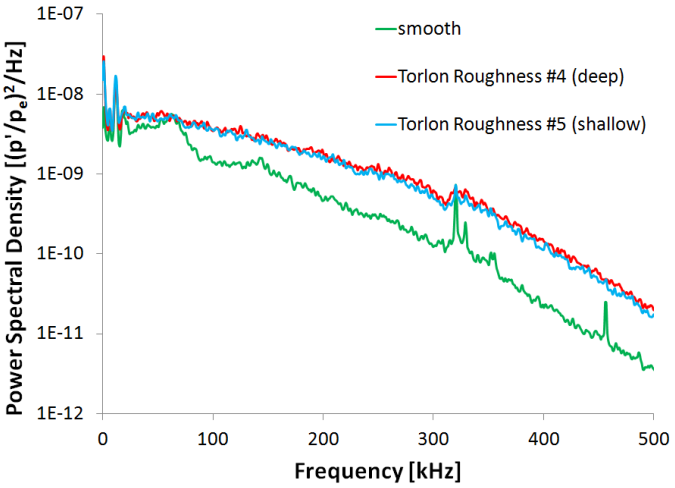

Figure 5.81.: PSD of PCB sensor at an axial distance of x = 0.36 m (circled in red in Figure 5.76) at an azimuthal angle of 195° with varying dimple depths. Quiet flow. Re = 10.4×10^6/m.

5.5.5 Effect of Roughness Elements Under Noisy Flow

According to low speed experiments and theory [16], the stationary crossflow waves are sensitive to surface roughness and dominate transition for low-turbulence environments, and travelling crossflow waves are sensitive to freestream turbulence and dominate transition in high-turbulence environments. Therefore, at low speeds it might be expected that altering the roughness on a model in a high-disturbance environment would not have a significant effect on crossflow-induced boundary-layer transition since the travelling mode would be the dominant mode and is not particularly sensitive to roughness.

To show if the low-speed expectation might hold at high speeds, tests were done with three different roughness inserts (smooth, 50 and 72 dimples) under noisy flow at approximately the same Reynolds number. TSP images at a Reynolds number of approximately 11.0×10^6/m are shown in Figure 5.82. Regardless of which roughness insert is tested, the onset of transition on the lee ray appears to be occurring at the same location (upstream of 0.1 m from the nosetip). It is possible that transition in this case is not due to the crossflow instability but due to some other lee ray instability. The mechanism that is causing transition in this case does not appear to be sensitive to the controlled roughness near the nosetip.

Axial heat transfer profiles along the lee ray for the TSP images in Figure 5.82 are shown in Figure 5.83. Transition appears to occur near the nosetip along the 180° ray. At an axial distance of 0.17 m the onset of turbulence appears to occur, where a peak in heat transfer occurs. Downstream of this location, the heat transfer decreases due to the thickening turbulent boundary layer. There is a second peak in heat transfer near 0.37 m. This may be caused by boundary-layer transition that begun near the 90° ray and has propagated towards the lee ray.

Tests were then performed with the yaw side of the cone imaged at a Reynolds number of 8.1×10^6/m (Figure 5.84) with both the smooth and 50-dimpled insert

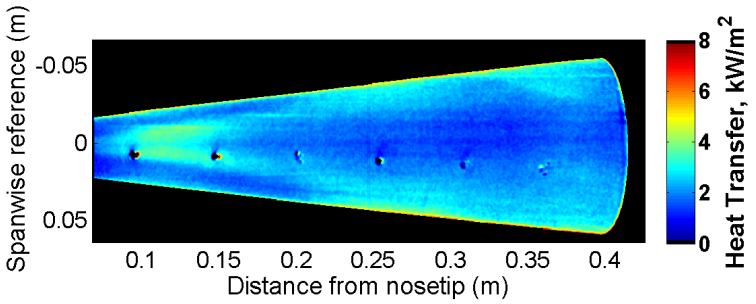

(a) Smooth. $p_0 = 139$ psia, Re $= 10.9\times10^6$/m, $T_0 = 433$ K, $T_w = 303$ K.

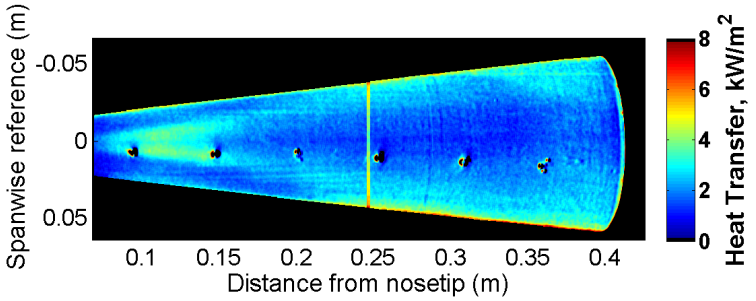

(b) 50 dimples (#4). $p_0 = 140$ psia, Re $= 11.1\times10^6$/m, $T_0 = 432$ K, $T_w = 303$ K.

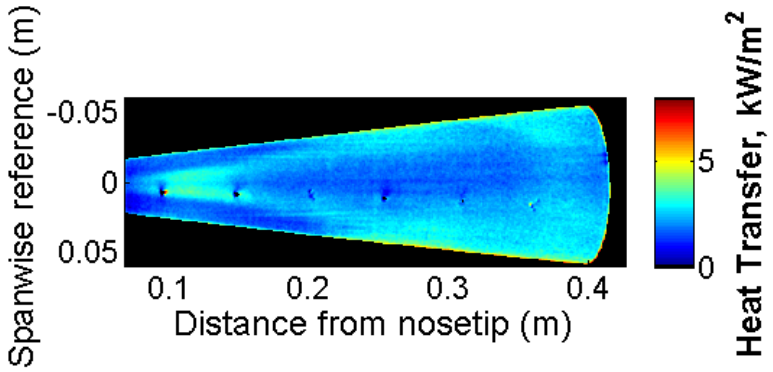

(c) 72 dimples (#6). $p_0 = 139$ psia, Re $= 11.1\times10^6$/m, $T_0 = 428$ K, $T_w = 298$ K.

Figure 5.82.: TSP images under noisy flow with smooth, 50-dimpled and 72-dimpled Torlon inserts. Lee side of the cone.

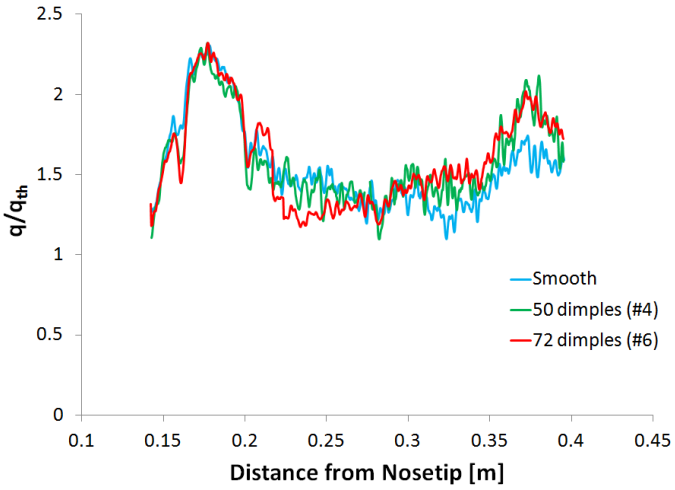

Figure 5.83.: Axial heat transfer profiles at an azimuthal angle of 180° for the TSP images in Figures 5.82. Noisy flow. Re = 11.1×10^6/m.

under noisy flow. At this Reynolds number the boundary layer appears to be laminar with the smooth insert. Adding roughness does not appear to have any effect.

Axial heat transfer profiles of the two noisy cases in Figure 5.84 at an azimuthal angle of 75 and 105° are shown in Figure 5.85. Again, it can be seen that the roughness is having a minimal effect on the surface heat transfer. For both roughness cases on both rays, transition appears to begin near 0.35 m from the nosetip, based on the increase in heat transfer from the theoretical laminar level.

Power spectral densities of PCB sensors 0.19 m from the nosetip (upstream of the imaged area) and 0.32 m from the nosetip (circled in white in Figure 5.84) and a Kulite sensor 0.36 m from the nosetip (circled in black in Figure 5.84) for the smooth and 50 dimple cases are shown in Figure 5.86. The sensors are at an azimuthal angle of 90° and under noisy flow with an approximate Reynolds number of 8.1×10^6/m. At 0.32 m and 0.36 m from the nosetip, the rough case produces a PSD with slightly higher power at higher frequencies. It is not known if this increase in power is caused by the roughness or slightly differing tunnel conditions. The two downstream lo-

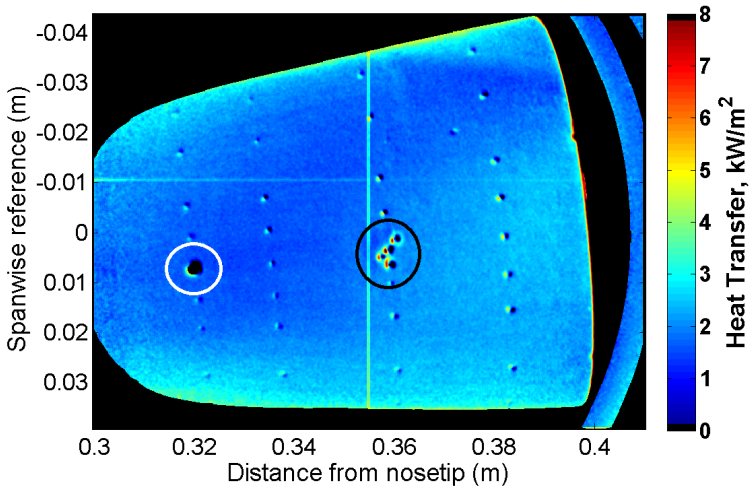

(a) Smooth. $p_0 = 98$ psia, Re $= 8.1\times10^6$/m, $T_0 = 423$ K. $T_w = 306$ K.

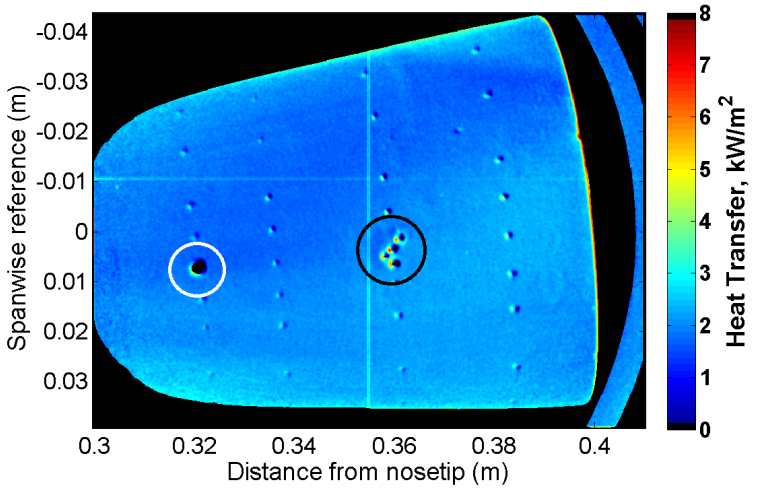

(b) 50 dimples (#4). $p_0 = 98$ psia, Re $= 8.1\times10^6$/m, $T_0 = 421$ K. $T_w = 311$ K.

Figure 5.84.: TSP images under noisy flow with smooth and 50-dimpled Torlon inserts. Yaw side of the cone. Sensors along the 790° ray.

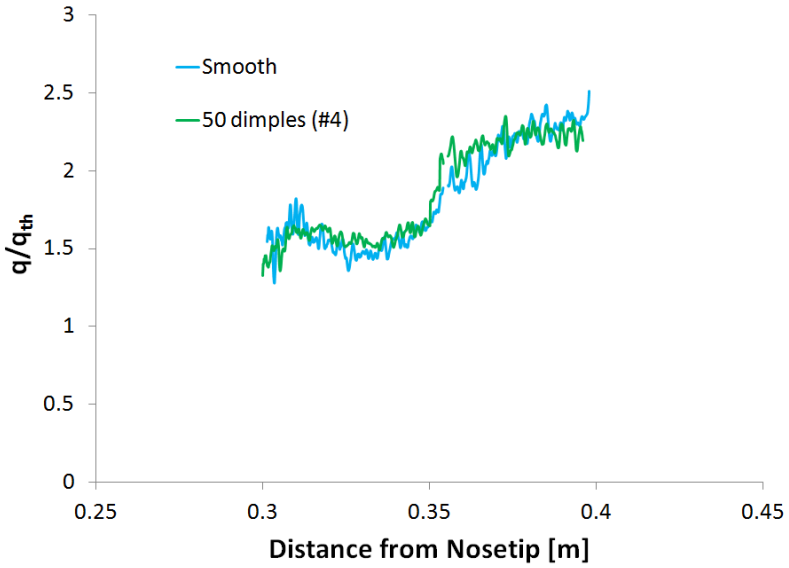

(a) $\phi = 105°$.

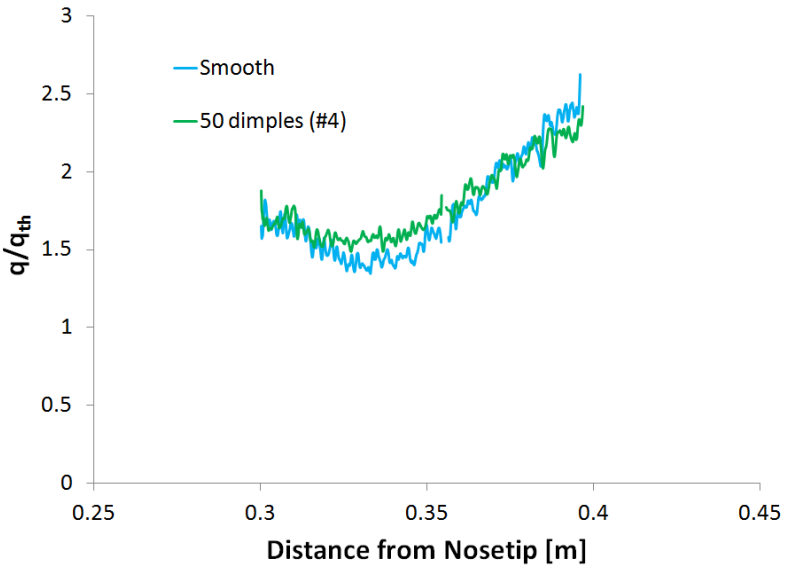

(b) $\phi = 75°$.

Figure 5.85.: Axial heat transfer profiles for the TSP images in Figures 5.84. Noisy flow. Re = 8.1×10^6/m.

cations show a peak near 40 kHz. This may be caused by the primary travelling crossflow instability, and will be discussed in further detail in Chapter 6.

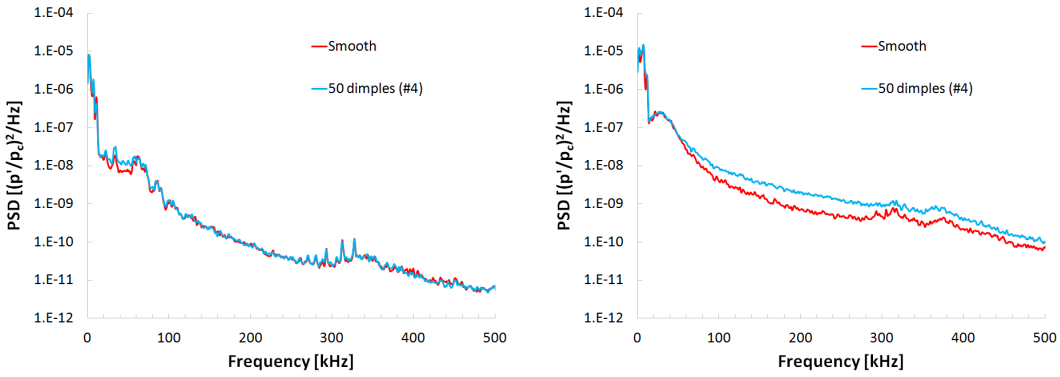

(a) PCB sensor, 0.19 m from the nosetip.

(b) PCB sensor, 0.32 m from the nosetip. Circled in white in Figure 5.84.

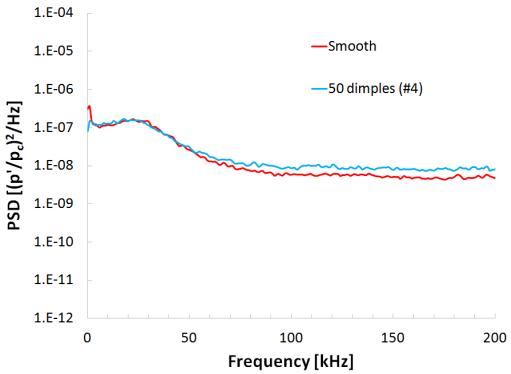

(c) Kulite sensor, 0.36 m from the nosetip. Circled in black in Figure 5.84.

Figure 5.86.: PSD of Kulite and PCB pressure data at an azimuthal angle of 90° under noisy flow with smooth and 50-dimpled Torlon inserts. Re = 8.1×10^6/m.

Tests were also performed at a higher Reynolds number of 10.6×10^6/m with the yaw side of the cone imaged under noisy flow. The TSP images with both the smooth and rough inserts are shown in Figure 5.87. At the higher Reynolds number (Figure 5.87), the boundary layer appears to be transitioning on the 90° ray just upstream of the imaged area. The transition on the 90° ray may be due to the crossflow instability. When the roughness is added, the heat transfer appears to be slightly affected.

Figure 5.88 plots the axial heat transfer profiles at an azimuthal angle of 105° and 75° for the TSP images in Figure 5.87. At 105° from the windward ray, boundary-layer

transition appears to have begun upstream of the imaged area for both cases. The decrease in heat transfer is likely due to the thickening of the turbulent boundary layer. At 75° from the windward ray, the smooth case shows a constant non-dimensional heat transfer rate. Note that a constant non-dimensional heat transfer rate corresponds to a decreasing wall heat transfer rate in the axial distance because the theoretical heat transfer also decreases with an increasing axial distance. The rough case shows a higher heat transfer rate from 0.3 m to 0.35 m from the nosetip. This may suggest that boundary layer transition begins later for the rough case, as the smooth case already shows a fully turbulent boundary layer along the 75° ray. Or it is possible that the rough case is showing a transitional overshoot in heat transfer.

Power spectral densities of PCB sensors 0.19 m from the nosetip (upstream of the imaged area) and 0.32 m from the nosetip (circled in white in Figure 5.88) and a Kulite sensor 0.36 m from the nosetip (circled in black in Figure 5.88) for the smooth and 50 dimple cases are shown in Figure 5.89. The sensors are at an azimuthal angle of 90° and under noisy flow with an approximate Reynolds number of 10.7×10^6/m. Along the 90° ray, the PSDs for the smooth and rough case are similar. At the furthest upstream sensor, a low-frequency peak is seen near 40 kHz, again possibly caused by the travelling crossflow instability. At the two downstream locations, the boundary layer appears to be turbulent, based on the increase in broadband noise. Along the 90° ray, the roughness does not appear to have a significant effect on boundary-layer transition under noisy flow.

One final case was investigated, at a Reynolds number of 11.3×10^6/m, using the large rectangular window allowing for more of the cone to be imaged. Both the smooth and the 50 dimple Torlon inserts were used. The TSP images are shown in Figure 5.90. The sensor ray is along the 90° ray. The two TSP images appear to be similar, with transition occurring at a similar location on the 90° ray.

Axial heat transfer profiles for the TSP images in Figure 5.90 are shown in Figure 5.91. The profiles were taken along the 70 and 110° ray. Along both rays, the smooth and rough axial profiles are quite similar. There is an initial peak of heat

transfer near 0.15 m from the nosetip. This initial peak in heat transfer may be spurious because the TSP layer is thin in the upstream region. The increase in heat transfer seen at 0.24 m from the nosetip on the 110° ray and 0.27 m from the nosetip on the 80° ray appears to be the onset of transition. Transition is occurring further downstream on the 80° ray than the 110° ray.

Power spectral densities of the two PCB sensors circled in Figure 5.90 with both the smooth and 50 dimple inserts are shown in Figure 5.92. Again, the roughness does not appear to have any effect on the boundary layer under noisy flow. At the upstream location, the two PSDs show a peak in the spectra near 50 kHz, which may be caused by the primary travelling crossflow instability. At the downstream location, the two PSDs show an increase in broadband noise suggesting that the boundary-layer has transitioned to turbulence. This agrees with the axial heat transfer profiles. If transition near the 90° ray is due to crossflow, it might be expected that the travelling mode is the dominant mode based on low speed work, and the travelling mode tends to not be as sensitive to roughness as the stationary mode. The TSP images here show that under noisy flow the mechanisms that cause transition on the yaw and lee ray do not appear to be particularly sensitive to roughness near the nosetip.

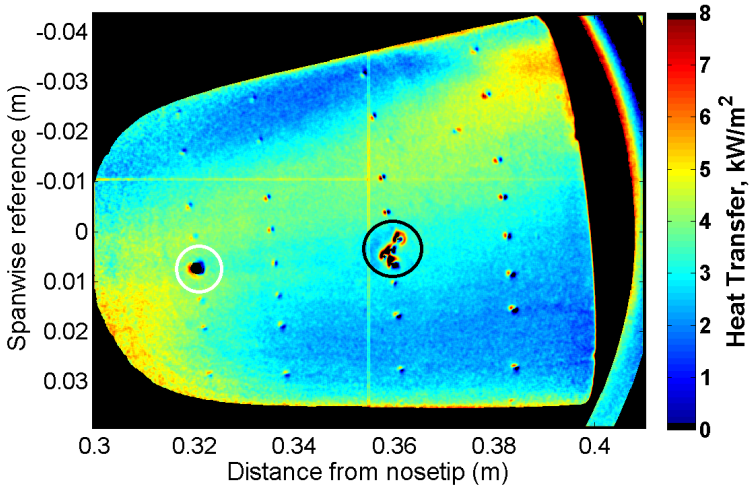

(a) Smooth. $p_0 = 130$ psia, Re $= 10.6\times10^6$/m, $T_0 = 425$ K. $T_w = 304$ K.

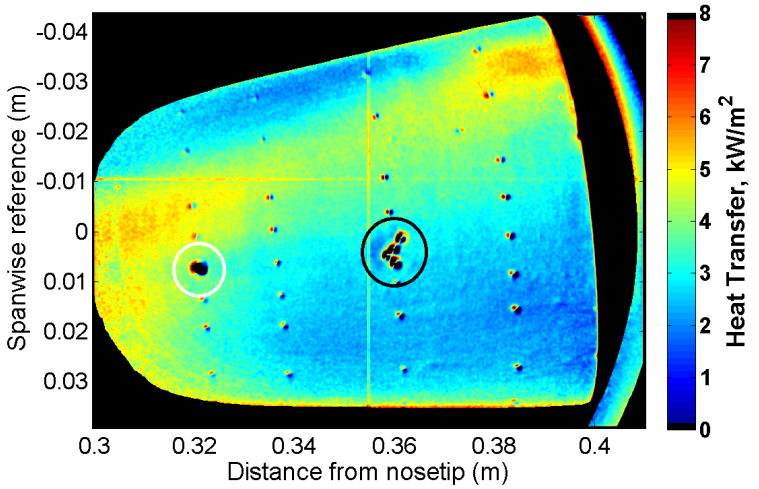

(b) 50 dimples (#4). $p_0 = 131$ psia, Re $= 10.7\times10^6$/m, $T_0 = 423$ K. $T_w = 305$ K.

Figure 5.87.: TSP images under noisy flow with smooth and 50-dimpled Torlon inserts. Yaw side of the cone. Sensors along the 90° ray.

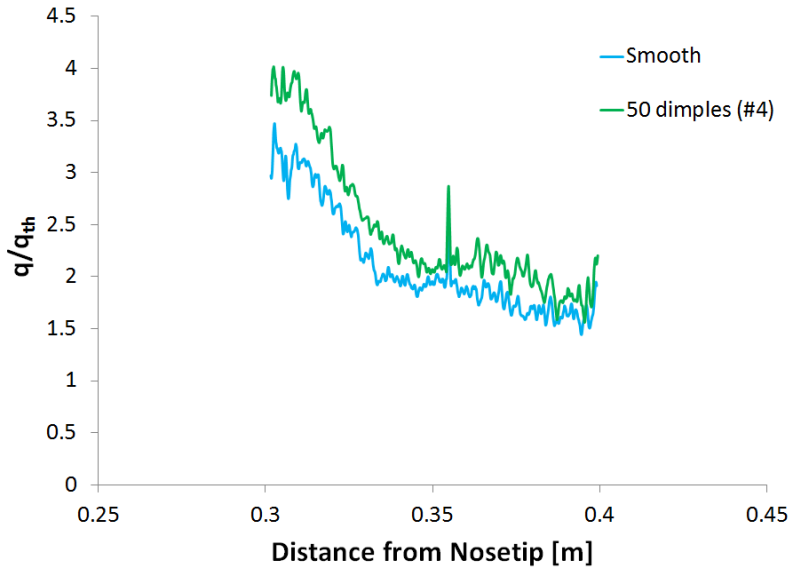

(a) $\phi = 105°$.

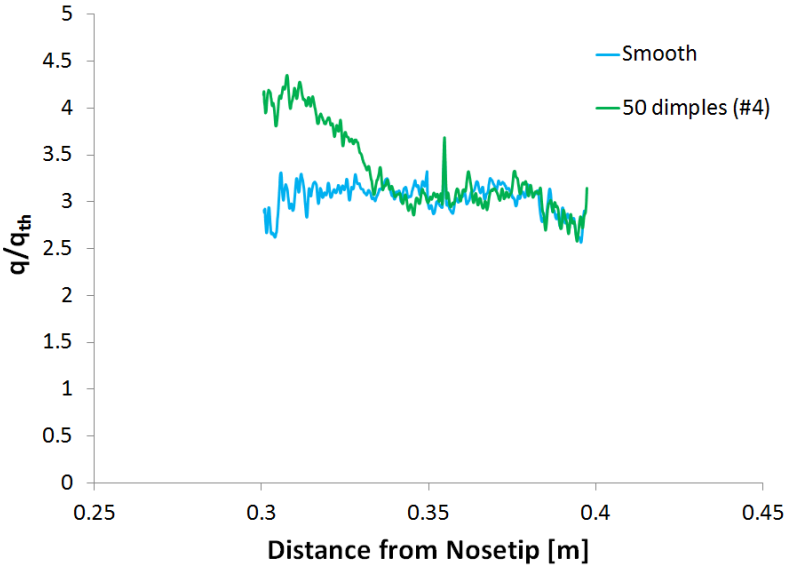

(b) $\phi = 75°$.

Figure 5.88.: Axial heat transfer profiles for the TSP images in Figures 5.87. Noisy flow. Re = 10.7×10^6/m.

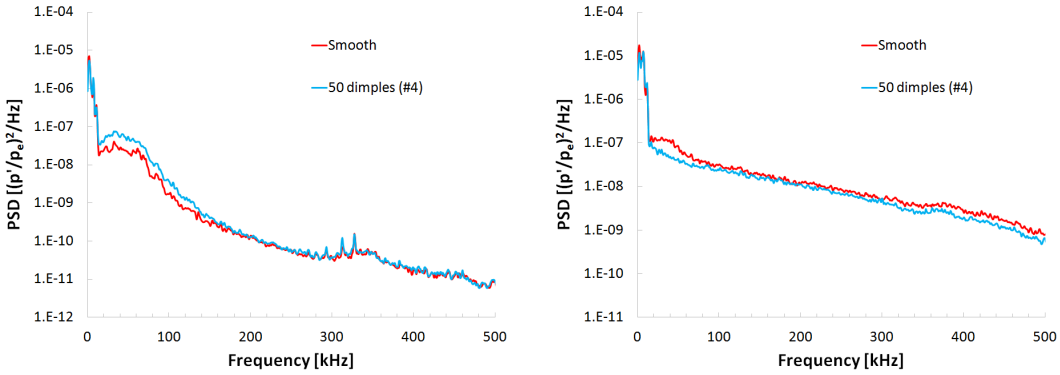

(a) PCB sensor, 0.19 m from the nosetip. (b) PCB sensor, 0.32 m from the nosetip. Circled in white in Figure 5.87.

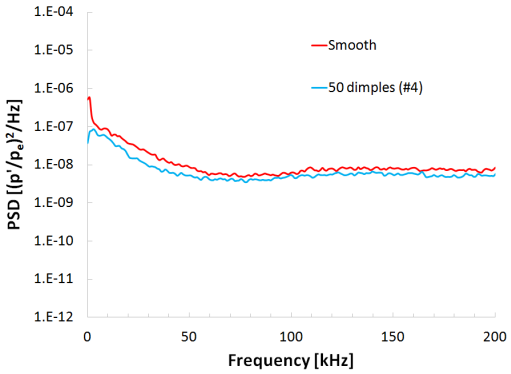

(c) Kulite sensor, 0.36 m from the nosetip. Circled in black in Figure 5.87.

Figure 5.89.: PSD of Kulite and PCB pressure data at an azimuthal angle of 90° under noisy flow with smooth and 50-dimpled Torlon inserts. Re = 10.7×10^6/m.

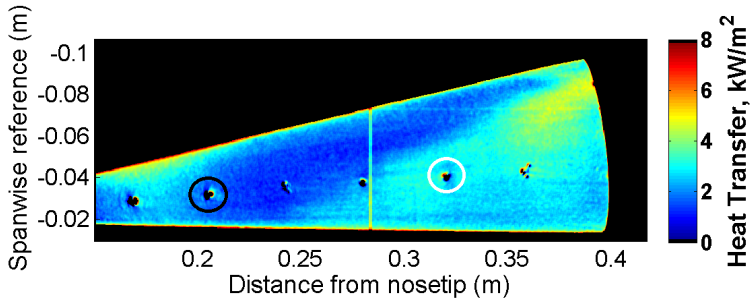

(a) Smooth. $p_0 = 141.5$ psia, Re $= 11.3\times10^6$/m, $T_0 = 424$ K. $T_w = 301$ K.

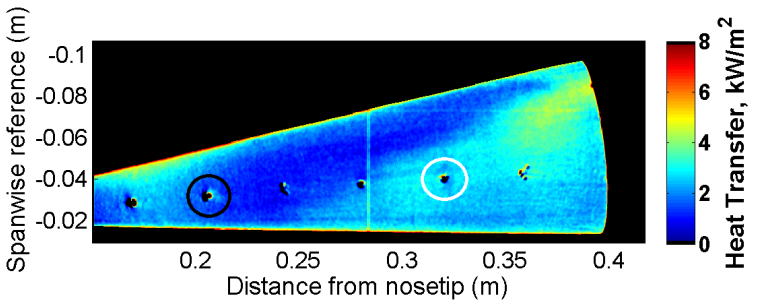

(b) 50 dimples (#4). $p_0 = 141.1$ psia, Re $= 11.3\times10^6$/m, $T_0 = 425$ K. $T_w = 300$ K.

Figure 5.90.: TSP images under noisy flow with smooth and 50-dimpled Torlon inserts. Yaw side of the cone. Sensors along the 90° ray.

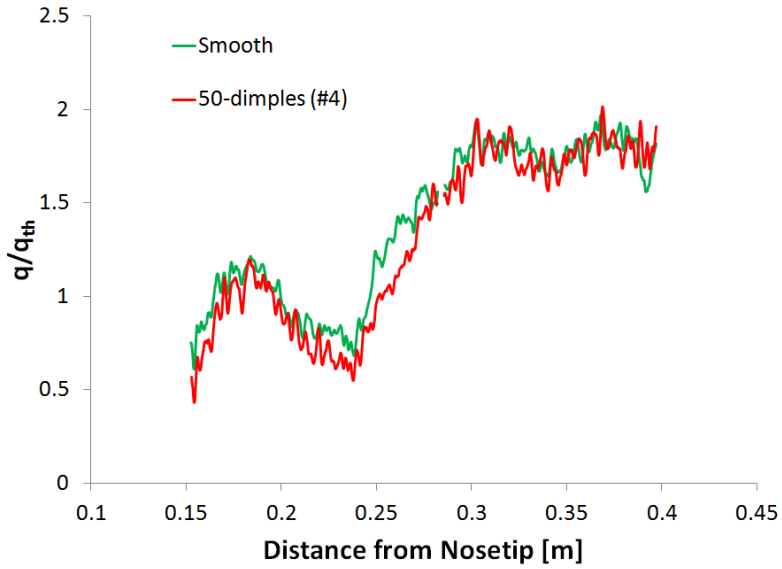

(a) $\phi = 110°$.

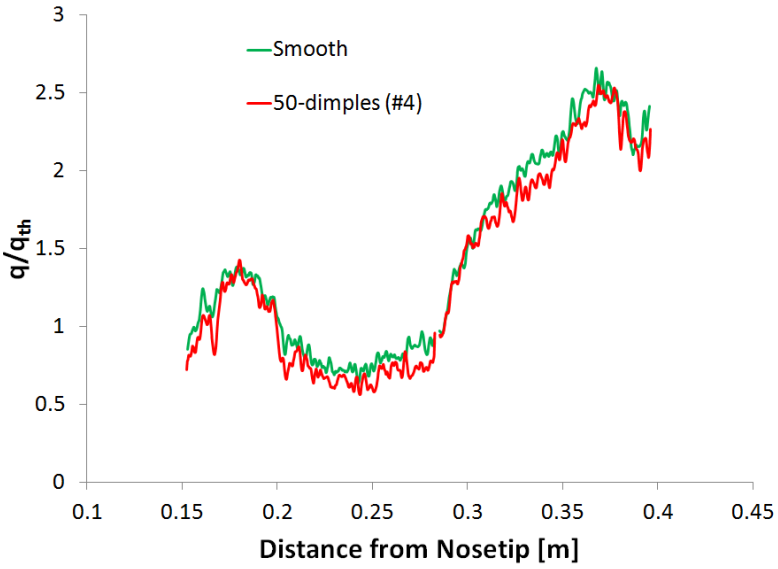

(b) $\phi = 80°$.

Figure 5.91.: Axial heat transfer profiles for the TSP images in Figures 5.90. Noisy flow. Re = 11.3×10^6/m.

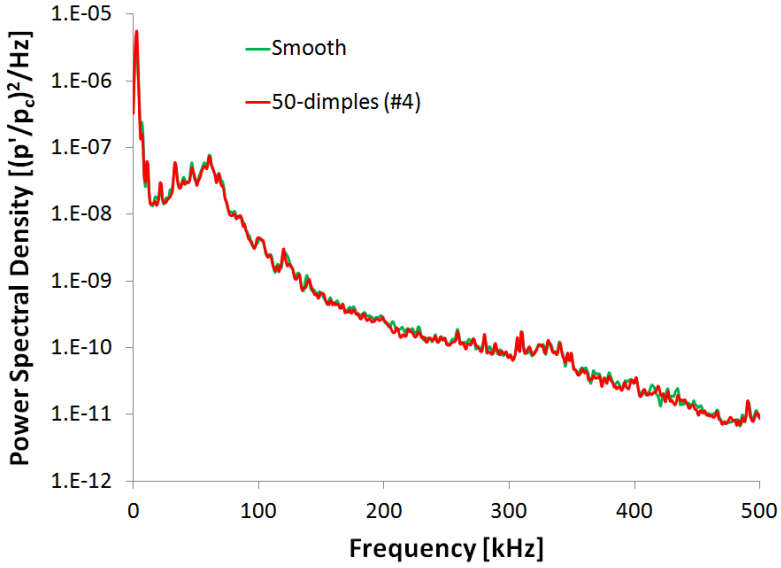

(a) PCB sensor, 0.19 m from the nosetip. Circled in black in Figure 5.90.

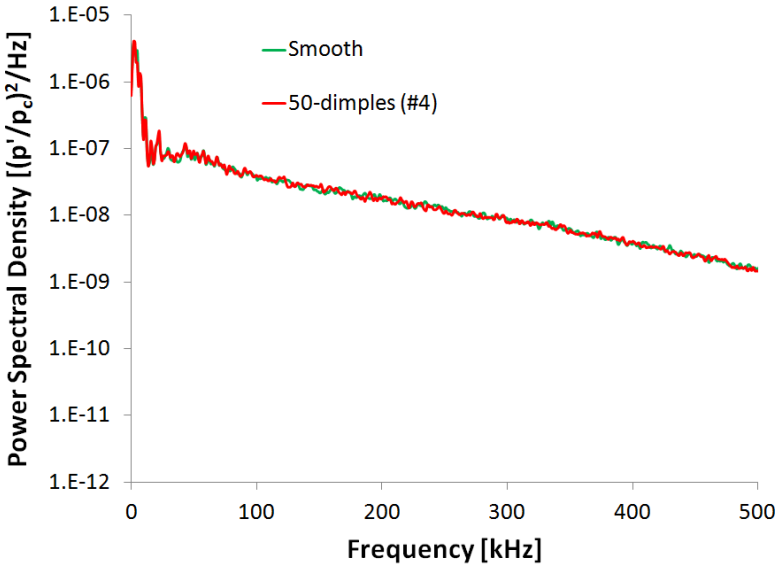

(b) PCB sensor, 0.32 m from the nosetip. Circled in white in Figure 5.90.

Figure 5.92.: PSD of Kulite and PCB pressure data at an azimuthal angle of 90° under noisy flow with smooth and 50-dimpled Torlon inserts. Re = 11.3×10^6/m.

6. MEASUREMENTS OF TRAVELLING CROSSFLOW WAVES

6.1 Properties of Travelling Crossflow Waves

In order to calculate the properties of the travelling crossflow waves, including the phase speed and the propagation angle, measurements from 3 or 4 sensors are required. The more general case utilizes four sensors, as discussed in Reference 107. The method in References 67 and 73 utilizes three sensors, and is also used by the author. The cross spectrum of two signals $s_1(t)$ and $s_2(t)$ is defined as:

$$S_{12}(f) = \lim_{T\to\infty} (1/T) E[\hat{s_1}^*(f,T)\hat{s_2}(f,T)] \tag{6.1}$$

where $\hat{s}$ represents the Fourier transform of the signal, * is the complex conjugate and E[] is the expected value operator.

The magnitude-squared coherence (γ^2) determines how well a signal $s_1(t)$ correlates to another signal $s_2(t)$ at each frequency and is defined as:

$$\gamma^2(f) = \frac{|S_{12}(f)|^2}{S_{11}(f)S_{22}(f)} \tag{6.2}$$

The magnitude-squared coherence yields values between 0 and 1, where 0 represents no correlation and 1 represents a perfect correlation.

The phase difference (Θ) between the two signals is determined by the following equation:

$$\Theta(f) = \arctan\left[\frac{\Im(S_{12})}{\Re(S_{12})}\right] \tag{6.3}$$

where $\Im(S_{12})$ and $\Re(S_{12})$ are the imaginary and real parts of the cross spectrum. The time delay (τ) between the two signals is determined by:

$$\tau(f) = \frac{\Theta(f)}{2\pi f}. \tag{6.4}$$

A diagram of the Kulite sensor array is shown in Figure 6.1(a). An axial and circumferential surface coordinate system was transformed into a two-dimensional plane for small regions of surface curvature. The coordinate system can then be rotated by an angle Ψ, shown in Figure 6.1(b). Ψ represents the angle between the wave propagation and the x-axis. For most experiments, sensor 1 was closest to the leeward ray and sensor 4 was closest to the windward ray.

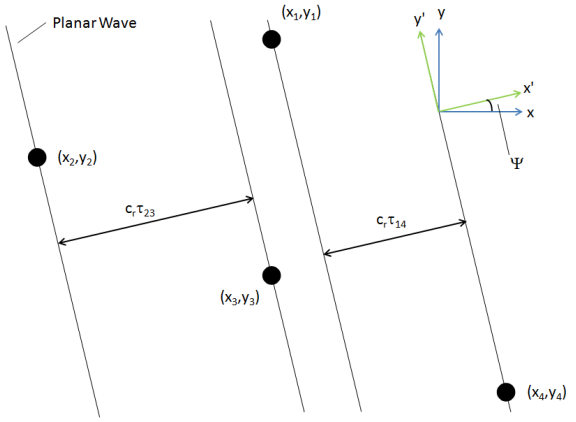

(a) Original Coordinate System with planar wave

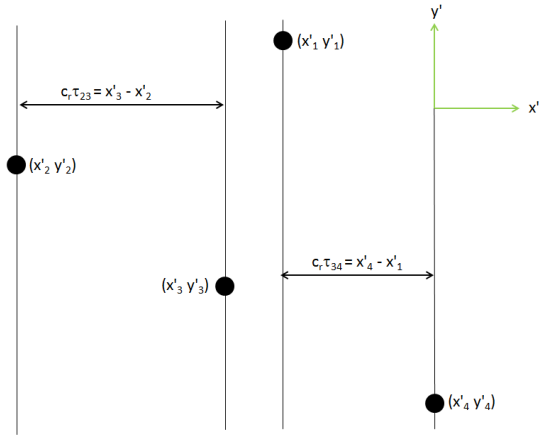

(b) Rotated Coordinate System

Figure 6.1.: Diagram of Kulite sensor array. Not to scale.

Points in the original coordinate system (x,y) can be transformed into the rotated coordinate system (x',y') with the following equations:

$$x' = x\cos\Psi + y\sin\Psi \tag{6.5}$$

$$y' = -x\sin\Psi + y\cos\Psi \tag{6.6}$$

The phase speed of the wave (c_r) multiplied by the time delay between the two signals (τ_{12}) is simply the distance between the two sensors in the rotated coordinate system:

$$c_r\tau_{12} = x'_2 - x'_1 \tag{6.7}$$

Plugging equation 6.5 into equation 6.7 yields the following result:

$$c_r\tau_{12} = (x_2 - x_1)\cos\Psi + (y_2 - y_1)\sin\Psi \tag{6.8}$$

Utilizing equation 6.8 for two sensor pairs (1,2) and (3,4), the propagation angle and phase speed can be determined:

$$\Psi = \arctan\left[\frac{\tau_{34}(x_2 - x_1) - \tau_{12}(x_4 - x_3)}{\tau_{12}(y_4 - y_3) - \tau_{34}(y_2 - y_1)}\right] \tag{6.9}$$

$$c_r = \frac{(x_2 - x_1)\cos\Psi + (y_2 - y_1)\sin\Psi}{\tau_{12}} \tag{6.10}$$

The only restriction for this analysis is that sensor $1 \neq 2$, and sensor $3 \neq 4$. Therefore this analysis can be done with 3 or 4 sensors.

6.2 Properties of the Travelling Crossflow Waves

Measurements were made with the array of Kulite sensors on the 90° ray under both noisy and quiet flow for Reynolds numbers of 6.5×10^6/m and 11.5×10^6/m, respectively. The PSD of the Kulites is shown in Figure 6.2. Under both noisy and quiet flow, the PSD shows a low-frequency peak in the spectra near 30–40 kHz.

Utilizing the array of Kulite sensors, the wave angle and phase velocity of the low-frequency instability can be calculated to better determine if the low-frequency instability is due to the travelling crossflow instability. Figures 6.3 and 6.4 show the PSD, magnitude-squared coherence, phase difference and time delay for the 11.5×10^6/m Reynolds number case under quiet flow. It was decided to only look at frequencies with a magnitude-squared coherence greater than 0.2, based on work by Kimmel et al [108]. Figures 6.4(a) and 6.4(b) show that the wave is passing over sensor 1, sensor 2 and sensor 3 in that order.

Figure 6.5 plots the wave angle and phase speed, utilizing equations 6.9 and 6.10, for various Reynolds numbers where the low-frequency instability is measured. The wave angle is measured with respect to a line from the nosetip along the cone's surface, where negative angles correspond to waves travelling from the leeward to windward ray (opposite direction of crossflow). Table 6.1 contains the wave angle and phase speed at the peak frequency for each case. For all cases, whether noisy or quiet, the wave angle is approximately -70° to -62°. The fact that the most amplified travelling waves travel in the opposite direction of the crossflow agrees with computations by Malik et al [15], although Malik's computations were done at low speeds on a swept wing. Comparing the noisy and quiet cases, the peak frequency is lower for the noisy cases. This is likely caused by several factors. The Mach number is 5.8 when the BAM6QT is run noisy, the Reynolds number is lower for the noisy tests leading to a thicker boundary layer and therefore lower frequencies, and the differing noise levels may also introduce different frequencies of travelling waves. Despite having different peak frequencies, the wave propagation angle is approximately constant regardless of the noise level. Focusing on the quiet cases, a slight drop in Reynolds number does not cause a change in the propagation angle, but the phase speed is lower. It was not possible to make a direct Reynolds number comparison under noisy and quiet flow. If the noisy Reynolds number was increased the flow over the sensors was turbulent, and if the quiet Reynolds number was decreased the waves were too weak to measure.

The phase speed of the travelling waves are similar, near 200–230 m/s. Under noisy flow, the phase speed appears to be higher for a given peak frequency. This may be related to the thicker boundary layer under noisy flow at the lower Reynolds numbers. Figure 6.6 plots the phase speed of low-frequency instability divided by the velocity at the edge of the boundary layer against frequency. The velocity at the edge of the boundary layer was found by using the Taylor-Maccoll solution for a 7° cone at 0° angle of attack. Obviously there will be some error in the edge velocity calculation since the calculation does not include the angle of attack, but these errors can easily be accounted for. Dividing by the edge velocity does not appear to collapse the data. This is likely because the stagnation temperature does not vary significantly from run to run (approximately ±1.5%). When determining the theoretical edge velocity, the only variables are the Mach number and the stagnation temperature (for determining the speed of sound).

Table 6.1.: Wave angle and phase speed corresponding to the peak frequency of the low-frequency instability wave at differing conditions.

Noise Level	**Reynolds Number [/m]**	**Peak Frequency [kHz]**	**Wave Angle [degrees]**	**Phase Speed [m/s]**
Quiet	12.3×10^6	32–38	-62 to -68	206–232
Quiet	12.2×10^6	32–40	-67 to -70	220–259
Quiet	11.5×10^6	30–34	-64 to -65	179–197
Quiet	11.4×10^6	28–36	-66 to -68	169–212
Noisy	6.8×10^6	22–26	-62 to -65	208–248
Noisy	6.5×10^6	24–28	-63 to -66	222–255

Munoz performed similar experiments in the Hypersonic Ludwieg Tube Braunschweig (HLB) at TU Braunschweig on a 7° half-angle cone at 6° angle of attack with a nominally sharp nosetip [58]. The HLB tunnel is a conventional noisy tunnel. He measured an instability with a frequency between 35 and 40 kHz and a propagation

angle between 62 and 70°. Computations by Perez [59] and Munoz [60] showed that this low-frequency instability corresponds to the travelling crossflow waves. Computations by Li et al [62] also show that the travelling crossflow waves with the largest N-factors (between 10 and 20) have a frequency between 20 and 65 kHz. Based on all of this, it appears that the low-frequency instability measured by the author is the travelling crossflow instability. New computations are needed to confirm this.

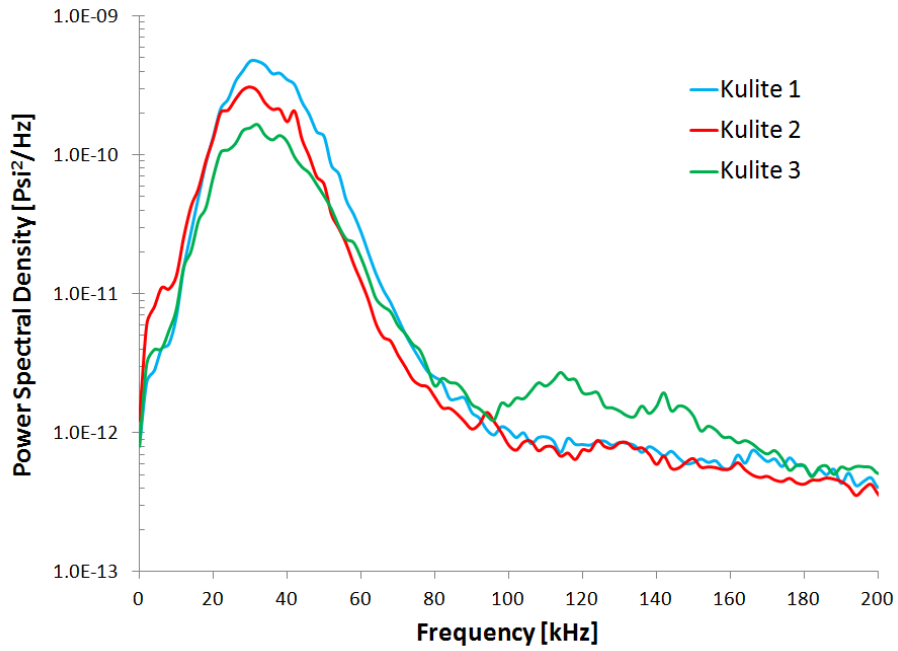

(a) Quiet, Re - 11.5×10^6/m

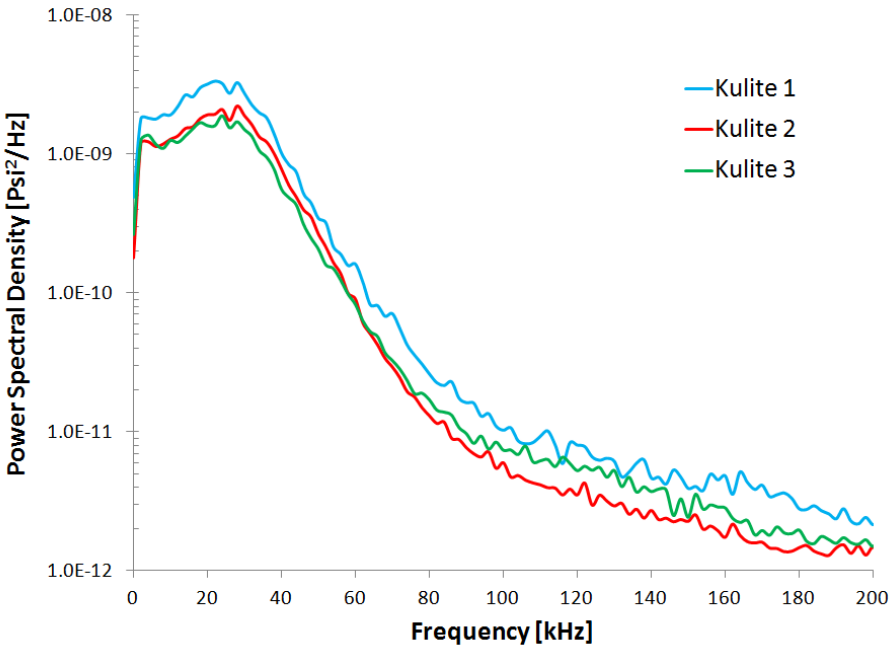

(b) Noisy, Re - 6.5×10^6/m

Figure 6.2.: PSD of Kulites measuring a low-frequency instability under both noisy and quiet flow. Sensors on the 90° ray (measured from the windward ray).

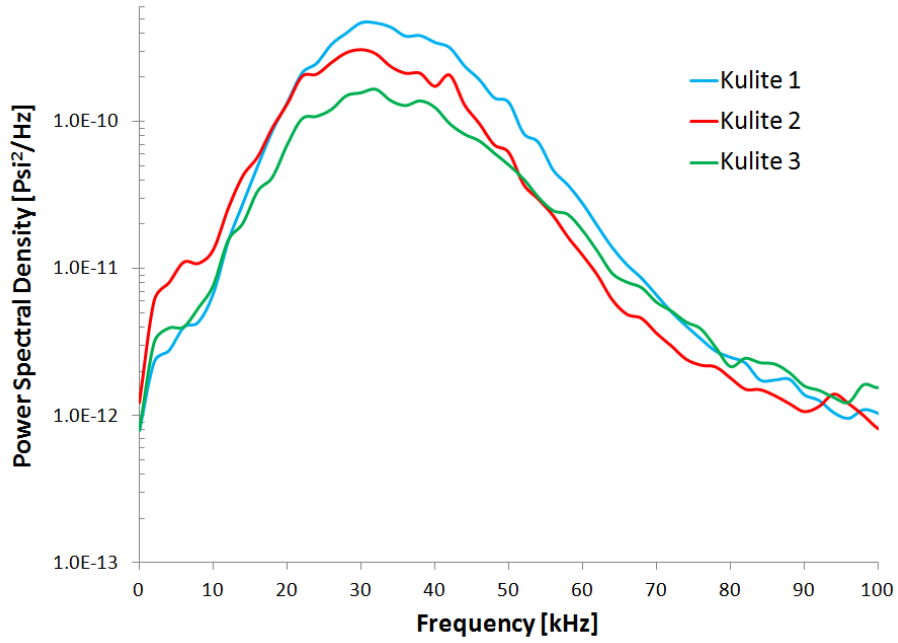

(a) PSD

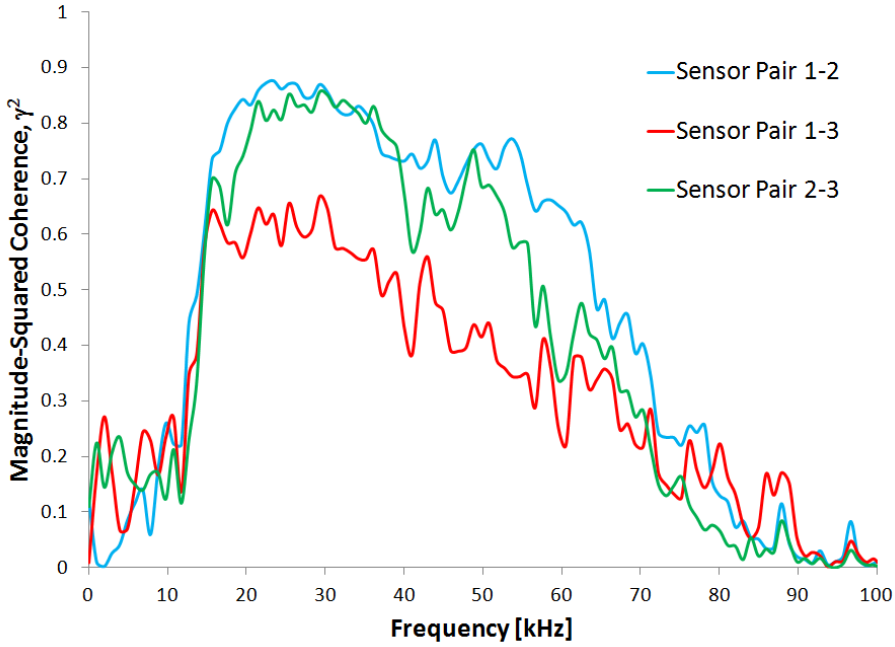

(b) Magnitude-squared coherance

Figure 6.3.: Sample PSD and magnitude-squared coherence for Re - 11.5×10^6/m.

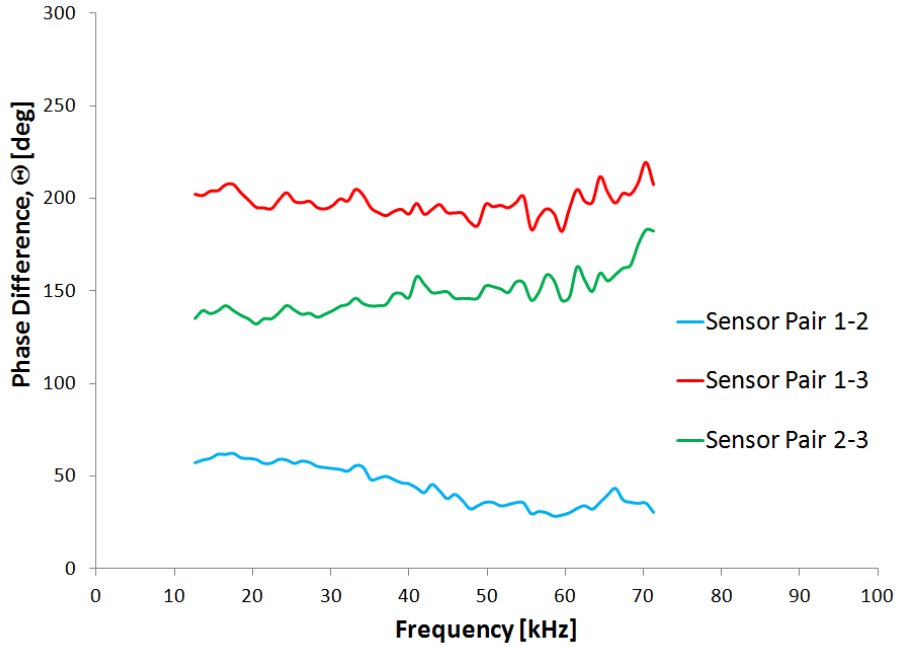

(a) Phase difference

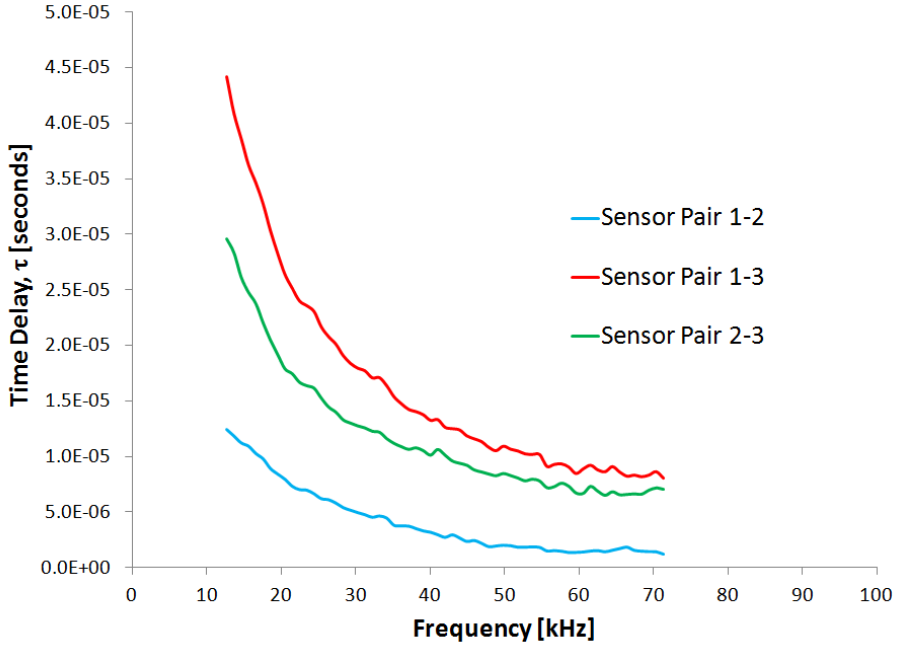

(b) Time delay

Figure 6.4.: Sample phase difference and time delay for Re - 11.5×10^6/m.

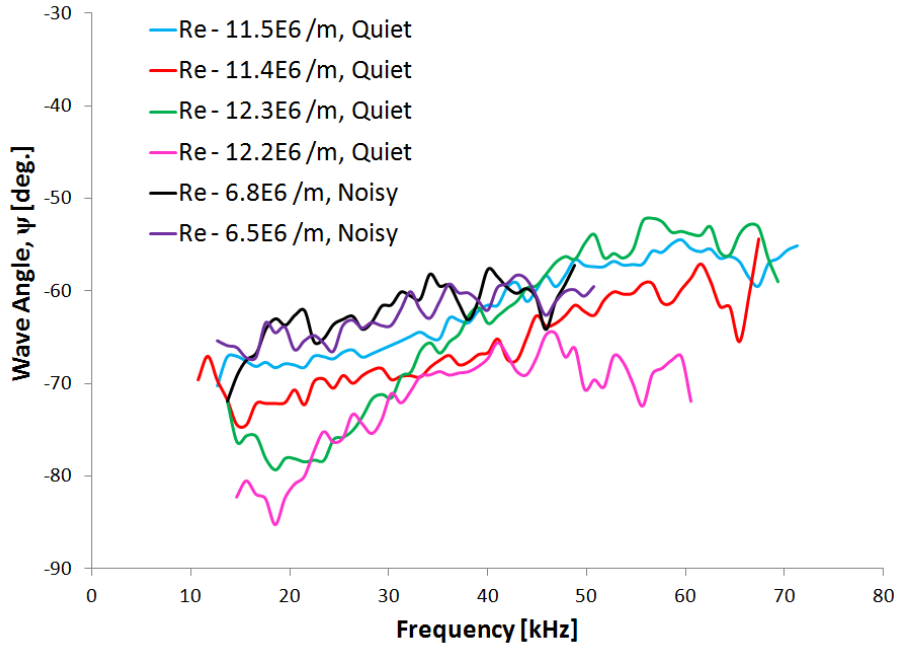

(a) Wave Angle

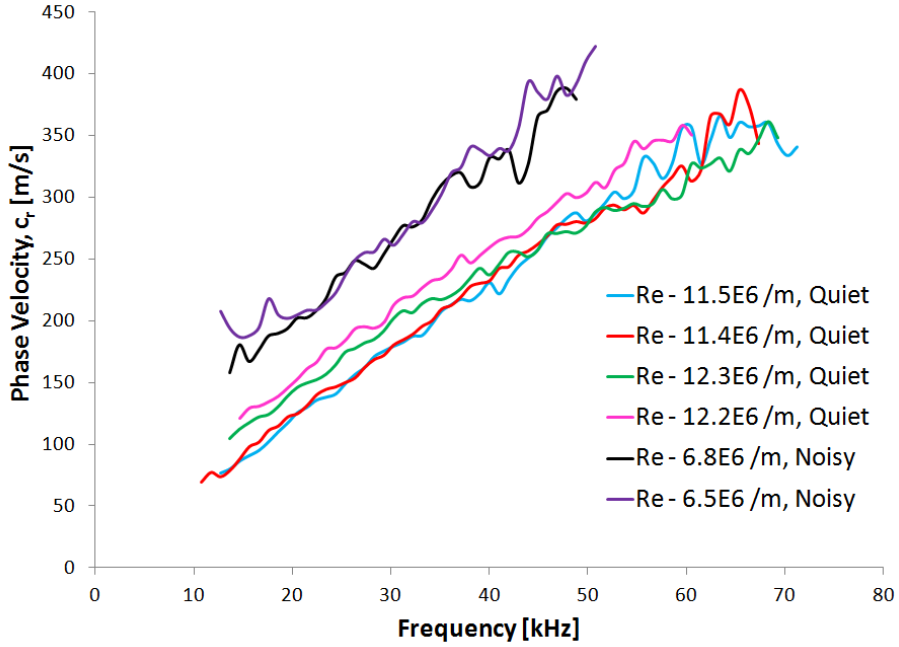

(b) Phase Speed

Figure 6.5.: Wave angle and phase speed for low-frequency instability wave.

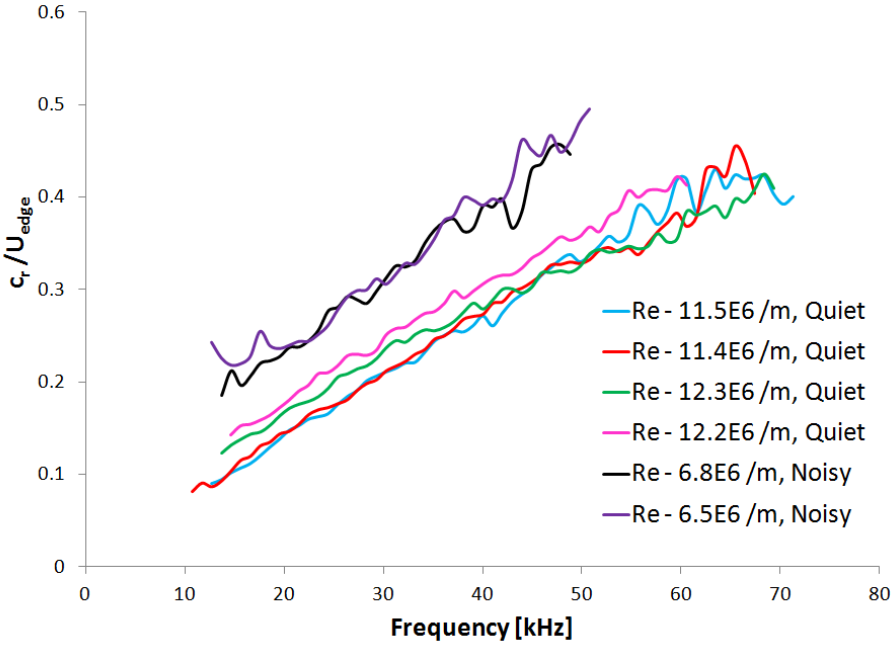

Figure 6.6.: Phase speed for low-frequency instability wave non-dimensionalized by the velocity at the edge of the boundary layer.

6.3 Reynolds Number and Tunnel Noise Effects

The effect of Reynolds number on the travelling crossflow waves was studied by varying the initial stagnation pressure of the BAM6QT. Figure 6.7 plots the PSD of a Kulite sensor 0.362 m from the nosetip and on an azimuthal ray of 90°, for varying Reynolds numbers. At the lowest Reynolds number, the travelling crossflow waves are barely visible near 40 kHz. As the Reynolds number increases, the magnitude of the travelling wave increases, while the peak frequency stays roughly constant. At this azimuthal ray, the boundary layer appears to remain laminar at the maximum quiet Reynolds number near the sensor location, but this inference will be further verified by the TSP images.

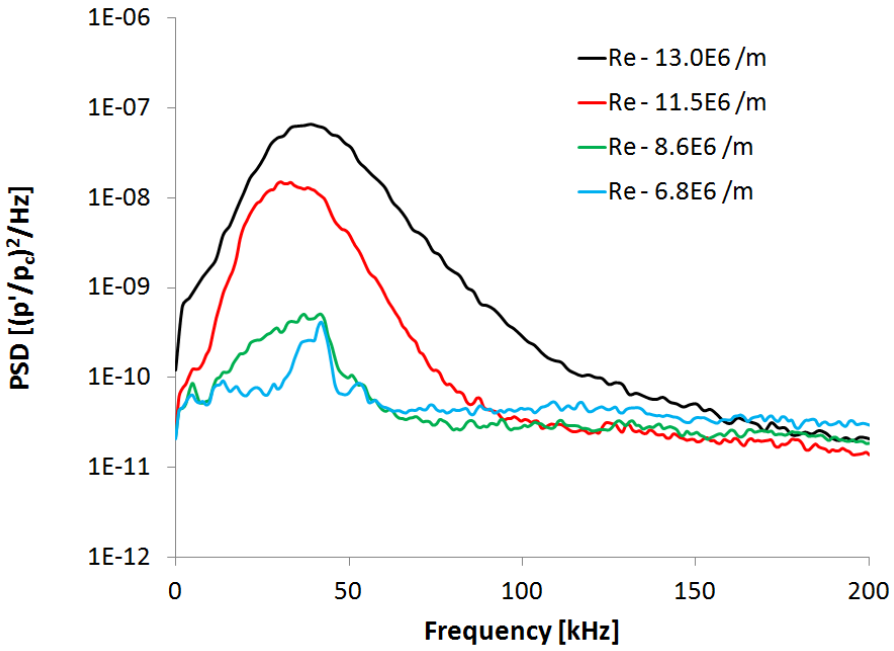

Figure 6.7.: PSD of Kulite 0.362 m from the nosetip and an azimuthal angle of 90°. Smooth insert. Quiet flow.

The TSP images corresponding to the spectra in Figure 6.7 are shown in Figure 6.8. The Kulite array is circled in Figure 6.8(a). At the lowest Reynolds number, when the travelling waves are barely visible, the stationary waves are not visible in the

TSP and the boundary layer appears to be fully laminar. Increasing the Reynolds number, the stationary waves become barely visible near the leeward ray, and the travelling wave amplitude increases. At the two highest Reynolds numbers, both the stationary and travelling waves have increased in amplitude. The boundary layer appears to be laminar near the Kulite array, but may be breaking down to turbulence closer to the lee ray.

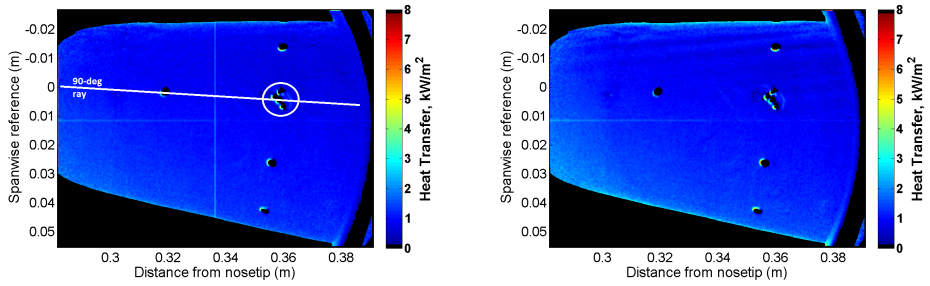

(a) Re = 6.8×10^6/m, p_0 = 84.8 psia, T_0 = 428 K, T_w = 304 K.

(b) Re = 8.6×10^6/m, p_0 = 107.5 psia, T_0 = 428 K, T_w = 301 K.

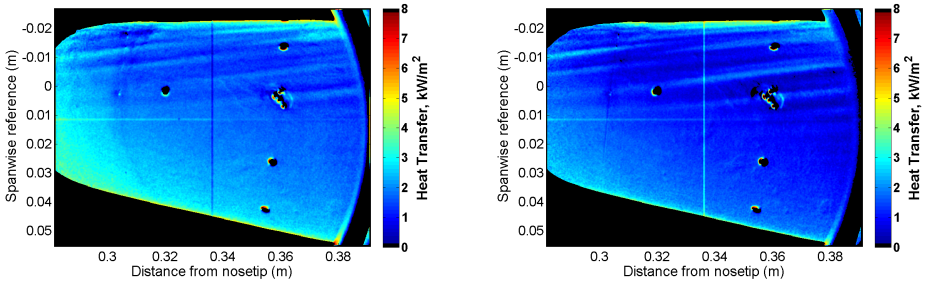

(c) Re = 11.5×10^6/m, p_0 = 140.6 psia, T_0 = 423 K, T_w = 298 K.

(d) Re = 13.0×10^6/m, p_0 = 160.0 psia, T_0 = 425 K, T_w = 302 K.

Figure 6.8.: TSP images for varying Reynolds number with smooth insert under quiet flow. Yaw side of the cone.

A similar set of tests was done under noisy flow. The PSD of a Kulite on the 90° azimuthal ray is shown in Figure 6.9 at various Reynolds numbers. At the lowest Reynolds number, the boundary layer appears to be fully laminar over the sensor

based on the low levels of broadband noise, and the travelling waves are not visible in the spectra. At a Reynolds number of 4.3×10^6/m, there is a slight increase in noise near 30–50 kHz. This may be due to the travelling crossflow wave, but this is not clear. When the Reynolds number is 6.3×10^6/m, the travelling waves become visible, with a peak frequency near 30 kHz. Increasing the Reynolds number to 8.0×10^6/m, there is a broadband increase in noise, indicating that the boundary layer is turbulent. Finally, increasing the Reynolds number to 10.6 and 13.3×10^6/m produces a similar turbulent spectra.

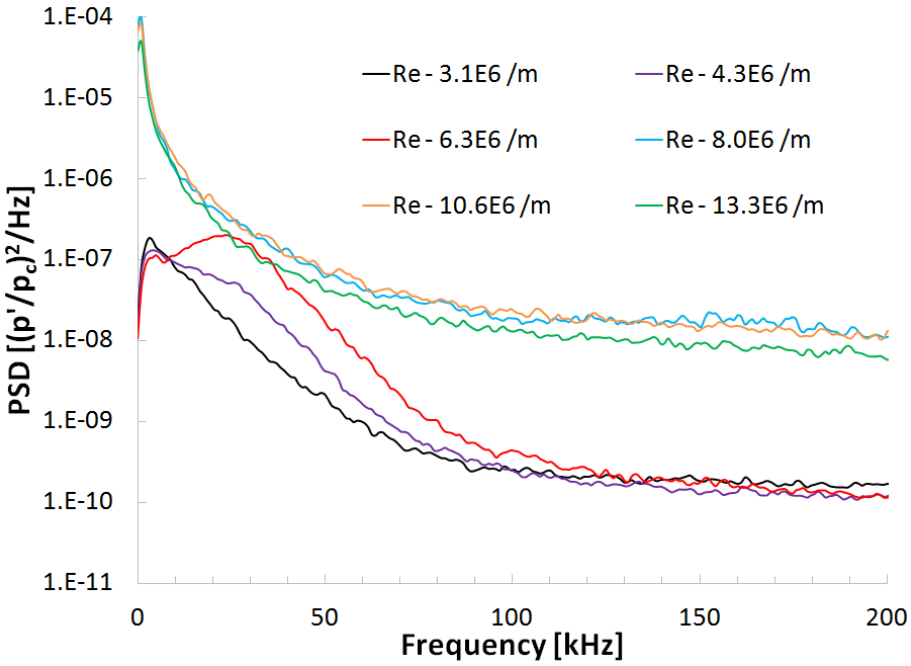

Figure 6.9.: PSD of Kulite pressure data 0.362 m from the nosetip and an azimuthal angle of 90°. Smooth insert. Noisy flow.

Figure 6.10 plots the RMS of the non-dimensional pressure fluctuations measured from the Kulite transducer on the 90° ray under noisy flow. The RMS was found by integrating under the PSD in Figure 6.9 from 0 to 100 kHz. There is a clear increase in RMS pressure when the Reynolds number is increased to 8×10^6/m, indicating that the boundary layer is turbulent over the sensor at this and larger Reynolds numbers.

At the low Reynolds numbers, the boundary layer appears to be laminar according to the low RMS levels.

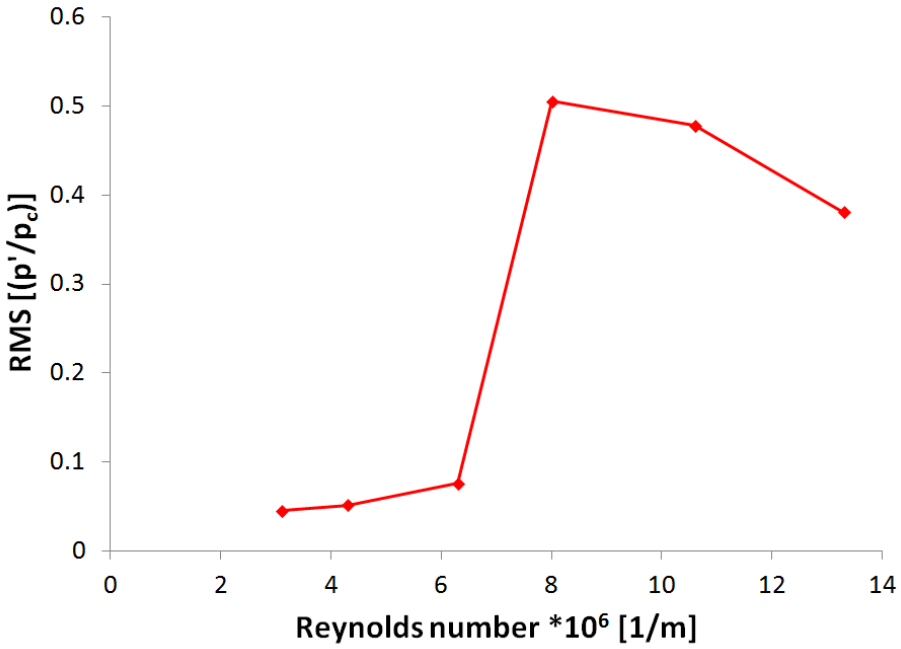

Figure 6.10.: RMS of Kulite pressure 0.362 m from the nosetip and an azimuthal angle of 90°. Smooth insert. Noisy flow.

The TSP images, shown in Figure 6.11, agrees with the PSD and RMS of the pressure data shown in Figures 6.9. The Kulite sensor array is circled in Figure 6.11(a). At the two lowest Reynolds numbers, the boundary layer appears fully laminar. At a Reynolds number of 6.3×10^6/m, the travelling crossflow waves are visible in the spectra, and the TSP shows what appears to be a fully laminar boundary layer near the sensors. At a Reynolds number of 8.0×10^6/m, the Kulite sensor shows what appears to be a turbulent spectra, and the TSP shows an increase in heating near the sensor which is likely caused by a turbulent or transitional boundary layer. Increasing the Reynolds number causes the location of boundary layer transition to move upstream. Transition also appears to be occurring near the 90° ray, and propagating towards the windward and leeward rays.

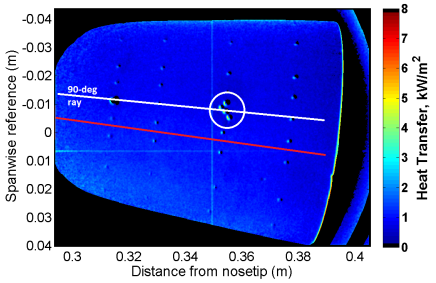

(a) Re = 3.1×10^6/m, p_0 = 37.1 psia, T_0 = 421 K, T_w = 305 K.

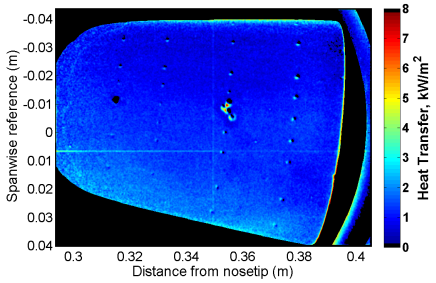

(b) Re = 4.3×10^6/m, p_0 = 52.3 psia, T_0 = 420 K, T_w = 310 K.

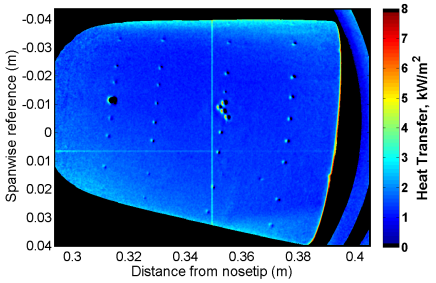

(c) Re = 6.3×10^6/m, p_0 = 76.8 psia, T_0 = 423 K, T_w = 304 K.

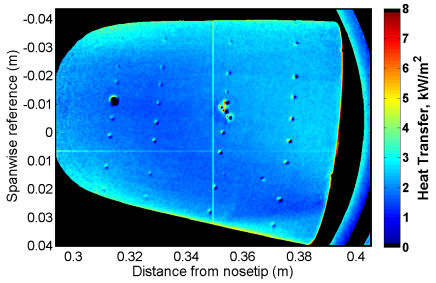

(d) Re = 8.0×10^6/m, p_0 = 98.5 psia, T_0 = 425 K, T_w = 302 K.

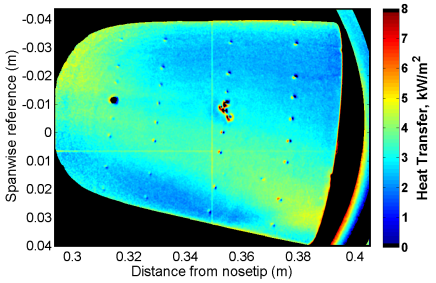

(e) Re = 10.6×10^6/m, p_0 = 130.2 psia, T_0 = 425 K, T_w = 304 K.

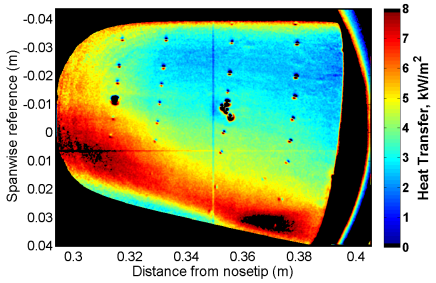

(f) Re = 13.3×10^6/m, p_0 = 162.8 psia, T_0 = 424 K, T_w = 306 K.

Figure 6.11.: TSP images for varying Reynolds number with smooth insert under noisy flow. Yaw side of the cone.

Axial non-dimensional heat transfer profiles were taken along the 105° ray for the TSP images in Figure 6.11 and are shown in Figure 6.12. The 105° ray is denoted as a red line in Figure 6.11(a). At the two lowest Reynolds numbers, the boundary layer appears to remain laminar as the non-dimensional heat transfer remains roughly constant. At a Reynolds number of 6.3×10^6/m, the onset of transition may be occurring near 0.37 m from the nosetip where the non-dimensional heat transfer departs from the laminar level. Increasing the Reynolds number to 8.0×10^6/m, the axial heat-transfer profile departs from the laminar heating further upstream (0.34 m), suggesting that transition is moving upstream with increasing Reynolds numbers. At the two highest Reynolds numbers, the boundary layer has transitioned to turbulence upstream of the imaged region.

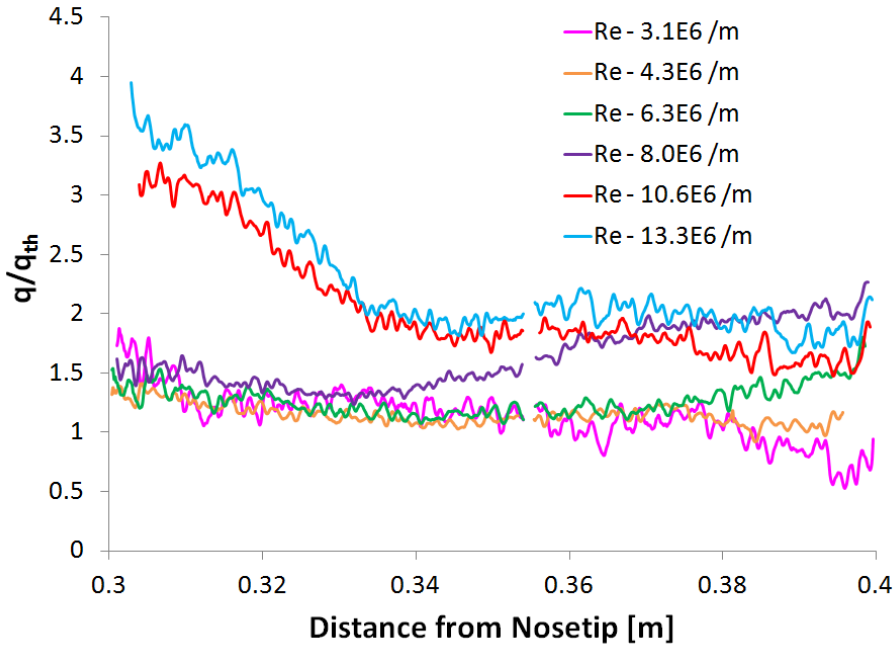

Figure 6.12.: Axial heat transfer profile along the 105° ray for the TSP images in Figure 6.11. Smooth insert. Noisy flow.

The PSD of the pressure data from the Kulite 0.362 m from the nosetip under both quiet and noisy flow at various Reynolds numbers is shown in Figure 6.13. The noisy

flow cases are plotted with the diamond symbols and the quiet flow cases are plotted with no symbols. The same colour is used for cases at similar Reynolds numbers. At a Reynolds number of 6.3×10^6/m (blue curves) the travelling waves are barely visible under quiet flow near 40 kHz. Under noisy flow, the travelling waves are visible as a peak near 30 kHz, almost 3 orders of magnitude larger in power than in the quiet case. It is not known how much the difference in wave amplitude is caused by non-linear growth of the waves or by the differing free-stream noise levels which likely alters the initial conditions of the travelling waves. As the Reynolds number for the quiet cases increases the magnitude of the stationary wave increases, but the boundary layer over the sensor is transitional or turbulent for the higher Reynolds number noisy cases so therefore a direct Reynolds number comparison between noisy and quiet flow cannot be made.

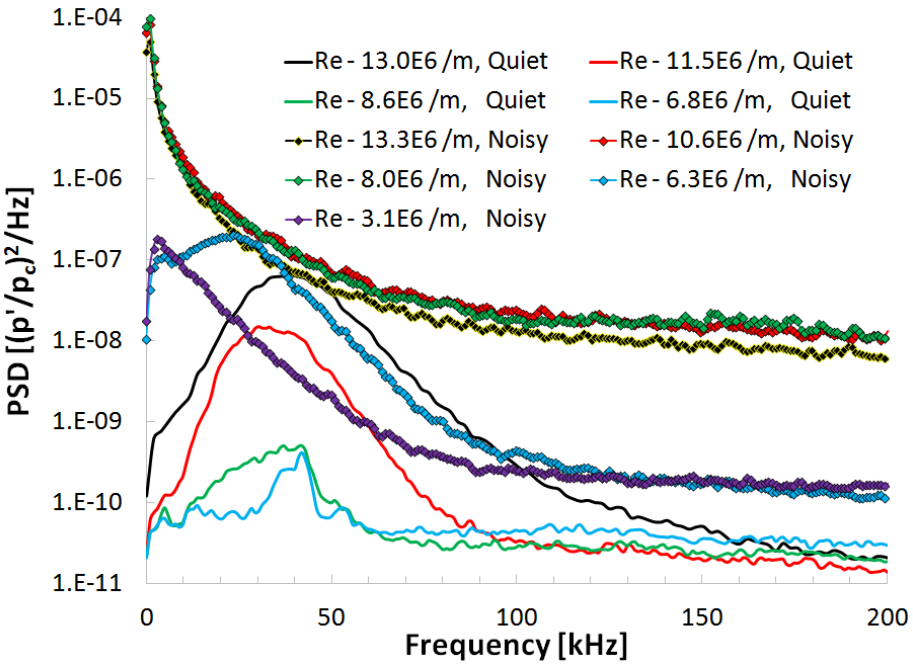

Figure 6.13.: PSD of Kulite 0.362 m from the nosetip and an azimuthal angle of 90°. Smooth insert under both noisy and quiet flow.

The RMS pressure amplitude and the RMS pressure amplitude divided by P_c (the 0° AoA surface pressure) expressed as a percentage are shown in Table 6.2. The RMS pressure amplitude was calculated by taking the square root of the area under the PSD from approximately 10–70 kHz. Under quiet flow, the travelling crossflow waves reach a maximum of 4.36% of the 0° AoA edge pressure. Under noisy flow the waves reach 7.60% of the 0° AoA edge pressure before breaking down to turbulence over the sensor at higher Reynolds numbers. At a similar Reynolds number (6.3×10^6/m), the travelling waves are 21 times larger in amplitude under noisy flow than under quiet flow.

Table 6.2.: RMS amplitudes of travelling crossflow waves at an azimuthal angle of 90° under noisy and quiet flow.

	Reynolds Number	**RMS amplitude [Psi]**	**% of 0° AoA edge pressure (P_c)**
Quiet	13.0×10^6/m	0.00864	4.36%
	11.5×10^6/m	0.00328	1.87%
	8.6×10^6/m	0.00052	0.39%
	6.8×10^6/m	0.00034	0.32%
Noisy	6.3×10^6/m	0.00727	7.60%

The repeatability of the data was then determined. Multiple repeat runs were performed at three different Reynolds numbers. The PSD of the Kulite sensor data on the 90° azimuthal ray is shown in Figure 6.14. At the lowest Reynolds, the three runs show a similar laminar spectra. For the middle Reynolds number, all four runs show similar spectra, with a peak near 30 kHz due to the travelling crossflow instability. Finally, at the highest Reynolds number, all three runs show a similar turbulent spectra. The data appear to show good repeatability.

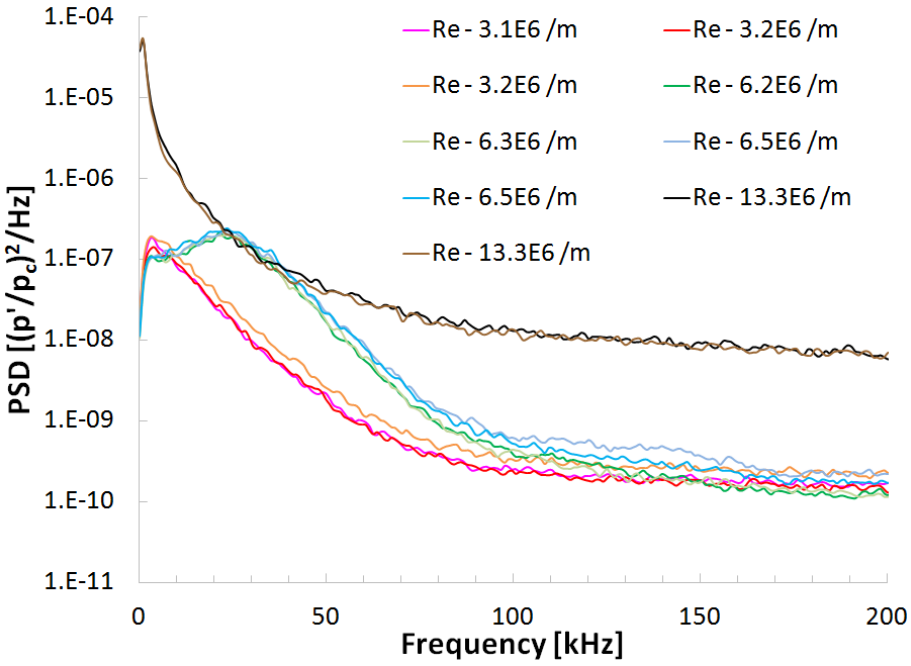

Figure 6.14.: PSD of Kulite 0.362 m from the nosetip and an azimuthal angle of 90°. Smooth insert under noisy flow.

6.4 Effects of Azimuthal Angle and Axial Location on the Travelling Waves

One set of tests had Kulite sensors installed in the upstream and downstream sensor ports (0.235 and 0.363 m from the nosetip) at azimuthal angles of 90° under quiet flow. The power spectral density of the two sensors is shown in Figure 6.15 for two different Reynolds numbers. At the upstream location, the travelling waves are barely visible as a slight increase in power near 40–50 kHz. At the downstream location, the travelling waves are much more distinct.

The RMS amplitude of the pressure signal in psi from 0–70 kHz is shown in Table 6.3. The RMS amplitude for both the upstream and downstream Kulites is larger when the Reynolds number is increased. Unfortunately these two signals cannot be used to compute a growth rate of the travelling waves since the waves are not

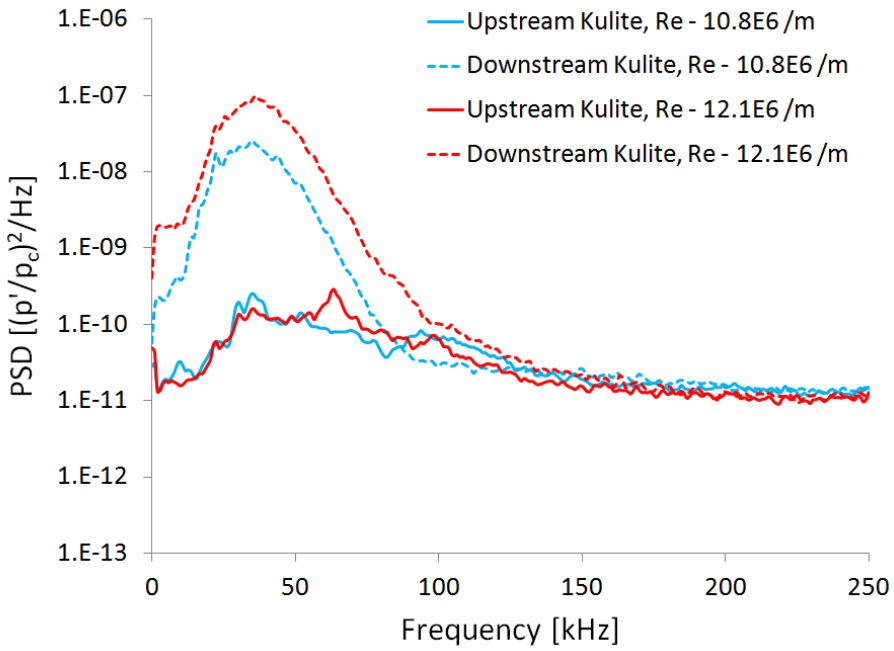

Figure 6.15.: PSD of Kulites 0.235 m (upstream) and 0.363 m (downstream) from the nosetip at an azimuthal angle of 90°. Smooth insert. Quiet flow.

expected to travel along the 90° azimuthal ray, but at an inclined angle as computed in Section 6.2.

Table 6.3.: RMS amplitude travelling crossflow waves at an azimuthal angle of 90°. Upstream Kulites at 0.235 m axially and downstream Kulite at 0.363 m axially. Quiet flow.

	Reynolds Number	**RMS Amplitude [Psi]**	**% of 0° AoA edge pressure (P_c)**
Upstream Kulite	10.8×10^6/m	0.000517	0.3%
Downstream Kulite		0.003415	1.9%
Upstream Kulite	12.1×10^6/m	0.000630	0.3%
Downstream Kulite		0.009322	4.6%

The next set of tests looked at how the travelling crossflow waves varied with azimuthal angle. The PCB sensors could not reliably measure the travelling crossflow waves (as will be discussed in Section 6.5). Therefore, to study how the travelling waves evolve over a range of azimuthal angles, a Kulite sensor was rotated from 90° to 180° from the windward ray. The PSD of the Kulite is shown in Figure 6.16 under quiet flow with the smooth insert at a Reynolds number of 8.4×10^6/m. At 90°, the travelling crossflow waves are visible near 40 kHz. Moving towards the leeward ray at 130° and 150°, the amplitude of the waves increases while the frequency remains roughly constant. At 180°, the waves appear to be breaking down to turbulence as the peak near 40 kHz becomes much broader. A secondary peak near 200 kHz appears. This may signify the appearance of the secondary instability of the stationary waves (which will be discussed in Chapter 8), or it could be the second-mode wave.

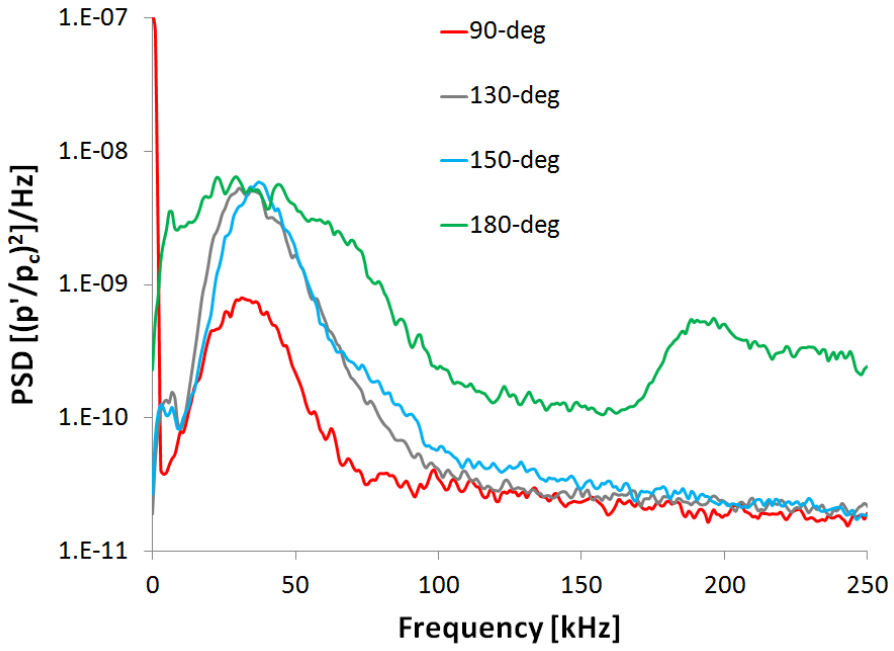

Figure 6.16.: PSD of Kulites 0.362 m from the nosetip at varying azimuthal angles. Smooth insert. Quiet flow. Re - 8.4×10^6/m.

Figure 6.17 plots the PSD of the same Kulite at a higher Reynolds number (10.3×10^6/m). At 90°, the travelling waves are clearly visible. Moving to 110°, the amplitude of the travelling waves increased slightly, but there is also an increase in broadband noise. At 130° and 135° the travelling crossflow peak is becoming obscured as the broadband noise levels are continuing to increase. The boundary layer is breaking down to turbulence at azimuthal angles from 150° to 180°. There is a broad secondary peak near 150 kHz at 150°. Once again this may be due to the secondary instability of the stationary waves, and will be discussed further in Chapter 8.

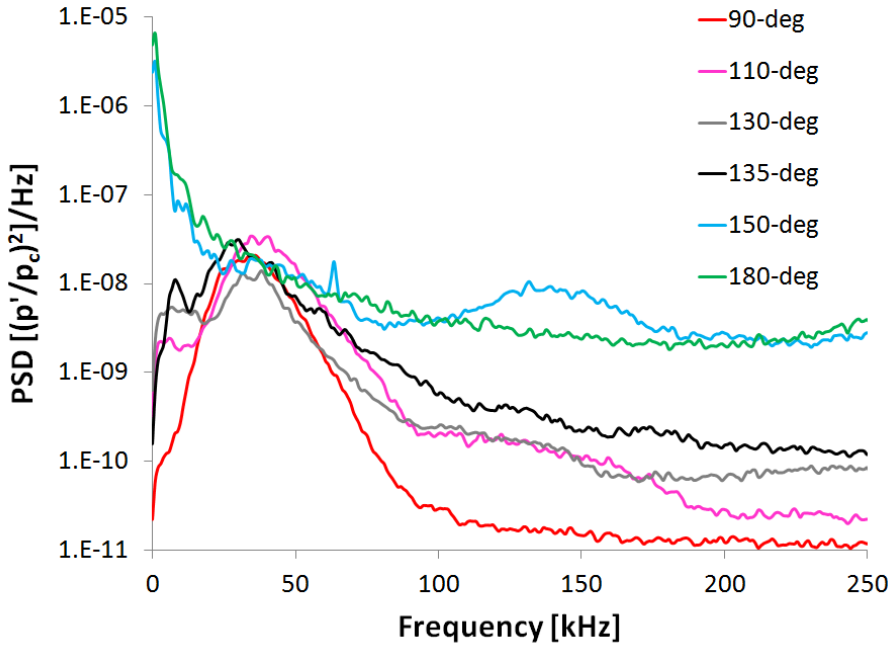

Figure 6.17.: PSD of Kulites 0.362 m from the nosetip at varying azimuthal angles. Smooth insert. Quiet flow. Re = 10.3×10^6/m.

The Reynolds number was increased to 12.0×10^6/m, and the PSD of the Kulite is plotted in Figure 6.18. Once again, the travelling crossflow waves are seen at an azimuthal angle of 90°. At angles closer to the lee ray, the boundary layer has broken down to turbulence as the peak is no longer visible near 40 kHz and there is

a broadband increase in noise. A secondary higher-frequency peak is not visible for any of the azimuthal angles.

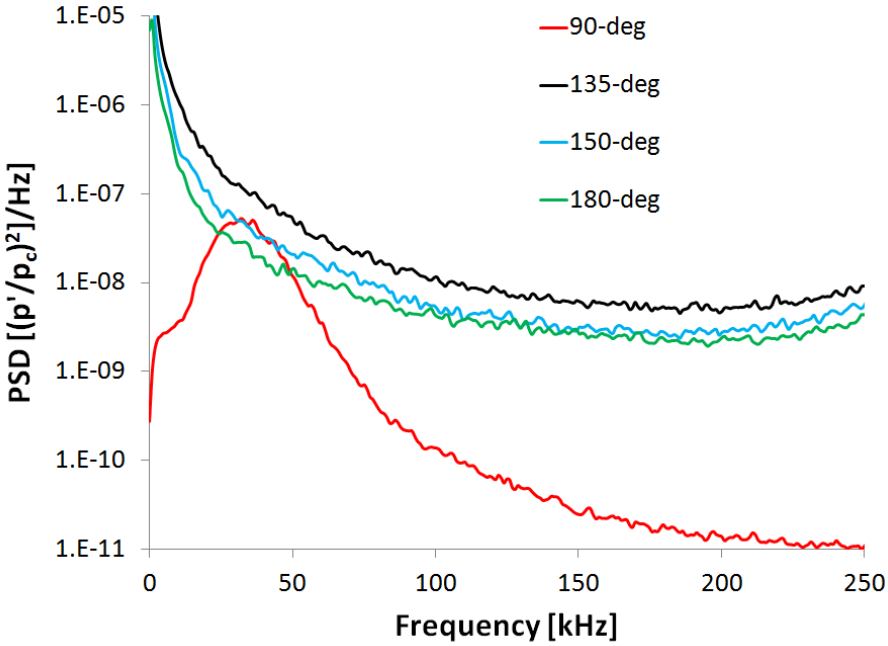

Figure 6.18.: PSD of Kulites 0.362 m from the nosetip at varying azimuthal angles. Smooth insert under quiet flow. Re - 12.0×10^6/m.

Figure 6.19 plots the RMS of the non-dimensional pressure fluctuations between 0 and 70 kHz for the spectra shown in Figures 6.16–6.18, along with the average non-dimensional heat transfer just upstream of the sensor. The heat transfer was found by averaging across a square with approximately the same area as the Kulite sensor, just upstream of the Kulite sensor. The RMS of the pressure fluctuations is plotted with respect to the primary y-axis with the filled in symbols. The average heat transfer is plotted with respect to the secondary y-axis with the empty symbols. At the lowest Reynolds number, the RMS of the pressure increases moving towards the lee ray as the travelling wave grows in amplitude. At the middle Reynolds number, the RMS of the pressure remains relatively constant until reaching an azimuthal angle of 150°, where the amplitude of the travelling wave increases significantly. At the highest

Reynolds number, the RMS of the pressure increases then decreases significantly. This is because the travelling wave is beginning to break down at the larger azimuthal angles. The average heat transfer does not appear to follow a trend. When the RMS pressure increases, the average heat transfer may increase or decrease. The lack of trend is likely due to the occasional presence of a stationary vortex passing over the sensor. The relationship between the stationary and travelling crossflow waves will be discussed in Chapter 7.

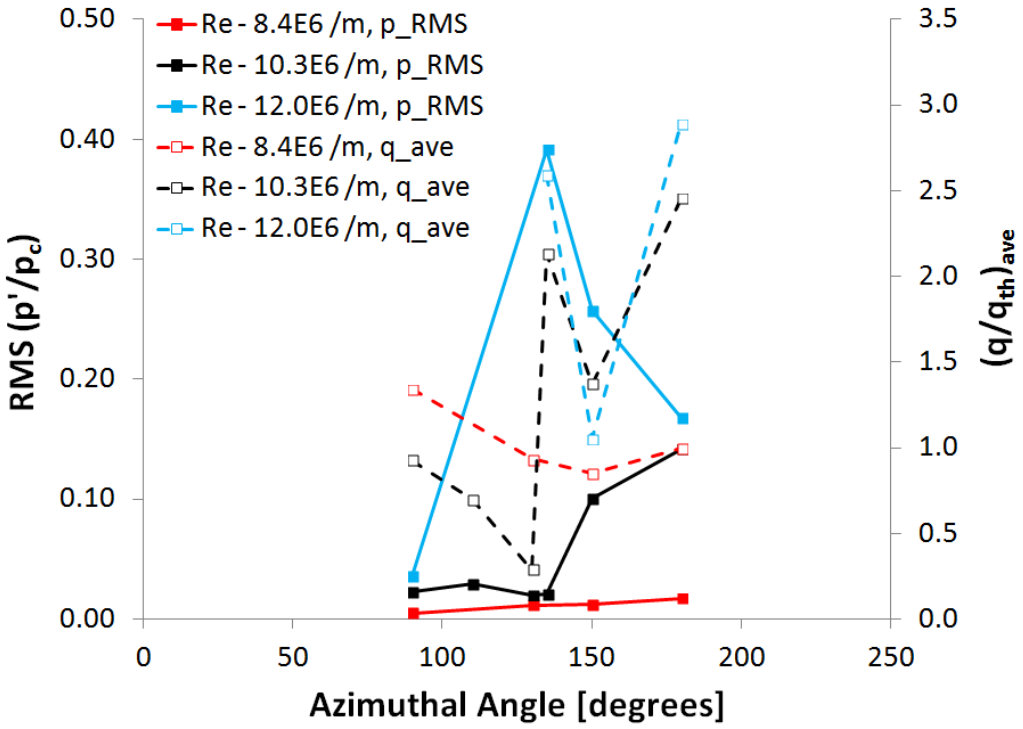

Figure 6.19.: RMS of pressure and average heat transfer at various Reynolds numbers and azimuthal angles. Sensor located at 0.362 m from the nosetip. Heat transfer determined at 0.35 m from the nosetip. Smooth insert under quiet flow.

6.5 Validation of Travelling Wave Measurements with PCB Sensors

PCB sensors were used to verify the results with the Kulite sensors. This was done to show that the measurements of the travelling waves were not sensor dependent or affected by sensor resonance. Figure 6.20 shows the PSD of pressure data from a PCB and Kulite sensor at the same azimuthal and axial location (90° and 0.36 m, respectively) under approximately the same quiet flow conditions. Both sensors show a peak in the spectra near 40–50 kHz, due to the travelling crossflow instability. The amplitude of the peaks differ, and this difference may be due to either the uncertainty in the PCB calibration or the larger spatial averaging than the Kulite. Recall that the PCB is high-pass filtered at 11 kHz, which is not far below the peak frequency of the travelling crossflow wave. Therefore, Kulites were typically used for the travelling crossflow measurements when possible. The PCB sensor shows additional content at higher frequencies. It is not clear if this is an additional higher-frequency instability, or electronic noise. Unfortunately, no TSP images are available on the 90° ray for this run. The Kulite resonance is seen as a peak near 300 kHz.

Both sensors were then tested near an azimuthal angle of 120° under quiet flow. The PSD of pressure data from two different PCBs and one Kulite are shown in Figure 6.21. The red and blue traces were obtained at a Reynolds number of approximately 10.3×10^6/m. The blue trace was obtained at a Reynolds number of approximately 12.0×10^6/m. Once again, both the PCB and Kulite sensors show a low-frequency peak near 40 kHz, this time with similar amplitudes. At a Reynolds number of 10.3×10^6/m, the spectra for the PCB sensor shows slightly higher broadband noise. It is not known if this is because of electrical noise or transitional flow. The sensor was not in view for this particular run so no TSP images are available. At the higher Reynolds number, the PCB shows an increase in broadband noise that is likely caused by transitional flow.

Many times, the Kulites measure the travelling waves, but the PCBs do not. A sample case is shown in Figure 6.22, at a Reynolds number of 10.3×10^6/m. Perhaps

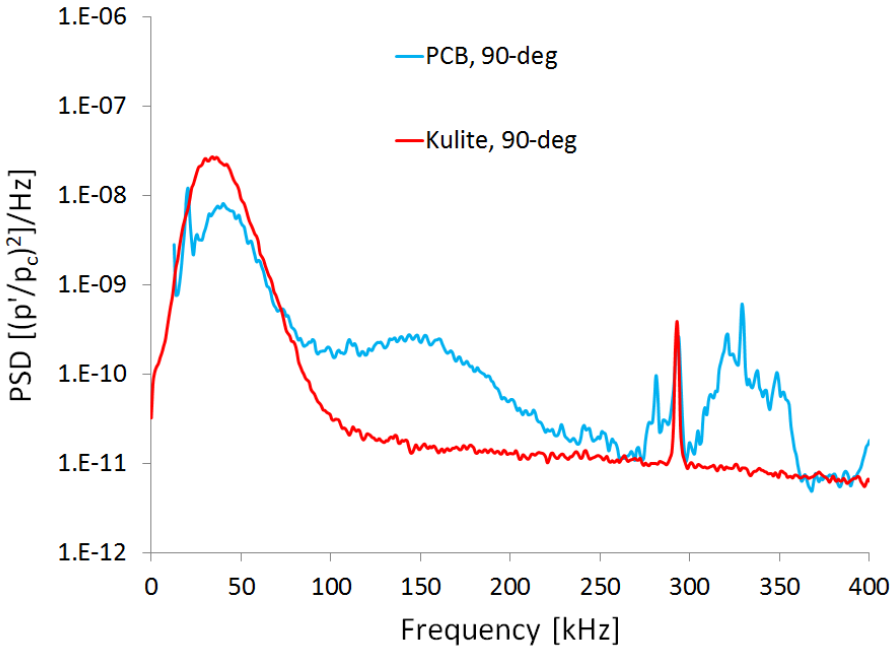

Figure 6.20.: PSD of Kulite and PCB 0.36 m from the nosetip and an azimuthal angle of 90°. Smooth insert under quiet flow. Re - 10.3×10^6/m.

the amplitude of the waves is close to the resolution limit of the PCB. Table 6.2 listed the RMS amplitude of the travelling crossflow waves at various Reynolds numbers under both noisy and quiet flow. Under quiet flow, other than at the highest Reynolds number, the RMS amplitude was either close to the 0.001 psi pressure resolution of the PCB, or much smaller. The most amplified travelling waves have a frequency near 40 kHz and a wave speed near 200 m/s, yielding a wavelength of approximately 5 mm. The PCB sensor has a diameter of 3.75 mm, while the actual sensing area is a 1.3 by 1.3 mm square. The PCB sensing length is almost 26% of the most amplified travelling crossflow wavelength. The Kulite sensing length is approximately 18% of the most amplified travelling crossflow wavelength. Therefore, the difference in the spatial averaging of the Kulite and the PCB sensor is not significantly different. It appears that pressure resolution may be the dominant issue with the PCB sensors for measuring the travelling waves, as compared to the Kulite sensor. Under quiet flow,

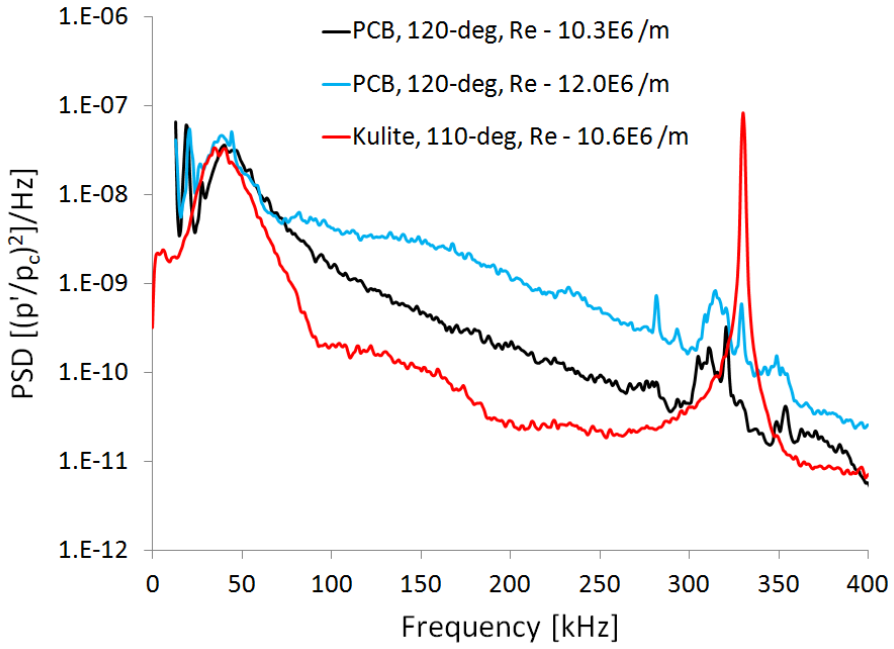

Figure 6.21.: PSD of Kulite and PCB 0.36 m from the nosetip and an azimuthal angle near 120°. Smooth insert under quiet flow. Reynolds number of 10.3×10^6/m or 12.0×10^6/m.

it appears that the Kulite sensors are more apt for measuring the travelling crossflow waves.

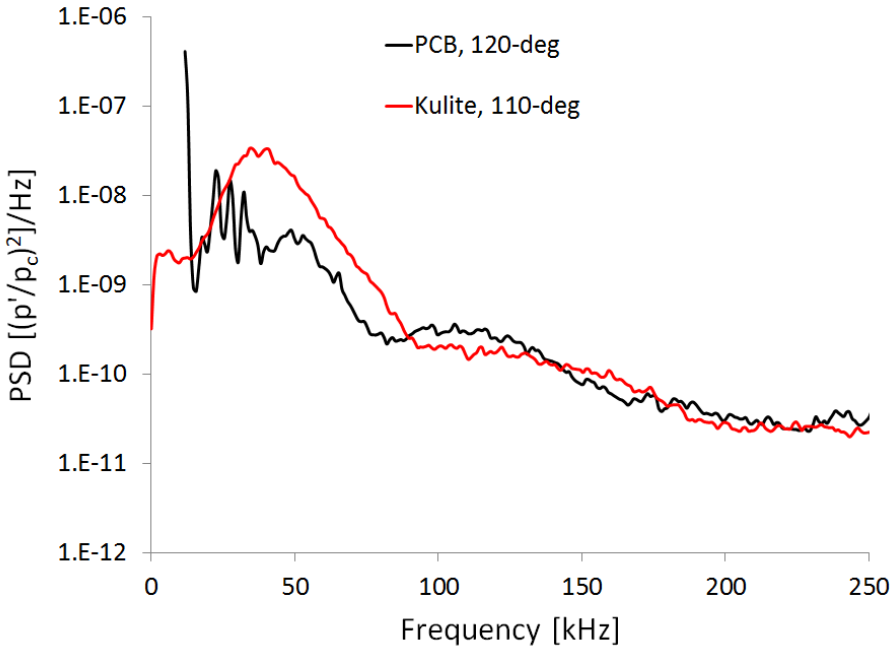

Figure 6.22.: PSD of Kulite and PCB 0.36 m from the nosetip and an azimuthal angle near 120°. Smooth insert under quiet flow. Re - 10.3×10^6/m. Travelling wave not visible on PCB.

6.6 Comparison to TUB Measurements

Comparisons were made between data collected in the TU Braunschweig conventional tunnel (HLB) by Munoz [58] and data from the quiet tunnel at Purdue. HLB has a free-stream noise level of 1–1.5% and a Mach number of 5.8–5.95. When the BAM6QT is run noisy, the freestream noise level is 3% and the Mach number is 5.8. Under quiet flow, the BAM6QT has a freestream noise level of approximately 0.02% and a Mach number of 6.0.

Figure 6.23 plots the PSD of pressure measurements from both tunnels under noisy flow. The HLB data were collected from a PCB sensor on the 90° ray, 0.257 m from the nosetip. The BAM6QT data were collected from a PCB sensor 0.321 m from the nosetip and a Kulite sensor 0.362 m from the nosetip, with both sensors on the 90° ray. The Reynolds number is based on the axial distance from the nosetip

along the centerline. Both the HLB and BAM6QT raw datasets were analyzed with the same MATLAB code and non-dimensionalized by the theoretical edge pressure of a 7° half-angle cone at 0° angle of attack.

All the sensors show a low-frequency travelling crossflow instability, near 30 to 40 kHz. The difference in amplitudes between the measurements made in the two tunnels with the PCB sensors is likely caused by slightly differing conditions, tunnel noise levels, and sensor calibrations. The Kulite in the BAM6QT also measures the travelling waves, at a slightly lower frequency (likely because the Kulite is further downstream than the PCBs).

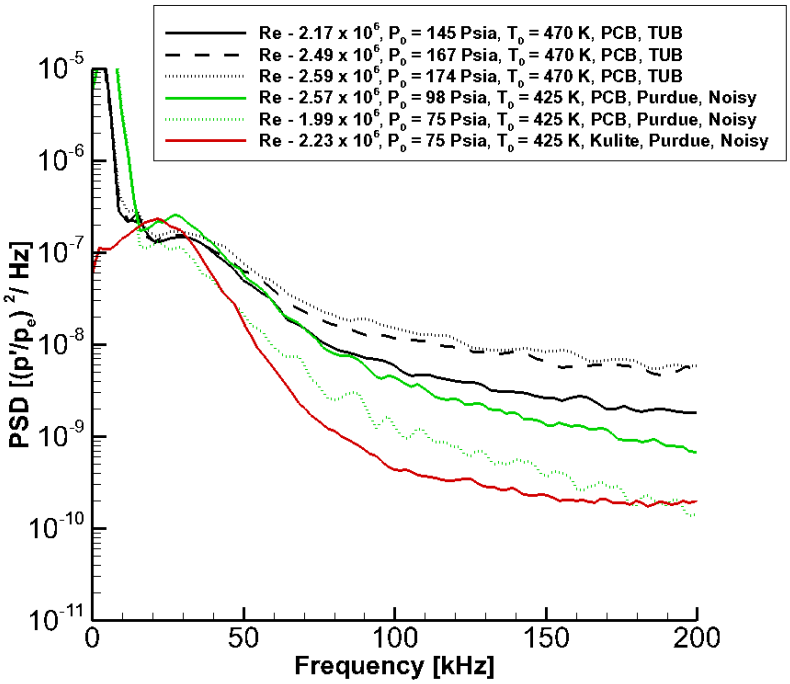

Figure 6.23.: PSD of Kulite and PCB sensors in both the HLB and BAM6QT under noisy flow. HLB PCB at x = 0.257 m from nosetip. BAM6QT PCB at x = 0.321 m and Kulite at x = 0.362 m from the nosetip.

The BAM6QT was also run quiet, and this data is shown along with the noisy flow data in Figure 6.24. At similar Reynolds numbers as the HLB and BAM6QT noisy runs, the travelling waves are barely visible under quiet flow and almost three orders of magnitude smaller in power than the waves under noisy flow. As the Reynolds number increases, the magnitude of the travelling waves increases, but it is still smaller than the amplitude of the travelling waves under noisy flow at lower Reynolds numbers. Once again, it is not known whether the difference in wave amplitude is caused by non-linear growth of the waves or the differing free-stream noise levels which alters the initial conditions of the waves, or both.

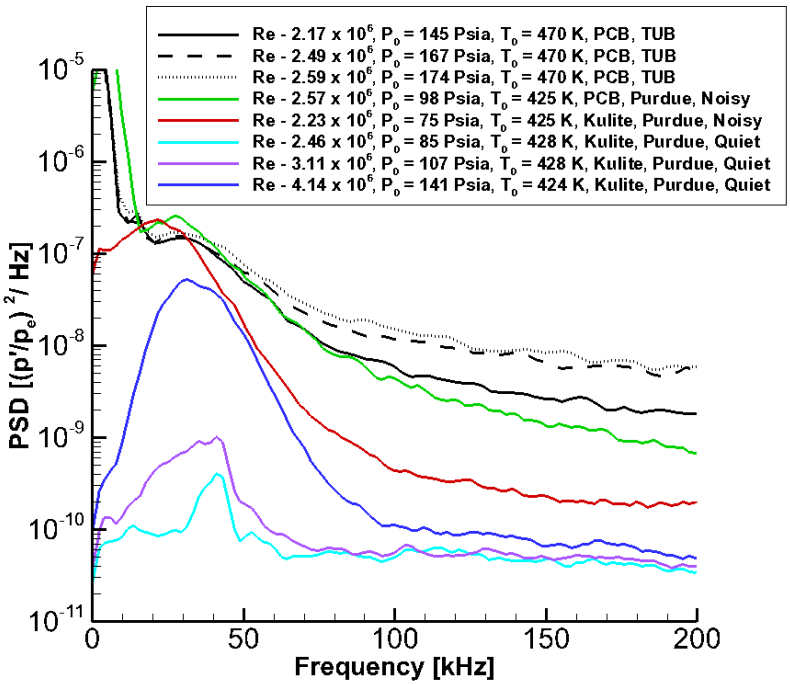

Figure 6.24.: PSD of sensors in the BAM6QT under noisy and quiet flow, and in the HLB. HLB PCB at x = 0.257 m from nosetip. BAM6QT PCB at x = 0.321 m and Kulite at x = 0.362 m from the nosetip.

6.7 Effect of Wall Temperature on Travelling Crossflow Waves

Borg looked at the repeatability of travelling wave measurements on an elliptical cone in the BAM6QT [73]. It was found that the measured peak frequency agreed from run to run, but the amplitude of the waves did not. The amplitudes were found to vary by up to an order of magnitude. It was hypothesized that the amplitudes of the waves were being affected by the increasing model temperature throughout the course of a day, because after each run the model temperature increases due to subsonic convection. The model temperature was not measured so therefore this hypothesis could not be confirmed.

Here, five consecutive runs were performed at approximately the same Reynolds number of 10.0×10^6/m. For the first four runs, the runs were performed as quickly as possible, allowing the model to heat up as much as possible. The fifth run was performed after allowing the model to cool down for several hours. Figure 6.25 plots the PSD of pressure data from a Kulite 0.36 m axially from the nosetip and at an azimuthal angle of 110° from the windward ray for the five runs. For all five runs, the spectra show approximately the same travelling-crossflow peak frequency near 40 kHz. As the wall temperature increases, the amplitude of the wave increases. Comparing runs 1 and 4, the wall temperature increases by about 4.3% and the amplitude increases by a factor of approximately 1.8. This increase in amplitude is not as significant as the order of magnitude change Borg measured. Run 5, which was performed after allowing the model to cool down, shows a similar amplitude to Run 3 and both have similar wall temperatures. Thus, the travelling waves seem to be very sensitive to small changes in the model wall temperature. This may be a linear amplification effect, but computations are necessary to understand the issue.

The Kulites are quoted as being temperature compensated between 70°F and 400°F (294 K to 478 K). The thermal sensitivity is ±1% of voltage amplitude per 100°F (56 K). Figure 6.26 includes the same data as Figure 6.25, but with allowing for a ±1% change in the voltage output for Run4. The grey curve represents the Run 4

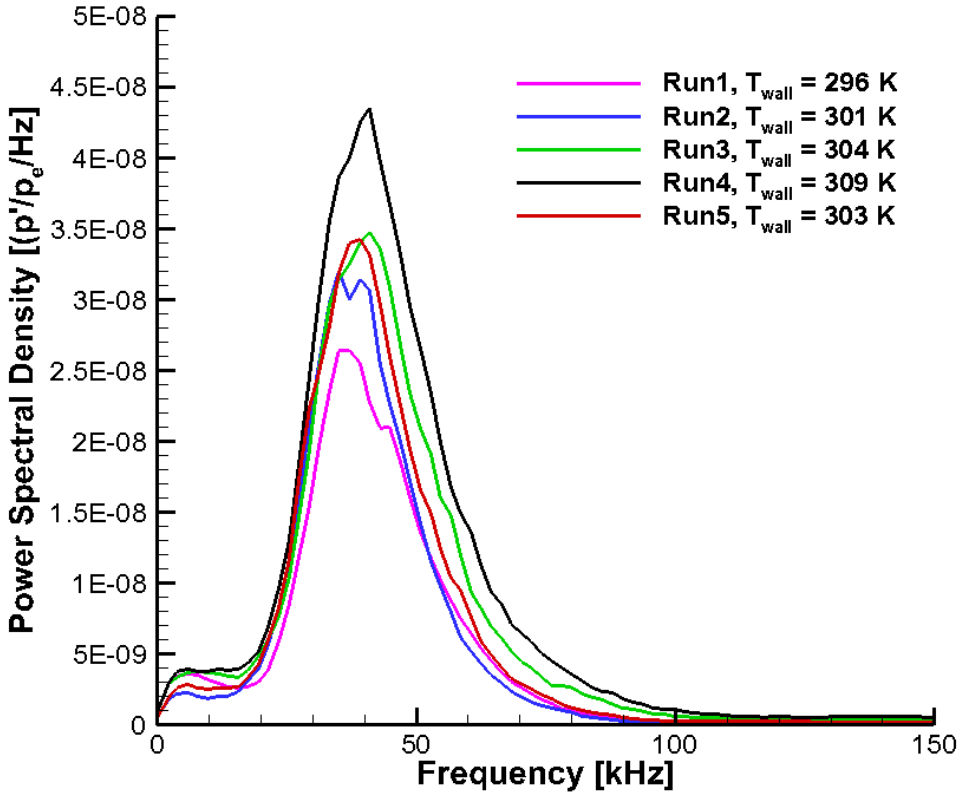

Figure 6.25.: Power spectral density of surface pressure at an axial distance of 0.36 m and an azimuthal angle of 110° with varying wall temperatures. Re = 10.0×10^6/m.

data with a 1% increase in amplitude, and the brown curve represents the data with a 1% decrease in amplitude. The ±1% change in amplitude simulates a ±56 K change in model wall temperature, much larger than is seen in the tunnel. The differences between the three curves is small, and much smaller than the amplitude difference from Run 1 to Run 4, which represents a 13 K change in temperature. Therefore the thermal sensitivity of the sensors appears to have minimal impact on the change in amplitude of the travelling waves as the wall temperature changes.

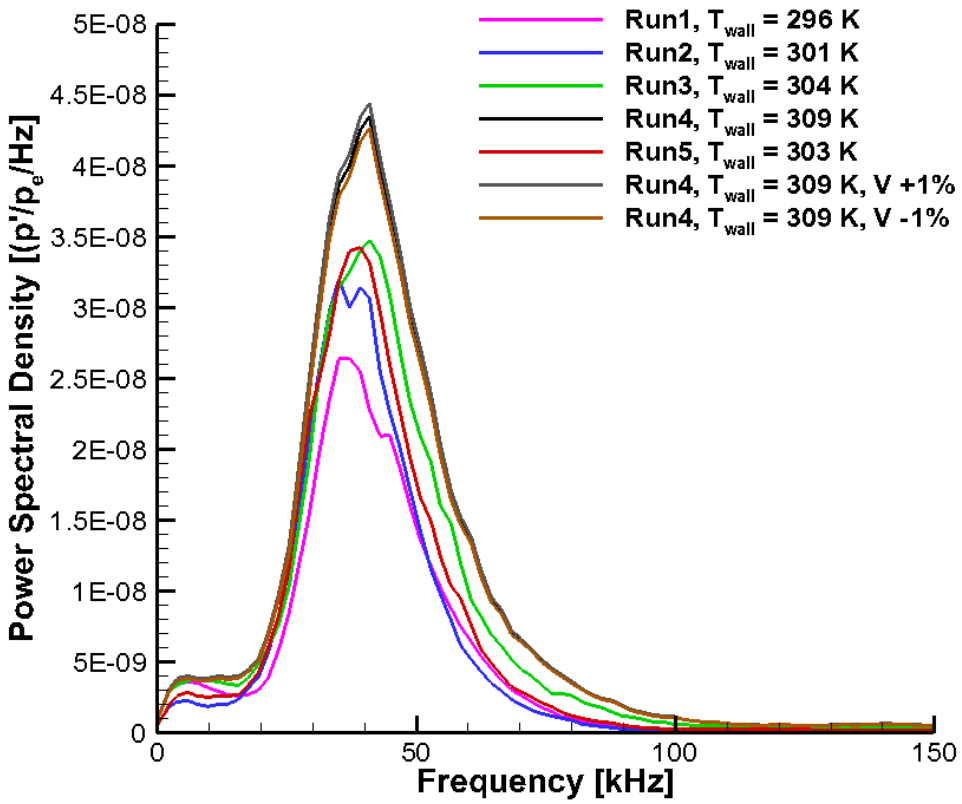

Figure 6.26.: Data from Figure 6.25 including data showing impact of Kulite thermal sensitivity. Re = 10.0×10^6/m.

7. INTERACTION OF STATIONARY AND TRAVELLING WAVES

7.1 Random Distributed Roughness

Tests were done with distributed roughness patches added to the cone, far downstream of the neutral point of the most amplified stationary waves [62]. Roughness was added to the cone via nail polish as shown in Figure 7.1 or by a rough paint finish. Three sets of tests were done; one with a smooth paint finish, one with a patch of rough paint, and one with two patches of rough nail polish. The RMS roughness of the smooth paint and the nail polish was measured with a Mitutoyo (Model number SJ-301) surface roughness tester. The smooth paint had an RMS roughness of 0.37 μm. The downstream nail polish patch had an RMS roughness of 0.90 μm, an axial location of 23.5 cm, and spanned from approximately 80–100° azimuthally. The upstream nail polish patch had an RMS roughness of 3.1 μm, an axial location of 19.2 cm, and spanned from approximately 60–100° azimuthally. Unfortunately, the rough paint patch was not characterized before removing via sanding. Figure 7.1 also shows the location of the Kulite pressure transducer array for the nail-polish-roughness tests. The Kulite array was fixed at an azimuthal angle of approximately 90° from the windward ray.

The three sets of tests were performed under quiet flow at a unit Reynolds number of approximately 10×10^6/m. The TSP images for the tests are shown in Figure 7.2. Comparing the smooth wall to the rough paint patch, it is clear that the rough paint is generating larger stationary waves. The case with the nail polish roughness also shows stationary waves with a slightly larger magnitude as compared to the smooth case. The higher heat transfer seen near the lee ray for the smooth and nail-polish roughness cases may be due to the slightly lower model wall temperature, or

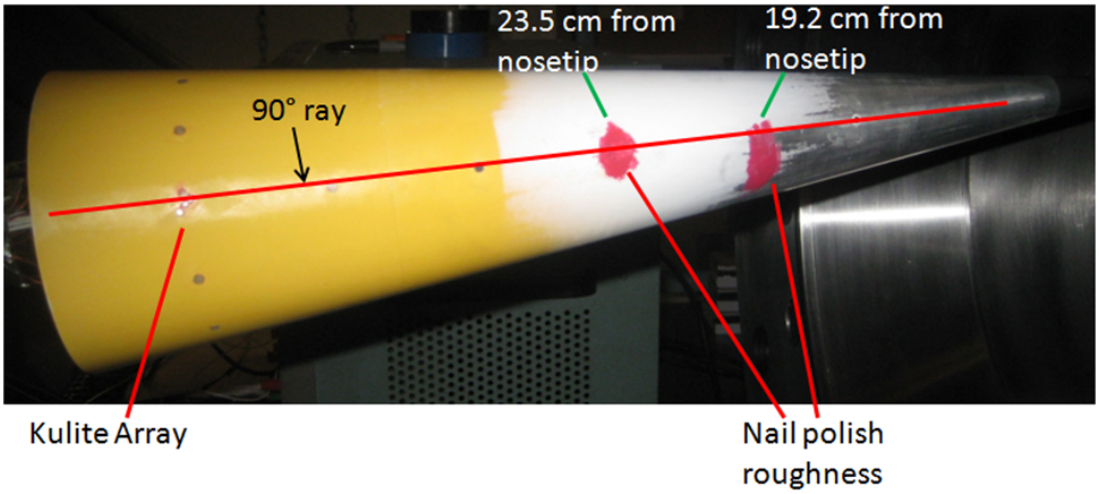

Figure 7.1.: 7° half-angle cone with Kulite array and nail polish roughness patches. Kulite sensors shown on 90° ray.

inaccuracies in the TSP calibration process. This becomes more clear in Figure 7.3, which plots the spanwise heat transfer profiles (normalized by the theoretical mean heat transfer of a 7° half-angle cone at 0° AoA) of the TSP images in Figure 7.2, at an axial location of 0.35 m. Once again, the nail polish roughness and rough paint cases are producing larger magnitude stationary waves compared to the smooth paint case, with the rough paint case producing the largest stationary waves. The Kulite array is near an azimuthal angle of 90°.

Table 7.1 shows the RMS of the non-dimensional heat transfer for the three spanwise profiles shown in Figure 7.3. The first row shows the RMS levels between 60 and 120°, and the second row shows the RMS levels between 80 and 100°. For both azimuthal ranges, the rough paint profile shows the largest RMS values. The nail polish roughness shows the second largest RMS values. The RMS levels for the smaller azimuthal range were calculated because they represents the magnitude of the waves that pass over the Kulite sensor array.

Travelling crossflow waves were measured using a Kulite 90° from the windward ray. The PSD of the Kulite is shown in Figure 7.4 for the three roughness cases.

Table 7.1.: RMS of non-dimensional heat transfer profiles shown in Figure 7.3.

Azimuthal Range	**Smooth**	**Nail Polish Roughness**	**Rough Paint**
60–120°	0.13	0.18	0.47
80–100°	0.12	0.22	0.45

The smooth case shows a peak at approximately 40 kHz, which appears to be the travelling crossflow waves. When the random roughness is increased on the cone and the magnitude of the stationary waves increases, the magnitude of the travelling waves decreases. The nature of this interaction between the travelling and stationary waves may be significant in the growth of the crossflow instability modes and the nature of crossflow-induced transition, but it is poorly understood.

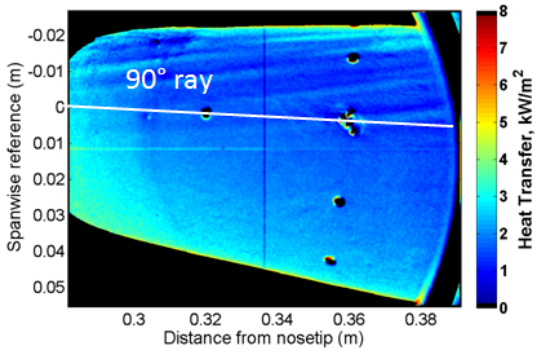

(a) Smooth paint. $p_0 = 141$ psia, Re $= 11.5\times10^6$/m, $T_0 = 423$ K, $T_w = 298$ K

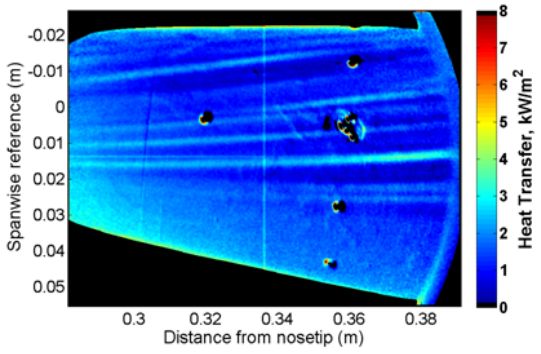

(b) Rough paint patch. $p_0 = 140$ psia, Re $= 11.2\times10^6$/m, $T_0 = 430$ K, $T_w = 304$ K

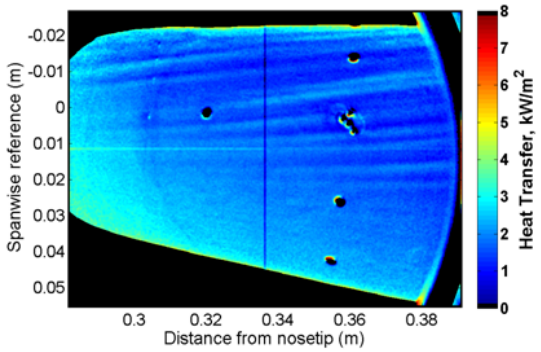

(c) Nail polish roughness. $p_0 = 139$ psia, Re $= 11.5\times10^6$/m, $T_0 = 421$ K, $T_w = 299$ K

Figure 7.2.: TSP images of the yaw side of the cone with varying random roughness under quiet flow.

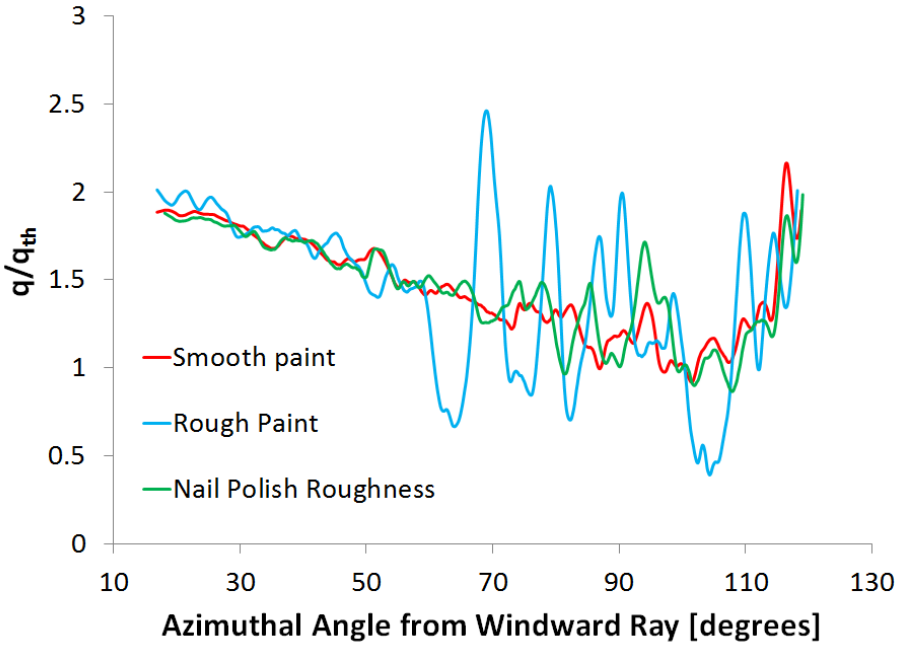

Figure 7.3.: Spanwise heat-transfer profiles at an axial distance of 0.35 m from the TSP images in Figure 7.2. Kulite pressure transducer located at 90°.

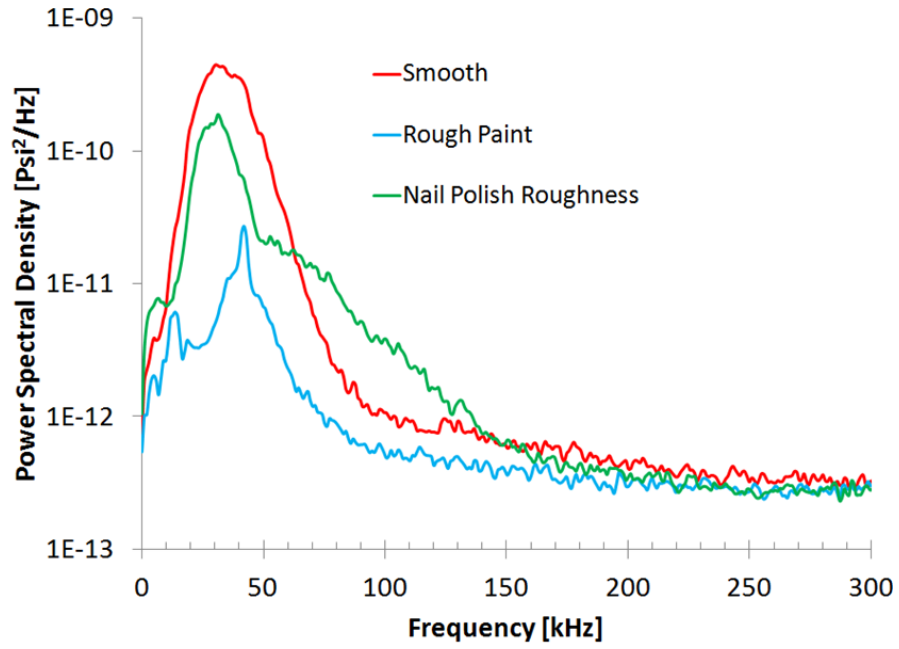

Figure 7.4.: Power spectral density of surface pressure from a Kulite sensor at an axial distance 0.36 m and an azimuthal angle of 90°.

Sometimes between tunnel entries the cone has to be repainted due to photo-degradation of the TSP. Each time the cone is repainted, the random roughness of the smooth paint job is altered despite the RMS roughness being approximately the same. Therefore, each time the cone is repainted, a slightly differing pattern of stationary vortices is realized, because it is thought that the stationary vortices are introduced by the random roughness on the cone. Figure 7.5 shows three TSP images with three different smooth paint jobs with the yaw side of the cone imaged. The Kulite array is circled in the second TSP image. The first Kulite (k61) is nearer to the leeward ray (top of the image) and the fourth Kulite (k64) is nearer to the windward ray (bottom of image) for all three images. In Figure 7.5(a) (case 1), there appears to be a stationary vortex just downstream of the Kulite array but not passing over the array, although it is not entirely clear in the image. In Figure 7.5(b) (case 2), a stationary vortex is passing over the fourth Kulite (k64). In Figure 7.5(c) (case 3), a stationary vortex is passing over the second and third Kulites (k62 and k63).

The PSD of the pressure data from the Kulites for the three cases are shown in Figure 7.6. The Kulites are located approximately 0.36 m from the nosetip on the 90° azimuthal ray. When there appears to be no stationary waves passing over the sensors (case 1), the spectra in Figure 7.6(a) show all three Kulites measuring the low frequency travelling waves, although at slightly differing frequencies with slightly differing amplitudes. The first Kulite (k61) also measures slightly more power at frequencies near 0 kHz. The reason for this is not known. Note that the fourth Kulite was not working for this test.

The spectra for the case when the stationary vortex is passing over the fourth Kulite (k64) is shown in Figure 7.6(b). The first two Kulites show a similar spectra, measuring the travelling crossflow waves near 40 kHz. The fourth Kulite shows a significant damping of the travelling waves (approximately an order of magnitude), along with an increase in content at frequencies near 0 kHz. Note that the third Kulite was not working for this test.

The third case shows a stationary vortex passing over the second and third Kulites, and the spectra is shown in Figure 7.6(c). The first and fourth Kulites show a similar spectra, measuring the travelling waves with a peak frequency near 40 kHz, although the fourth Kulite measures the waves with a smaller amplitude. The second Kulite measures a distorted wave, where the magnitude of travelling wave is decreased. The second Kulite also measures an increase in content near 0 kHz. The third Kulite shows an even greater damping of the travelling waves. From this data, it appears that when a stationary vortex is near or passing over a pressure sensor, the pressure sensor measures a distorted or damped travelling crossflow wave as compared to a sensor that does not have a stationary vortex passing over it. Once again, the nature of this travelling-stationary wave interaction may be significant but is poorly understood.

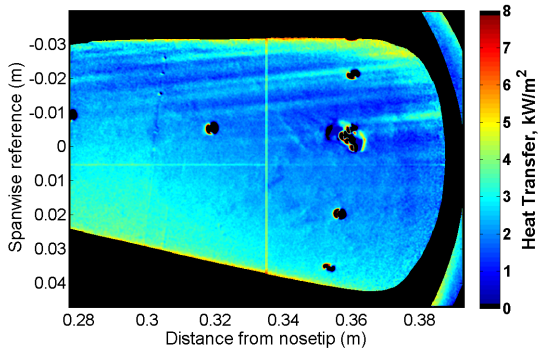

(a) Case 1: Stationary wave passing over no sensors. $p_0 = 158$ psia, Re $= 12.1\times10^6$/m, $T_0 = 421$ K, $T_w = 298$ K

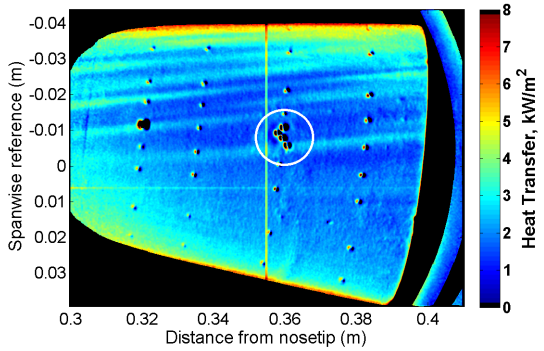

(b) Case 2: Stationary wave passing over k64. $p_0 = 160$ psia, Re $= 12.3\times10^6$/m, $T_0 = 422$ K, $T_w = 303$ K.

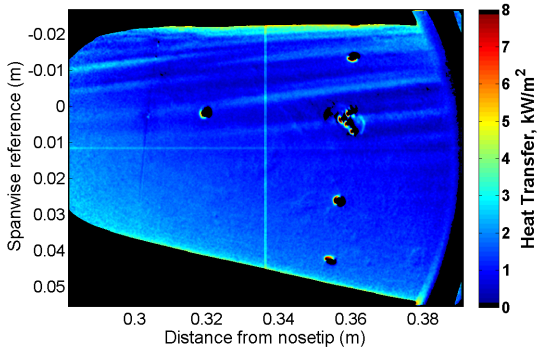

(c) Case 3: Stationary wave passing over k62 and k63. $p_0 = 160$ psia, Re $= 12.4\times10^6$/m, $T_0 = 425$ K, $T_w = 302$ K

Figure 7.5.: TSP images under quiet flow with smooth insert. Yaw side of the cone.

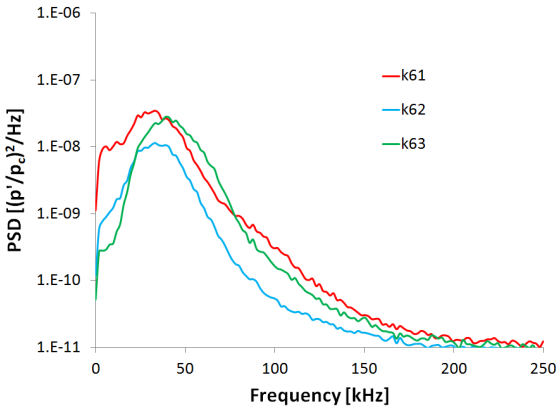

(a) Case 1: Stationary wave passing over no sensors.

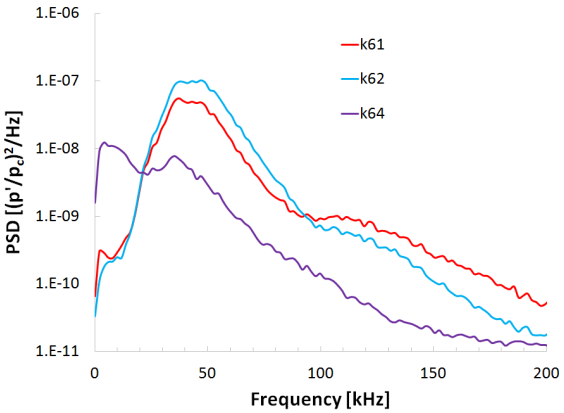

(b) Case 2: Stationary wave passing over k64.

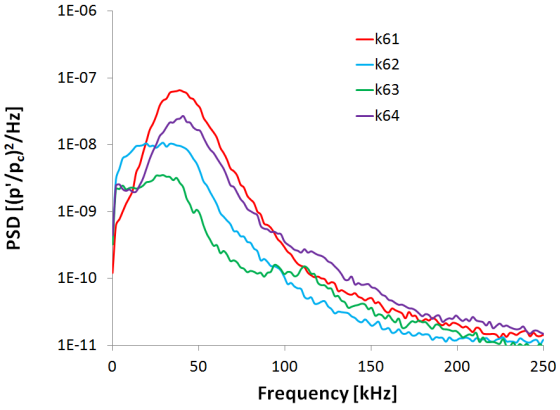

(c) Case 3: Stationary wave passing over k62 and k63.

Figure 7.6.: Power spectral density of the Kulite sensor array, 0.36 m from the nosetip, near 90° from the windward ray. Quiet flow with smooth insert. Re = 10.3×10^6/m.

7.2 Controlled Roughness With Torlon Inserts

Experiments were then performed to see if this effect could be induced in a controlled way with the Torlon inserts. The first set of tests were done with the Kulite array (circled in Figure 7.7(a)) on the 90° azimuthal ray, with both the smooth and 50-dimpled (#3) Torlon inserts at three different Reynolds numbers under quiet flow. The TSP images are shown in Figure 7.7. Restricting focus to near the Kulite sensor array, at the lowest Reynolds number, there is not a significant difference in terms of stationary vortex amplitude or location between the smooth and roughness insert cases. At the middle Reynolds number, the roughness insert appears to be producing larger stationary vortices near the Kulite array, but not entirely clear. At the largest Reynolds number, the stationary vortices appear larger in magnitude near the Kulite array when the 50-dimpled insert is used.

Spanwise heat transfer profiles at an axial distance of 0.35 m of the TSP images in Figure 7.7 are shown in Figure 7.8. Once again, the Kulite array is at the 90° azimuthal angle. For all three cases, the peak-to-peak amplitude of the stationary waves appears to be slightly larger near the Kulite array when the roughness insert is used. This is not a surprising result as many of the experiments presented in Chapter 5 showed that the roughness insert had a significant effect on the stationary waves, although it is expected that the roughness insert will show a larger effect on the stationary waves nearer to the lee ray (for the downstream location imaged in the TSP figures).

The power spectral density of a Kulite (k61, closest to the top of the image) in the sensor array is shown in Figure 7.9. At the lowest Reynolds number, the PSD are similar, with the rough case showing a slightly smaller amplitude peak at the travelling-wave frequency. Increasing the Reynolds number, the rough case shows a reduction in the travelling wave amplitude, while the amplitude of the stationary waves increase with the added roughness. This is similar to the results shown in Section 7.1, but the effect is now present with controlled roughness.

Figure 7.10 plots the RMS of the non-dimensional pressure fluctuations between 0 and 70 kHz measured with the Kulite pressure transducer 0.36 m from the nosetip on the 90° ray for the three Reynolds numbers. The RMS pressure fluctuations are plotted with closed symbols. Plotted on the secondary axis with open symbols is the RMS of the non-dimensional heat transfer (q/qth) at an axial distance of 0.35 m between 85 and 95°. This plot shows that the smooth case produces larger travelling waves based on the larger pressure fluctuation amplitudes, for a given Reynolds number. The spanwise heat transfer profiles showed that in the region of the sensor, the stationary vortices were typically larger when the roughness was used. This results in a larger RMS of the non-dimensional heat transfer in the region of the sensor, as seen in the plot. For a given Reynolds number, the smooth case shows a larger pressure fluctuation amplitude while the rough case shows a larger heat transfer amplitude. Therefore, it appears that the larger stationary vortices are damping the travelling waves.

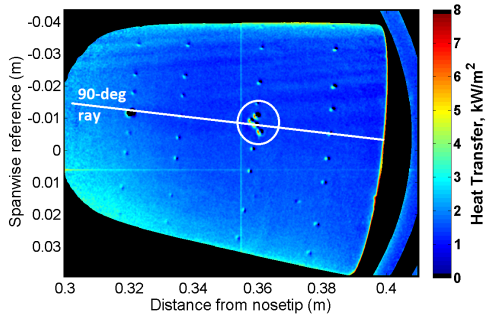

(a) Smooth. $p_0 = 110$ psia, Re $= 8.5\times10^6$/m, $T_0 = 420$ K, $T_w = 306$ K

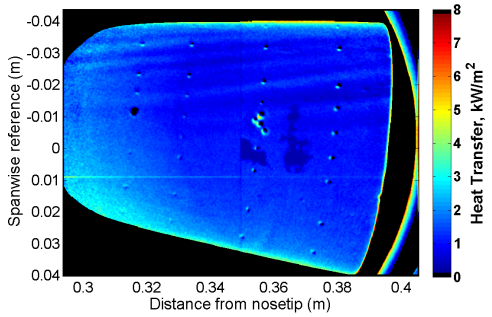

(b) 50 dimples (#4). $p_0 = 110$ psia, Re $= 8.4\times10^6$/m, $T_0 = 425$ K, $T_w = 298$ K

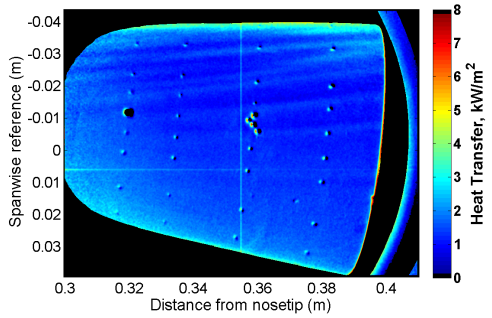

(c) Smooth. $p_0 = 140$ psia, Re $= 10.8\times10^6$/m, $T_0 = 420$ K, $T_w = 307$ K

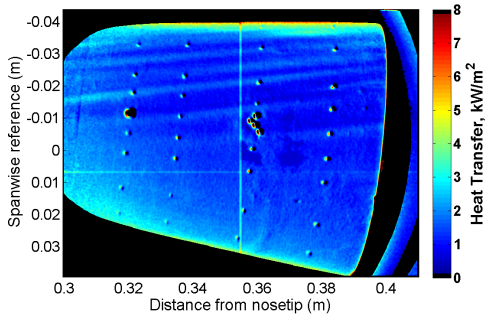

(d) 50 dimples (#4). $p_0 = 141$ psia, Re $= 10.7\times10^6$/m, $T_0 = 424$ K, $T_w = 301$ K

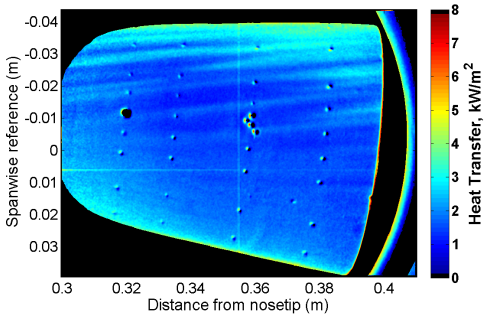

(e) Smooth. $p_0 = 160$ psia, Re $= 12.4\times10^6$/m, $T_0 = 419$ K, $T_w = 306$ K

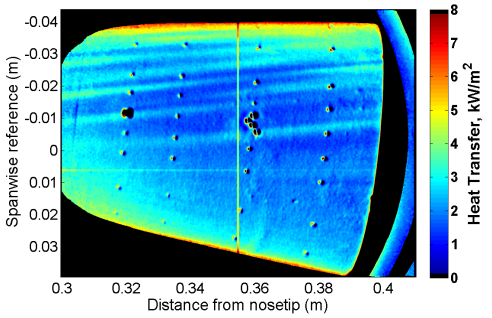

(f) 50 dimples (#4). $p_0 = 161$ psia, Re $= 12.3\times10^6$/m, $T_0 = 422$ K, $T_w = 304$ K

Figure 7.7.: TSP images under quiet flow with smooth and 50-dimpled insert. Yaw side of the cone. Kulite sensors on 90° ray.

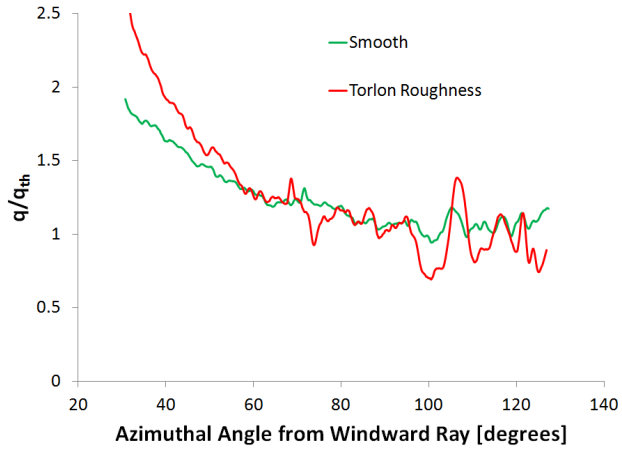

(a) Re = 8.5×10^6/m

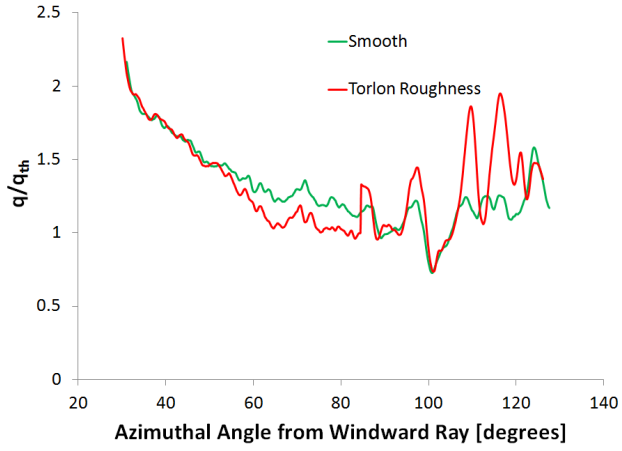

(b) Re = 10.8×10^6/m.

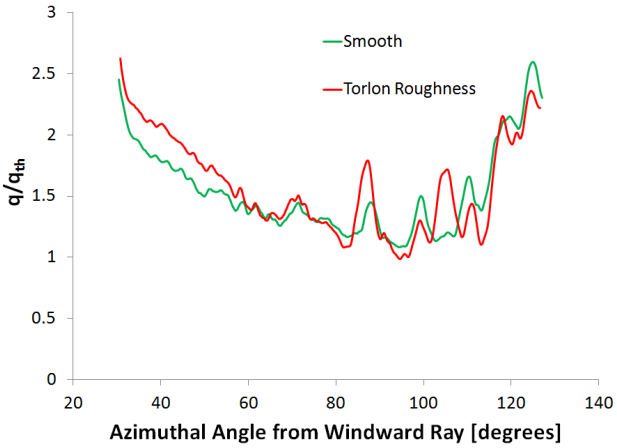

(c) Re = 12.3×10^6/m.

Figure 7.8.: Spanwise temperature profiles at x =0.35 m of TSP images in Figure 7.7. Kulite sensor near 90° azimuthal angle.

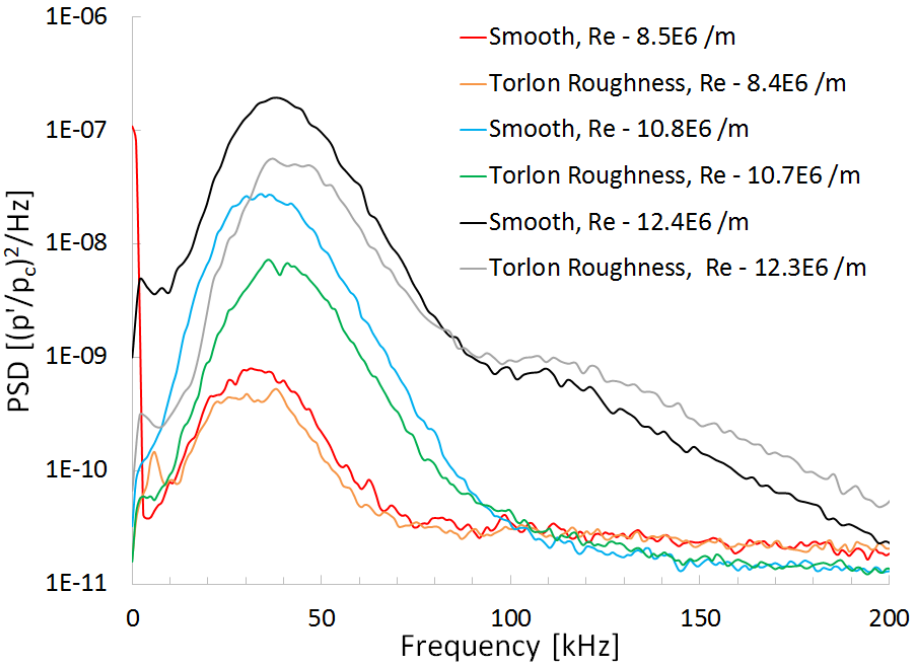

Figure 7.9.: Power spectral density of surface pressure (measured by k61) at an axial distance 0.36 m and an azimuthal angle of 90° under quiet flow.

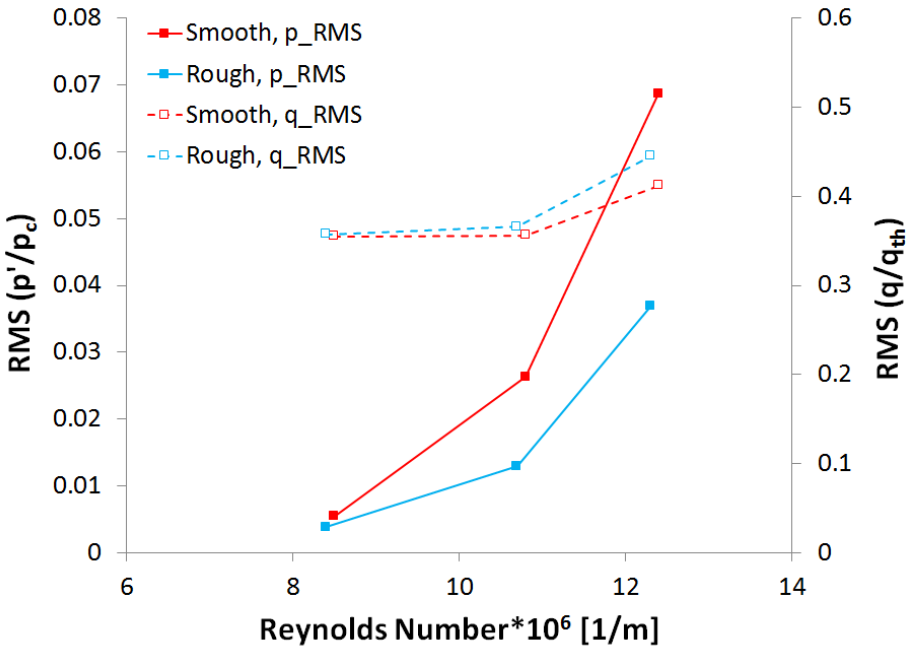

Figure 7.10.: RMS of the pressure fluctuations between 0 and 70 kHz (sensor 0.36 m from the nosetip on the 90° azimuthal ray) and the RMS of the heat transfer near the sensor for a range of Reynolds numbers with both the smooth and rough (#4) Torlon inserts under quiet flow.

The same set of tests were done with the Kulite array 130° from the windward ray under quiet flow. The TSP images are shown in Figure 7.11, with the Kulite array circled in Figure 7.11(a) for reference. The patch of TSP near an axial distance of 0.33 m and a spanwise reference of 0.0 m that shows a much lower level of heat transfer than the surrounding TSP several images is due to saturation of some of the CCD camera pixels and should be ignored. The lowest Reynolds number case shows two TSP images that almost look identical, although stationary vortices may be faintly visible just downstream of the Kulite array for the rough case but not in the smooth case. The stationary vortices become visible when the Reynolds number is increased, and it appears that the roughness insert is producing larger stationary vortices. At the highest Reynolds number, the pattern of stationary vortices is clearly different when the roughness is added, and there appears to be larger stationary vortices near the sensor array.

Spanwise heat transfer profiles of the TSP images are shown in Figure 7.12, at an axial distance of 0.35 m. The lowest Reynolds number spanwise profiles for both the smooth and rough cases are similar. The middle Reynolds number shows similar amplitude stationary vortices near the Kulite array, but with a slightly different spacing. At the highest Reynolds number, the smooth and rough profiles are very dissimilar.

The power spectral density of the pressure data from the Kulite (k61) on the 130° ray is shown in Figure 7.13. At the lowest Reynolds number, the smooth and rough cases show almost identical spectra, which agrees with the TSP data, and the travelling waves are not seen. The middle Reynolds number shows a dampening of the travelling waves when the roughness insert is added. Even though the amplitudes of the stationary waves did not increase appreciably when the roughness was added for the middle Reynolds number case, the spacing of the vortices did change. At the largest Reynolds number, the smooth cases shows the travelling crossflow waves near 40 kHz. When the roughness insert is added, the peak in the spectra is no longer visible, and there is a broadband increase in noise suggesting that the boundary layer is breaking down to turbulence near the Kulite sensor. Again the dampening of the

travelling waves is seen when the sensor measures the wave with both the smooth and rough insert. It appears that not only the amplitude but the location of the stationary wave has an effect on the travelling wave.

Figure 7.14 plots the RMS of the non-dimensional pressure fluctuations between 0 and 70 kHz measured with the Kulite pressure transducer 0.36 m from the nosetip on the 130° ray for the three Reynolds numbers. The RMS pressure fluctuations are plotted with closed symbols. Plotted on the secondary axis with open symbols is the RMS of the non-dimensional heat transfer (q/qth) at an axial distance of 0.35 m between 125° and 135°. Only points where the travelling waves were clear in Figure 7.13 were added. Once again, it is seen that for a given Reynolds number, the smooth case shows a larger pressure fluctuation amplitude while the rough case shows a larger heat transfer amplitude near the sensor.

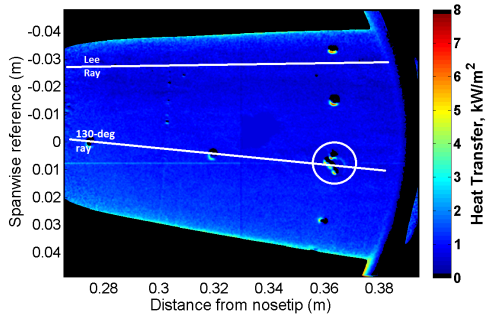

(a) Smooth. $p_0 = 82.4$ psia, Re $= 6.4\times10^6$/m, $T_0 = 418$ K, $T_w = 302$ K

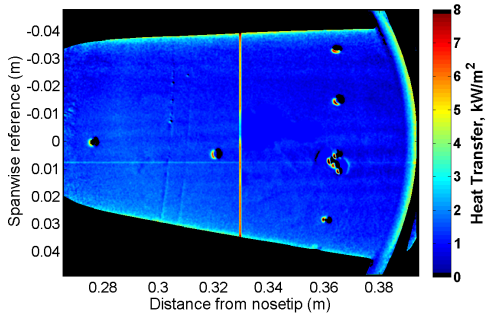

(b) 50 dimples (#4). $p_0 = 82.6$ psia, Re $= 6.4\times10^6$/m, $T_0 = 419$ K, $T_w = 302$ K

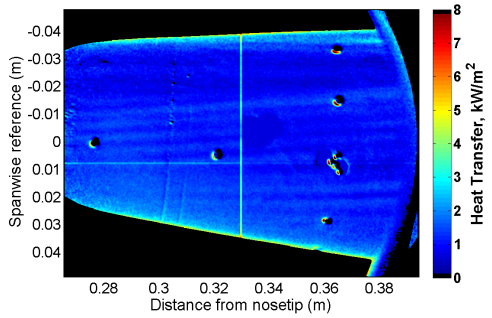

(c) Smooth. $p_0 = 107.7$ psia, Re $= 8.2\times10^6$/m, $T_0 = 423$ K, $T_w = 301$ K

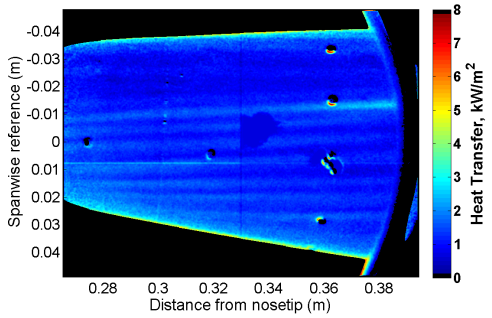

(d) 50 dimples (#4). $p_0 = 107.3$ psia, Re $= 8.2\times10^6$/m, $T_0 = 420$ K, $T_w = 302$ K

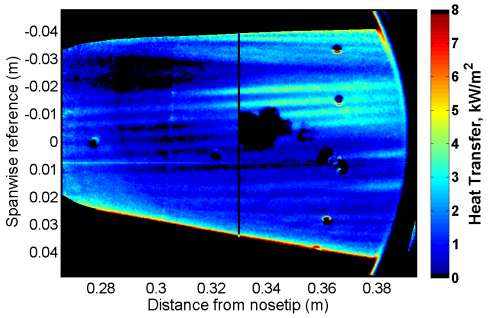

(e) Smooth. $p_0 = 133.6$ psia, Re $= 10.1\times10^6$/m, $T_0 = 425$ K, $T_w = 297$ K

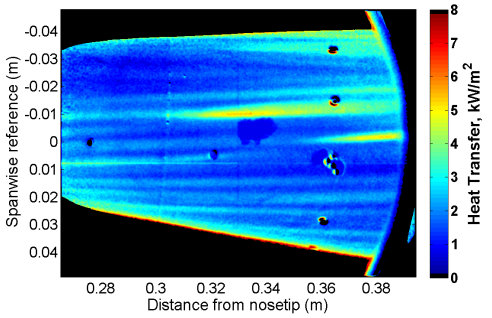

(f) 50 dimples (#4). $p_0 = 135.3$ psia, Re $= 10.4\times10^6$/m, $T_0 = 421$ K, $T_w = 301$ K

Figure 7.11.: TSP images under quiet flow with smooth and 50-dimpled insert. Yaw side of the cone Kulite sensors on 130° ray.

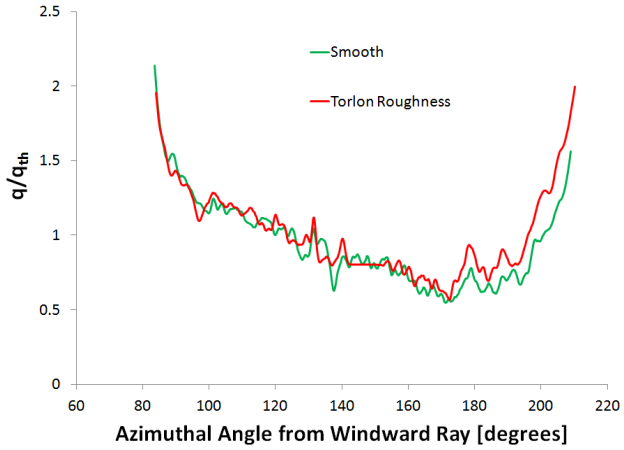

(a) Re = 6.4×10^6/m

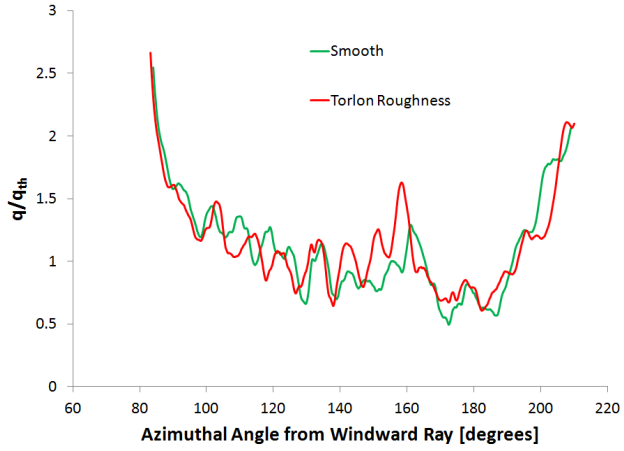

(b) Re = 8.2×10^6/m.

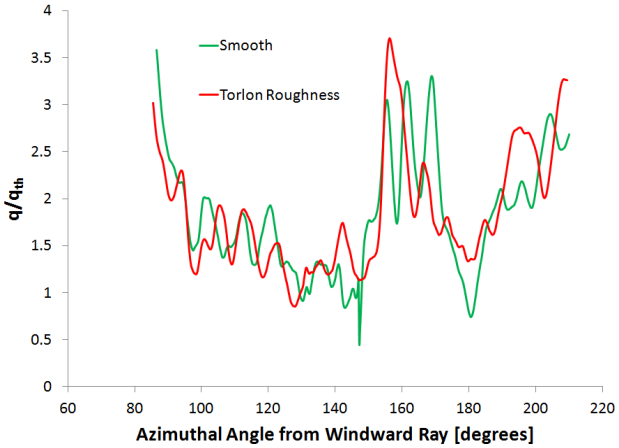

(c) Re = 10.4×10^6/m.

Figure 7.12.: Spanwise heat transfer profiles at x =0.35 m of TSP images in Figure 7.11 under quiet flow. Kulite sensor near the 130° azimuthal ray.

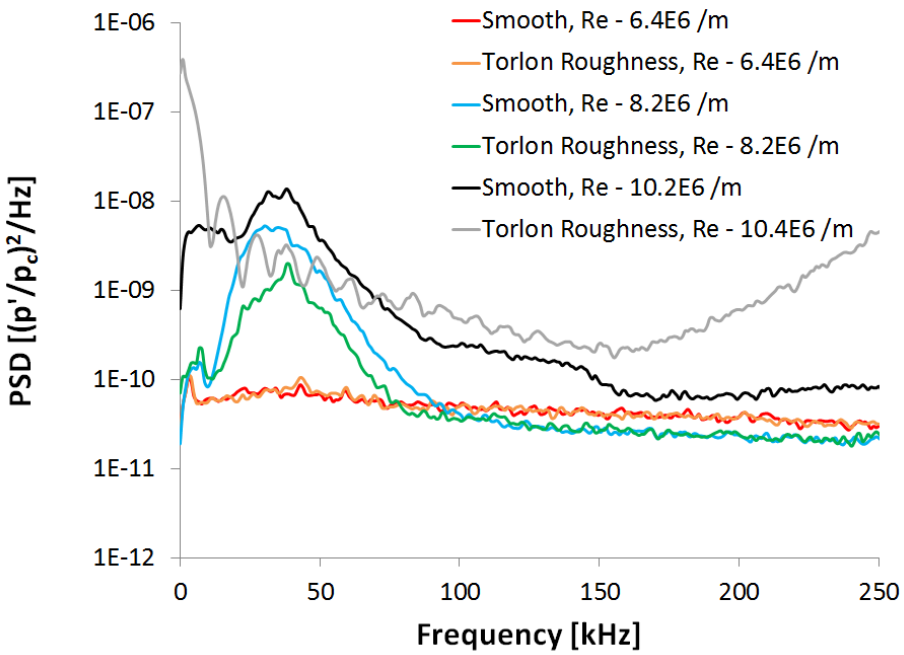

Figure 7.13.: Power spectral density of surface pressure (measured by k61) at an axial distance 0.36 m and an azimuthal angle of 130° under quiet flow.

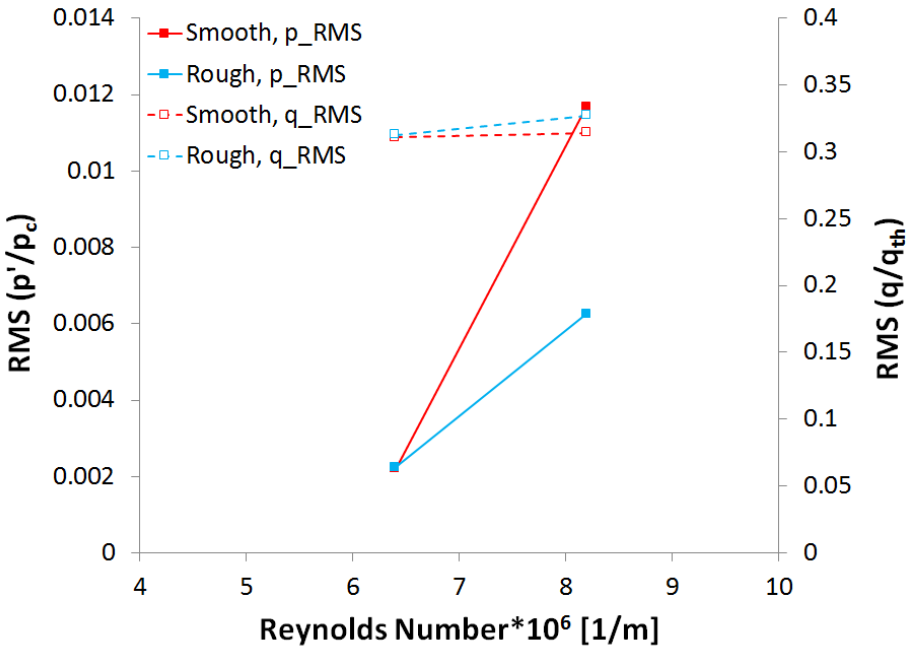

Figure 7.14.: RMS of the pressure fluctuations between 0 and 70 kHz (sensor 0.36 m from the nosetip on the 130° azimuthal ray) and the RMS of the heat transfer near the sensor for a range of Reynolds numbers with both the smooth and rough (#4) Torlon inserts.

Finally, the Kulite sensor array was moved to an azimuthal array of 150°. The TSP images are shown in Figure 7.15 for a range of Reynolds numbers with the Kulite array circled in Figure 7.15(a). At the smallest Reynolds number, there is not a significant difference between the smooth and rough cases. At the middle Reynolds number, the stationary vortices are barely visible for the smooth case. Adding the roughness insert, the stationary vortices are more clear, especially near the Kulite array. At the largest Reynolds number, there is clearly a different pattern of stationary vortices being generated by the roughness insert. Near the Kulite array, the stationary vortices may be breaking down to turbulence for both the smooth and the rough case, but this is not entirely clear in the TSP image.

Spanwise heat transfer profiles at an axial distance of 0.35 m were taken of the TSP images in Figure 7.15, and shown in Figure 7.16. At the lowest Reynolds number, the most significant difference between the rough and smooth cases are seen near the location of the Kulite array (150°). The smooth case shows two larger stationary vortices at approximately 145° and 155°, but the rough case shows a larger stationary vortex at 150°. At the middle Reynolds number, the rough case shows much larger stationary vortices from approximately 110° to 180°, but at the location of the Kulite both cases appear to be producing a similar sized stationary vortex. At the highest Reynolds number, the rough case produces larger stationary vortices near the location of the Kulite array (150°). Close to the lee ray, the smooth case produces large stationary vortices while it appears that the boundary layer may be breaking down to turbulence for the rough case. The transitioning of the boundary layer will become more clear when looking at the PSD of the pressure sensors.

The spectra of one Kulite in the sensor array (k61) is shown in Figure 7.17. The Kulite k61 was chosen for all the plots because it is the only Kulite that worked for all the runs. The other Kulites, when working, showed similar trends. At the lowest Reynolds number, the travelling crossflow waves are visible at 40 kHz for the smooth case. When the rough insert is used, the waves are damped. Recall that the rough-case spanwise profile showed a larger stationary vortex near the sensor location.

At the middle Reynolds number, the stationary vortices had a similar amplitude for both cases near the Kulite sensor. Although the spectra show a smaller amplitude travelling wave for the rough case, there is a broadband increase in noise suggesting that the travelling and or the stationary waves may be breaking down to turbulence. There is also the appearance of a second peak in the frequency near 200 kHz. This peak may be caused by the secondary instability of the stationary crossflow waves, and will be discussed further in Chapter 8. At the highest Reynolds number, both spectra show an increase in broadband noise, suggesting that the boundary layer is breaking down to turbulence. The rough insert spectra shows a slight peak near 150 kHz, which once again may suggest the presence of the secondary instability of the stationary waves.

Figure 7.18 plots the RMS of the non-dimensional pressure fluctuations between 0 and 70 kHz measured with the Kulite pressure transducer 0.36 m from the nosetip on the 150° ray for the three Reynolds numbers. The RMS pressure fluctuations are plotted with closed symbols. Plotted on the secondary axis with open symbols is the RMS of the non-dimensional heat transfer (q/qth) at an axial distance of 0.35 m between 145 and 155°. Once again, only points where the travelling waves were clear in Figure 7.13 were added. As with the other plots, this plot shows that as the amplitude of the stationary wave increases based on the increase in the RMS heat transfer, the amplitude of the travelling wave decreases based on the decrease in RMS pressure.

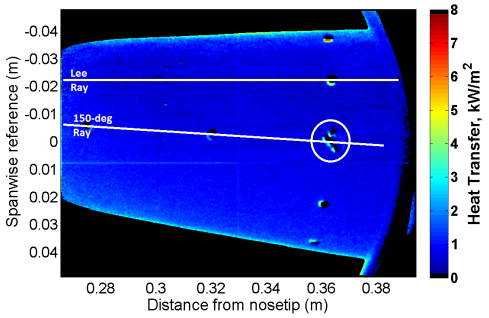

(a) Smooth. $p_0 = 82.6$ psia, Re $= 6.4\times10^6$/m, $T_0 = 419$ K, $T_w = 306$ K

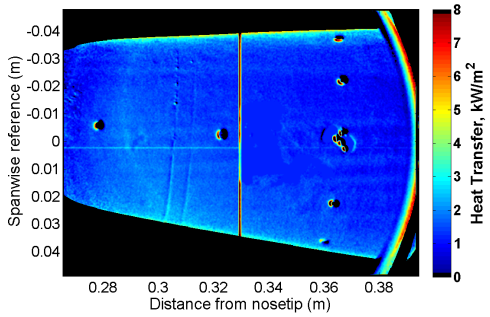

(b) 50 dimples (#4). $p_0 = 82.8$ psia, Re $= 6.4\times10^6$/m, $T_0 = 420$ K, $T_w = 302$ K

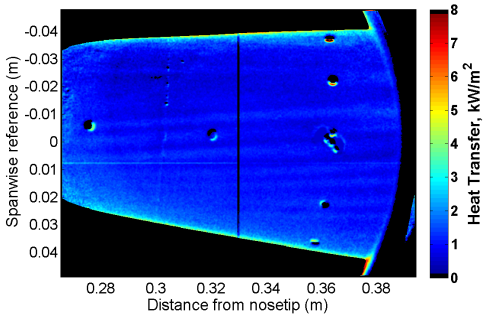

(c) Smooth. $p_0 = 107.7$ psia, Re $= 8.3\times10^6$/m, $T_0 = 420$ K, $T_w = 303$ K

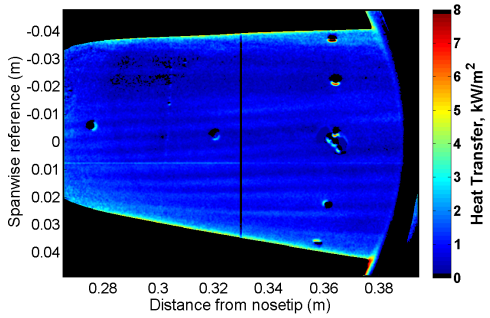

(d) 50 dimples (#4). $p_0 = 107.1$ psia, Re $= 8.2\times10^6$/m, $T_0 = 422$ K, $T_w = 302$ K

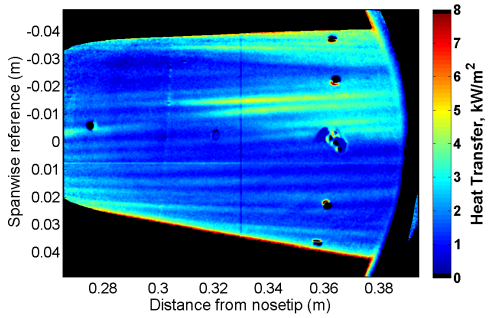

(e) Smooth. $p_0 = 133.2$ psia, Re $= 10.2\times10^6$/m, $T_0 = 421$ K, $T_w = 303$ K

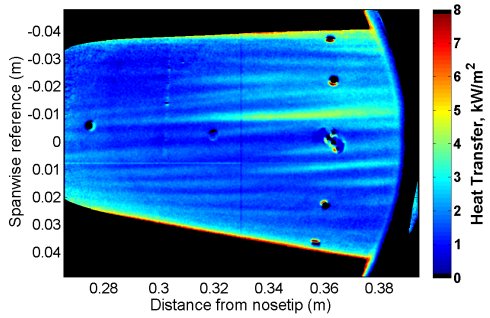

(f) 50 dimples (#4). $p_0 = 134.1$ psia, Re $= 10.4\times10^6$/m, $T_0 = 418$ K, $T_w = 304$ K

Figure 7.15.: TSP images under quiet flow with smooth and 50-dimpled insert. Yaw side of the cone. Kulite sensors on 150° ray.

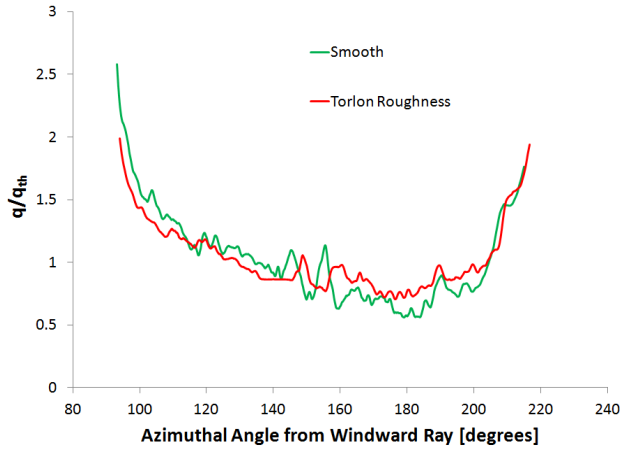

(a) Re = 6.4×10^6/m

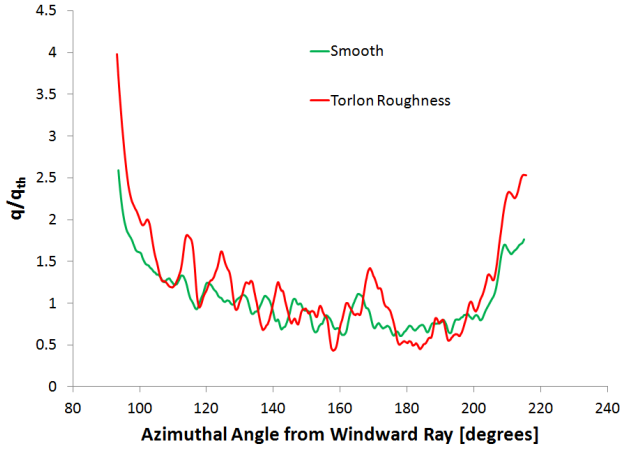

(b) Re = 8.2×10^6/m.

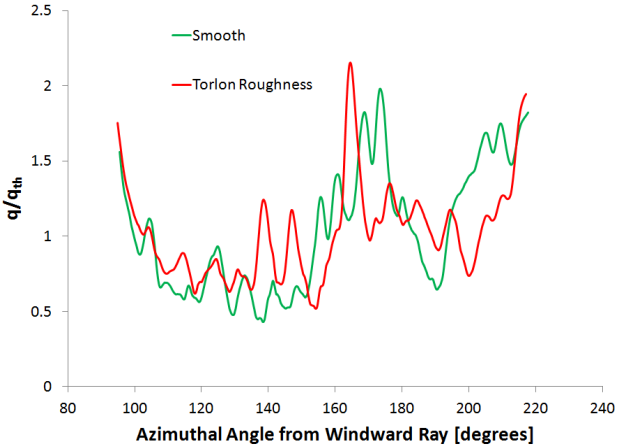

(c) Re = 10.3×10^6/m.

Figure 7.16.: Spanwise temperature profiles at x =0.35 m of TSP images in Figure 7.15. Kulite sensor near 150° azimuthal angle.

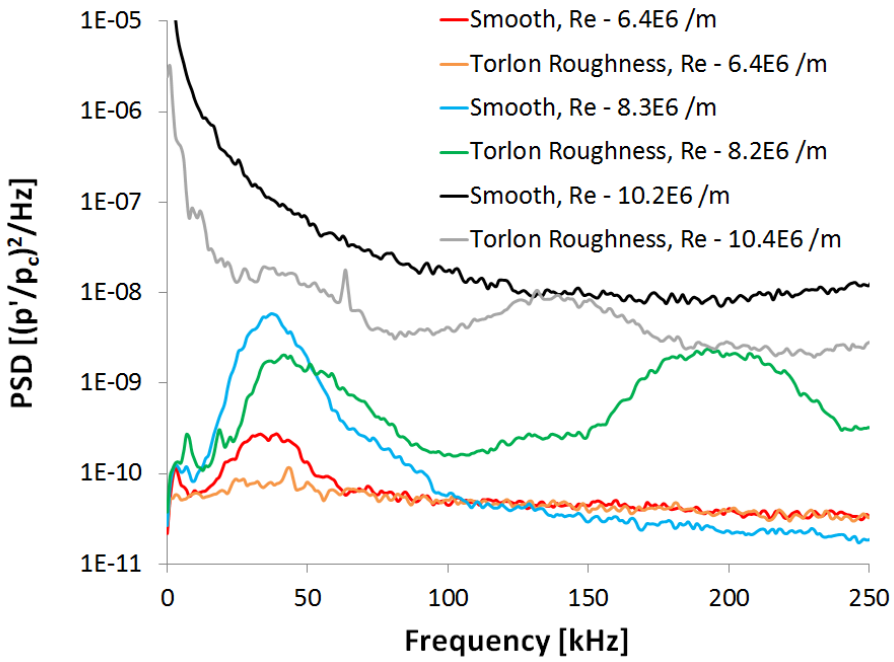

Figure 7.17.: Power spectral density of surface pressure (measured by k61) at an axial distance 0.36 m and an azimuthal angle of 150° under quiet flow.

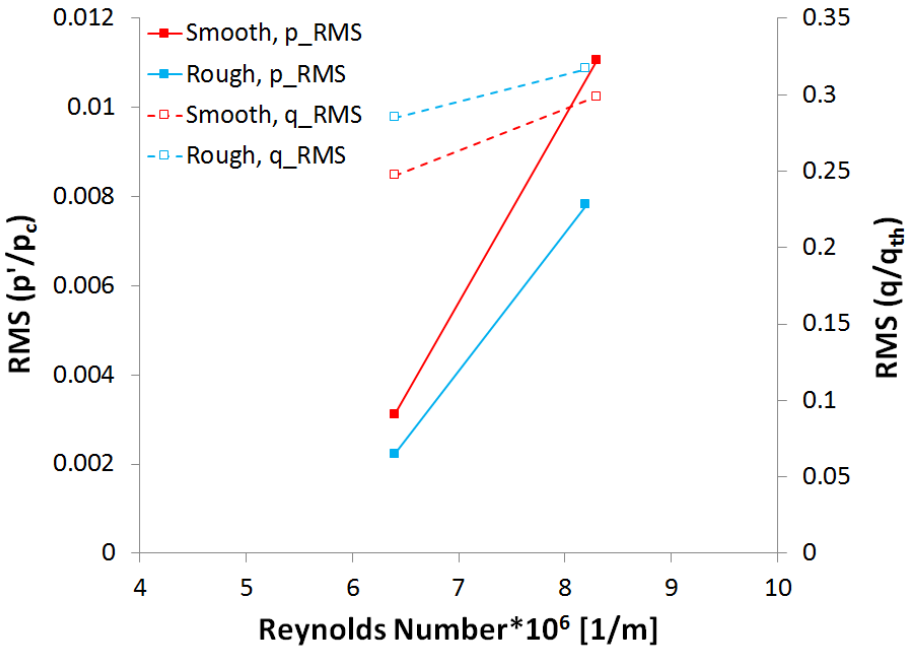

Figure 7.18.: RMS of the pressure fluctuations between 0 and 70 kHz (sensor 0.36 m from the nosetip on the 150° azimuthal ray) and the RMS of the heat transfer near the sensor for a range of Reynolds numbers with both the smooth and rough (#4) Torlon inserts.

8. SECONDARY INSTABILITY OF STATIONARY CROSSFLOW WAVES

Data has been collected that seems to show the travelling secondary instability of the stationary crossflow waves. The secondary instability appears near the point of saturation of the stationary vortices and grows rapidly until the waves break down. Figure 8.1 shows two TSP images at similar quiet flow conditions with the smooth insert and a 50-dimpled Torlon insert (#3). The red line represents the lee ray, and the Kulite array is 150° from the windward ray (circled in image). Limiting focus to near the Kulite array, for the smooth case the stationary vortices are barely visible. When the roughness insert is added, the magnitude of the stationary waves increases greatly near the Kulite array, especially near the Kulite closest to the windward ray. The stationary waves may be breaking down to turbulence just downstream of the sensors.

The PSD of the Kulite sensor closest to the windward ray is shown in Figure 8.2 with both the smooth and rough Torlon inserts. For both cases, the primary travelling crossflow waves are measured near 40–50 kHz. When the roughness insert is added and the stationary waves grow large near and downstream of the sensors, a second peak in the PSD appears near 150 kHz. This peak may correspond to the travelling secondary instability of the primary stationary waves.

Figure 8.3 shows both the maximum heat transfer and the amplitude of the stationary vortex identified in Figure 8.1(b). This stationary vortex passes over the Kulite (k64) closest to the wind ray. The maximum heat transfer at each axial location was found by taking a spanwise heat transfer profile and picking out the maximum values. From low speed experiments and theory, the secondary instability of the stationary waves is said to appear near the saturation point of the station-

ary vortices [21, 22]. From these plots, it appears that the stationary vortex may be saturating near 0.375 m from the nosetip, just downstream of the sensor location.

Figure 8.4 plots the growth rate of the stationary vortex. The growth rate was calculated based on the maximum heat transfer measured in the streak. There is a significant amount of scatter in the plot due to the fluctuations in amplitudes seen in Figure 8.3(b). The general trend is a decrease in growth rate. The growth rate approaches 0 (saturating) at an axial distance of approximately 0.375 m, agreeing with the amplitude data. The sensor is just upstream of this saturation point (approximately 0.015 m). Depending how large the surface pressure footprint of the secondary instability is, the upstream sensor may be measuring this instability (assuming that the secondary instability appears at the saturation location).

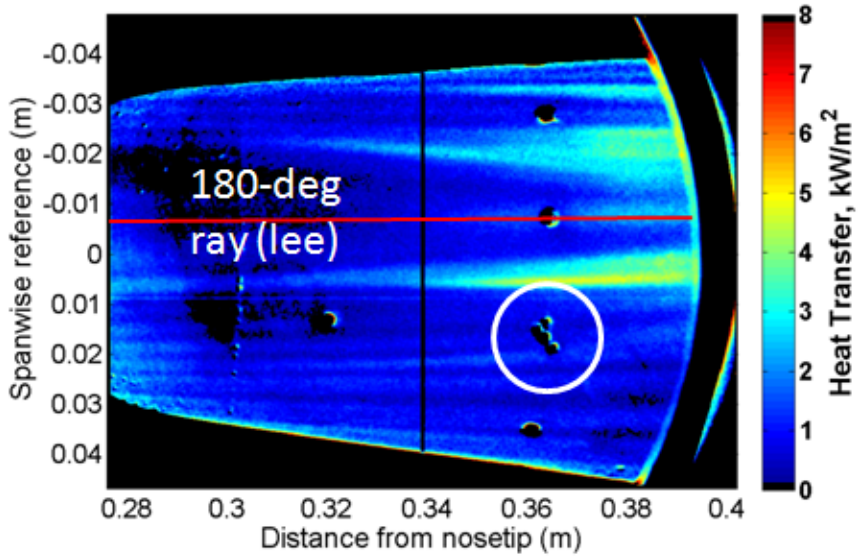

(a) Smooth. $T_{wall} = 300$ K

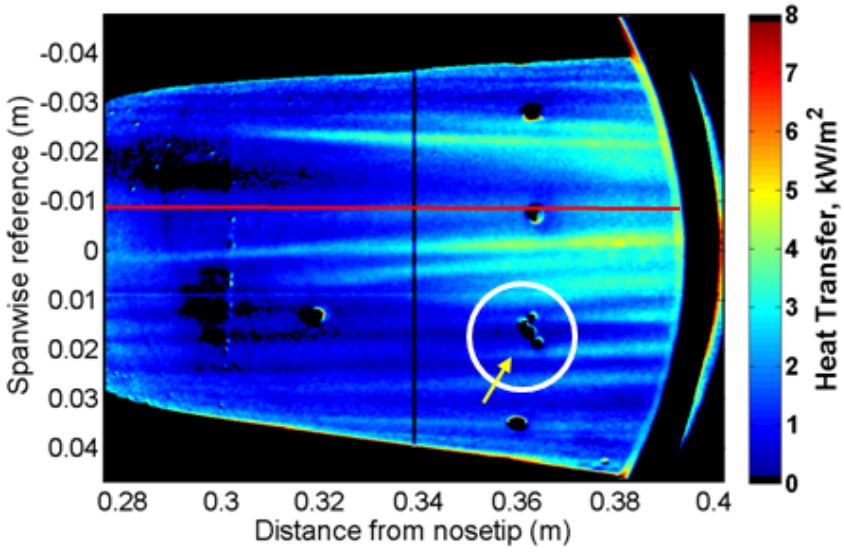

(b) 50-dimpled insert (#3). $T_{wall} = 300$ K

Figure 8.1.: TSP images with smooth and rough inserts under quiet flow. Red line indicates the lee ray, and the Kulite array is 150° from the windward ray (circled in the images). Re = 9.3×10^6/m, $p_0 = 140$ psia, $T_0 = 435$ K.

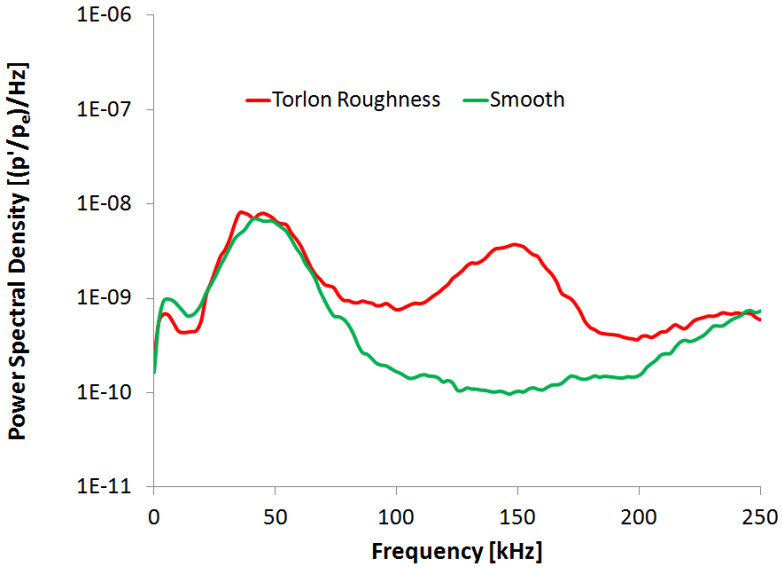

Figure 8.2.: PSD of Kulite sensor circled in Figure 8.1. Sensor was 0.36 m from the nosetip and 150° from the windward ray under quiet flow. p_0 = 142 psia, Re = 10.8×10^6/m, T_0 = 425 K.

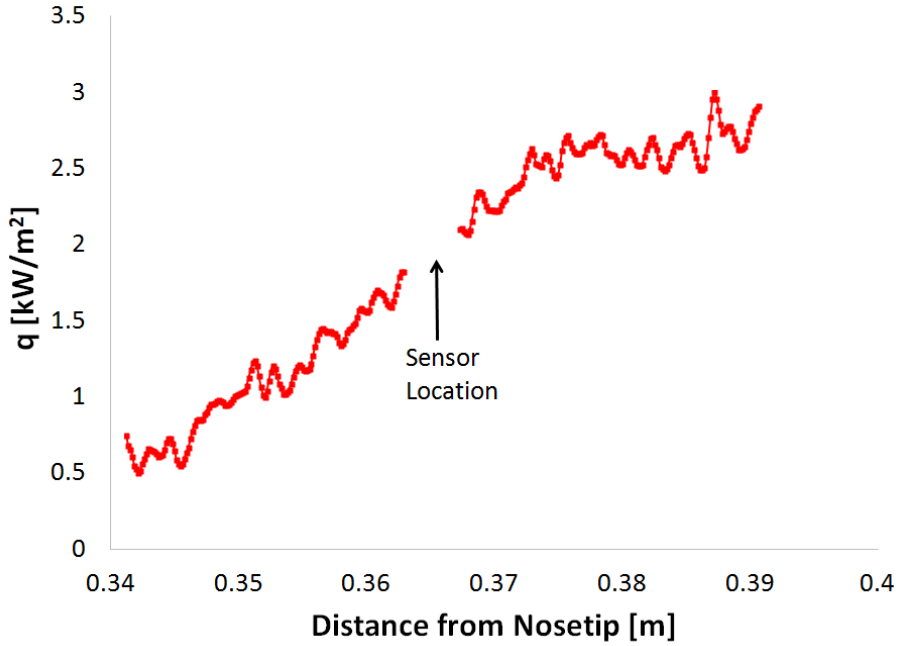

(a) Maximum heat transfer.

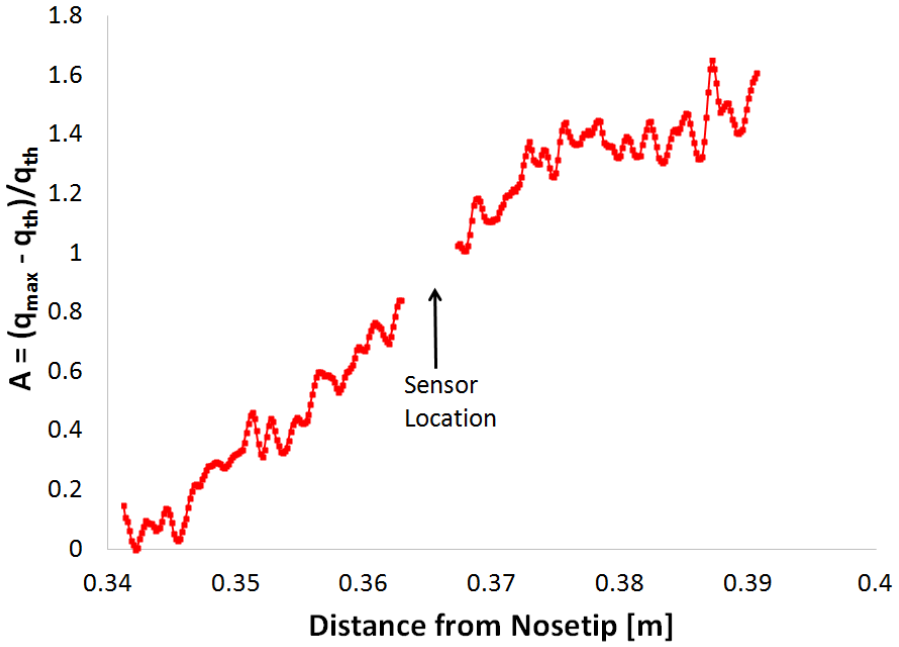

(b) Amplitude.

Figure 8.3.: Maximum heat transfer and amplitude of the stationary vortex identified in Figure 8.1(b).

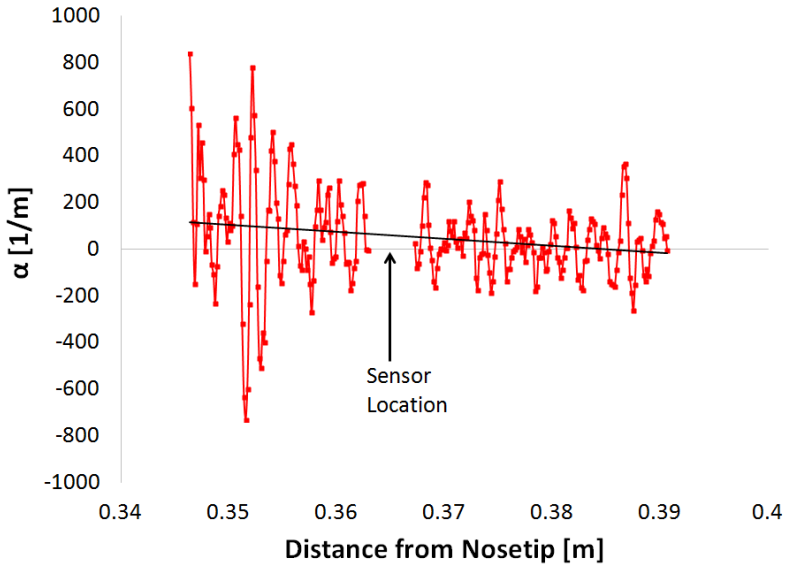

Figure 8.4.: Growth rate of stationary vortex identified in Figure 8.1(b).

Another set of tests were done to investigate the possibility of the presence of a secondary instability. Unfortunately due to time restrictions TSP was not added to the model. The model was equipped with PCB and Kulite sensors 0.36 m from the nosetip at various different azimuthal angles.

The initial test was done near the maximum quiet Reynolds number with the sensors spanning 0° to 180° azimuthally from the windward ray in 30° increments. Torlon roughness insert #3 (50 dimples) was used. The PSD of each sensor is shown in Figure 8.5. The two sensors closest to the lee ray show a turbulent spectra. The three sensors closest to the windward ray show a laminar spectra, with a slight peak near 300 kHz. This peak may be due to the second-mode instability, but it is unclear since the frequency of the second-mode wave would be expected to decrease when moving towards the lee ray because of the thickening boundary layer, but it does not. The Kulite at 90° from the windward ray shows a very clear peak at approximately 40 kHz, corresponding to the primary travelling crossflow instability. Kulite sensor resonance is seen as a narrow peak at 300 kHz. Finally, the PCB sensor at 120° from the windward ray shows a large peak near 400 kHz. It wasn't known if this peak is due to the second-mode waves, or the secondary instability of the stationary crossflow waves, therefore further testing was conducted. This peak has a frequency significantly higher than the peak measured in Figure 8.2. If both of these instabilities correspond to the secondary instability of the stationary waves, it might be expected that the frequency would be lower nearer to the lee ray where the boundary layer is thicker, which agrees with the data.

The sensors were then rotated towards and away from the lee ray by up to 5°, and the PSD of a single PCB is shown in Figure 8.6 under approximately the same conditions. The red trace at the 120° ray shown in Figure 8.6 is the same as the red trace in Figure 8.5. A run under noisy flow showing a turbulent spectra was added as reference. When the sensor was moved to the 117.5° ray (green trace), the spectrum is almost identical to the one for the 120° ray case. Moving the sensors to 115° ray (blue trace), the peak near 400 kHz disappears. If the peak in the spectra

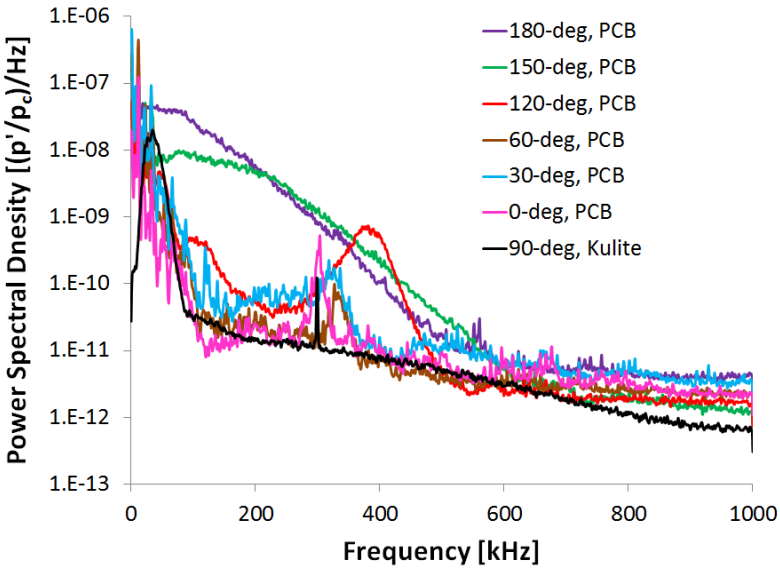

Figure 8.5.: PSD of sensors at 7 different azimuthal locations, 0.36 m from the nosetip during one run. Torlon Roughness #3 (50 dimples) under Quiet flow. $p_0 = 142$ psia, Re $= 10.8\times10^6$/m, $T_0 = 425$ K.

corresponds to the second-mode instability, it would not be expected that such a small change in azimuthal angle would cause the peak to completely disappear. Note that it has been shown earlier that the stationary vortices are body fixed and therefore they mostly roll with the cone and sensor (for small angles). But when the cone is rolled, each roughness element will be on a slightly different azimuthal angle with respect to the windward ray. Downstream, the stationary vortices will be in similar but not in exactly the same azimuthal location, therefore the sensor may be rolling a small amount underneath the stationary vortex. Repeating these tests with TSP would help clarify this issue. When the sensor is moved to the 121° and 122.5° rays (purple and black traces, respectively), the peak at 400 kHz disappears, but a lower frequency peak near 150 kHz appears. It is not known if the peak at 150 kHz is related to the peak at 400 kHz. This is at a similar frequency as the peak measured in Figure 8.2. The width of a stationary vortex under similar conditions is between 5 and 10° azimuthally, therefore if the peak at 400 kHz is due to the secondary

instability of the stationary waves, it is not surprising that the peak disappears when the sensors are moved ±5°.

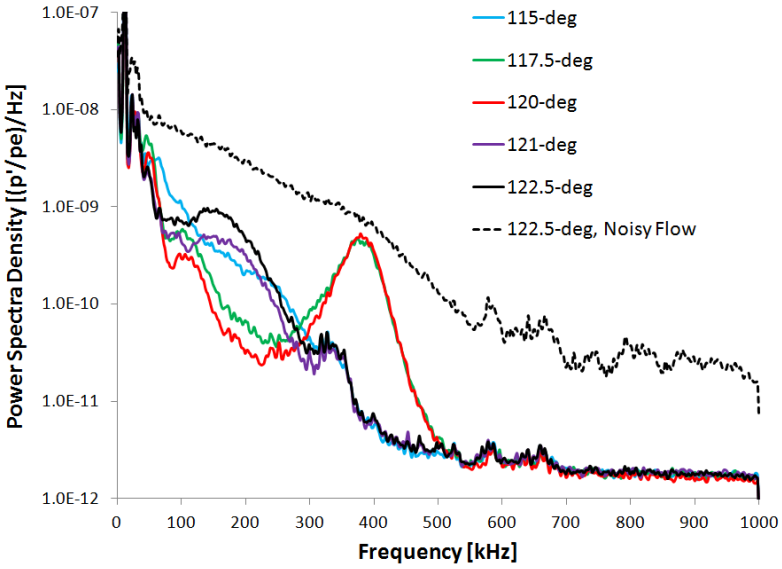

Figure 8.6.: PSD of PCB sensor 0.36 m from the nosetip. Azimuthal angle measured from the windward ray. All tests with Torlon Roughness #3 (50 dimples) and under quiet flow. Re = 10.8×10^6/m, p_0 = 142 psia, T_0 = 425 K.

Focusing solely on the test done with the PCB sensor at 120° from the windward ray, different times in the run was examined. As time progresses in a run, the stagnation pressure, stagnation temperature and Reynolds number decreases. Figure 8.7 plots the PSD of a PCB at different times during a run under quiet flow. There is a significant peak near 400 kHz that may be caused by the secondary instability, and this peak decreases in both amplitude and frequency as time increases and the Reynolds number decreases. Note that there is a slight increase in noise after two seconds [56]. The noise levels are still considered quiet after two seconds (less than 0.05%), but it is not known how this increase in noise affects the data. The decrease in frequency as the run progresses may be caused by the thickening boundary layer as the Reynolds number decreases. The decrease in amplitude may be caused by the onset of transition moving downstream as Reynolds number decreases, and therefore

the growth of the secondary instability may be in an earlier stage and at a lower amplitude. Unfortunately, no TSP was available for this test. Future tests should repeat this run with TSP.

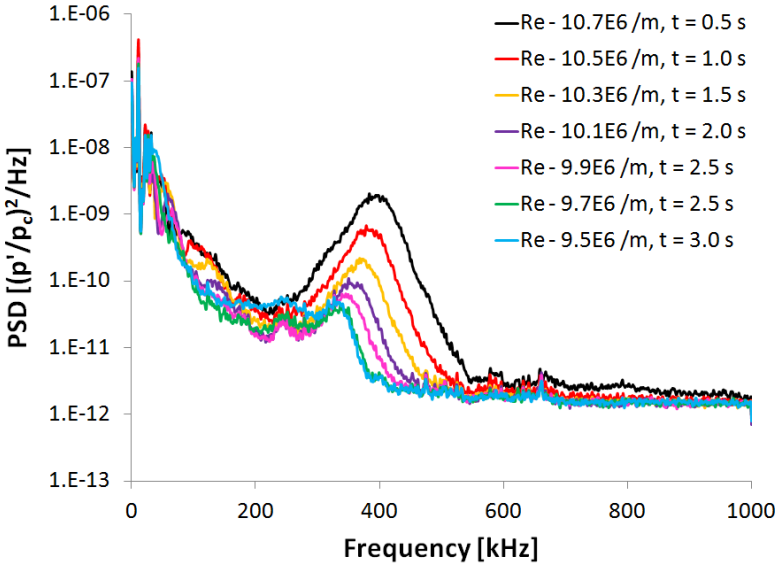

Figure 8.7.: PSD of PCB sensor 0.36 m from the nosetip at an azimuthal angle of 120°during the same run at different times. Torlon Roughness #3 (50 dimples) and under quiet flow.

The next set of tests was done to determine how roughness affects this apparent secondary instability. Four tests were done, two with the 50-dimpled insert #3 (the largest based on depth), one with the smooth insert and one with the 50-dimpled insert #5 (the smallest roughness based on depth). For the two 50-dimpled insert #3 tests, a PCB sensor was present on the 120 or the 117° ray. For the smooth and 50-dimpled #5 inserts, the PCB sensor was present on the 120° ray. Figure 8.8 plots the PSD of a single PCB sensors from these four runs. When the roughness is large, the PCB shows a peak near 400 kHz. When the smooth insert is used or the roughness is reduced, the peak near 400 kHz disappears. Unfortunately no TSP data were available for these tests, but it is hypothesized that the larger roughness is producing larger amplitude stationary waves that are breaking down near the sensor,

while the smooth or small roughness case produces smaller stationary waves that break down further downstream.

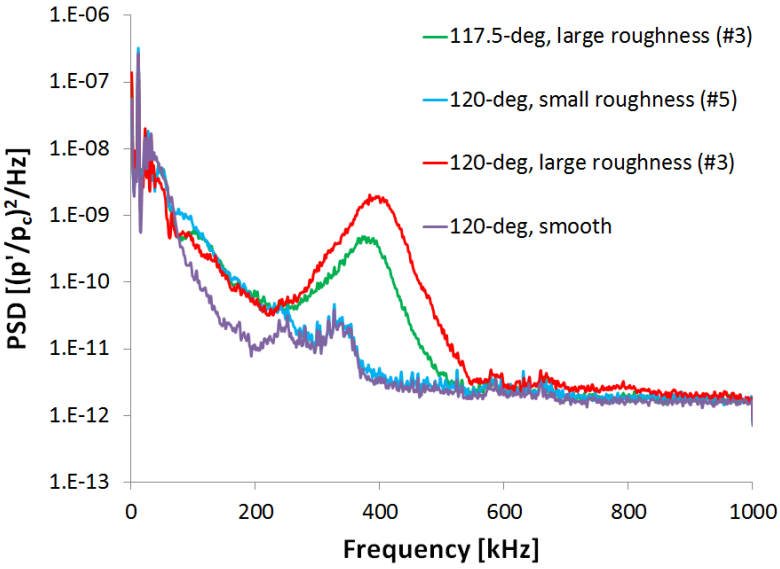

Figure 8.8.: PSD of PCB sensor 0.36 m from the nosetip showing effect of roughness on the high-frequency instability. Smooth and 50-dimpled Torlon inserts under quiet flow. Re = 11.0×10^6/m, p_0 = 143 psia, T_0 = 420 K.

The repeatability of the data was determined by performing repeat runs with a PCB sensor on the 120° and 115° rays. The PSD is shown in Figure 8.9. For the 120° ray case, the same peak in the PSD is seen near 400 kHz. The sensor was rotated to 115° and back to 120°, and the repeat run at 120° also shows a peak at the same 400 kHz frequency with a very similar magnitude. When the PCB is on the 115° ray, the peak at 400 kHz disappears. Thus, the results show good repeatability.

The final set of data looking at the secondary instability is shown in Figure 8.10 and 8.11. Figure 8.10 shows the TSP images with the smooth Torlon insert for two different Reynolds numbers under quiet flow. The Kulite sensors are circled and situated on the 150° ray. Focusing on the region near the Kulite array and specifically the Kulite closest to the leeward ray, the lower Reynolds number case appears to be

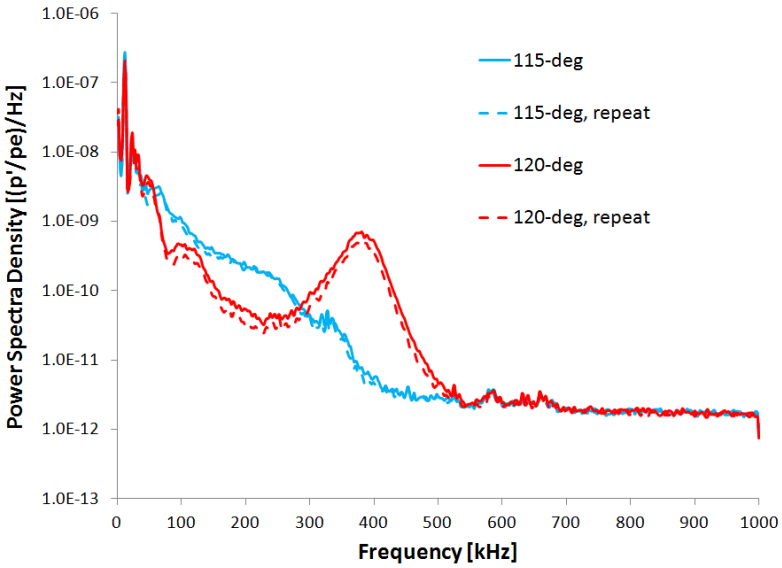

Figure 8.9.: PSD of PCB sensor 0.36 m from the nosetip showing repeatability of measurements. Torlon insert #3 (50 dimples) and under quiet flow. $p_0 = 143$ psia, Re $= 11.0\times10^6$/m, $T_0 = 420$ K.

fully laminar near the sensor. When the Reynolds number is increased, the stationary waves appear to be breaking down near the Kulite sensor array.

Figure 8.11 shows two TSP images with a 50-dimpled Torlon insert (#3), at similar conditions as the TSP images in Figure 8.10. At the lower Reynolds number, the boundary layer appears to be laminar near the Kulite sensors, similar to the smooth case. When the Reynolds number is increased, the stationary waves again appear to be breaking down in the region of the Kulite array, especially near the most leeward sensor.

The PSD of the Kulite nearest to the lee ray is shown in Figure 8.12 for the TSP images in Figures 8.10 and 8.11. The Kulite sensor is 0.36 m from the nosetip. The lower Reynolds number smooth case (green curve) shows a laminar PSD, with the existence of the primary travelling crossflow wave near a frequency of 40 kHz. When the Reynolds number is increased for the smooth case (blue curve), there is a broadband increase in noise and the primary travelling wave is no longer visible,

suggesting that the boundary layer is becoming turbulent. This agrees with the TSP data. There is a higher frequency peak near 150 kHz. It is possible that this peak corresponds to the secondary instability of the stationary waves, but this cannot be said for certain without computations for comparison.

When the roughness insert is added, the low and high Reynolds number cases (purple and red curves, respectively) also appear to show a transitional or turbulent boundary layer. Again there is a higher-frequency instability near 125 kHz (slightly lower frequency than the smooth case) that may be evidence of the secondary instability of the stationary waves. The PSD does not quite agree with the TSP data, as it appeared for the lower Reynolds number case that the boundary layer was laminar near the Kulite sensors. The reason for the disagreement between the Kulite sensor and the TSP is not known. Additional experiments have been performed by Henderson on a sharp cone at 2–4° AoA in the BAM6QT that also measured the possible secondary instability of the stationary crossflow waves [109].

8.1 Summary of Secondary-Instability Experiments

A high-frequency instability, 3–10 times higher in frequency than the primary travelling instability, has been measured near the region of stationary-wave breakdown. This high-frequency instability may correspond to the travelling secondary instability of the stationary crossflow waves. Tests with a Kulite sensor on the 150° azimuthal ray, 0.36 m from the nosetip, measured an instability near 150 kHz when the stationary waves appeared to begin to break down as imaged by the TSP.

Additional tests measured an instability near 400 kHz on the 120° azimuthal ray, 0.36 m from the nosetip. When the cone was rotated ±5°, the instability was either still present, no longer present, or no longer present and a lower frequency peak (around 150 kHz) appeared. If the 400 kHz instability was the 2nd-mode instability, small changes in azimuthal angle would be expected to cause a slight change in peak frequency (because of the azimuthal variation in boundary-layer thickness), but the

instability peak disappears when the sensor is rotated $\pm 5^{\circ}$. It is then possible that the secondary instability of the stationary crossflow waves is being measured. However, computations are needed, along with further measurements.

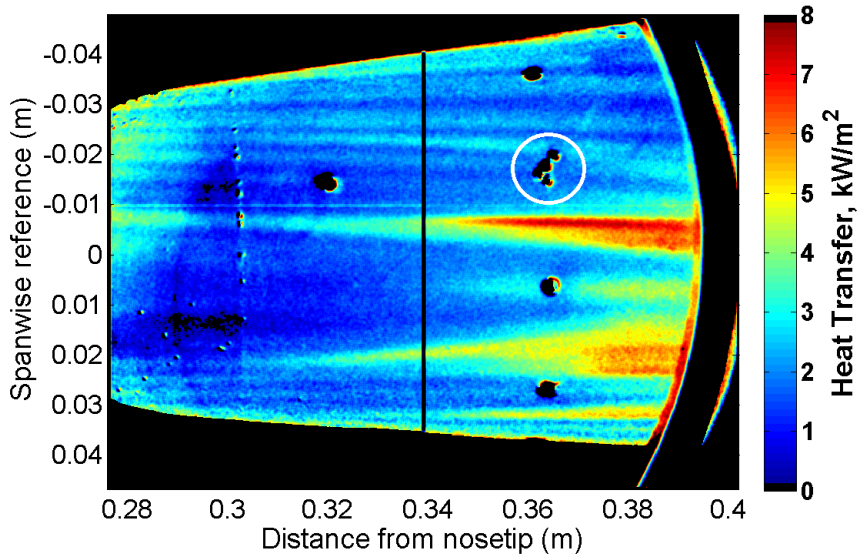

(a) Re = 9.3×10^6/m, P_0 = 128 psia, T_0 = 435 K, T_{wall} = 300 K.

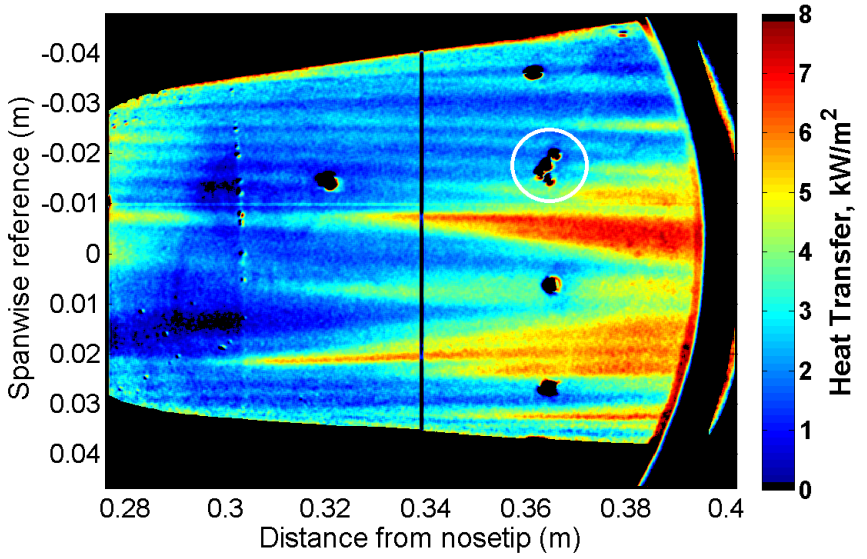

(b) Re = 10.3×10^6/m, P_0 = 140 psia, T_0 = 435 K, T_{wall} = 301 K.

Figure 8.10.: TSP images with smooth Torlon insert under quiet flow. Kulite sensors circled and on the 150° azimuthal ray.

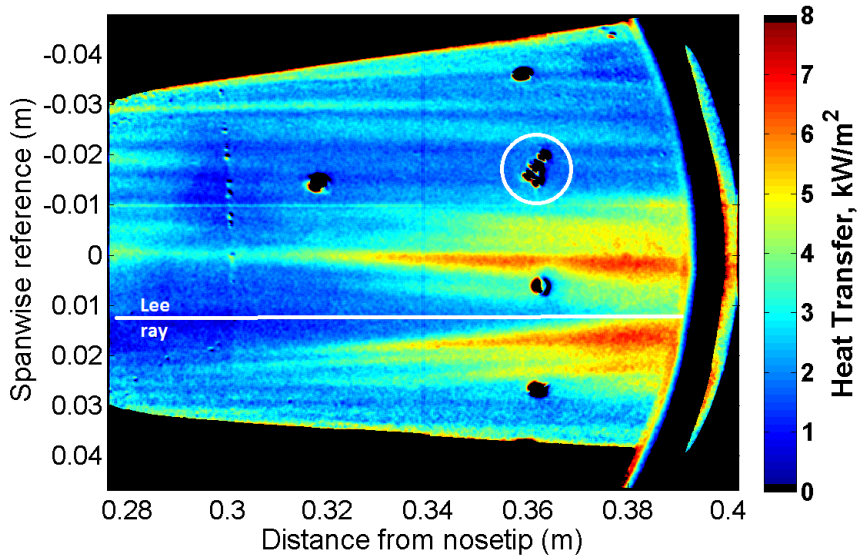

(a) Re = 9.6×10^6/m, P_0 = 128 psia, T_0 = 427 K, T_{wall} = 297 K.

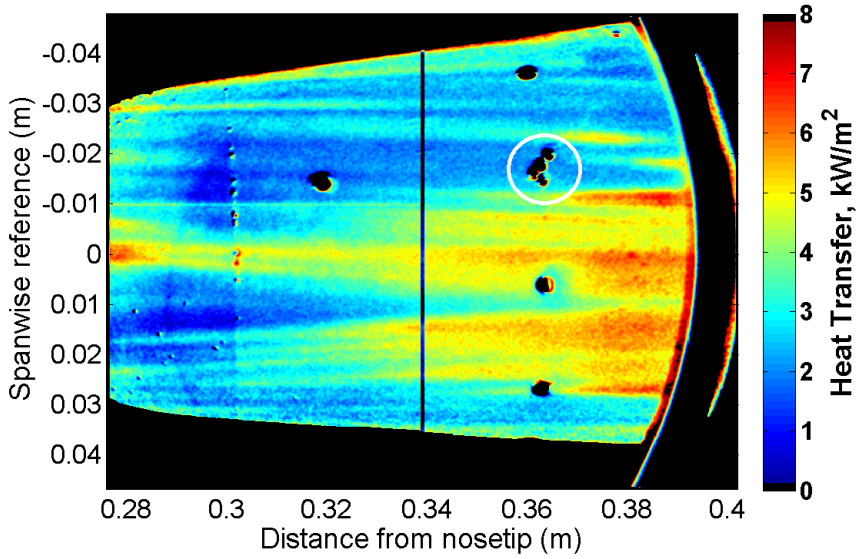

(b) Re = 10.4×10^6/m, P_0 = 139 psia, T_0 = 428 K, T_{wall} = 301 K.

Figure 8.11.: TSP images with Torlon roughness insert #3 under quiet flow. Kulite sensors circled and on the 150° azimuthal ray.

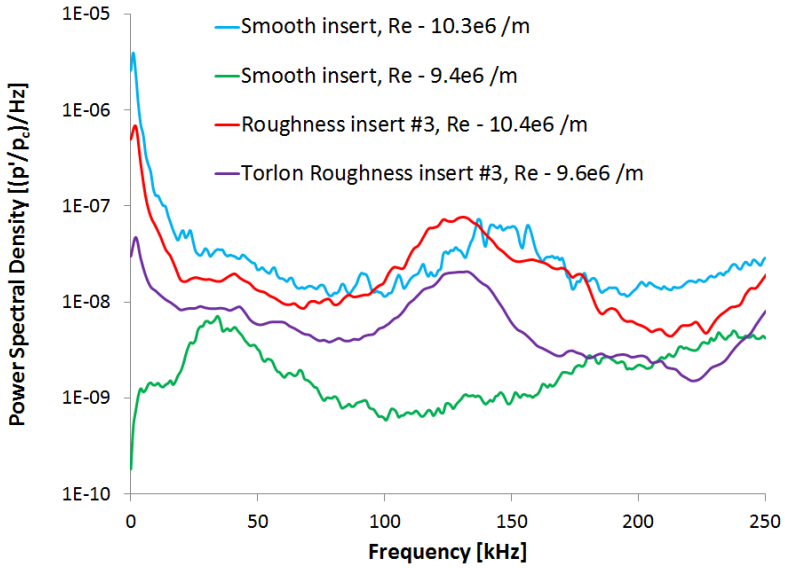

Figure 8.12.: PSD of Kulite sensors 0.36 m from the nosetip at an azimuthal angle of 150° and under quiet flow.

9. SUMMARY OF WORK AND FUTURE RECOMMENDATIONS

9.1 Summary

The purpose of this research was to study and measure the stationary and travelling crossflow waves in a controlled manner. A sharp 7° half-angle cone at 6° angle of attack was used in the Boeing/AFOSR Mach-6 Quiet Tunnel, equipped with temperature-sensitive paint, roughness inserts and fast pressure transducers. Transition was induced by the crossflow instability under fully quiet flow.

1. Roughness elements were placed 2 inches from the nosetip in a Torlon insert section of the cone. Roughness elements were created with varying depths, diameters and spacing. The 50-roughness-elements insert had a significant effect on the generation of the stationary vortices, as compared to the smooth case. The effect of the 72-roughness-elements insert was less clear, as many of the measured stationary vortices were similar to the smooth wall case. It is possible that the depth or height of the roughness in the 72-element insert was too small to effectively generate stationary vortices. Crossflow-induced transition was found to occur with both the smooth and rough cases with a sufficiently high Reynolds number.

   The depth or the height of the roughness elements led to significantly stronger stationary crossflow vortices and, consequently, when the depth and height was increased simultaneously the location of crossflow-induced transition moved upstream. The stationary vortices were found to not break down to turbulence until close to the lee ray. This is a surprising result as linear stability computations found that the stationary vortices had the largest N-factors closer to

the yaw ray. The roughness elements had the biggest effect on the stationary vortices at approximately 150° to 180° from the windward ray. The roughness elements had a minimal impact on boundary-layer transition under noisy flow. The transition locations near both lee and yaw rays remained nearly unchanged when the roughness element array was used.

2. The travelling crossflow waves were measured with Kulite pressure transducers under both noisy and quiet flow at a frequency near 40 kHz. The wave properties including propagation angle and phase speed of the most amplified travelling waves were determined with an array of Kulites at an axial distance of 0.36 m, and agreed well with computations by Texas A&M and experiments by TU Braunschweig under similar conditions. PCB sensors were able to measure the travelling waves with similar frequencies and amplitudes. When the BAM6QT was run noisy, the amplitude of the travelling waves at the axial location of the sensors was approximately 20 times larger than when run quiet. The travelling waves had the largest amplitude between 90° and 150° from the windward ray, depending on the freestream conditions.

3. An interaction between the stationary and travelling crossflow waves was observed. Large stationary crossflow waves were induced with either controlled or uncontrolled roughness and these stationary waves were visualized near the location of a fast pressure transducer. When the stationary wave passed over or near the fast pressure transducer, a damped or distorted travelling crossflow wave was measured. It is not clear at hypersonic speeds the role the travelling waves have under quiet flow in causing crossflow-induced transition, and therefore this travelling-stationary wave interaction may be significant.

4. A high-frequency instability was measured near the breakdown of the stationary waves. This instability disappeared when the sensors when the sensor was displaced away from the footprint of the strong stationary crossflow vortex. The instability also disappeared when the roughness near the nosetip was reduced,

i.e., when the amplitude of the stationary crossflow mode was smaller. The azimuthally concentrated signature and the apparent dependence on a threshold stationary amplitude indicate that this instability may be caused by the secondary instability of the primary stationary crossflow wave, but computational comparisons and additional experiments are needed. If this is in fact the secondary instability of the stationary waves, the amplitude or growth of the secondary instability might be correlated to the transition location, as in Malik's work at low speeds [20].

9.2 Future Work

While the author performed many experiments looking at the effect of roughness on crossflow-induced transition, there are certainly many limitations in the work and there is still much research to be done before crossflow-induced transition over slender cones in hypersonic flows is much better understood. The author suggests that the following work should be done in the future.

1. The random roughness on the cone was shown to have an effect on the stationary vortices, and may interact with the controlled roughness elements. It would be ideal to keep the baseline TSP roughness constant for all tests. Simply by observation, it appears that the TSP does not photo-degrade as quickly as the author once thought. Therefore it may be possible to keep the same TSP paint finish for longer than previously thought. It is suggested to paint a 7° cone and install a couple of Schmidt-Boelter gauges, and follow the usual procedure of keeping the cone in a drawer when not being used. This cone could be run every couple months at 0° angle of attack, and the calibrated heat transfer could be compared to theory. Even though the TSP may experience some photo-degradation, if the measured heat transfer agrees well with the theoretical heat transfer, then it may be possible to continue with a constant TSP paint job on the Crossflow Cone for many consecutive tunnel entries.

It is also suggested to start the paint as far downstream and away from the windward ray as possible. This should minimize the effect the random background roughness of the paint has on the stationary vortices. The roughness amplitude should be created as high as possible without triggering bypass transition, thus providing another method of minimizing the effect any background roughness has on the stationary modes.

2. The author only began to study the effect different roughness parameters have on the stationary crossflow vortices. Future tests can look more closely at the effect that the protruding surface of the roughness element has, by incrementally sanding it down and studying the effect on crossflow-induced transition. The same can be done with the depth, where the depth is increased while the protruding surface is removed via sanding. Different roughness spacings should also be studied, along with repeating the experiments with the 72 roughness elements around the azimuth but with larger dimple depths or diameters. It would be good to try Chynoweth's RIM roughness inserts on a cone at angle of attack [110]. It may be easier to obtained more controlled roughness elements with Chynoweth's method.

3. Additional experiments should be performed to look at the secondary instability of the stationary waves. The experiments where the 400 kHz peak disappeared when the cone was rotated by small angles should be repeated with TSP. Measurements of the possible secondary instability should be conducted on various rays of the cone to determine if the frequency is a function of the boundary-layer thickness. The future researcher should seek computational comparisons.

4. The effect of wall temperature on the travelling crossflow waves should be studied in more depth. If the travelling waves can be reliably measured with the PCB sensors, the same set of tests could be done where the wall temperature is varied and the amplitude of the travelling waves is measured. This would remove any potential effect that the Kulite temperature compensation has on

the measurements, although it is not clear how temperature changes will impact the PCB sensor measurements.

LIST OF REFERENCES

LIST OF REFERENCES

[1] Steven P. Schneider. Laminar-Turbulent Transition on Reentry Capsules and Planetary Probes. *Journal of Spacecraft and Rockets*, 43(6):1153–1173, November-December 2004.

[2] Deepak Bose, Todd White, Jose A. Santos, Jay Feldman, Milad Mahzari, Michael Olson, and Bernie Laub. Initial Assessment of Mars Science Laboratory Heatshield Instrumentation and Flight Data. AIAA Paper 2013-0908, January 2013.

[3] Sandy C. Tirtey. *Characterization of a Transitional Hypersonic Boundary Layer in Wind Tunnel and Flight Conditions*. PhD thesis, Von Karman Institute for Fluid Dynamics, Brussels, Belgium, August 2006.

[4] William Saric, Eli Reshotko, and Daniel Arnal. Hypersonic Laminar-Turbulent Transition. AGARD AR-319, Hypersonic Experimental and Computational Capability, Improvement and Validation. 1998, pp. 2-1–2-27.

[5] M. Morkovin. Critical Evaluation of Transition from Laminar to Turbulent Shear Layers with Emphasis on Hypersonically Travelling Bodies. Air Force Flight Dynamics Laboratory Rep. AFFDL-TR-68-149, April 1969.

[6] H. Reed, W. Saric, and D. Arnal. Linear Stability Theory Applied to Boundary Layers. *Annual Review of Fluid Mechanics*, 28:389–428, 1996.

[7] Steven P. Schneider. The Development of Hypersonic Quiet Tunnels. *Journal of Spacecraft and Rockets*, 45(4):641–664, July-August 2008.

[8] Steven P. Schneider. Effects of High-Speed Tunnel Noise on Laminar-Turbulent Transition. *Journal of Spacecraft and Rockets*, 38(3):323–333, May-June 2001.

[9] Steven P. Schneider. Hypersonic Laminar-Turbulent Transition on Circular Cones and Scramjet Forebodies. *Progress in Aerospace Sciences*, 40(1-2):1–50, 2004.

[10] Helen L. Reed and William S. Saric. Stability and Transition of Three-Dimensional Boundary Layers. *Annual Review of Fluid Mechanics*, 21:235–284, 1989.

[11] William S. Saric. Görtler Vortices. *Annual Review of Fluid Mechanics*, 26:379–409, 1994.

[12] Eli Reshotko. Boundary-Layer Stability and Transition. *Annual Review of Fluid Mechanics*, 8:311–349, 1976.

[13] Leslie M. Mack. Linear Stability Theory and the Problem of Supersonic Boundary-Layer Transition. *AIAA Journal*, 13(3):278–289, March 1974.

[14] N. Gregory, J. T. Stuart, and W. S. Walker. On the Stability of Three-Dimensional Boundary Layers with Application to the Flow Due to a Rotating Disk. *Philosophical Transactions of the Royal Society of London. Series A, Mathematical and Physical Sciences*, 248(943):155–199, 1955.

[15] M. R. Malik, F. Li, and C. L. Chang. Crossflow Disturbances in Three-Dimensional Boundary Layers: Nonlinear Development, Wave Interaction and Secondary Instability. *Journal of Fluid Mechanics*, 268:1–36, April 1994.

[16] W. Saric, H. Reed, and E. White. Stability and Transition of Three-Dimensional Boundary Layers. *Annual Review of Fluid Mechanics*, 35:413–440, 2003.

[17] J. C. Adams Jr. and W. R. Martindale. Engineering Analysis of Hypersonic Lifting Body Windward Surface Inviscid and Viscous Flowfields at High Angles of Attack. AIAA Paper 1973-637, July 1973.

[18] Hans Bippes. Basic Experiments on Transition in Three-Dimensional Boundary Layers Dominated by Crossflow Instability. *Progress in Aerospace Sciences*, 35:363–412, 1999.

[19] Edward B. White and William S. Saric. Secondary Instability of Crossflow Vortices. *Journal of Fluid Mechanics*, 525:275–308, February 2005.

[20] Mujeeb R. Malik, Fei Li, Meelan M. Choudhari, and Chau-Lyan Chang. Secondary Instability of Crossflow Vortices and Swept-Wing Boundary-Layer Transition. *Journal of Fluid Mechanics*, 399:85–115, 1999.

[21] Y. Kohama. Some Expectations on the Mechanism of Cross-Flow Instability in a Swept-Wing Flow. *Acta Mechanica*, 66:22–38, February 1987.

[22] D. I. A. Poll. Some Observations of the Transition Process on the Windward Face of Long Yawed Cylinder. *Journal of Fluid Mechanics*, 150:329–356, 1985.

[23] Robert T. Jones. Effects of Sweepback on Boundary Layer and Separation. NACA Report No. 884, 1948.

[24] William R. Sears. The Boundary Layer of Yawed Cylinders. *Journal of the Aeronautical Sciences*, 15:28–34, 1948.

[25] W. E. Gray. The Effect of Wing Sweep on Laminar Flow. Royal Aircraft Establishment Technical Memo No. 255, 1952.

[26] P. R. Owen and D G. Randall. Boundary Layer Transition on a Swept-Back Wing. R.A.E. TM Aero 277, May 1952.

[27] H. B. Squire. Addendum on Sweepback and Transition. R.A.E. TM Aero 277, 1952.

[28] L. D. Allen and F. M. Burrows. Flight Experiments on the Boundary Layer Characteristics of a Swept Back Wing. Technical Report Coll. Aero Report 104, Cranfield Institute of Technology, 1956.

[29] F. M. Burrows. A Theoretical and Experimental Study of the Boundary Layer Flow on a 45-deg Swept Back Wing. Technical Report Coll. Aero Report 109, Cranfield Institute of Technology, 1956.

[30] Ronald H. Radeztsky Jr., Mark S. Reibert, and William S. Saric. Effect of Isolated Micron-Sized Roughness on Transition in Swept-Wing Flows. *AIAA Journal*, 37(11):1370–1377, November 1999.

[31] P. Nitschke-Kowsky and H. Bippes. Instability and Transition of a Three-Dimensional Boundary Layer on a Swept Flat Plate. *The Physics of Fluids*, 31(4):786–795, April 1987.

[32] H. Bippes and P. Nitschke-Kowsky. Experimental Study of Instability Modes in a Three-Dimensional Boundary Layer. AIAA Paper 1987-1336, June 1987.

[33] H. Deyhle and H. Bippes. Disturbance Growth in an Unstable Three-Dimensional Boundary Layer and its Dependence on Environmental Conditions. *Journal of Fluid Mechanics*, 316:73–113, December 1996.

[34] H. Bippes and T. Lerche. Transition Prediction in Three-Dimensional Boundary-Layer Flows Unstable to Crossflow Instability. AIAA Paper 1997-1906, June-July 1997.

[35] M. R. Malik and D. I. A. Poll. Effect of Curvature on Three-Dimensional Boundary Layer Stability. AIAA Paper 1984-1672, June 1984.

[36] R. H. Radeztsky, M. S. Reibert, and W. S. Saric. Development of Stationary Crossflow Vortices on a Swept Wing. AIAA Paper 1994-2373, June 1994.

[37] William S. Saric and Lawrence G. Yeates. Experiments on the Stability of Crossflow Vortices in Swept-Wing Flows. AIAA Paper 85-0493, January 1985.

[38] A. M. O. Smith and D. W. Clutter. The Smallest Height of Roughness Capable of Affecting Boundary-Layer Transition. *Journal of the Aerospace Sciences*, 26(4):229–245, 1959.

[39] William S. Saric, Ruben B. Carillo Jr., and Mark S. Reibert. Nonlinear Stability and Transition in 3-D Boundary Layers. *Meccanica*, 33:469–487, 1998.

[40] Edward B. White and William S. Saric. Application of Variable Leading-Edge Roughness for Transition Control on Swept Wings. AIAA Paper 2000-0283, January 2000.

[41] M. Choudhari, F. Li, C.-L. Chang, M. Carpenter, C. Streett, and M. Malik. Towards Bridging the Gaps in Holistic Transition Prediction via Numerical Simulations. AIAA Paper 2013-2718, June 2013.

[42] Lian Duan and Meelan M. Choudhari. Direct Numerical Simulation of Transition in a Swept-Wing Boundary Layer. AIAA Paper 2013-2617, June 2013.

[43] Fei Li and Meelan Choudhari. Spatially Developing Secondary Instabilities and Attachment Line Instability in Supersonic Boundary Layers. AIAA Paper 2008-0590, January 2008.

[44] William S. Saric and Helen L. Reed. Supersonic Laminar Flow Control on Swept Wings Using Distributed Roughness. AIAA Paper 2002-0147, January 2002.

[45] N. V. Semionov, A. D. Kosinov, and V. Ya. Levchenko. Experimental Study of Turbulence Beginning and Transition Control in a Supersonic Boundary Layer on Swept Wing. In *6th IUTAM Symposium on Laminar-Turbulent Transition*, pages 355–361, 2006.

[46] Chan Yong Schuele. *Control of Stationary Cross-Flow Modes in a Mach 3.5 Boundary Layer Using Patterned Passive and Active Roughness*. PhD thesis, University of Notre Dame, South Bend, Indiana, December 2011.

[47] Chan Yong Schuele, Thomas C. Corke, and Eric Matlis. Control of Stationary Crossflow Modes in a Mach 3.5 Boundary Layer Using Patterned Passive and Active Roughness. *Journal of Fluid Mechanics*, 718:5–38, 2013.

[48] Ponnampalam Balakumar. Stability of Supersonic Boundary Layers on a Cone at an Angle of Attack. AIAA Paper 2009-3555, June 2009.

[49] Rudolph A. King. Three-Dimensional Boundary-Layer Transition on a Cone at Mach 3.5. *Experiments in Fluids*, 13:305–314, 1999.

[50] Gary T. Chapman. Some Effects of Leading-Edge Sweep on Boundary-Layer Transition at Supersonic Speeds. NASA Techincal Note D-1075, 1961.

[51] J. R. Dagenhart. Amplified Crossflow Disturbances in the Laminar Boundary Layer on Swept Wings With Suction. NASA Technical Paper 1902, November 1981.

[52] Erick O. Swanson. *Boundary-Layer Transition on Cones at Angle of Attack in a Mach-6 Quiet Tunnel*. PhD thesis, Purdue University, West Lafayette, Indiana, August 2008.

[53] Erick O. Swanson and Steven P. Schneider. Boundary-Layer Transition on Cones at Angle of Attack in a Mach-6 Quiet Tunnel. AIAA Paper 2010-1062, January 2010.

[54] Christopher Ward. Hypersonic Crossflow Instability and Transition on a Circular Cone at Angle of Attack. Master's thesis, Purdue University, West Lafayette, IN, December 2010.

[55] Thomas J. Juliano. *Instability and Transition on the HIFIRE-5 in a Mach-6 Quiet Tunnel*. PhD thesis, Purdue University, West Lafayette, Indiana, August 2010.

[56] Laura E. Steen. Characterization and Development of Nozzles for a Hypersonic Quiet Wind Tunnel. Master's thesis, Purdue University, West Lafayette, IN, December 2010.

[57] J. F. McKenzie and K. O. Westphal. Interaction of Linear Waves with Oblique Shock Waves. *The Physics of Fluids*, 11(11):2350–2362, November 1968.

[58] Federico Muñoz, Dirk Heitmann, and Rolf Radespiel. Instability Modes in Boundary Layers of an Inclined Cone at Mach 6. AIAA Paper 2012-2823, June 2012.

[59] Eduardo Perez, Helen L. Reed, and Joseph J. Kuehl. Instabilities on a Hypersonic Yawed Straight Cone. AIAA Paper 2013-2879, June 2014.

[60] Federico Muñoz, Rolf Radespiel, Alexander Theiss, and Stefan Hein. Experimental and Numerical Investigation of Instabilities in Conical Boundary Layers at Mach 6. AIAA Paper 2014-2778, June 2014.

[61] Aline van den Kroonenberg, Rolf Radespiel, Graham Candler, and Malte Estorf. Infrared Measurements of Boundary-Layer Transition on an Inclined Cone at Mach 6. AIAA Paper 2010-1063, January 2010.

[62] Fei Li, Meelan Choudhari, Chau-Lyan Chang, and J. White. Analysis of Instabilities in Non-Axisymmetric Hypersonic Boundary Layers over Cones. AIAA Paper 2010-4643, June 2010.

[63] Thorwald Herbert. Parabolized Stability Equations. *Annual Review of Fluid Mechanics*, 29:245–283, 1997.

[64] Shann J. Rufer and Steven P. Schneider. Hot-Wire Measurements of Instability Waves on Cones at Mach 6. AIAA Paper 2006-3054, June 2006.

[65] Amanda Chou. Characterization of Laser-Generated Perturbations and Instability Measurements on a Flared Cone. Master's thesis, Purdue University, West Lafayette, Indiana, December 2010.

[66] Joel E. Gronvall, Heath B. Johnson, and Graham V. Candler. Hypersonic Three-Dimensional Boundary Layer Transition on a Cone at Angle of Attack. AIAA Paper 2012-2822, June 2012.

[67] Jonathan Poggie, Roger L. Kimmel, and Stephen N. Schwoerke. Traveling Instability Waves in a Mach 8 Flow over an Elliptic Cone. *AIAA Journal*, 38(2):251–258, February 2000.

[68] Roger L. Kimmel and Jonathan Poggie. Three-Dimensional Hypersonic Boundary Layer Stability and Transition. Air Force Research Laboratory Technical Report WL-TR-97-3111, 1997.

[69] Mark Huntley and Alexander Smits. Transition Studies on an Elliptic Cone in Mach 8 Flow Using Filtered Rayleigh Scattering. *European Journal of Mechanics B: Fluids*, 19:695–706, 2000.

[70] Thomas J. Juliano and Steven P. Schneider. Instability and Transition on the HIFiRE-5 in a Mach-6 Quiet Tunnel. AIAA Paper 2010-5004, June 2010.

[71] Matthew P. Borg, Roger Kimmel, and Scott Stanfield. HIFiRE-5 Attachment-Line and Crossflow Instability in a Quiet Hypersonc Wind Tunnel. AIAA Paper 2011-3247, June 2011.

[72] Matthew P. Borg, Roger Kimmel, and Scott Stanfield. Crossflow Instability for HIFiRE-5 in a Quiet Hypersonic Wind Tunnel. AIAA Paper 2012-2821, June 2012.

[73] Matthew P. Borg, Roger Kimmel, and Scott Stanfield. Traveling Crossflow Instability for HIFiRE-5 in a Quiet Hypersonic Wind Tunnel. AIAA Paper 2013-2737, June 2013.

[74] Meelan Choudhari, Chau-Lyan Chang, Thomas Jentink, Fei Li, Karen Berger, Graham Candler, and Roger Kimmel. Transition Analysis for the HIFiRE-5 Vehicle. AIAA Paper 2009-4056, June 2009.

[75] Bradley M. Wheaton. Roughness-Induced Instability in a Laminar Boundary Layer at Mach 6. Master's thesis, Purdue University, West Lafayette, IN, December 2009.

[76] Steven Beresh, John Henfling, Russell Spillers, and Brian Pruett. Measurements of Fluctuating Wall Pressures Beneath a Supersonic Turbulent Boundary Layer. AIAA Paper 2010-0305, January 2010.

[77] David S. Dolling and Jean-Paul Dussauge. Fluctuating Wall-Pressure Measurements. AGARD-AG-315, A survey of Measurements and Measuring Techniques in Rapidly Distorted Compressible Turbulent Boundary Layers. 1989, pp. 8-1–8-18.

[78] Keisuke Fujii. Experiment of the Two-Dimensional Roughness Effect on Hypersonic Boundary-Layer Transition. *Journal of Spacecraft and Rockets*, 43(4):731–738, July-August 2006.

[79] Katya M. Casper. *Pressure Fluctuations Beneath Instability Wave Packets and Turbulent Spots in a Hypersonic Boundary Layer*. PhD thesis, Purdue University, West Lafayette, Indiana, August 2012.

[80] Ryan P. K. Luersen. Techniques for Application of Roughness for Manipulation of Second-Mode Waves on a Flared Cone at Mach 6. Master's thesis, Purdue University, West Lafayette, IN, December 2012.

[81] Malte Estorf, Rolf Radespiel, Steven P. Schneider, Heath B. Johnson, and Stefan Hein. Surface-Pressure Measurements of Second-Mode Instability in Quiet Hypersonic Flow. AIAA-2008-1153, January 2008.

[82] Christopher A. C. Ward, Bradley M. Wheaton, Amanda Chou, Dennis C. Berridge, Laura E. Letterman, Ryan P. K. Luersen, and Steven P. Schneider. Hypersonic Boundary-Layer Transition Experiments in the Boeing/AFOSR Mach-6 Quiet Tunnel. AIAA Paper 2012-0282, January 2012.

[83] John D. Anderson. *Computational Fluid Mechanics and Heat Transfer*. McGraw-Hill Book Company, 1st edition, 1984.

[84] Medtherm Corporation. Personal Communication - Phone Call, October 2010.

[85] Peter L. Gilbert. Effect of Tunnel Noise on Laminar Stagnation-Point Heating at Mach 6. Master's thesis, Purdue University, West Lafayette, IN, August 2010.

[86] T. Liu and J. Sullivan. *Pressure and Temperature Sensitive Paints*. Springer, 1st edition, 2005.

[87] Di Peng, James W. Gregory, Jim Crafton, and Sergey Fonov. Development of a Two Layer Dual-Luminophore Pressure Sensitive Paint for Unsteady Pressure Measurements. AIAA Paper 2010-4918, June 2010.

[88] Matthew P. Borg. *Laminar Instability and Transition on the X-51A*. PhD thesis, Purdue University, West Lafayette, Indiana, August 2009.

[89] Tianshu Liu, Bryan T. Campbell, Steven P. Burns, and John P. Sullivan. Temperature and Pressure-Sensitive Luminescent Paints in Aerodynamics. *Applied Mechanics Review*, 50(4):227–246, 1994.

[90] Shin Matsumura. Streamwise Vortex Instability and Hypersonic Boundary-Layer Transition on the Hyper-2000. Master's thesis, Purdue University School of Aeronautics & Astronautics, West Lafayette, IN, August 2003.

[91] John P. Sullivan, Steven P. Schneider, Tianshu Liu, Justin Rubal, Christopher Ward, Joseph Dussling, Cody Rice, Ryan Foley, Zeimin Cai, Bo Wang, and Sudesh Woodiga. Quantitative Global Heat Transfer in a Mach-6 Quiet Tunnel. Technical Report NASA/CR-2012-217331, November 2011.

[92] Frank M. White. *Viscous Fluid Flow*. McGraw-Hill, 1st edition, 1974.

[93] E. W. Lemmon and R. T. Jacobson. Viscosity and Thermal Conductivity Equations for Nitrogen, Oxygen, Argon and Air. *International Journal of Thermophysics*, 25(1):21–69, 2004.

[94] Dennis C. Berridge, Amanda Chou, Christopher A.C. Ward, Laura E. Steen, Peter L. Gilbert, Thomas J. Juliano, Steven P. Schneider, and Joel E. Gronvall. Hypersonic Boundary-Layer Transition Experiments in a Mach-6 Quiet Tunnel. AIAA Paper 2010-1061, January 2010.

[95] Christopher A.C. Ward, Bradley M. Wheaton, Amanda Chou, Peter L. Gilbert, Laura E. Steen, and Steven P. Schneider. Boundary-Layer Transition Measurements in a Mach-6 Quiet Tunnel. AIAA Paper 2010-4721, June 2010.

[96] Craig R. Skoch and Steven P. Schneider Matthew P. Borg. Disturbances from Shock/Boundary-Layer Interactions Affecting Upstream Hypersonic Flow. AIAA Paper 2005-4897, June 2005.

[97] Meelan Choudhari. NASA Langley. Personal Communication - Email, November 2012.

[98] T. Corke, E. Matlis, C-Y Schuele, S. Wilkinson, L. Owens, and P. Balakumar. Control of Stationary Cross-flow Modes Using Patterned Roughness at Mach 3.5. In *7th IUTAM Symposium on Laminar-Turbulent Transition*, pages 123–128, 2010.

[99] Tianshu Liu. Western Michigan University. Personal Communication - Email, October 2011.

[100] Brandon Chynoweth. Purdue University. Personal Communication, July 2014.

[101] Robert E. Wilson. Turbulent Compressible Boundary Layer with Heat-Transfer Effects on Conditions at the Sublayer. *AIAA Journal*, 17(7):275–308, July 1979. Technical Note.

[102] Joel Gronvall. University of Minnesota. Personal Communication - Email, April 2012.

[103] Joseph J. Kuehl, Eduardo Perez, and Helen L. Reed. JoKHeR: NPSE Simulations of Hypersonic Crossflow Instability. AIAA Paper 2012-0921, January 2012.

[104] Joel Gronvall. University of Minnesota. Personal Communication - Email, April 2014.

[105] Katya M. Casper. Hypersonic Wind-Tunnel Measurements of Boundary-Layer Pressure Fluctuations. Master's thesis, Purdue University, West Lafayette, IN, August 2009.

[106] P. Balakumar and Michael A. Kegerise. Receptivity of Hypersonic Boundary Layers over Straight and Flared Cones. AIAA Paper 2010-1065, January 2010.

[107] Julius S. Bendat and Allan G. Piersol. *Engineering Applications of Correlation and Spectral Analysis*. Wiley-Interscience, 2nd edition, 1980.

[108] Roger L. Kimmel, Anthony Demetriades, and Joseph C. Donaldson. Space-Time Correlation Measurements in a Hypersonic Transitional Boundary Layer. *AIAA Journal*, 34(12):2484–2489, December 1996.

[109] Ryan O. Henderson. Crossflow Transition at Mach 6 on a Cone at Low Angles of Attack. Master's thesis, Purdue University, West Lafayette, IN, December 2014.

[110] Brandon C. Chynoweth, Christopher A. C. Ward, Roger T. Greenwood, Gregory R. McKiernan, Roy A. Fisher, and Steven P. Schneider. Measuring Transition and Instabilities in a Mach 6 Hypersonic Quiet Wind Tunnel. AIAA Paper 2014-2643, June 2014.

APPENDICES

A. Methods for Painting Models and Installing Sensors

This appendix outlines the methods used by the author to paint the models and install the various pressure and heat transfer sensors.

- The model is first prepared for painting. The surface is cleaned with acetone and any sensor holes are plugged with cylindrical stainless-steel dowels. Depending on the model, the nosetip may or may not be left installed in the frustum.
- Four coats of the LustreKote White Primer spray paint are applied to the model surface, waiting approximately 3 minutes between coats. Paint should be added sparingly near the upstream region of the cone, creating a smooth transition from the bare metal to the full thickness of the paint. The relative humidity in the room should be maintained as low as possible or the paint will not dry properly. The relative humidity was typically held near 40% in the summer and 20% in the winter.
- The paint is not typically sanded after the application of the White Primer unless the paint is significantly uneven. If sanding is required, the paint should be allowed to dry for 24 hours. The dowel pins plugging the sensor holes are removed, and 700 grit paper is used. The sandpaper is fixed to a small piece of wood and allowed to soak in water. The wet sanding is always done in the streamwise direction.
- Four coats of the LustreKote Jet White spray paint is applied after allowing the White Primer to dry for 24 hours. If sanding of the White Primer is required, the Jet White can be added directly after sanding. Again, paint is added sparingly near the upstream region.
- The Jet White paint is allowed to dry for 24 hours before sanding. The paint is wet sanded first with 700 grit sandpaper fixed to a small piece of wood. Again,

sanding is done in the streamwise direction. The paint is then wet sanded with 1000 grit sandpaper. If additional sanding is required, 2000 or 3000 grit sandpaper is used.

- Once the insulating layers (White Primer and Jet White) are allowed to dry and are sanded, the temperature-sensitive paint is applied. The temperature sensitive paint is composed of ethanol, Clearcoat, activator and luminophore molecules. The luminophore molecules used are 99.95% Tris (2,22-bipyridine) dichlororuthenium(II) Hexahydrate (Ru(bpy)), or Ru(bpy) for short. For every 12 mg of Ru(bpy), 10 mL of ethanol is needed to dissolve the molecules. The Ru(bpy) dissolved in ethanol is then added to 20 mL of Urethane Clearcoat. The Urethane Clearcoat used is AmTech AM-500-4. Finally, the AmTech AM-570-12 medium hardener activator is added. The bottle of activator calls for a 4:1 ratio of clearcoat to activator, so therefore 5 mL of the activator is added. TSP should be mixed on the same day that it will be applied.
- Four to six coats of the temperature-sensitive paint is applied with a spray gun, waiting 15 to 20 minutes between coats. It is suggested to wait at least 24 hours before sanding the TSP layer, but it is better to wait 48 hours. The TSP is wet sanded with the same procedure as used for the insulating layers.
- It is possible to expedite this process if time is restricted. The 8 layers of insulating paint (White Primer and Jet White) can be added with no waiting period between the White Primer and Jet White. It is not known if there are any additional risks in expediting the process. The Lustre Kote spray paint cans suggested waiting 24 hours between the Primer and Jet White layers, and this suggestion was typically followed. It is still suggested to wait 24 hours for the insulating layers to dry before they are sanded.
- The sensors are installed using nail polish. Cured nail polish securely holds the sensors in the sensor ports, and can be fairly easily dissolved with acetone. The sensors are made flush with the model surface by slowing pushing the sensors

down with a small ruler, until the ruler lies flat on the model surface. The ruler is left in place for approximately one minute, allowing the nail polish to partially dry. The step between the model surface and the sensor was typically between -15 μm (backward-facing step) and +15 μm (forward-facing step) as measured with the profilometer.

B. Effect of Sensor Height on Measured Heat Transfer

Experiments were performed in August and September 2011 looking at the effect of the step between the model surface and the gauge on the measured heat transfer. Table B.1 gives the gauge model numbers for these set of tests. An initial set of tests did not produce accurate heat transfer results, with many of the gauges showing heat transfer more than 20% above the theoretical heat transfer (Case 1 in Figure B.1). Figure B.1 shows the non-dimensional heat transfer plotted against axial distance along the cone. It was noticed that several of the gauges in Case 1 were not flush with the cone. The last gauge was protruding by roughly 300 μm. It was decided to remove the model from the tunnel, and fix the last gauge. The last gauge was pushed down, reducing the step to about 30μm. Case 2 in Figure B.1 shows that the furthest downstream gauge is in better agreement with the theoretical heat transfer. This is an expected result, as a gauge protruding into the boundary layer would most likely measure a higher heat transfer than a gauge flush with the surface. Note that the first four gauges agree very well between Cases 1 and 2. Also note that the 5th gauge was broken during the second model installation, so no data was gathered from this gauge for Case 2.

It was then decided to reinstall all the Schmidt-Boelter gauges. Table B.2 lists the steps created by the each gauge for each case. The steps were measured using a Mitutoyo surface roughness tester (Model number SJ–301). All the gauges were installed as flush as possible for Case 3, using a small ruler to push down the gauge until it was flush with the surface and the ruler was lying flat on the surface of the cone. The ruler was held in place for roughly 1 minute to allow the nail polish to dry slightly. Case 3 in Figure B.1 shows the heat transfer obtained from this third test. Five of the six gauges are within 20% of the theoretical heat transfer. Only SB–E shows heat transfer more than 20% above the theoretical.

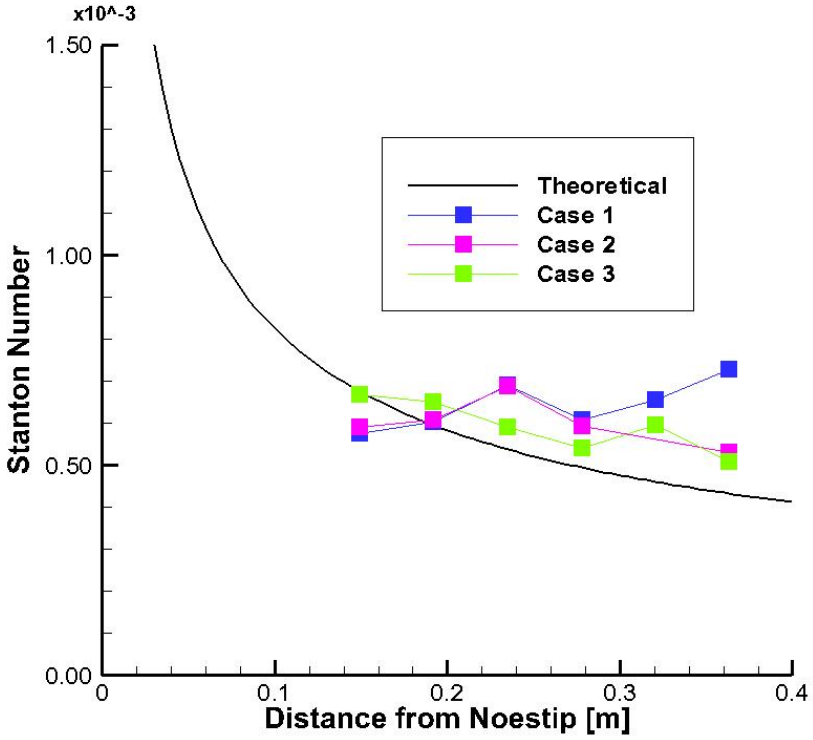

Figure B.1.: Heat transfer from SB gauges with varying protuberance heights into the boundary layer. $p_0 = 131$ psia, Re $= \times 10^6$/m. Quiet flow. All data shown with pre-run offset subtracted. August-September 2011 experiments.

The TSP image for Case 3 is shown in Figure B.2. The boundary layer is most likely laminar since the TSP shows a low even level of heating. Figure B.3 shows the heat transfer reduced from the TSP using SB–C for Case 3, along with the heat transfer obtained from the six heat transfer gauges and the theoretical heat transfer. Once again, the linear heat transfer reduction method works well. The reduced heat transfer agrees well with the theory if the gauge also agrees with the theory. Figure B.4 shows the heat transfer from SB–C over the course of a run, along with the calibrated TSP at the comparative patch. The curve fit algorithm seems to work fairly well when the flow over the gauge remains laminar. Issues tend to arise when the boundary layer

Table B.1.: Position and serial number of the Schmidt-Boelter heat transfer gauges for the August-September 2011 experiments.

Position	**Gauge Name**	**Serial Number**	**Calibration Range**
1	SB–C	167032	0–22 kW/m^2
2	SB–L	164576	0–11 kW/m^2
3	SB–I	169255	0–11 kW/m^2
4	SB–D	167034	0–22 kW/m^2
5	SB–E	167036	0–22 kW/m^2
6	SB–J	169254	0–11 kW/m^2

Table B.2.: Step created by the heat transfer gauges for the August-September 2011 experiments.

Position	**Gauge Number**	**Case 1 Step**	**Case 2 Step**	**Case 3 Step**
1	SB–C	-10μm	-10μm	+8μm
2	SB–L	-26μm	-26μm	-10μm
3	SB–I	+40μm	+40μm	+5μm
4	SB–D	-26μm	-26μm	-19μm
5	SB–E	-10μm	-10μm	+10μm
6	SB–J	+300μm	-30μm	+5μm

transitions [54], and it is not yet clear how well the linear reduction method works in a case where transition is present near the SB gauge.

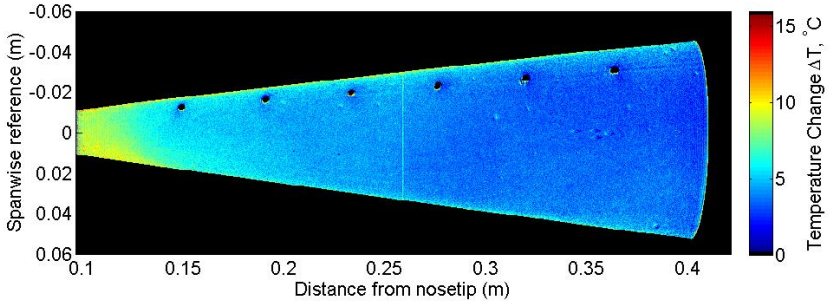

Figure B.2.: TSP image of the 7° half-angle cone at 0° angle of attack. Case 3 from Figure B.1. p_0 = 131 psia, Re = 9.9×10^6/m. Quiet flow. August-September 2011 experiments.

.

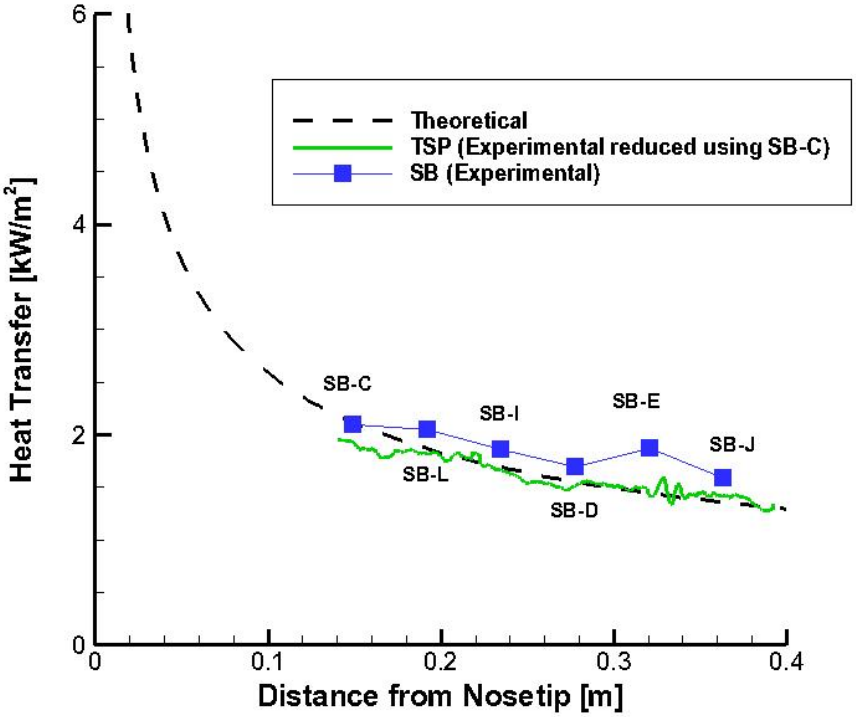

Figure B.3.: Heat transfer rates calculated from TSP with the reduction method and compared to theory. p_0 = 131 psia, Re = 9.9×10^6/m. Quiet flow. All data shown with pre-run offset subtracted.

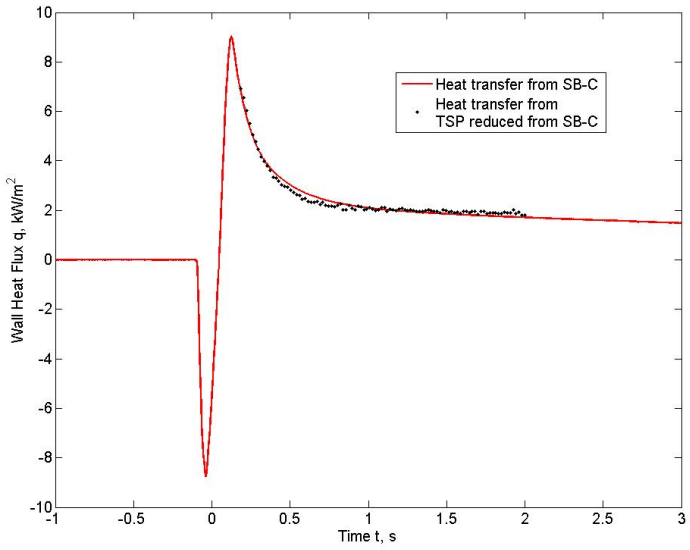

Figure B.4.: Plot of heat transfer from SB–C along with the heat transfer calculated at the comparison patch of TSP. Case 3 from Figure B.1. $p_0 = 130$ psia, Re $= 9.9\times10^6$/m. Quiet flow.

C. Drawings of the Conical Models

Schematics of the five sections of the Crossflow Cone are provided in Figures C.1–C.7. Schematics of the two sections of the Heat Transfer Cone are provided in Figures C.8 and C.9. The steps at the joints are shown in Section 3.7.

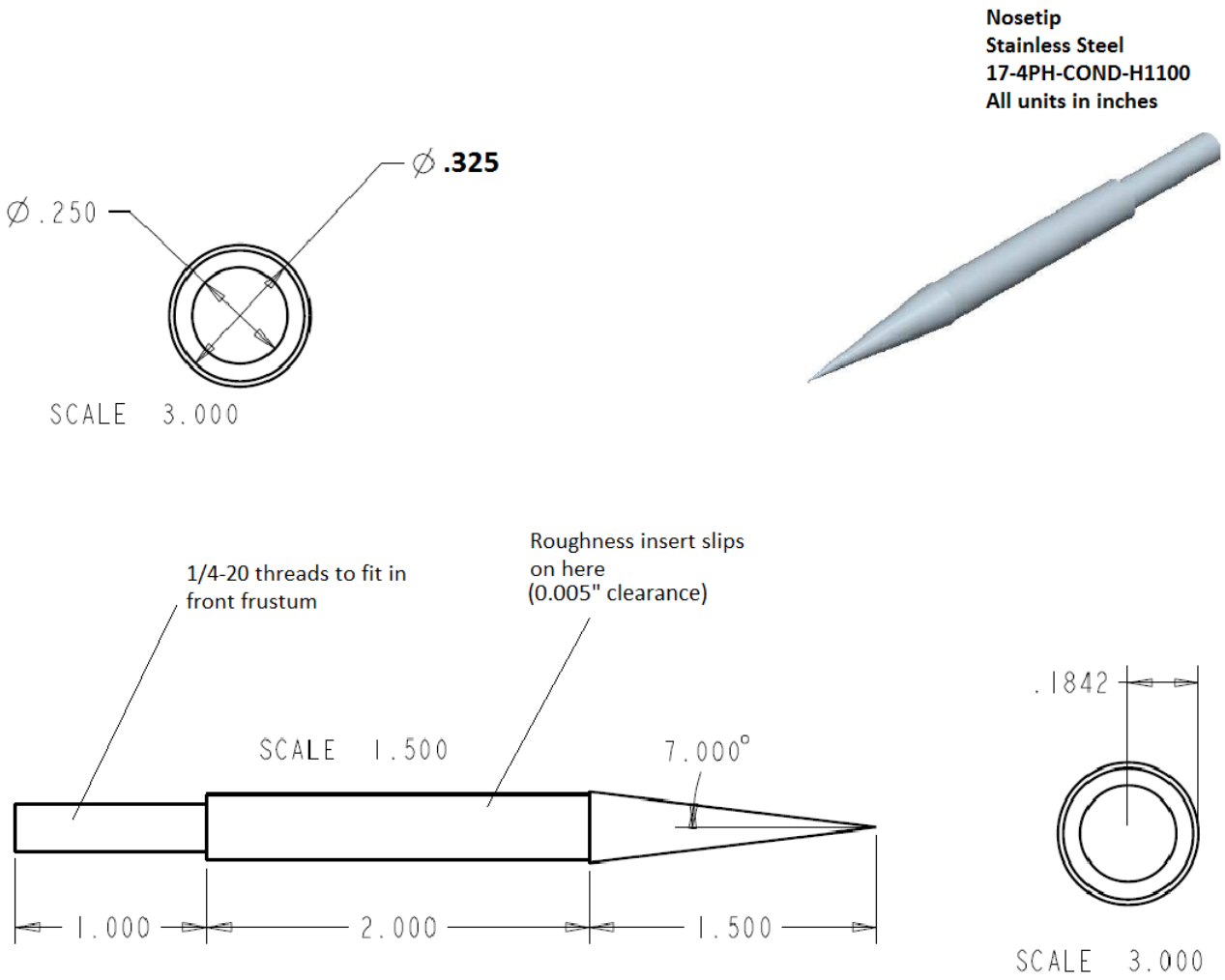

Figure C.1.: Schematic of the Nosetip (Section 1) of the Crossflow Cone.

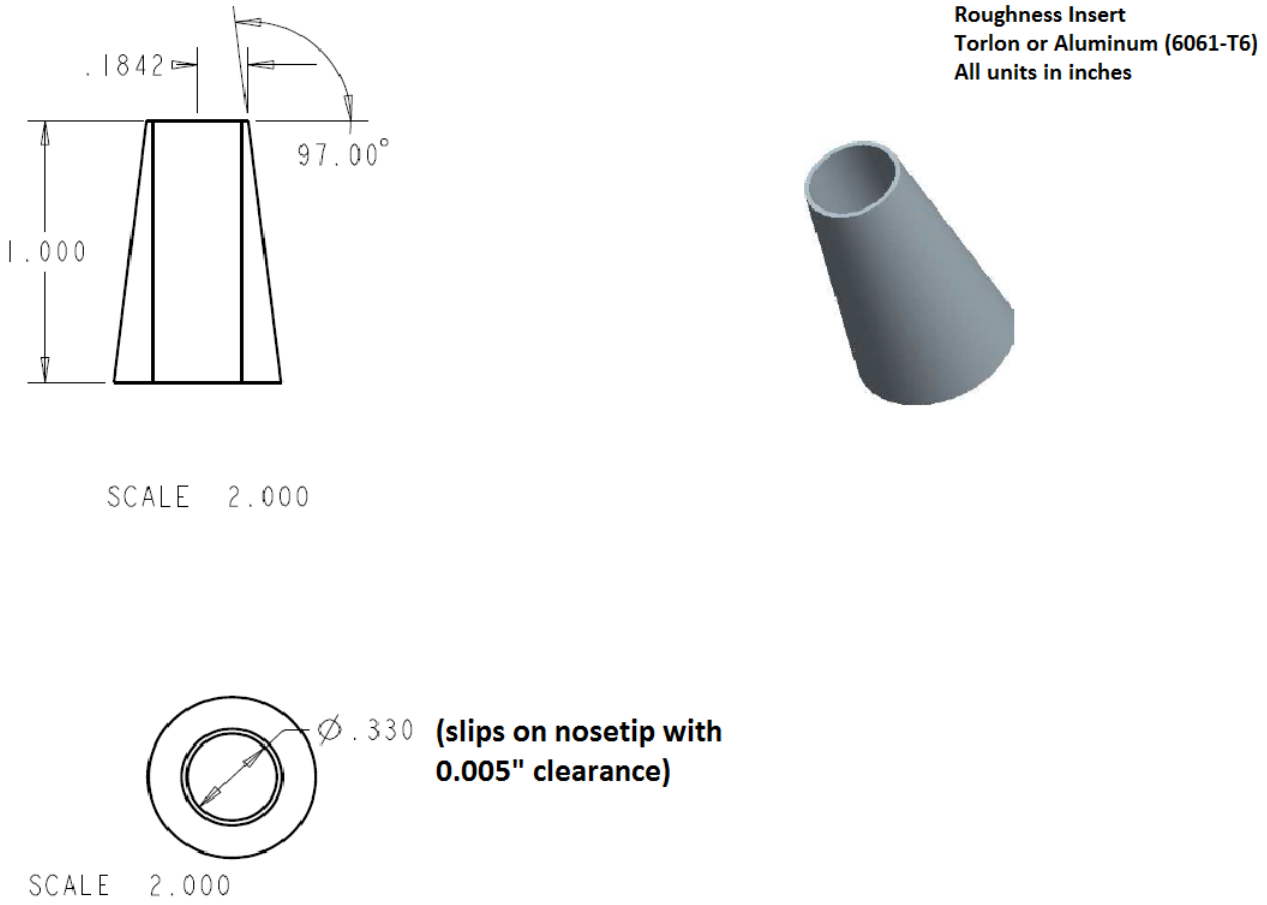

Figure C.2.: Schematic of the Roughness insert (Section 2) of the Crossflow Cone.

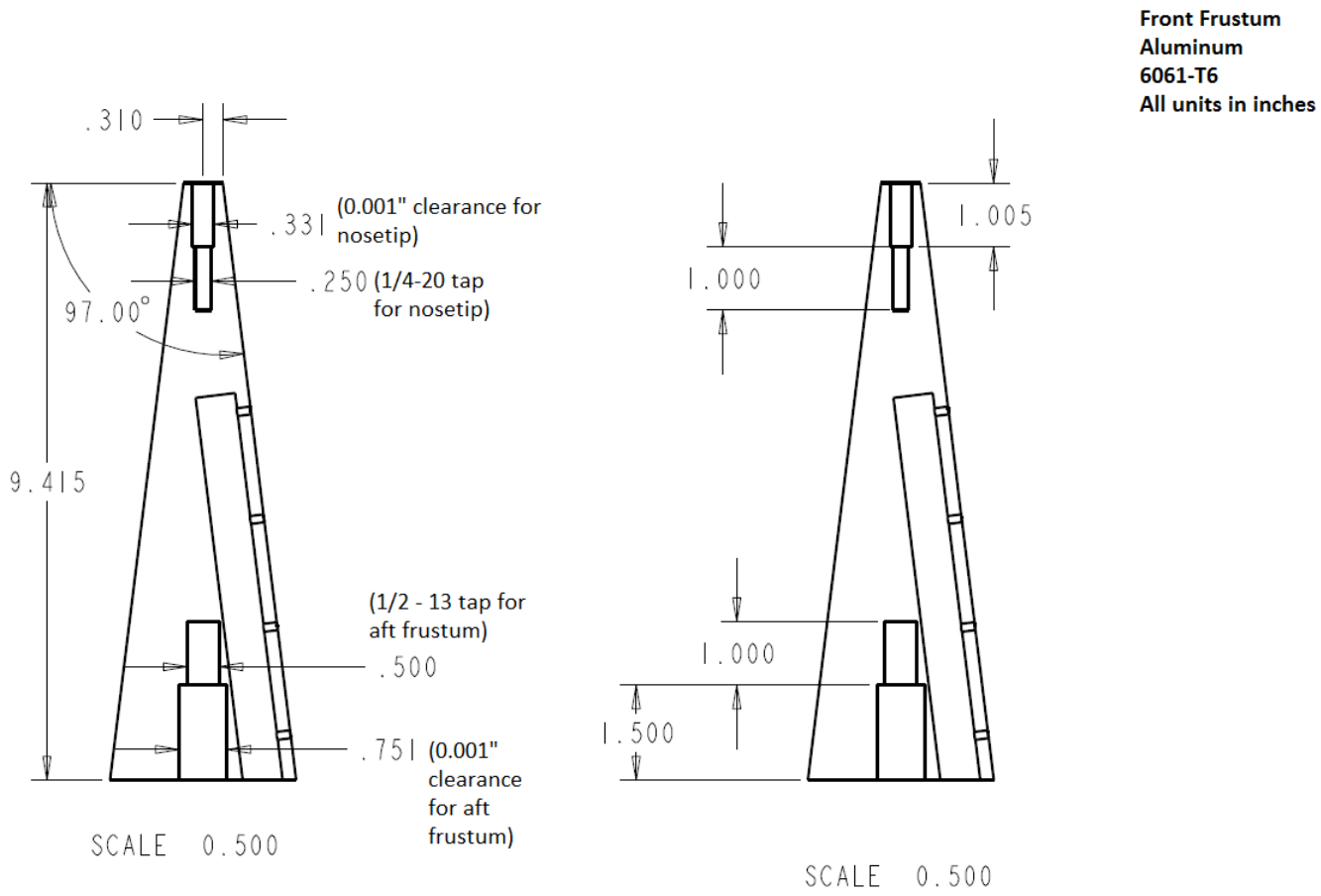

Figure C.3.: Schematic of the Front Frustum (Section 3) of the Crossflow Cone.

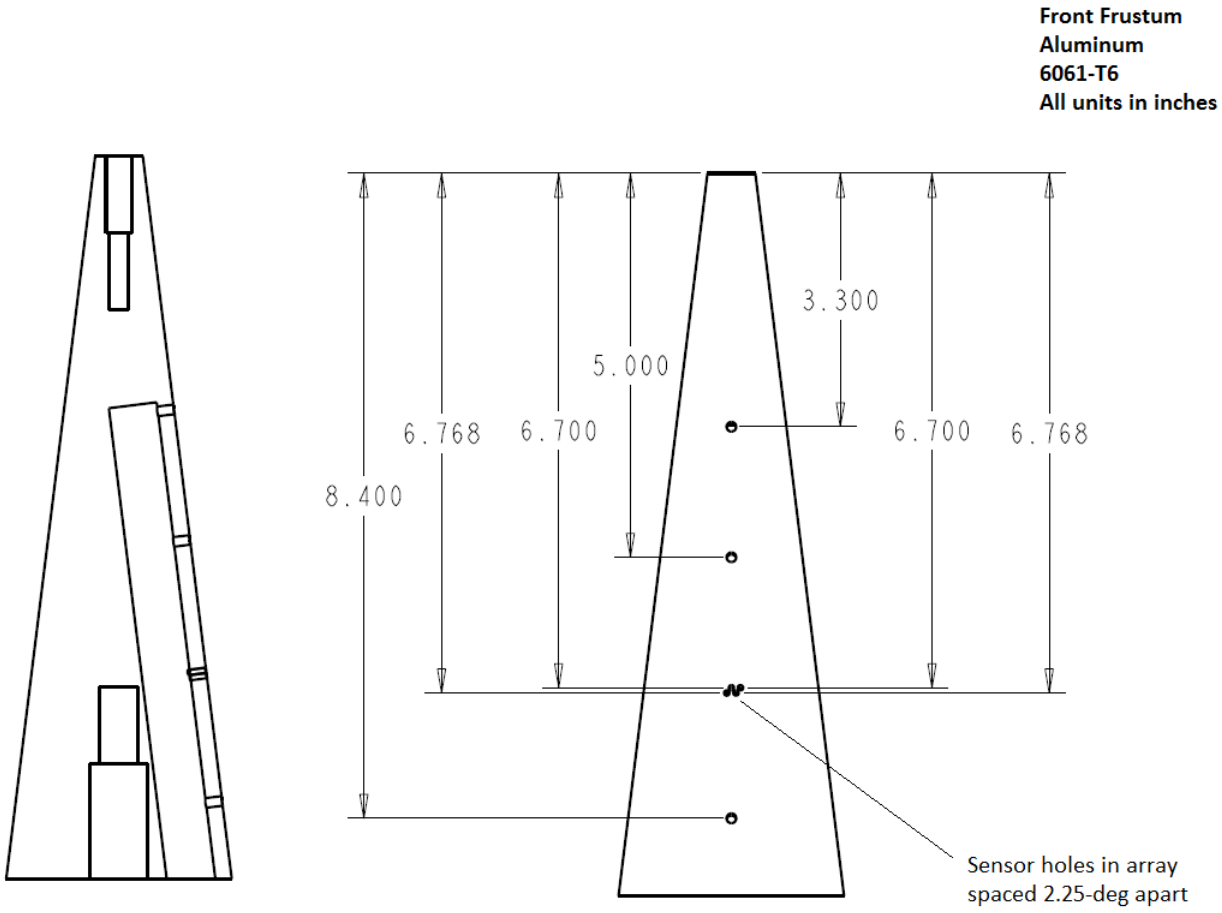

Figure C.4.: Schematic of the Front Frustum (Section 3) with the sensor locations shown of the Crossflow Cone.

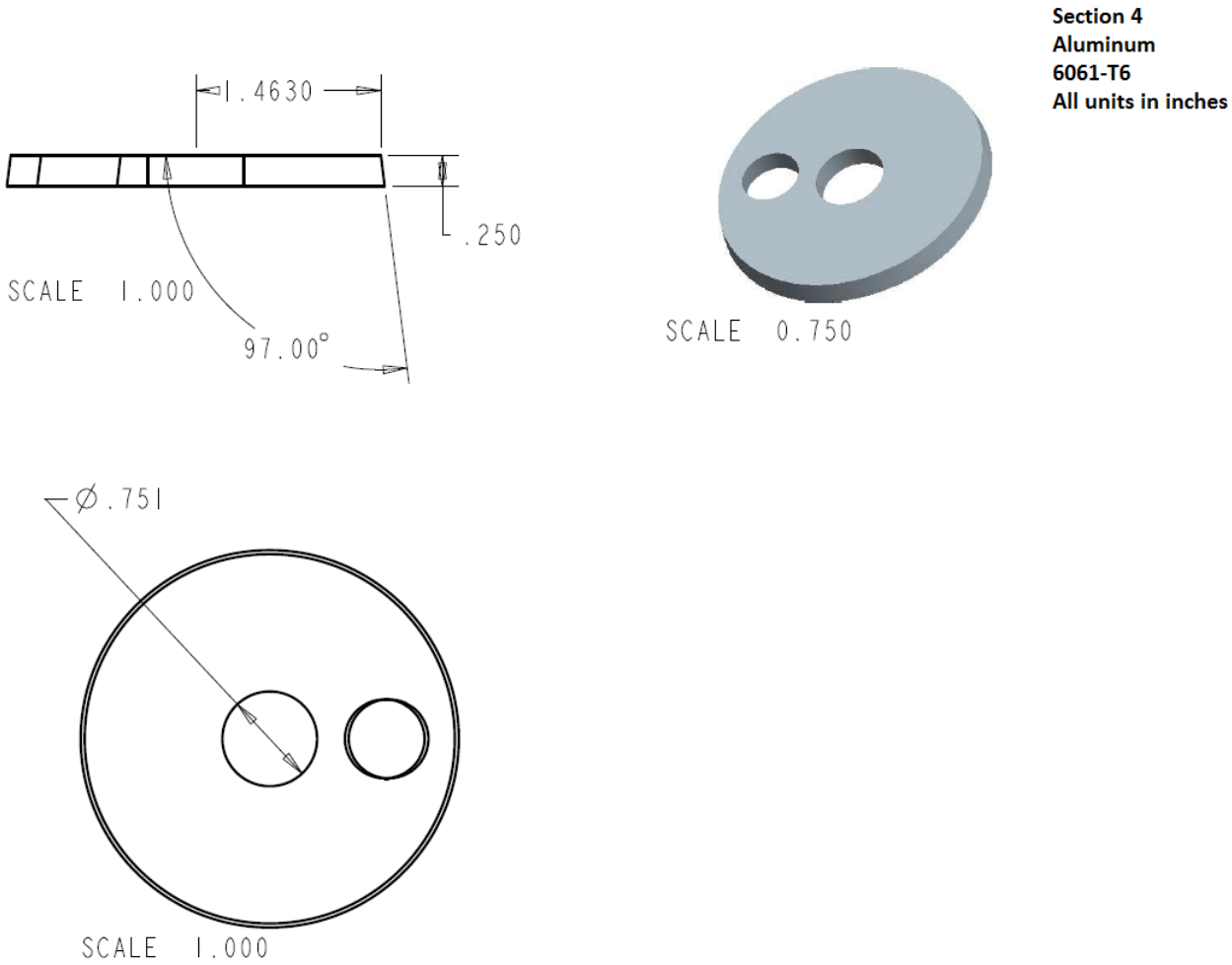

Figure C.5.: Schematic of the Section 4 of the Crossflow Cone.

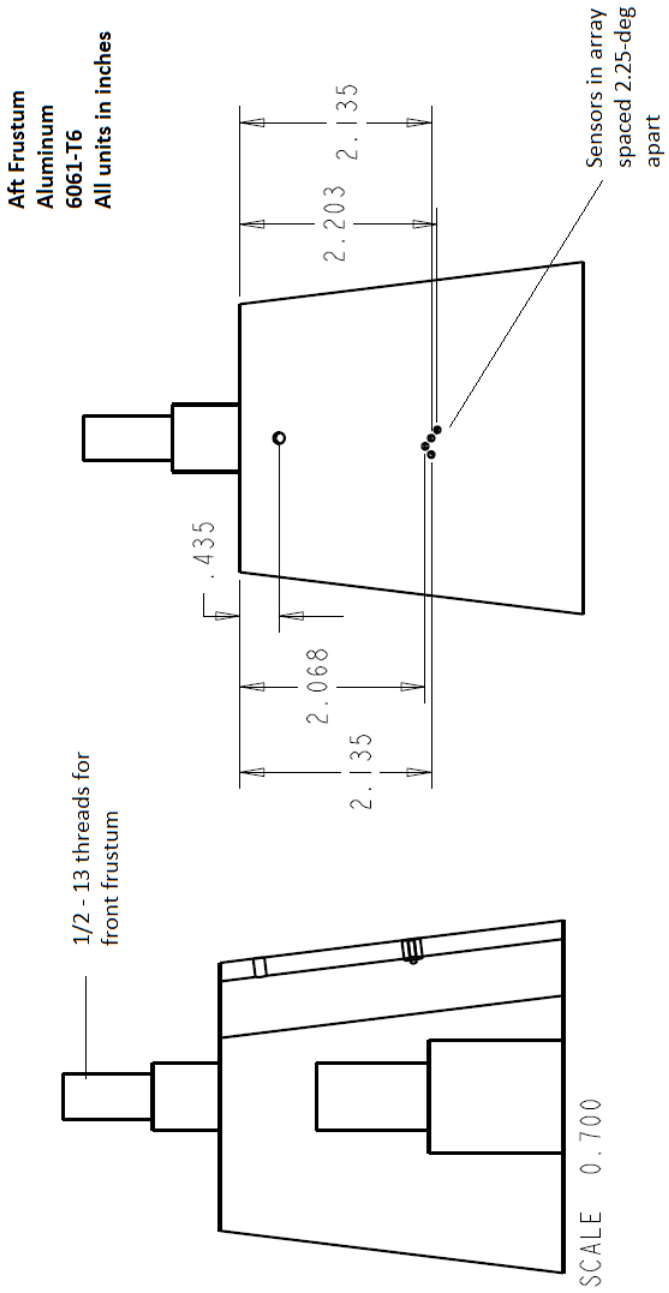

Figure C.6.: Schematic of the Aft Frustum (Section 5) of the Crossflow Cone.

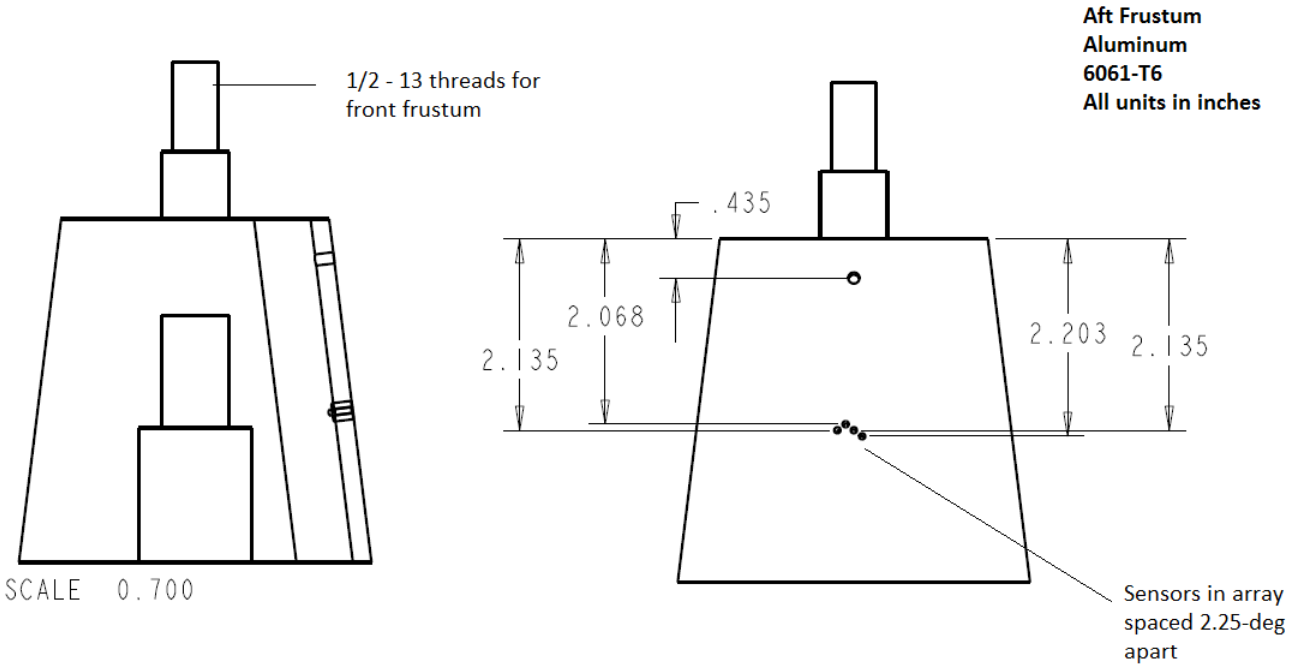

Figure C.7.: Schematic of the Front Frustum (Section 5) with the sensor locations shown of the Crossflow Cone.

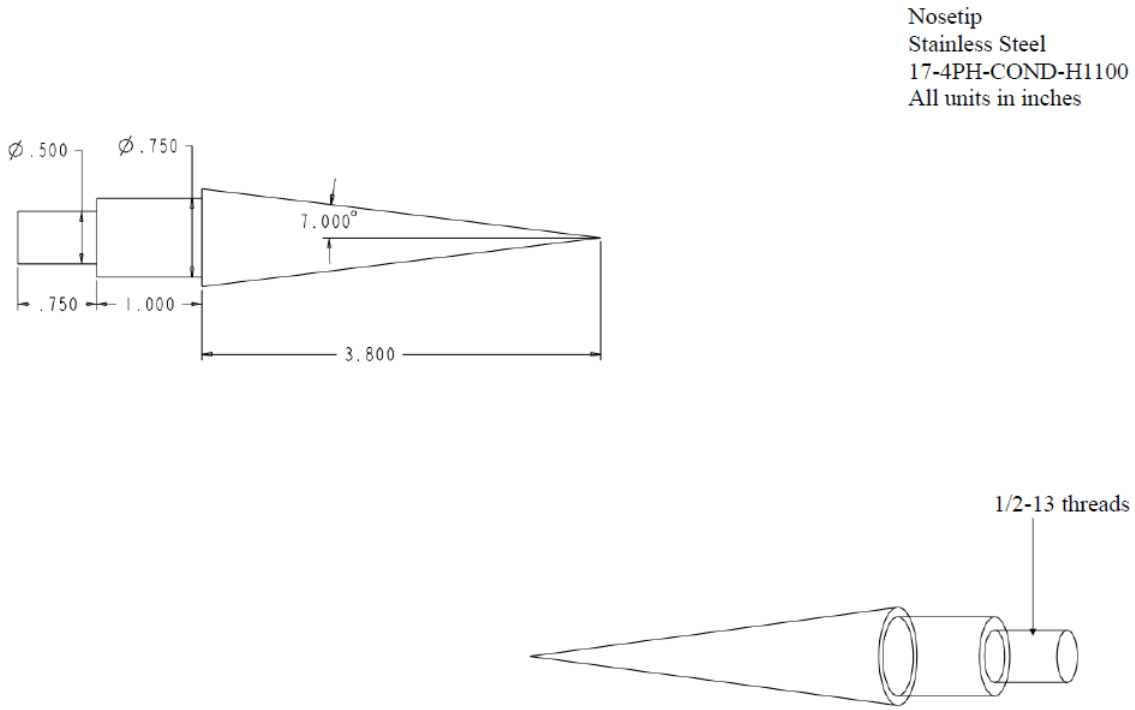

Figure C.8.: Schematic of the nominally sharp nosetip of the Heat Transfer Cone.

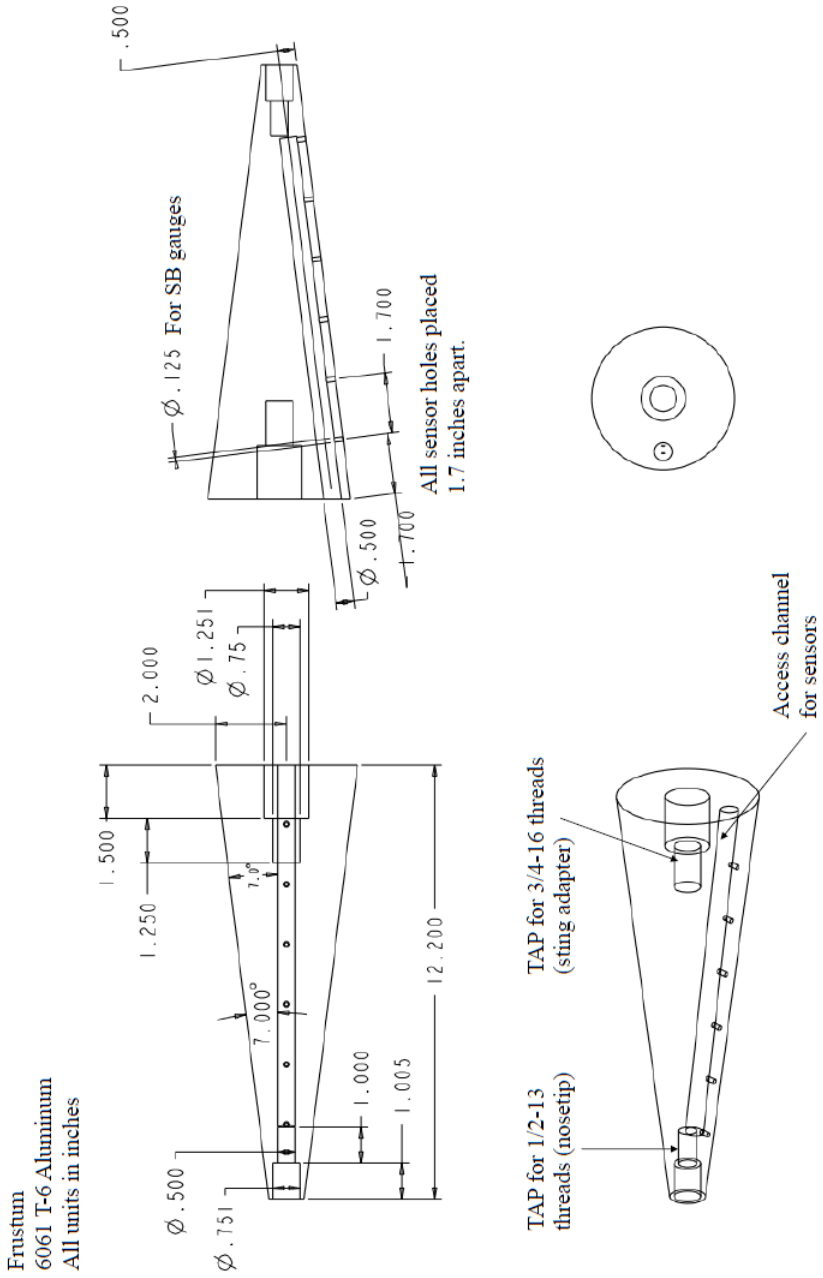

Figure C.9.: Schematic of the frustum of the Heat Transfer Cone.

D. Computer Codes

TSP Image Alignment Code, provided by Professor John Sullivan, modified by Chris Ward.

```
%  call Iratio function
% save IratioMatrix to file
clear all
close all
clc

for i = 35:37

tic

%%%%%%%%%%%% INPUTS %%%%%%%%%%%%%%%

entry               =   8;          % Entry Number
run                 =   i;          % Run Number
drive               =   'F';        % drive for hard drive
model               =   'CF2';
dark_name           =   'Dark';     % name of dark file
Tref                =   297;
B                   =   363;
fsize               =   2;          % size of averaging filter
fnumber             =   2;          % number of times to run
                                    % through filter
a                   =   [0 8];      % scale of dT colourbar
filtering           =   1;          % 0 for no filtering,
                                    % 1 for filtering
minframe            =   1;          % min frame for TSP tiff
```

```
27                                          % files, typically use 1
28 skip                =   1;               % if you want to skip every
29                                          % other frame for example
30 frameoff            =   15;              % number of frames in off image
31 framedark           =   10;              % number of frames in dark image
32 NoiseLevel          =   5000;
33 exposure            =   5/1000;          % not always
34 loop                =   0;               % 1 if you want to loop through
35                                          % all the images
36 %%%%%%%%%%%%%%%%%%%%%%%%%
37
38
39 % gathering necessary info for TSP images
40
41 string1 = char(strcat('b',num2str(run+1)));
42 string2 = char(strcat('k',num2str(run+1)));
43 TSP_Image_Details = xlsread(char(strcat(drive,':\Research Data\', ...
44   num2str(model),'\Entry',num2str(entry),'\Entry',num2str(entry), ...
45   '_TSP_Image_Details.xlsx')),strcat(string1,':',string2));
46
47 x_offset = TSP_Image_Details(1);    % offset in x-axis of image
48 y_offset = TSP_Image_Details(2);    % offset in y-axis of image
49 pix_per_m = TSP_Image_Details(3);   % number of pixels per metre in
50                                     % images
51 pixelcompx = TSP_Image_Details(4);  % pixel value of left x-coordinate
52                                     % where comparison to tsp will be
53                                     % made
54 pixelcompy = TSP_Image_Details(5);  % pixel value of top y-coordinate
55                                     % where comparison to tsp will
56                                     % be centered
57 max_time = TSP_Image_Details(6);    % max time to be used in TSP ht
58                                     % reduction, seconds
59 desired_time = TSP_Image_Details(7);% desired time to examine more
60                                     % closely, seconds
61 freq = TSP_Image_Details(9);        % frequency of camera pictures
```

```
62 mid_y = TSP_Image_Details(10);      % the pixel that approximately
63                                     % lines up with the middle of
64                                     % the model in the y-direction
65
66 maxframe = max_time*freq+minframe;
67
68 desired_frame = round(desired_time*freq);
69
70
71 imagefile = char(strcat(drive,':\Research Data\',num2str(model), ...
72   '\Entry',num2str(entry),'\Paint Data\Run',num2str(run),'\run', ...
73   num2str(run),'.tif'));
74 offimage = char(strcat(drive,':\Research Data\',num2str(model), ...
75   '\Entry',num2str(entry),'\Paint Data\Run',num2str(run),'\off.tif'));
76 darkimage = char(strcat(drive,':\Research Data\',num2str(model), ...
77   '\Entry',num2str(entry),'\Paint Data\',num2str(dark_name),'.tif'));
78
79
80 ts =                .16;
81 B =                 363;
82
83
84 timeframe   = freq * skip;  %seconds per frame
85
86 [ IratioMatrix shiftX shiftY] = Iratio( offimage,imagefile,...
87     darkimage,minframe,maxframe,skip,framedark,frameoff,...
88     NoiseLevel, filtering);
89
90 toc
91 max_x = length(IratioMatrix(1,:,1));   % maximum x-pixel in TSP image
92 max_y = length(IratioMatrix(:,1,1));   % maximum y-pixel in TSP image
93 save (strcat(drive,':\Research Data\',num2str(model),'\Entry',...
94     num2str(entry),'\Paint Data\Run',num2str(run),...
95     '\IratioFile.mat'),'IratioMatrix')
96 toc
```

```
97
98
99
100 fontsize = 16;
101 load TSPcolormap;
102
103 xpixel = 1:max_x;
104 ypixel = 1:max_y;
105 xaxis = x_offset + xpixel/pix_per_m;
106 yaxis = y_offset - ypixel/pix_per_m;
107
108
109 figure(1)
110 DeltaT = (Tref-B) .* IratioMatrix(:,:,desired_frame) + B - Tref;
111 imagesc(xaxis,yaxis,DeltaT,a)
112 colormap(TSPcolormap);
113 colorbar;
114 xlabel('Distance from nosetip (m)','FontSize',16);
115 ylabel('Spanwise reference (m)','FontSize',16);
116 t = colorbar('peer',gca);
117 set(get(t,'YLabel'),'String','Temperature Change \DeltaT, ^\circC')
118 set(get(t,'YLabel'),'FontSize',16)
119 set(get(t,'YLabel'),'FontWeight','bold')
120 set(t,'FontSize',16)
121 set(t,'FontWeight','bold')
122 axis image
123
124
125 shiftX = 1000*shiftX/pix_per_m;
126 shiftY = 1000*shiftY/pix_per_m;
127
128 maxtime=(1/timeframe)*(maxframe-1);
129 mintime=(1/timeframe)*(minframe-1);
130 t_tsp = (mintime:1/timeframe:maxtime)';
131 figure (2)
```

```
132 % change sign for "on" model motion not ref motion
133 plot(t_tsp,-shiftX,'g')
134 hold on
135 plot(t_tsp,-shiftY,'r')
136 grid
137 xlabel('t (s)','FontSize', fontsize);
138 ylabel('Displacement (pixels)','FontSize', fontsize);
139 legend('Xshift', 'Yshift');
140 hold off
141
142
143 %leave this in if you want to loop through all the images
144 if loop == 1
145     for j = 1:maxframe
146         figure(j+2)
147         DeltaT = (Tref-B) .* IratioMatrix(:,:,j) + B - Tref;
148         imagesc(xaxis,yaxis,DeltaT,a)
149         colormap(TSPcolormap);
150         colorbar;
151         xlabel('Distance from nosetip (m)','FontSize',16);
152         ylabel('Spanwise reference (m)','FontSize',16);
153         t = colorbar('peer',gca);
154     set(get(t,'YLabel'),'String','Temperature Change \DeltaT,^\circC')
155         set(get(t,'YLabel'),'FontSize',16)
156         set(get(t,'YLabel'),'FontWeight','bold')
157         set(t,'FontSize',16)
158         set(t,'FontWeight','bold')
159         axis image
160     end
161 end
162
163 end
```

```
1 function [ IratioMatrix shiftX shiftY ] = Iratio( Off_file,...
```

```
2       On_file,Dark_file,minframe,maxframe,skip,framedark,...
3       frameoff,NoiseLevel, filtering)
4   % Returns IratioMatrix with image registration and
5   % cleanup outside the model
6   %
7
8   % setup filter parameters
9   fsize   = 4;
10  h       = fspecial('average',fsize);
11
12
13  %get dark image
14  j = 0;
15  darksum = zeros(size(double(imread(Dark_file,1))));
16  for i=1:framedark
17      darksum=  darksum + double(imread(Dark_file,i));
18  end
19  dark=  darksum ./ framedark;
20
21
22  %get off image
23  offsum = zeros(size(double(imread(Off_file,1))));
24  for i=1:frameoff
25      offsum=  offsum + double(imread(Off_file,i));
26  end
27  off=  offsum ./ frameoff;
28
29  if filtering==1
30      dark    = filter2(dark,h,'full');
31      off     = filter2(off,h,'full');
32  end
33
34  % Get on images
35   [m n ]=size(off);
36   IratioMatrix=single(zeros(m,n,(maxframe-minframe+1)/skip));
```

```
for i=1:skip:maxframe-minframe+1
    on = double(imread(On_file,i+minframe-1));

    if filtering==1
        on      = filter2(on,h,'full');
    end

    % image registration
    [output off1] = dftregistration(fft2(on),fft2(off),100);
    shiftX(i)=output(4);
    shiftY(i)=output(3);
    offShift=abs(ifft2(off1));

    % remove noise outside of model
    IndexNoise=on<NoiseLevel;
    on(IndexNoise)=0;

    Iratio = (on-dark) ./ (offShift-dark);
    Iratio=single(Iratio);
%     if filtering==0
%         Iratio      =fliplr(Iratio);
%     elseif filtering==1
%         Iratio      = flipud(Iratio);
%     end
    IratioMatrix(:,:,i)= Iratio;
 end
% j = 0;
% if skip>1
%     for i=1:skip:maxframe-minframe
%         j = j+1;
%         IratioMatrix2(:,:,j)=IratioMatrix(:,:,i);
%     end
% IratioMatrix = IratioMatrix2;
end
```

```
1
2
3  function [output Greg] = dftregistration(buf1ft,buf2ft,usfac)
4  % function [output Greg] = dftregistration(buf1ft,buf2ft,usfac);
5  % Efficient subpixel image registration by crosscorrelation. This
6  % code gives the same precision as the FFT upsampled cross
7  % correlation in a small fraction of the computation time and with
8  % reduced memory requirements. It obtains an initial estimate of
9  % the crosscorrelation peak by an FFT and then refines the shift
10 % estimation by upsampling the DFT only in a small neighborhood of
11 % that estimate by means of a  matrix-multiply DFT. With this
12 % procedure all the image points are used to compute the upsampled
13 % crosscorrelation.
14 % Manuel Guizar - Dec 13, 2007
15
16 % Portions of this code were taken from code written by
17 % Ann M. Kowalczyk and James R. Fienup.
18 % J.R. Fienup and A.M. Kowalczyk, "Phase retrieval for a
19 % complex-valued Object by using a low-resolution image,"
20 % J. Opt. Soc. Am. A 7, 450-458 (1990).
21
22 % Citation for this algorithm:
23 % Manuel Guizar-Sicairos, Samuel T. Thurman, and James R. Fienup,
24 % "Efficient subpixel image registration algorithms," Opt. Lett. 33,
25 % 156-158 (2008).
26
27 % Inputs
28 % buf1ft    Fourier transform of reference image,
29 %           DC in (1,1)   [DO NOT FFTSHIFT]
30 % buf2ft    Fourier transform of image to register,
31 %           DC in (1,1) [DO NOT FFTSHIFT]
32 % usfac     Upsampling factor (integer). Images will be registered to
33 %           within 1/usfac of a pixel. For example usfac = 20 means
34 %           the images will be registered within 1/20 of a pixel.
```

```
35 %           (default = 1)
36
37 % Outputs
38 % output =  [error,diffphase,net_row_shift,net_col_shift]
39 % error     Translation invariant normalized RMS error between
40 %           f and g
41 % diffphase     Global phase difference between the two images
42 %               (should be zero if images are non-negative).
43 % net_row_shift net_col_shift   Pixel shifts between images
44 % Greg      (Optional) Fourier transform of registered version of
45 %           buf2ft, the global phase difference is compensated for.
46
47 % Default usfac to 1
48 if exist('usfac')~=1, usfac=1; end
49
50 % Compute error for no pixel shift
51 if usfac == 0,
52     CCmax = sum(sum(buf1ft.*conj(buf2ft)));
53     rfzero = sum(abs(buf1ft(:)).^2);
54     rgzero = sum(abs(buf2ft(:)).^2);
55     error = 1.0 - CCmax.*conj(CCmax)/(rgzero*rfzero);
56     error = sqrt(abs(error));
57     diffphase=atan2(imag(CCmax),real(CCmax));
58     output=[error,diffphase];
59
60 % Whole-pixel shift - Compute crosscorrelation by an IFFT and locate
61 % the peak
62 elseif usfac == 1,
63     [m,n]=size(buf1ft);
64     CC = ifft2(buf1ft.*conj(buf2ft));
65     [max1,loc1] = max(CC);
66     [max2,loc2] = max(max1);
67     rloc=loc1(loc2);
68     cloc=loc2;
69     CCmax=CC(rloc,cloc);
```

```
70      rfzero = sum(abs(buf1ft(:)).^2)/(m*n);
71      rgzero = sum(abs(buf2ft(:)).^2)/(m*n);
72      error = 1.0 - CCmax.*conj(CCmax)/(rgzero(1,1)*rfzero(1,1));
73      error = sqrt(abs(error));
74      diffphase=atan2(imag(CCmax),real(CCmax));
75      md2 = fix(m/2);
76      nd2 = fix(n/2);
77      if rloc > md2
78          row_shift = rloc - m - 1;
79      else
80          row_shift = rloc - 1;
81      end
82
83      if cloc > nd2
84          col_shift = cloc - n - 1;
85      else
86          col_shift = cloc - 1;
87      end
88      output=[error,diffphase,row_shift,col_shift];
89
90  % Partial-pixel shift
91  else
92
93      % First upsample by a factor of 2 to obtain initial estimate
94      % Embed Fourier data in a 2x larger array
95     [m,n]=size(buf1ft);
96     mlarge=m*2;
97     nlarge=n*2;
98     CC=zeros(mlarge,nlarge);
99     CC(m+1-fix(m/2):m+1+fix((m-1)/2),n+1-fix(n/2):n+1+fix((n-1)/2)) ...
100         = fftshift(buf1ft).*conj(fftshift(buf2ft));
101
102     % Compute crosscorrelation and locate the peak
103     CC = ifft2(ifftshift(CC)); % Calculate cross-correlation
104     [max1,loc1] = max(CC);
```

```
105     [max2,loc2] = max(max1);
106     rloc=loc1(loc2);cloc=loc2;
107     CCmax=CC(rloc,cloc);
108
109     % Obtain shift in original pixel grid from the position of the
110     % crosscorrelation peak
111     [m,n] = size(CC); md2 = fix(m/2); nd2 = fix(n/2);
112     if rloc > md2
113         row_shift = rloc - m - 1;
114     else
115         row_shift = rloc - 1;
116     end
117     if cloc > nd2
118         col_shift = cloc - n - 1;
119     else
120         col_shift = cloc - 1;
121     end
122     row_shift=row_shift/2;
123     col_shift=col_shift/2;
124
125     % If upsampling > 2, then refine estimate with matrix multiply DFT
126     if usfac > 2,
127         %%% DFT computation %%%
128         % Initial shift estimate in upsampled grid
129         row_shift = round(row_shift*usfac)/usfac;
130         col_shift = round(col_shift*usfac)/usfac;
131         % Center of output array at dftshift+1
132         dftshift = fix(ceil(usfac*1.5)/2);
133         % Matrix multiply DFT around the current shift estimate
134         CC = conj(dftups(buf2ft.*conj(buf1ft),ceil(usfac*1.5)...
135             ,ceil(usfac*1.5),usfac,dftshift-row_shift*usfac,...
136              dftshift-col_shift*usfac))/(md2*nd2*usfac^2);
137         % Locate maximum and map back to original pixel grid
138         [max1,loc1] = max(CC);
139         [max2,loc2] = max(max1);
```

```
140         rloc = loc1(loc2); cloc = loc2;
141         CCmax = CC(rloc,cloc);
142       rg00 = dftups(buf1ft.*conj(buf1ft),1,1,usfac)/(md2*nd2*usfac^2);
143       rf00 = dftups(buf2ft.*conj(buf2ft),1,1,usfac)/(md2*nd2*usfac^2);
144         rloc = rloc - dftshift - 1;
145         cloc = cloc - dftshift - 1;
146         row_shift = row_shift + rloc/usfac;
147         col_shift = col_shift + cloc/usfac;
148
149     % If upsampling = 2, no additional pixel shift refinement
150     else
151         rg00 = sum(sum( buf1ft.*conj(buf1ft) ))/m/n;
152         rf00 = sum(sum( buf2ft.*conj(buf2ft) ))/m/n;
153     end
154     error = 1.0 - CCmax.*conj(CCmax)/(rg00*rf00);
155     error = sqrt(abs(error));
156     diffphase=atan2(imag(CCmax),real(CCmax));
157     % If its only one row or column the shift along that dimension
158     % has no effect. We set to zero.
159     if md2 == 1,
160         row_shift = 0;
161     end
162     if nd2 == 1,
163         col_shift = 0;
164     end
165     output=[error,diffphase,row_shift,col_shift];
166 end
167
168 % Compute registered version of buf2ft
169 if (nargout > 1)&&(usfac > 0),
170     [nr,nc]=size(buf2ft);
171     Nr = ifftshift([-fix(nr/2):ceil(nr/2)-1]);
172     Nc = ifftshift([-fix(nc/2):ceil(nc/2)-1]);
173     [Nc,Nr] = meshgrid(Nc,Nr);
174     Greg = buf2ft.*exp(i*2*pi*(-row_shift*Nr/nr-col_shift*Nc/nc));
```

```
175     Greg = Greg*exp(i*diffphase);
176 elseif (nargout > 1)&&(usfac == 0)
177     Greg = buf2ft*exp(i*diffphase);
178 end
179 return
180 
181 function out=dftups(in,nor,noc,usfac,roff,coff)
182 % function out=dftups(in,nor,noc,usfac,roff,coff);
183 % Upsampled DFT by matrix multiplies, can compute an upsampled DFT
184 % in just a small region.
185 % usfac         Upsampling factor (default usfac = 1)
186 % [nor,noc]     Number of pixels in the output upsampled DFT, in
187 %               units of upsampled pixels (default = size(in))
188 % roff, coff    Row and column offsets, allow to shift the output
189 %               array to a region of interest on the DFT (default = 0)
190 % Recieves DC in upper left corner, image center must be in (1,1)
191 % Manuel Guizar - Dec 13, 2007
192 % Modified from dftus, by J.R. Fienup 7/31/06
193 
194 % This code is intended to provide the same result as if the
195 % following operations were performed
196 %   - Embed the array "in" in an array that is usfac times larger in
197 %     each dimension. ifftshift to bring the center of the image
198 %     to (1,1).
199 %   - Take the FFT of the larger array
200 %   - Extract an [nor, noc] region of the result. Starting with the
201 %     [roff+1 coff+1] element.
202 
203 % It achieves this result by computing the DFT in the output array
204 % without the need to zeropad. Much faster and memory efficient than
205 % the zero-padded FFT approach if [nor noc] are much smaller than
206 % [nr*usfac nc*usfac]
207 
208 [nr,nc]=size(in);
209 % Set defaults
```

```
210 if exist('roff')≠1, roff=0; end
211 if exist('coff')≠1, coff=0; end
212 if exist('usfac')≠1, usfac=1; end
213 if exist('noc')≠1, noc=nc; end
214 if exist('nor')≠1, nor=nr; end
215 % Compute kernels and obtain DFT by matrix products
216 kernc=exp((-i*2*pi/(nc*usfac))*( ifftshift([0:nc-1]).'...
217     - floor(nc/2) )*( [0:noc-1] - coff ));
218 kernr=exp((-i*2*pi/(nr*usfac))*( [0:nor-1].' - roff )*...
219     ( ifftshift([0:nr-1]) - floor(nr/2)  ));
220 out=kernr*in*kernc;
221 return
```

Code for Calculating the Reynolds Number, written by Chris Ward.

```
function [Re_ft, Re_m, T0] = Re_Calc(p0, p0_init,T0_init, M)

% reads in stagnation pressure at t = 0 and the desired time,
% the stagnation temperature at t = -0
% outputs the Reynolds number per foot and meter and stagnation
% temperature at desired time

g = 1.4;                    % ratio of specific heats
R = 287;                    % Specific gas constant (air) J / kg K
T0_init = T0_init+273.15; % initial Stagnation Temperature, K

% converting the pressure at the desired time and the initial time to
% pascals
p0 = p0 .* 101325 ./ 14.7;
p0_init = p0_init .* 101325 ./ 14.7;

% calculating the stagnation and static temperatures and static
% pressure at the desired time based on isentropic relations
T0 = T0_init.*(p0./p0_init).^((g-1)/g);
p = p0 ./ (1+(g-1)/2*M.^2).^(g/(g-1));
T = T0 ./ (1+(g-1)/2*M.^2);

%viscosity calculated from Sutherland's Law
mu = 0.00001716 .* (T./273).^(3/2) .* (384./(T+111));

% finally calculating Reynolds number
Re_m = p .* M ./ mu .* sqrt(g ./ (R.*T)); % per meter
Re_ft = Re_m*.3048; % per foot
```

VITA

VITA

Christopher A. C. Ward is from Winnipeg, Manitoba, Canada. He attended high school at both Grant Park High School in Winnipeg, MB and Fargo South High School in Fargo, ND. Christopher obtained his B.S. in Aerospace Engineering with Honors from the Illinois Institute of Technology in May 2008. Christopher received his M.S. in Aeronautics and Astronautics from Purdue University in December 2010. He received his Ph.D. from Purdue University in December 2014.